UNIVERSITÀ DEGLI STUDI DI TRIESTE

XXXIII CICLO DEL DOTTORATO DI RICERCA IN

FISICA

Progetto di ricerca cofinanziato dal Fondo Sociale Europeo – Programma Operativo della Regione Friuli Venezia Giulia 2014/2020 – Asse 3 istruzione e formazione
Borsa FSE - EUSAIR/EUSALP

Ultrafast lattice and carrier dynamics in Weyl and Kane quantum materials

Settore scientifico-disciplinare: **FISICA DELLA MATERIA**

DOTTORANDO / A
DAVIDE SORANZIO

COORDINATORE
PROF. FRANCESCO LONGO

SUPERVISORE DI TESI
PROF.SSA MARIA PERESSI

CO-SUPERVISORE DI TESI
DR. FEDERICO CILENTO

ANNO ACCADEMICO 2019/2020

University of Trieste
Doctorate in physics

Ultrafast lattice and carrier dynamics in Weyl and Kane quantum materials

Candidate
Davide Soranzio

Advisor
Prof. Maria Peressi

Co-advisor
Dr. Federico Cilento

Academic Year 2019/2020

Preface

This three-year doctorate research project gave me the opportunity to work with, meet and learn from many people. Thanks to the assigned scholarship, I was able not only to come in contact with Trieste's research community where I spent two years, but also to experience a different environment in Zurich where I was a guest for the second year.

I would like to start this acknowledgment section with my supervisors prof. Maria Peressi and Dr. Federico Cilento. Although both specialized in condensed matter physics, their activities focus distinctly on the numerical simulation and experimental aspects of physics respectively. This combination of different views on physical problems has been a characterizing feature of my work, going from calculations based on density functional theory at the University of Trieste till out-of-equilibrium optical experiments in the T-ReX group at Elettra Sincrotrone Trieste. Their support, suggestions and availability for discussion, including the hundreds of e-mail exchanges, were decisive to overcome even the most complicated moments.

During the year I spent abroad, I was fortunate to be a guest in prof. Steven Johnson's Ultrafast Dynamics Group (UDG) at ETH Zurich. Not only he kindly accepted me as a visiting student, but he also created the best conditions for me to work and feel comfortable in his group as well as in Zurich. From the scientifical point of view, a large portion of this thesis includes work performed under his leadership which helped me to acquire a broader knowledge on the condensed matter physics world.

I wish to thank prof. Fulvio Parmigiani from the University of Trieste and Elettra Sincrotrone Trieste for providing opportunity of discussion during my experience in Trieste regarding not only scientific discussion, but also important advice for the perspectives of a physics student. Moreover, he had a key role in suggesting and establishing the collaboration with the right place for my period abroad.

In Switzerland, I also found a great group of people. During my stay, I worked mostly in close-contact with Dr. Matteo Savoini and prof. Sarah Houver. They both had an unquestionable role in the x-ray and THz experiments presented in this thesis work, which would not have been successful without their expertise and work. However, valuable help for the experiments came also from Dr. Elsa Abreu and Janine Dössegger whose competence was especially necessary for the experiments on HgCdTe, Larissa Boie, Vladimir Ovuka and Dr. Martin J. Neugebauer.

From the Bernina beamline at SwissFEL (PSI, Villigen, Switzerland), I wish to ac-

knowledge the work from Dr. Paul Beaud, Dr. Henrik T. Lemke, Dr. Serhane Zerdane, Dr. Roman Mankowsky, Dr. Yunpei Deng and Dr. Mathias Sander during the x-ray beamtime.

Although we did not work together on works included in the thesis, but I would like to thank for the nice discussions Dr. Bulat Burganov, Dr. Martin Kubli and Dr. Simone Biasco from UDG.

Further aid came from Dr. Frédéric Teppe (Laboratoire Charles Coulomb (L2C), Université Montpellier II, France) who allowed us to borrow the HgCdTe sample and David Stark (ETH Zurich) who helped us in starting the following experiment. Moreover, I would like to recognize the technical support from Valentina Demontis (University of Trieste), Rosita Glavina (University of Trieste) and Erna Hug (ETH Zurich) for the period abroad.

In Trieste, I had the pleasure to share my working time with multiple people. In the T-ReX laboratory, Dr. Andrea Sterzi, Damir Kopič, Dr. Daniel T. Payne, Dr. Simone Peli, Denny Puntel and Dr. Wibke Bronsch. At the department of physics, Dr. Virginia Carnevali and Simone Del Puppo.

In Elettra Sincrotrone Trieste, I received important suggestions to plan future experiments of the FERMI facility from Dr. Filippo Bencivenga, Dr. Riccardo Mincigrucci, Dr. Laura Foglia and Dr. Claudio Masciovecchio.

Last but not least, I would like to thank my family for putting up with me during this three-year period. In particular, my parents Rossana and Sergio, my aunt Tiziana and my grandmothers Luciana and Giuseppina. To conclude, a special thought goes to the remaining members who unfortunately passed away too soon.

Contents

CHAPTER 1

Introduction

This thesis work is centered around the electronic and lattice dynamics in materials exhibiting double-cone energy-momentum dispersions close to their Fermi levels. These systems have been the focus of multidisciplinary studies in recent years, starting from the discovery of the peculiar electrical properties in two-dimensional systems like graphene, which then inspired a vast research interest for three-dimensional systems with analogous characteristics like Dirac and Weyl semimetals. In particular, this last category of materials has its most famous examples in compounds of the transition metal pnictides (TMPs) and transition metal dichalcogenides (TMDCs) families. These study of these systems is motivated by the high-mobility of their electron carriers, nonlinear response in the optical properties, non-trivial topology involving quasi-massless fermions as well as the simultaneous occurrence of a plethora of unusual compound-specific phenomena like extremely high and non-saturating magnetoresistance, quantum spin hall effect, ferroelectricity at room temperature, chiral anomaly and many more.

Moreover, the TMDCs class presents a large number of exfoliable systems, composed by strata of distinct compound layers, which can be used to obtain flakes which resemble graphene, making them appealing materials to create ultrathin devices based on their unique properties.

In this PhD project, the study was dedicated to the out-of-equilibrium phenomena resulting from the excitation of Weyl and Kane semimetals using laser pulses in a wide photon energy range. The results were obtained experimentally through table-top laser systems and setups as well as a large-scale facility such as a free electron laser generating ultrashort hard x-ray pulses. Numerical simulations were carried out using semi-empirical models as well as *ab initio* electronic structure codes to complement our observations. Our conclusions were derived comparing the data resulting from the experimental and theoretical methods, highlighting the important of the advantage of their combined use for studies in condensed matter physics.

The thesis first describes the physics of the materials together with the experimental and computational methods that were employed. Then it is dedicated to the results coming from both experimental and numerical methods. It is organized as follows.

In Chapter 2, we describe the materials under analysis, the Weyl semimetals tantalum arsenide (TaAs) and tungsten ditelluride (WTe_2) and the Kane semimetal mercury cadmium telluride (HgCdTe). Particular attention is dedicated to the properties connected to their double-cone dispersion, such as high carrier mobility and topological properties.

The probes employed to study the cited quantum materials are discussed in Chapter 3, where the physics one can study through laser systems of beams of different photon energy is examined in relation to the performed experiments. The spotlight is set on the ultrafast phenomena occurring from the order of hundred femtoseconds until tens of picoseconds.

Chapter 4 considers the computational methods exploited for the numerical simulations, which have at their center a description of the electronic structure based on density functional theory. We describe its implementation in open-source codes utilized to obtain our results. These allowed us to simulate the response for two of the presented experiments.

The first one is showcased in Chapter 5. It is centered around the possibility to quantify, with a joint use of experimental measurements of the time-resolved broadband reflectivity the T-ReX laboratory at Elettra Sinctrotrone Trieste and numerical simulations of the optical properties, the amplitude of ultrafast oscillations of the atomic positions induced by coherent optical phonons, triggered using a 800 nm pump laser pulse and registered using a supercontinuum of frequencies in the near-infrared/visible frequency range.

The normal modes of the crystals are center of attention also in Chapter 6, where we monitored the time-resolved x-ray diffraction of WTe_2, resulting from the perturbation of the system with a 800 nm pump pulse, detecting the intensity for selected Bragg peaks probed using the SwissFEL free electron laser (Paul Scherrer Institute, Villigen, Switzerland). Once again, the combined use of experiment and computer calculations provides a clearer understanding of the underlying dynamics, together with the additional implementation of a displacive model and complementary time-resolved single-color reflectivity experiments.

In Chapter 7 we switch our focus on the low-energy excitation on Weyl semimetals studying the nonlinear response of the system with two-dimensional terahertz spectroscopy employing broadband THz pulses at different temperature and impinging field conditions. The study, performed in a reflection geometry, concentrates on the effect of accelerating low effective mass carriers provoking nonlinear effects in the dielectric function of the investigated systems centered around their plasma edges.

Chapter 8 is dedicated to another two-dimensional terahertz spectroscopy study, but on the Kane semimetal HgCdTe, exploring, in transmission geometry, the nonlinear effects exhibited by the material using much lower temperature and THz field amplitude conditions. Here, the complementary analysis carried out both in the time and frequency domains, evidencing a highly-nonlinear response, much more pronounced than in the Weyl semimetals under similar thermodynamic conditions. Nevertheless, the underlying dynamics shares similar traits with the Weyl semimetals. The induced effects on the optical properties are understood as deriving from the impact ionization phenomenon leading to carrier multiplication which in turn alters optical properties impacting on the nonlinear polarization through the third-order electric susceptibility.

Finally, we outline the conclusions of the PhD work in Chapter 9, summarizing the main results of the projects as well as their perspectives.

Due to the maximum size for the ArTS upload, the quality of the figures had to be reduced. The best-quality version of the thesis is provided by the author upon request.

CHAPTER 2

Electronic double-cone dispersions

A fundamental feature that sets apart the materials studied in condensed matter physics is the presence of eigenstates in the neighborhood of the chemical potential, when considering an electronic grand canonical ensemble [1].

In condensed matter, this energy parameter is often referred to as Fermi level. In the low-temperature limit towards 0 K, its position can be interpreted as the boundary between occupied and unoccupied states at equilibrium. As the temperature increases, this description becomes increasingly flawed as the occupancy deviates from a strict step function. A direct evidence comes from photoemission studies of metallic systems where, in the non-interacting limit at equilibrium, the bending of the kink of the Fermi-Dirac distribution can be reconstructed [2]. While in such materials this behavior can become of central importance in the properties of samples even at room temperature, in semiconductors and band-insulating systems these effects are in many cases negligible due to the presence of an energy gap separating the states close to the Fermi level. The possibility of having occupation above the band gap is however never strictly zero as tunneling effects may occur, whose probability depends on the size of the band gap, as well as experimental perturbations which may drive the system away from its equilibrium conditions.

In this thesis, the materials under study are semimetals that, while retaining characteristics similar to a metallic behavior, possess low electron-like and hole-like carriers concentrations due to a reduced number of eigenstates close to the Fermi level. As the physical dimensions of the samples are of the order of several hundreds of unit cells, we can employ, in the non-interacting and infinitely periodic limits, an electronic band structure description for their energy levels. In this framework, the reduced number of carriers in equilibrium conditions can be attributed primarily to a small Fermi surface, which is the constant-energy surface in the Brillouin zone corresponding to the Fermi level.

Materials with double-cone dispersions of the bands close to the Fermi level can be associated to quasi-point-like Fermi surfaces [3]. This is the case for graphene and type-I Weyl semimetal tantalum arsenide (TaAs)[4][5]. However, when such structures are tilted, they can also be associated with the distinct electron and hole pockets, such as type-II Weyl semimetal tungsten ditelluride (WTe_2)[6]. In some cases, they can manifest as part

of a more complex energy-momentum dispersion like in the Kane semimetals [7], where the double-cone dispersion is cut at the intersection by a flat band. Mercury cadmium telluride (HgCdTe) is an example of such behavior, where the linearly-dispersing case represents the boundary between the normal and inverted phases of the alloy.

The presence of linearly-dispersing bands at the Fermi level leads to extremely low-mass carriers which in turn may have a central role in the material mobility and thus conductivity properties. Moreover, several nonlinear phenomena due to their small carrier density and masses were predicted and observed [8][9][10][11][12][13][14][15], making these systems of particular interest for implementation in new devices [16][17].

In the following sections, the investigated materials are described with particular focus regarding the role of their double-cone-like dispersions.

2.1 Weyl semimetals

This category of materials is named after the Weyl particle, a massless fermion which obeys to the Dirac equation, originally proposed by the German physicist Hermann Weyl [18], although not for the condensed matter field. This fermion is a particular solution of the Dirac equation [19]

$$(i\gamma^\mu \partial_\mu - m)\psi(x) = 0 \tag{2.1}$$

where γ^μ are the Dirac matrices for the four-dimensional Minkowski space, which can be expressed in the 4x4 chiral representation as $\gamma^0 = \left(\begin{smallmatrix} 0 & 1 \\ 1 & 0 \end{smallmatrix}\right)$,$\gamma^i = \left(\begin{smallmatrix} 0 & \sigma^i \\ -\sigma^i & 0 \end{smallmatrix}\right)$ with σ^i being the 2x2 Pauli matrices $\sigma^1 = \left(\begin{smallmatrix} 0 & 1 \\ 1 & 0 \end{smallmatrix}\right)$, $\sigma^2 = \left(\begin{smallmatrix} 0 & -i \\ i & 0 \end{smallmatrix}\right)$ and $\sigma^3 = \left(\begin{smallmatrix} 1 & 0 \\ 0 & -1 \end{smallmatrix}\right)$, m is the rest mass and $\psi(x)$ is the field, also called Dirac spinor. When using the chiral representation, ψ can be conveniently written as $\left(\begin{smallmatrix} \psi_L \\ \psi_R \end{smallmatrix}\right)$, where the two components are named left-handed and right-handed Weyl spinors. The Dirac equation can be then rewritten as

$$\begin{pmatrix} -m & i(\partial_0 + \boldsymbol{\sigma}\cdot\boldsymbol{\nabla}) \\ i(\partial_0 - \boldsymbol{\sigma}\cdot\boldsymbol{\nabla}) & -m \end{pmatrix} \begin{pmatrix} \psi_L \\ \psi_R \end{pmatrix} = 0 \tag{2.2}$$

This matrix form can be viewed as a system of two equation coupled through the mass term. Setting $m = 0$ leads to the two separate Weyl equations

$$\begin{aligned} i(\partial_0 - \boldsymbol{\sigma}\cdot\boldsymbol{\nabla})\psi_L = 0 \\ i(\partial_0 + \boldsymbol{\sigma}\cdot\boldsymbol{\nabla})\psi_R = 0 \end{aligned} \tag{2.3}$$

Defining $\hat{\sigma} \equiv (1, \boldsymbol{\sigma})$ and $\bar{\sigma} \equiv (1, -\boldsymbol{\sigma})$ gives them in the more compact form

$$\begin{aligned} i\bar{\sigma}\cdot\partial\psi_L = 0 \\ i\hat{\sigma}\cdot\partial\psi_R = 0 \end{aligned} \tag{2.4}$$

Unlike massive particles, the Weyl spinors possess a Lorentz-invariant helicity given by the operator

$$h \equiv \hat{\boldsymbol{p}}\cdot\boldsymbol{S} = \frac{1}{2}\hat{p}_i \begin{pmatrix} \sigma^i & 0 \\ 0 & \sigma^i \end{pmatrix} \tag{2.5}$$

where $\hat{\boldsymbol{p}}$ is the unit vector along the linear momentum operator direction and $\boldsymbol{S}$ is the spin operator. The right-handed Weyl spinor is associated to a helicity $\tilde{h} = +1/2$ eigenvalue, while the left-handed Weyl spinor to $\tilde{h} = -1/2$ (in the literature one finds also ± 1 depending on how h is defined). For massless particles, fields with distinct helicities are

connected to separate chiralities. States of opposite chirality are found by applying the $\frac{1\pm\gamma^5}{2}$ operators, where $\gamma^5 \equiv i \prod_{\mu=0}^{3} \gamma^\mu = \left(\begin{smallmatrix} -1 & 0 \\ 0 & 1 \end{smallmatrix}\right)$ is the chiral operator in our representation, that correspond to

$$\frac{1-\gamma^5}{2} = \begin{pmatrix} 1 & 0 \\ 0 & 0 \end{pmatrix}, \frac{1+\gamma^5}{2} = \begin{pmatrix} 0 & 0 \\ 0 & 1 \end{pmatrix} \tag{2.6}$$

These are none other than projection operators on the left- and right-handed Weyl spinors, which in turn have negative (-1) and positive (+1) chiralities.

Historically, these solutions of the Dirac equation were proposed as a description of neutrinos before the discovery of their oscillation phenomenon which suggested their massive character. In condensed matter physics, interest for peculiar energy-momentum dispersions has been present since the beginning of the twentieth century [20], but only in recent years, thanks to advances in the experimental techniques, fine features of the electronic structure have been unveiled and studied in detail [21][22]. In particular, it was shown that linear crossings of multiple bands can host quasiparticles whose dispersions are described by effective Hamiltonians for massless particles [6][23]. In two-dimensional materials, the most well-known example is graphene [24], described by the 2D Dirac equation close to the K and K' points of the Brillouin zone. In three-dimensional materials, two categories sparked a vast research effort: Dirac semimetals and Weyl semimetals [22]. The semimetal naming is due to the fact that the double-cone intersections found in the energy-momentum space are present close to the Fermi level, usually leading to a small electronic density of states in its correspondence. This is associated to a low electronic carrier density in the material, especially at low temperatures.

These groups can be distinguished on the basis of their symmetries, band degeneracies and topological charge. Dirac semimetals comprise crystals with inversion and time-reversal symmetries with four-band degeneracies at the conic intersections, called Dirac points. This intersection is protected by space group symmetry elements which prevent the opening of a band gap.

Topological invariants are frequently highlighted when discussing topological systems in condensed matter physics. Given the one-particle Bloch wavefunction as $\psi_{n\boldsymbol{k}}(\boldsymbol{x}) = e^{i\boldsymbol{k}\cdot\boldsymbol{x}}|u_{n\boldsymbol{k}}(\boldsymbol{x})\rangle$, where n is the band index and $\mathbf{k}$ the linear momentum, and the transformed Bloch Hamiltonian $H_{\boldsymbol{k}} = e^{-i\boldsymbol{k}\cdot\boldsymbol{x}} H e^{i\boldsymbol{k}\cdot\boldsymbol{x}}$, one defines $\boldsymbol{A}_n(\boldsymbol{k}) = i\langle u_{n\boldsymbol{k}}(\boldsymbol{x})|\nabla_{\boldsymbol{k}} u_{n\boldsymbol{k}}(\boldsymbol{x})\rangle$ as the Berry connection and $\boldsymbol{\Omega}_n(\boldsymbol{k}) = \nabla_{\boldsymbol{k}} \times \boldsymbol{A}_n(\boldsymbol{k})$ as the geometric, or Berry, curvature [25]. When integrated over an enclosed surface ζ around the node, it gives

$$C = \sum_{n_i} \frac{1}{2\pi} \int_\zeta \boldsymbol{\Omega}_{n_i}(\boldsymbol{k}) \cdot d\boldsymbol{S} \tag{2.7}$$

where the summation is taken over the bands comprehending the states inside the considered surface. In topology, this number is called Chern number.

In the case of Dirac semimetals one obtains a null Chern number for the intersection node, making it topologically trivial. Nevertheless, its symmetry protection was found to be quite robust over a range of perturbations introduced in the effective Hamiltonians describing the systems, making this phase realizable not only as the boundary between phases in topological insulators, but also in various crystalline types [26][27][28][29][30][31][32]. Examples of Dirac semimetals include Na_3Bi, Cd_3As_2 and spinel-type crystals.

However, the energy-momentum window in which the Dirac semimetals can be considered as such is sometimes arguable when considering k-integrated properties such as

the magneto-optical response [33], where for Cd_3As_2 the behavior is closer to a Kane semimetal, which is discussed in the last part of this chapter.

When either parity or time-reversal symmetries are broken, it is possible to obtain a Weyl semimetallic phase. The nodes split in pairs and migrate towards different positions in the Brillouin zone. Each of the intersections, now named Weyl points, is characterized by a non-null Chern number (± 1), associated to an opposite chirality, which makes them monopoles of Berry curvature. The nodes, now two-band intersections, are connected by Fermi arcs, surface states, which link Weyl points of opposite Chern number, which plays the role of a topological charge. On a lattice, the Weyl points are strictly required to come in pairs of opposite chirality by Nielsen and Ninomiya's no-go theorem [34]. This means that the topological charge integrated over the Brillouin zone must be zero.

Although topologically protected, perturbations of the lattice structure can annihilate the Weyl points back to a single node or strengthen even more their separation. In principle, this can be done though equilibrium methods involving a change of the atomic coordinates applying uniaxial-strain and high-pressure techniques or inducing a phase instability employing out-of-equilibrium strategies [6][35][36].

While sharing similar characteristics, the topology of these double-cone intersections allows for subtle distinctions leading the type-I and type-II Weyl points [6][37] (Fig. 2.1). This separation comes from the observation that Weyl semimetals can also present Fermi surfaces other than point-like at the Weyl node (now referred to as type-I Weyl points). In fact, at the contact between electron and hole pockets in semimetals, a tilted double-cone intersection presenting the features of a Weyl node may occur.

Formally speaking, the distinction can be viewed starting from a model Hamiltonian describing a Weyl point [6]

$$H(\boldsymbol{k}) = \sum_{i,j} k_i A_{ij} \sigma_j \tag{2.8}$$

where the index i indicates the three momentum components relative to the Weyl point (x,y,z), j refers to the unit matrix plus the three 2x2 Pauli matrices and A_{ij} is a 3x4 matrix of coefficients. Its energy spectrum is found to be

$$\epsilon_{\pm}(\boldsymbol{k}) = \sum_i k_i A_{i0} \pm \sqrt{\sum_{j'} \left(\sum_i k_i A_{ij'} \right)^2} = T(\boldsymbol{k}) \pm U(\boldsymbol{k}) \tag{2.9}$$

where the j' index runs over the three x, y, z components. The two terms in the last step can be considered the kinetic ($T(\boldsymbol{k})$) and potential ($U(\boldsymbol{k})$) components. Being of odd power in the linear momentum, $T(\boldsymbol{k})$ tilts the energy-momentum dispersion and causes the loss of Lorentz invariance [6]. When there exits a $\hat{\boldsymbol{k}}$ direction for which $T(\hat{\boldsymbol{k}}) > U(\hat{\boldsymbol{k}})$, then the two cones intersect the Fermi level in more than just their node and the corresponding Weyl point is regarded as type-II.

This has a direct consequence is the density of states (DOS), and thus carrier density, when the Fermi level is set in correspondence of the Weyl point. In the type-I case, the Fermi surface is point-like with a vanishing DOS, while for type-II is always finite and, as in the case of the material considered in the thesis, usually means a higher carrier density when the Fermi level is located nearby the Weyl points. Another distinction comes from the chiral anomaly [38] in Weyl semimetals: for type-I the phenomenon is present whichever $\hat{\boldsymbol{k}}$; for type-II it occurs only when $\hat{\boldsymbol{k}}$ is within the conic space where $\left|T(\hat{\boldsymbol{k}})\right| > \left|U(\hat{\boldsymbol{k}})\right|$ while the Landau-level spectrum is gapped and no chiral zero-mode exists otherwise.

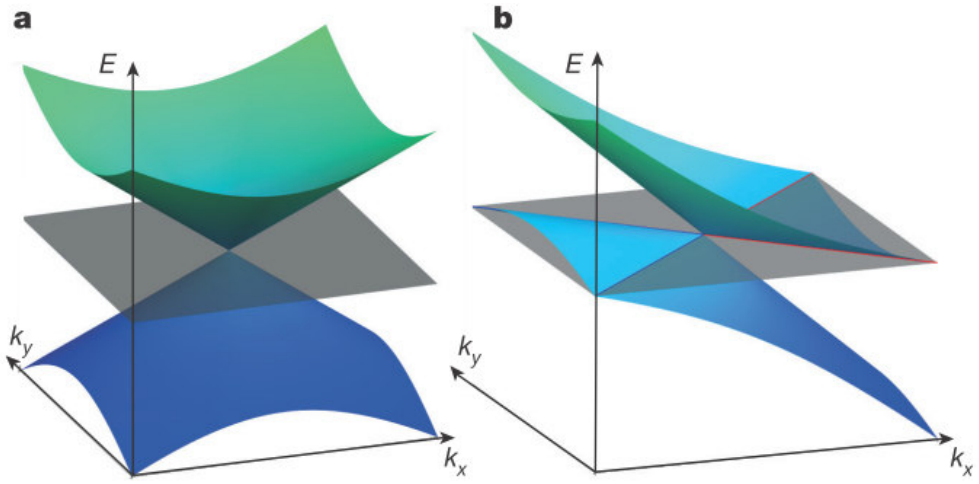

Figure 2.1. Schematic distinction between Weyl points where the Fermi level (grey) is set in correspondence of the double-cone intersection. The panels show the (a) point-like type-I Fermi surface and (b) hourglass-like type-II Fermi surface. From [6].

Usually, materials are named after one of these two types, although nothing in principle prevents their simultaneous presence in the system [6][39][40] as in OsC_2 and NbP, also depending on the thermodynamic conditions. Examples of type-I Weyl semimetals include TaAs [4][5], TaP [41] and NbAs [42]. Among the type-II Weyl semimetals there are WTe_2 [6], $MoTe_2$ [43], $YbMnBi_2$ [44]. As for the Dirac semimetals, the 'Weyl' character of some of these systems is put under question by experimental studies. The possibility to obtain topological and not-topological surfaces further complicates the recognition for surface-sensitive techniques like angle-resolved photoemission spectroscopy (ARPES), where Fermi arcs are analyzed to prove their topological character [45].

Another realization of Weyl physics in condensed matter is found in photonic crystals [46][47][48][49]. Here the linear crossings involve the propagation modes of electromagnetic radiation in the periodic nanostructure with various possible integer Chern numbers associated to the Weyl points. Although at the moment the interest is still predominantly connected to fundamental physics, photonic crystals are a promising platform to explore the Weyl physics under an accurate control of its dispersion features via nanofabrication and may have a relevant impact on predicted photonic analogous of electronic phenomena involving the Berry curvature [50][51][52][53].

2.1.1 TaAs

Tantalum arsenide is a transition metal pnictide (TMP) with a body-centered tetragonal unit cell, whose symmetry elements correspond to those of space group $I4_1md$ [54]. TaAs was the first material to be experimentally resolved as a type-I Weyl semimetal [4][5] together with other TMPs [41]. Usually the samples take the form of small rocks, although they can be cleaved to obtain fresh surfaces for ARPES measurements [4]. Optical peculiarities may be connected, at least partially, to the double-cone dispersion, as second-harmonic generation and chiral emission [55][56][57][58].

Being a semimetal with a point-like band intersection near the Fermi level (its exact position may depend on thermodynamic as well as growth conditions), its quasi-free carrier

density is expected to be relatively low compared to other gapless materials.

Although dedicated experimental studies do not seem currently available in the literature at the moment, this feature appears in the reflectivity spectrum (Fig. 2.2, [56]) under the formation of a plasma edge around 3 THz at 5 K. In a Drude-Lorentz description of the dielectric properties of a material [59], the plasma edge is connected to the plasma frequency of the Drude quasi-free electrons, which is proportional to the square root of the carrier density. Even though the reflectivity also depends on other parameters, such as scattering times and dielectric parameters [59], the edge position is considerably lower than in purely metallic systems, where it is usually found at a few hundred THz (eV order of magnitude)[1][59]. As temperature changes, so does the plasma edge, which bends and changes its characteristic frequency; this behavior is mainly attributed to scattering times and to the chemical potential variations [60].

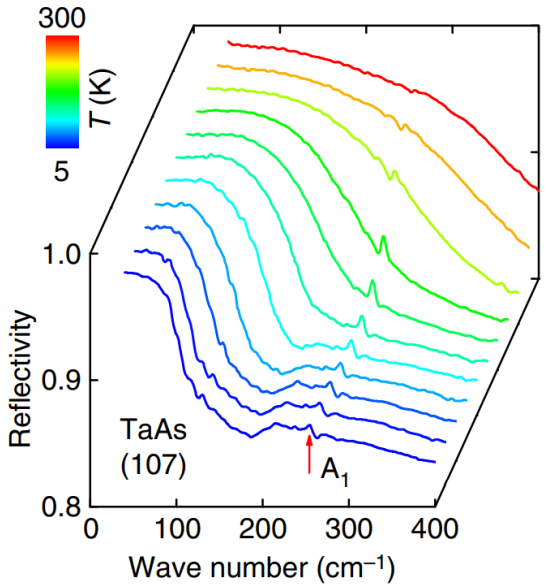

Figure 2.2. Temperature dependence of TaAs's (107) surface reflectivity. The red arrow highlights the peak corresponding to the Fano resonance of a A_1 phonon mode. Adapted from [56].

2.1.2 WTe_2

Tungsten ditelluride is a layered transition metal dichalcogenide (TMDC) with in-plane covalent bonding and weaker van der Waals interplanar interactions helping to hold together the individual layers. At equilibrium, its structure (tagged as Td) can be described by the orthorhombic space group $Pmn2_1$ [61], aside from high temperature (>600 K) [62] and high pressure conditions [63], where the material exhibits its monoclinic phase 1T'.

The sample is grown with the shape of thin ribbons, which can be easily exfoliated to obtain either flakes or freshly-cleaved surfaces. Usual growth processes [64] lead to samples elongated along the tungsten chains direction, usually reported as a or x, while for other perpendicular in-plane axis the crystal dimension, b or y, is normally shorter as well as for the interlayer axis, c or z. The material hosts various unusual properties, among which there are an extremely high and non-saturating magnetoresistance [65], possible type-II Weyl semimetal character [6], quantum spin hall effect [66] and room-temperature ferroelectricity [67].

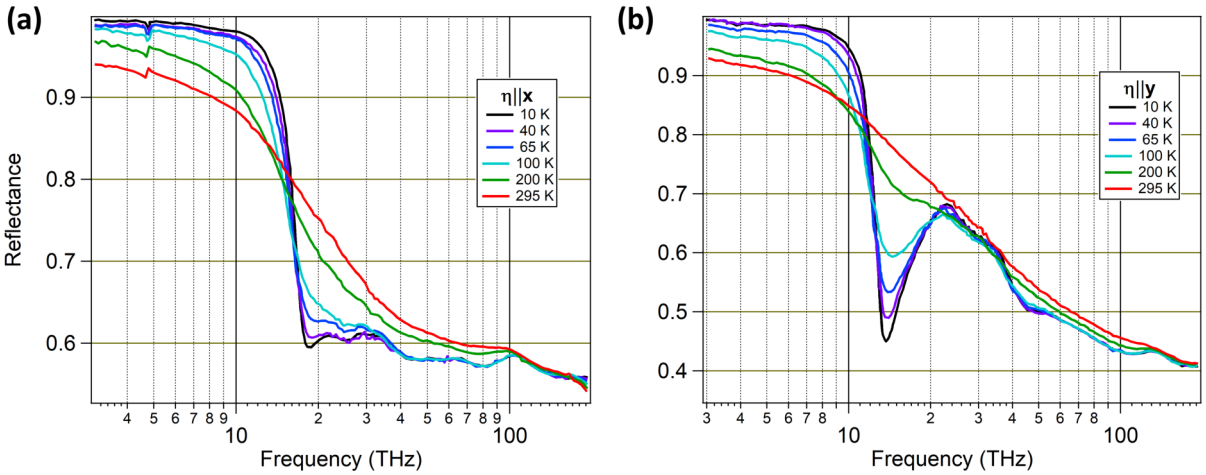

Figure 2.3. Temperature dependence of WTe_2's reflectance using linearly polarized light along the (a) x and (b) y crystallographic axes. Adapted from [68].

Being a type-II Weyl semimetal, its Fermi surface is not point-like regardless of the Fermi level position. As previously mentioned, this intrinsically means a higher density of states and, usually, a higher number of quasi-carriers. Following the same Drude-Lorentz picture described before, we see, in fact, that even though much lower than the usual metal, the plasma edge position is set at higher frequencies (Fig. 2.3, [68]) when compared to TaAs for analogous temperatures (Fig. 2.2).The reflectance response is reported for the two in-plane axes, showing a lower plasma frequency along y. This anisotropy has been mainly connected effective mass anisotropy of the quasi-free Drude-like carriers.

To conclude this section, two of the most peculiar WTe_2's properties are treated in more detail: its magnetoresistance and type-II Weyl semimetal character.

Magnetoresistance

Tungsten ditelluride's magnetoresistance was demonstrated to be extremely high and non-saturating even over 60 T [65] at low temperature. These characteristics depend on a series of factors: temperature [65][69][70], growth conditions [64], stoichiometry [71], defects [72], dopants [73][74], aging [75][76], strain [77], thickness [78][79][80], gating voltage [81][82][83], heterostructure engineering [84]. Moreover, under high (∼10 GPa) pressure conditions, the large magnetoresistance is suppressed with the emergence of superconductivity at low temperatures [85]. The origin of such phenomenon is still under debate. Several reports support [86][87][88] a compensation mechanism between electron and hole carriers to be the main source of the large magnetoresistance. The idea is suggested by a two-band model [78][89], where the magnetoresistance can be expressed as

$$MR = \frac{\sigma_e \sigma_h (\sigma_e/n + \sigma_e/p)^2 (B/e)^2}{(\sigma_e + \sigma_h)^2 + \sigma_e^2 \sigma_h^2 (1/n - 1/p)^2 (B/e)^2} \tag{2.10}$$

where σ_e is the electron conductivity, σ_h is the hole conductivity, n is the electron concentration, p is the hole concentration, B is the magnetic field magnitude and e is the fundamental charge.

Support for the compensation condition comes from magnetoresistance measurements in other semimetallic media such as bismuth [90][91], graphite [92], niobium phosphide (NbP) [93], molybdenum ditelluride ($MoTe_2$) [94][95], and tantalum diarsenide ($TaAs_2$) [96].

However, some papers present data leading to a different conclusion [97][98], suggesting other explanations for the magnetoresistance together with a possible role of bands around the center of the Brillouin zone Γ.

Some of the discrepancies among the experimental reports are likely connected to the growth conditions of the samples. For example, the residual resistivity ratio (RRR), defined as the ratio between the difference between the room temperature and low temperature (T→0 K) resistivity and the low temperature (T→0 K) resistivity, varies between 50 and 1256 [64]. This has been considered as an indication of the crystal quality, although it may also depend on the encapsulation environment if the sample is set in a device [88]. Moreover, distinct methods to derive the model parameters were employed either using a fitting procedure [82][88] using a few-band model or maximum entropy mobility spectrum (MEMS) analysis [72], which is claimed to avoid biases in the final results given by the initial conditions of the fitting procedure.

In conclusion, while the mechanism still needs to be fully clarified, most of the evidence points towards the compensation as a key ingredient. The semiclassical model can, in principle, be optimized for the system under analysis. In WTe_2, it is well-know from both experimental and ab-intio simulations that more than two bands cross the Fermi level: at low temperature, the analysis of the Shubnikov de Haas oscillations shows that at least three pockets [99] are present although the exact number varies in the literature [64]. The accurate description of the Fermi surface is quite tricky as WTe_2's transport properties are very sensitive to the precise position of the chemical potential [13]. Its T=0 K electronic configuration can be obtained in a relatively simple way using density functional theory codes, although the position of the Fermi level differs depending on the simulation details [13][100]. Moreover, ARPES studies, cited in the next section, have shown that the detailed Fermi surface configuration may be even more complex, together with the presence of surface states of different origin [101]. For these reasons, a solid all-round, possibly simultaneous, experimental and theoretical characterization is necessary when exploring the topic.

Topological properties

The material was predicted to be a type-II Weyl semimetal [6] sharing similar characteristics its close 'brother' molybdenum ditelluride ($MoTe_2$) [43]. While some reports show experimental data that support this claim [45][102], the presence of topologically trivial arcs complicates the picture [101] when considering the k-resolved energy dispersion.

Weyl signatures have been spotted from magnetotransport [83][103], although the assignment of the observed signatures may provide some debate since similar characteristics were observed at different frequencies [72]. The number, type and presence of Weyl topology can in principle be manipulated through strain [6] and out-of-equilibrium optical perturbations [35][36], which at certain photon energies are expected to destabilize the equilibrium phase, although together with an oscillating response due to the excitation of coherent optical phonons [104][105][106]. This is favored by the close vicinity between Weyl points of the same pair with opposite charity which can annihilate more easily than in other type-II Weyl semimetals [107].

2.2 Kane semimetals

The double-cone intersections in Weyl and Dirac are protected by topology and space group symmetry respectively. However, these characteristics are not always necessary for the existence of point-like degeneracies of linear bands. This is the case of the Kane semimetals.

Their name derives from the popular Kane model [108][109] which has been successfully employed to describe various semiconductors such as zinc blende compounds like InSb, CdTe [110]. The model is based on the $\boldsymbol{k}\cdot\boldsymbol{p}$ perturbation theory and it features a variable number of electronic bands depending on the system under study. It is usually utilized to describe the band structure of semiconductors close to the Fermi level expanding the k-dependent Hamiltonian expression around a certain $\boldsymbol{k}_0$ point where eigenvalues and eigenfunctions, or least the matrix elements with the $\boldsymbol{p}$ momentum operator are known [111].

In certain materials and thermodynamic conditions, it is possible to obtain a double-cone dispersion intersected by a flat, heavy hole band, which can be described through the Kane model. The electron carriers in the conduction band exhibit extremely low effective masses and high carrier mobility [112][113][114][115]. This configuration was realized in 3D systems like $Hg_{1-x}Cd_{1-x}Te$ (HgCdTe) [7] and Cd_3As_2 [33][116][117], where its Kane character may be concomitant with Dirac dispersion closer to the intersection, as well as a complex 2D system like π-conjugated bis(iminothiolato)nickel monolayer [118].

In this thesis, the investigated sample is $Hg_{1-x}Cd_{1-x}Te$ with x∼0.175, giving a material approaching the Kane semimetal phase at low temperature [113].

2.2.1 HgCdTe

Mercury Cadmium Telluride (MCT, $Hg_{1-x}Cd_xTe$) is a binary alloy compound between HgTe (semimetal) and CdTe (semiconductor, 1.5 eV band gap at room temperature) which is commonly found in infrared detectors [119][120]. Thanks to the small lattice mismatch between the two zinc-blende compounds [121], alloys can be produced for any stoichiometric composition represented by the 'x' index.

Its electronic band structure, in particular its band gap [122], varies with the temperature and it can be described using Kane's model [108][109]. Together with temperature and strain [123], stoichiometry is a parameter used to modify the MCT dispersion leading to either a 'normal' or an 'inverted' phase. This terminology refers to the relative energy difference between the Γ_6 and Γ_8 bands resulting in a positive (normal) or negative band gap (inverted) [7][113][124] (Fig. 2.4). Such possibility to manipulate its band structure received further attention after the prediction [125] and experimental confirmation [126] of the presence of quantum spin hall effect in MCT-based quantum wells. Its characteristic electronic structure is also central in the recently proposed implementation as Veselago lens [127]. As a boundary between the two phases, the electronic band structure showcases a linear dispersion close to the Fermi level, hosting Kane fermions [7][113]. Unlike Weyl and Dirac semimetals, such intermediate configuration is not topology- or symmetry-protected, although a topological $\mathbb{Z}_2$ can be defined to differentiate the phases.

The carrier concentration critically depends on both temperature and stoichiometry [113][128], which in turn affects its optical properties both in the quasi-free and more bound carrier, using once again a Drude-Lorentz picture [129]. Clear phonon resonances are present in the reflectivity response, with divided in HgTe- and CdTe-like phonon bands connected to the alloy nature of the sample [130][131].

This material has found a vast application in infrared detectors for both civil and military use, which is favoured by the band gap tunability and generation of secondary electrons from carrier multiplication, also called impact ionization [114].

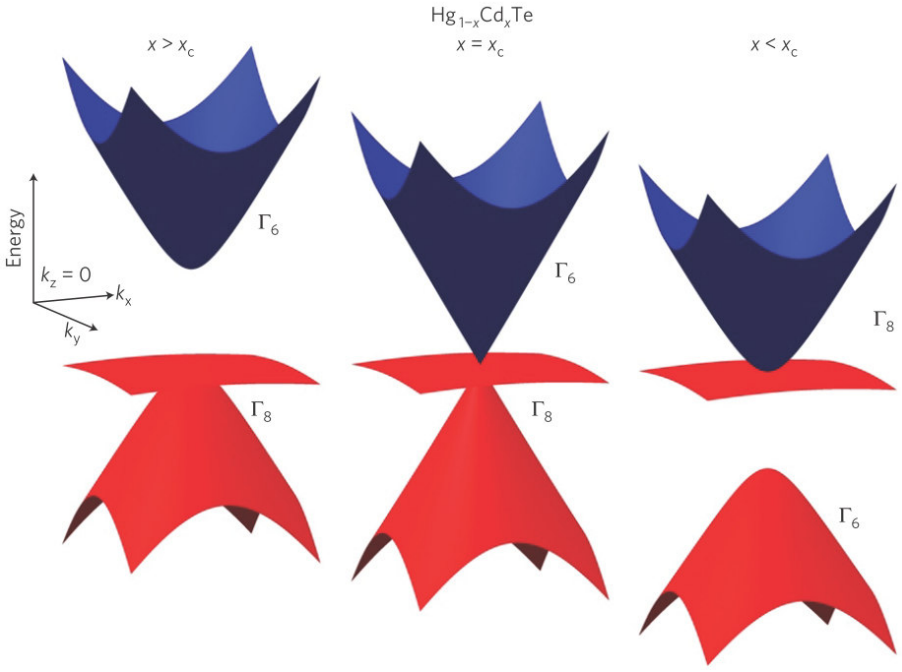

Figure 2.4. Possible band configurations for HgCdTe. (a) Normal phase (b) Boundary condition, Kane semimetal (c) Inverted phase. From [7]. 'x' represents indicates the stoichiometry, while 'x_c' is the critical composition, which depends on thermodynamic parameters like temperature.

CHAPTER 3

Ultrafast physics

Perturbing the equilibrium properties of a material can be used as an intriguing approach to either induce a different state in the system or to understand more profoundly the underlying mechanisms of certain equilibrium phenomena. In condensed matter physics, the electronic and lattice degrees of freedom play a major role in re-establishing an equilibrium condition after an impulsive excitation. Depending on the property one wants to study and the magnitude of the perturbation, the relaxation times may go from attoseconds when exploring the electronic interactions until hours when monitoring a chemical reaction to produce low-defect samples following their kinetic and thermodynamics laws [132][133][134].

Here by 'ultrafast physics', we regard the phenomena that require ultrashort, from hundreds of attoseconds until tens of femtoseconds, laser pulses to monitor the evolution of the involved degrees of freedom in a 'pump-probe' scheme.

The choice of the pump photon energy depends on the material under study, as the presence of a band gap, quasiparticles (*e.g.* excitons, polarons, trions) or energy dispersions of particular topology may be resonant with specific excitations of the system. The probe depends on the observable one wants to monitor which include induced photocurrent, polarization and atomic reorganization. The duration of the pulses is tied to the degrees of freedom of interest (*e.g.* electronic, ionic) and should be preferably shorter than its time scale [132].

As it would be dispersive to treat the large scope of this experimental approach with the required detail, I focus on the effects one can explore using all-optical terahertz and near-infrared/visible measurements as well as hard x-ray diffraction after a near-infrared pump excitation, which are relevant for the thesis.

3.1 Near infrared and visible

Most of table-top pulsed laser sources, such as Ti:sapphire and optical-fiber based lasers, emit a laser beam with photon energy between the near-infrared or visible ranges, usually

in the 500-1600 nm spectral region with varying repetition rate (*i.e.* pulses per second, from a few Hz passing through the kHz range of the amplifiers to the MHz range of the oscillators), pulse energy, temporal duration and energy spread [132][135].

Its accessibility made it the first and most explored spectral range for out-of-equilibrium optical, diffraction and photoemission experiments [132][136][137][138]. Sometimes, it is necessary to exploit higher photon energies. For example, in photoemission spectroscopy, such photon energy is not enough to extract a photoelectron due the work function of the material, typically a few eV, and higher harmonics of the near-infrared beam are necessary. These are usually generated through multiple nonlinear interactions in crystals and gases, providing the possibility not only to extract electrons from deeper levels, but also to explore regions of the Brillouin zone at higher momentum [139], especially in materials where point-like Fermi surfaces or small band gaps are present far from the Γ point like for graphene and superconductors [140][141]. Moreover, the reduced pulse length allows to resolve fast electronic phenomena, which often have time scales smaller than a picosecond. Obtaining lower photon energies can be also a precious tool for experiments. Such wavelengths may be obtained through optical parametric amplifiers (OPAs) or optical parametric oscillators (OPOs) [142][143].

Finally, another useful methodology is to generate a supercontinuum of frequencies in optical fibers or crystal windows leading to a pulse with a large spectral breadth [144][145]. This is typically implemented as a probe technique, for example to simultaneously detect the optical properties in a near-infrared/visible range, *e.g.* reflectivity and transmission, although other ranges are feasible as well [146].

In this thesis, the objective was to obtain the transient reflectivity of samples by measuring the reflected beam intensity. This was performed using photodiode detectors, either with single receivers, for single-color measurements, or using arrays, to register the broadband supercontinuum after dispersing its components through a glass prism.

3.1.1 Pump-probe phenomena

The materials studied in this thesis, being semimetals or small-band-gap semiconductors, are absorbing media in the near-infrared/visible range. This fact suggests that the pump excitation should involve both interband transitions, bringing electrons to higher unoccupied energy states with their initial excitation, and intraband transitions, leading carriers to different eigenstates with close energies, through the energy redistribution with electron-electron and electron-phonon scattering. Although the second mechanism may be expected to be the slower one, these phenomena are often concomitant. In many crystalline systems, the electrons are expected to reach an internal thermalization in a few picoseconds [138][147][148]. When probing the transient optical properties, *e.g.*, reflectivity or transmission, these phenomena correspond to an initial peak which decays with an exponential trend. If distinct carriers or phonon populations are present, multiple decaying-exponential terms may be required to describe the different relaxation channels [149]. It usually takes a longer time for the lattice to fully thermalize and finally re-establish an equilibrium condition through phonon-phonon interaction and dissipation with the surrounding media [150][151]. Time-resolved optical studies are usually limited to a few tens of picoseconds after time-zero to analyze primarily the electronic and coherent and 'hot' ionic response, however sizable transient effects may continue to impact the optical response for hundreds of picoseconds [106].

The excitation of the system may lead also to a synchronization of the lattice normal modes in the pumped area, named coherent phonons [152][153]. While the specific mech-

anism may differ from material to material, in absorbing media it can be often described through the 'displacive excitation of coherent phonons' (DECP) model [154]. The underlying mechanism is based on a change of the quasi-equilibrium coordinate of the atomic configuration as the electronic system is perturbed. The lattice then responds by moving towards the new equilibrium position through a superposition of its normal modes which may be in-phase for a large number of unit cells if the excitation and crystal quality are uniform enough.

In the literature, this model is often associated with a $\sim\cos[\omega(t\text{-}t_0)]$ temporal response, where ω is the angular frequency and t_0 is the time-zero, *i.e.* instant at which the temporal coincidence between pump and probe occurs. However, this happens only in special conditions. In fact, the model allows deviations from such behavior and is not in strict opposition with the impulsive stimulated Raman scattering (ISRS) $\sim\sin[\omega(t\text{-}t_0)]$ behavior [155]. This stimulated also the development of more general theories with the DECP and ISRS as particular cases [156].

3.2 X-ray diffraction

In order to examine the lattice structure of a periodic system, one of the most employed techniques applied since the beginning of the twentieth century is x-ray diffraction, exploiting wavelengths which are comparable to the lattice parameters, *e.g.* about one-two angstroms [157]. The atoms act as scattering centers for the impinging radiation and the resulting pattern rationalized in terms of the mathematical formalism founded by Laue equations, Bragg's law and Ewald's construction [158]. In crystalline systems, constructive interference conditions are described in terms of the reciprocal lattice vectors and space group symmetry. This allows, in principle, to reconstruct the lattice parameters and atomic disposition at equilibrium, as well as the composition ratio in mixed polycrystalline samples. Once the structure is known, it is possible to perturb the system using ultrafast laser perturbations. Usually, one monitors constructive conditions which leads to peaks of the scattered x-ray intensity, named Bragg peaks, related to the lattice or superlattice ordering (*e.g.* charge density wave systems).

It also finds a vast application in numerous fields such as medical diagnosis, biological research, where the structure determination is a key role to explain some of the functionalities of complex molecules, and studies about the most profound electronic levels in atomic and condensed matter physics.

This radiation can be generated through multiple methods [158]. Historically, x-ray tubes have been the first and most popular sources, where peaks of hard x-ray photons are obtained through electron-hole recombination, usually at the K-shell, after collisions between accelerated electrons and the anode, commonly copper, iron, molybdenum or tungsten, on top of Bremsstrahlung radiation. The desired wavelength is then selected by using a crystal monochromator.

In the last few decades, instruments at large-scale facilities have been developed to obtain high-resolution data at much faster rate, exploiting the high-brilliance radiation from synchrotron [159] and free-electron laser (FEL) [160] sources. As for x-ray tubes, accelerated, relativistically in this case, electrons are employed, although rather than using a collision target, the radiation is generated stirring the electron trajectory using bending magnets, undulators or wigglers. In synchrotrons, the spectral breadth of the resulting light is quite large, while in the FEL case it is narrower, even more so if a seeded mechanism is implemented on top of the self-amplified spontaneous emission (SASE).

Nowadays, the recording of Bragg peak intensities is performed using advanced electronic detectors. In the FEL experiment reported in this thesis, an areal detector with pixel subdivision was used (JUNGFRAU, [161]), where the peak intensity is reconstructed from the charge generated by the arriving x-ray photons.

3.2.1 Time-resolved x-ray diffraction

To explore the effects of an optical excitation with the x-ray diffraction, it is necessary to employ, as for lower-frequency ranges, pulsed probe beams. The reason comes from the fact that the electronic setups available at the moment do not allow a separation between pump and unpumped effect over a scale of a few tens or even hundreds of femtoseconds. Employing probe pulses whose pulse duration far exceeds the pump one would mean 'averaging' the transient response over it, which in most cases does not allow to study the ultrafast processes with the necessary resolution.

This is the case of the synchrotron radiation, where its pulses have a duration of tens of picoseconds. Nevertheless, a combined use of pulsed table-top laser systems and synchrotron radiation through the electron beam slicing technique [162] allowed to lift this limitation and obtain ∼100 fs hard x-ray pulses, which permitted numerous ultrafast diffraction experiments in the last two decades [163][164].

FELs are intrinsically designed to provide very short pulses, even in the 'attosecond' regime [165] to be used to explore the ultrafast response of atomic, biological and solid systems [166][167][168]. FEL radiation can be also applied to study nonlinear phenomena and thermal propagation taking advantage of its small wavelength through transient grating spectroscopy [169][170][171].

3.3 Terahertz fields

In optics, the light ranges explored in the previous sections are usually categorized under 'high-energy' photons. Conversely, terahertz (THz) radiation comprises of low-energy photons with frequencies between 0.1 and 30 THz, corresponding to 0.4-124 meV photon energy range [172][173]. In this energy range, one can find vibrational fingerprints of compounds, quasi-free carrier response and low-energy magnetic excitations. Due to its low photon energy and non-destructive nature, terahertz technology is viewed as a promising probe for molecular, biological and solid state research. Moreover, practical applications for medical diagnosis, security control identifying hidden dangerous substances, high-resolution radar technology and radars encourage multidisciplinary studies in this sector.

Nevertheless, various challenges have slowed down applicative research. First of all, THz radiation is absorbed by water vapor through numerous spikes which limit the operative frequency band [174]. In research, this effect is often reduced by enclosing the terahertz setup in a rigid box and purging inside with nitrogen. This allows to reduce the internal relative humidity at a few-percent value and thus obtain a clearer THz waveform.

Another important issue are the available THz sources. Research based on short THz pulses was favored by the advent of high pulse-energy sources at high repetition rate (e.g. Ti:sapphire lasers) together with the combined use of nonlinear processes, although there are various pathways to obtain them. These include photoconductive switches, optical rectification, plasma-based generation [175] and free electron lasers (FELs) either as the main operation use or in a parasitic configuration [176][177]. The commercial equivalent of table-top pulsed lasers in the near-infrared/visible range for the THz radiation are

the quantum cascade lasers (QCLs), working either in continuous wave or in few-cycle mode. While considerable progress has been achieved since their initial realization [178], the requirement of cooling, reduced frequency tunability and limited output power have limited their diffusion in laboratories.

In the experimental works presented in this thesis, the two methods employed to obtain THz pulses were optical rectification and plasma-based generation.

3.3.1 Optical rectification

This method is a particular case of a second-order nonlinear phenomenon occurring in non-centrosymmetric crystals, named difference frequency generation, in the zero frequency limit of the resulting pulse [175]. A simple formulation of this interaction can be expressed in terms of a semiclassical approach, considering two fields, periodic in time $\mathbf{E_1}(\omega_1, t) = \mathbf{E_{01}}(\omega_1)exp(-i\omega_1 t) + c.c.$ and $\mathbf{E_2}(\omega_2, t) = \mathbf{E_{02}}(\omega_2)exp(-i\omega_2 t) + c.c.$, where 'c.c.' stands for complex conjugate. When they pass through the crystal, aside from the linear response of the material, the two fields can interact so that a nonlinear polarization is induced. The second-order terms can be expressed in terms of the electric susceptibility χ as (with ϵ_0 being the vacuum dielectric constant)

$$P^{(2)}_{nl,i}(\omega_r, t) = \epsilon_0[\chi^{(2)}_{ijk}(\omega_r)E_{01,j}E_{02,k}exp(-i(\omega_1+\omega_2)t) + \\ + \chi^{(2)}_{ijk}(\omega_r)E_{01,j}E_{02,k}exp(-i(\omega_1-\omega_2)t) + c.c.] \quad (3.1)$$

Integrated in time, non-negligible contributions can be found when $\omega_r = \pm(\omega_1 + \omega_2)$ or $\omega_r = \pm(\omega_1 - \omega_2)$, together with $\chi^{(2)}_{ijk}(\omega_r) \neq 0$ for the corresponding interaction, geometry and frequency. Considering all the angular frequencies above to be positive-defined, the first possibility corresponds to sum-frequency generation (SFG) while the second case leads to difference-frequency generation (DFG). When $\omega_1 - \omega_2 \simeq 0$, a quasi-DC response may be obtained and the processes is called optical rectification. The quasi-DC character from the practical point of view means $\omega_1 - \omega_2 << \omega_1 \simeq \omega_2$, as it is for THz frequencies when compared to the near-infrared/visible range.

The nonlinear polarization becomes in turn the source term for the generated low frequency radiation in the wave equation.

$$\nabla^2 \boldsymbol{E} - \frac{1}{c^2}\frac{\partial^2}{\partial t^2}\boldsymbol{E} = \frac{1}{c^2\epsilon_0}\frac{\partial^2}{\partial t^2}\left[\boldsymbol{P}^{(1)} + \boldsymbol{P}_{nl}\right] \quad (3.2)$$

$$\nabla^2 \boldsymbol{E} - \frac{n^2(\omega_r)}{c^2}\frac{\partial^2}{\partial t^2}\boldsymbol{E} = \frac{1}{c^2\epsilon_0}\frac{\partial^2}{\partial t^2}\boldsymbol{P}_{nl} \quad (3.3)$$

with $\boldsymbol{P}^{(1)} = \epsilon_0\left(n^2(\omega_r) - 1\right)\boldsymbol{E}$ being the linear polarization, which can be expressed in terms of the refractive index $n(\omega_r) = \sqrt{\epsilon(\omega_r)}$, square root of the dielectric function, which becomes a complex tensor for anisotropic materials.

The above formula is an ideal expression for the interaction under various approximations. In reality, one has to consider the length of the nonlinear medium, its homogeneity and the absorption and reflectivity coefficients of the fields. Moreover, the finite pulse length and beam superposition, if using two separate sources for $\mathbf{E_1}(\omega_1, t)$ and $\mathbf{E_2}(\omega_2, t)$, must be taken into account for a quantitative expression to integrate the effects. Analogous contributions can be also generated at the surface [179], even for centrosymmetric samples as the surface itself is not symmetric under inversion.

Experimentally, nonlinear interactions are realized starting from the output of table-top laser systems. Important parameters to choose are the impinging beam wavelength, which depends on the efficiency of the conversion process, and the crystal thickness and orientation to ensure good phase- and velocity-matching [180][181]. Popular crystals include the zinc-blende type, like ZnTe, GaSe and GaP, LiN_bO_3 and organic crystals such as DAST, OH1 and DSTMS. The choice is generally based on the spectrum and power one needs to obtain for the experiment. The conversion can also take place using a single beam: in fact, provided that the matching conditions are satisfied, even transform-limited pulses can produce a broadband spectrum at about zero frequency.

3.3.2 Plasma-based generation

The mechanism of the generation of THz pulse through a plasma medium has been a topic of discussion for years [182]. Experimentally, the process occurs by focusing an intense laser beam in air and superimposing, in time and space, its second-harmonic field, generated through a nonlinear crystal like beta barium borate (BBO) in front of the plasma. Until recently, it was thought to be originating from a four-wave-mixing nonlinear effect contributing to the third-order nonlinear polarization through [175]

$$\begin{aligned} P^{(3)}_{nl,i}(\omega_r,t) = \epsilon_0[&\chi^{(3)}_{ijkl}(\omega_r)E_{01,j}E_{02,k}E_{03,l}exp(-i(\omega_1+\omega_2+\omega_3)t)+ \\ &\chi^{(3)}_{ijkl}(\omega_r)E_{01,j}E_{02,k}E_{03,l}exp(-i(\omega_1-\omega_2+\omega_3)t)+ \\ &\chi^{(3)}_{ijkl}(\omega_r)E_{01,j}E_{02,k}E_{03,l}exp(-i(\omega_1+\omega_2-\omega_3)t)+ \\ &\chi^{(3)}_{ijkl}(\omega_r)E_{01,j}E_{02,k}E_{03,l}exp(-i(\omega_1-\omega_2-\omega_3)t)+c.c.] \end{aligned} \quad (3.4)$$

As for the second-order nonlinearities, relevant non-zero contributions can be found, when integrating in time, only when $\omega_r = \omega_1 \pm \omega_2 \pm \omega_3$ is satisfied and $\chi^{(3)}_{ijkl}(\omega_r) \neq 0$ for the corresponding frequency.

In the scheme, usually one employs a single laser beam, where one of the input ω is the second-harmonic of the arriving beam, *e.g.* $\omega_1 = 2\omega_0$, while the other two are components within the original beam spectrum. Thus THz contributions may appear only if $2\omega_0 \simeq \omega_2 + \omega_3$, where the difference between left- and right-hand sides corresponds to the THz frequency.

However, the currently accepted explanation is that the plasma is a tunnel-ionized gas with asymmetric field-induced currents leading to the THz generation [182]. In a semiclassical picture, the ionization of gas by infrared photons can be obtained either through multiphoton absorption or tunneling effect, whose relative impact depends on the light frequency and intensity. The THz plasma generation takes place in the second regime and it can shown to give a broad frequency response.

Nevertheless, an accurate description of the experimental process requires also taking into account various optical processes, *e.g.* ionization, dephasing and focusing, and it is beyond the scope of this thesis.

Once generated, the THz beams are collimated or focused using parabolic mirrors to take them to the sample and then to the detection device. In this thesis, the THz field is registered using two different methods: electro-optic sampling [175] and air-biased coherent detection (ABCD) [183].

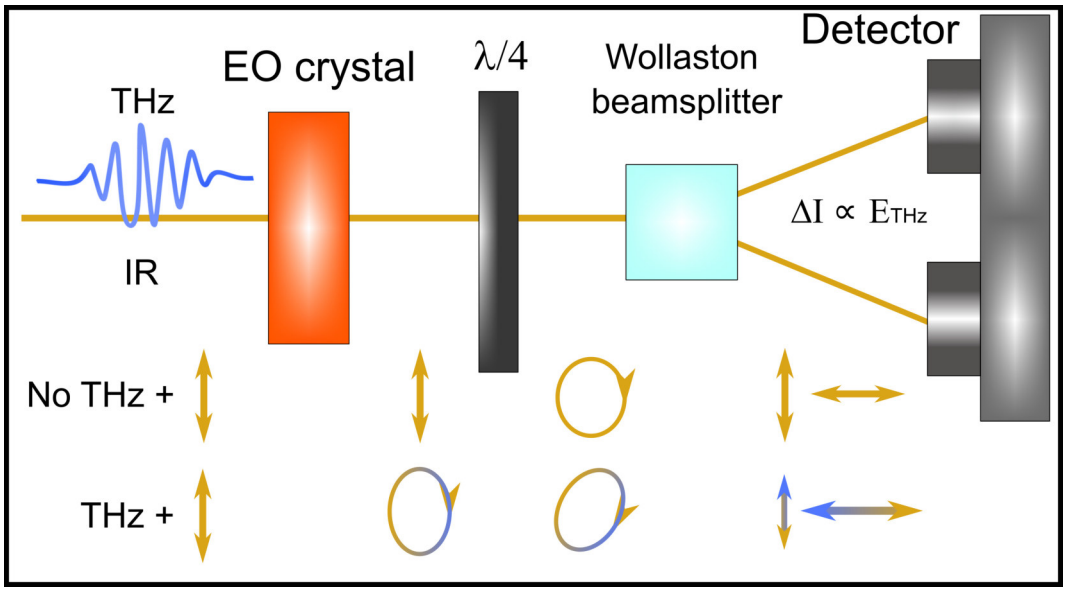

Figure 3.1. Sketch of the electro-optic sampling scheme. Without the THz field, the infrared beam remains linearly polarized after the electro-optic (EO) crystal; it is then converted in a circularly-polarized beam by the quarter-wave plate (λ/4) and split equally into horizontally and vertically polarized light by the Wollaston beamsplitter so that the detection is balanced between the two photodiodes. In presence of a THz pulse arriving at the EO crystal, the infrared beam becomes elliptically polarized after the crystal due to the electro-optic effect; consequently this leads to an unbalance at the detection, proportional to the THz electric field in the low-field limit.

3.3.3 Electro-optic sampling

The first one can be implemented by using most of the previously cited non-centrosymmetric nonlinear crystals, although with differences in the detection band, as it relies on the linear electro-optic effect (Pockels effect), which may be finite only for systems without inversion symmetry since it is related to the second order susceptibility tensor. The effect is such that when the THz pulse passes through the nonlinear crystal, it introduces an anisotropic change in the dielectric tensor at the wavelength of a near-infrared probing pulse. As the refractive index is deeply connected to the dieletric tensor [59], this provokes a change in the polarization plane of the probe pulse due to the phase difference between the components of the linearly-polarized probe field on the optical axes. This effect is linearly proportional to the THz electric field as long as the crystal thickness is much smaller than the coherence length between the group velocity of the near-infrared pulse and the phase velocity of the THz pulse [175].

To quantify it, a two-photodiode detection scheme is employed (Fig. 3.1). Initially, using a quarter-wave plate, the polarization state of the linearly-polarized near-infrared beam, *e.g.* parallel to the optical breadboard, is transformed into circularly polarized. Split by a Wollaston beamsplitter, its perpendicular and parallel components give the same average intensity as measured by two separate photodiodes. When the THz pulse arrives, the two measured intensities will be no longer balanced as the outcoming beam will be elliptical in general. Calibrating the unbalance gives the phase and amplitude of the measured field, which, at the lowest order, is proportional to the phase difference and thus to the THz electric field.

Since the THz field is actually a pulse, the induced change of the probe polarization

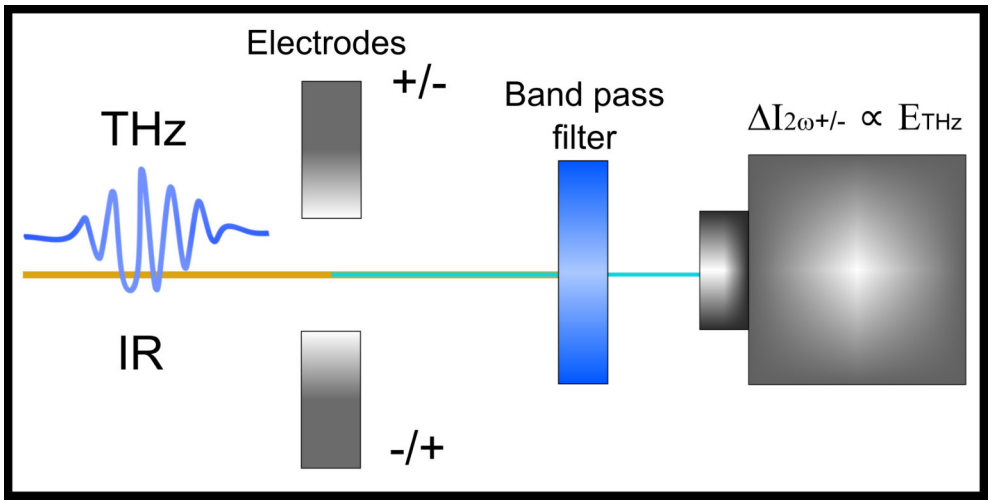

Figure 3.2. Sketch of the ABCD scheme. In the interaction region between the THz field and the infrared beam, a electric field bias in applied using two electrodes. The remaining portion of the infrared beam is filtered and the generated TFISH is detected by a photodiode.

will depend on the temporal superposition between the two beams. In particular, it is preferable to have a very short near-infrared pulse with respect to the THz one, so that the THz waveform can be accurately sampled. The mapping of the complete terahertz waveform is also named time-domain spectroscopy (TDS).

When using high THz fields, one should in principle take into account the appearance of higher-order electro-optic effect, such as the quadratic Kerr effect. However, particular configurations allow to extinguish the quadratic electro-optic effect so that the resulting rotation of the polarization plane of the impinging infrared beam can be attributed only to the linear effect under a very good approximation [184]. Another possibility is to use neutral density filters before the detection as the linear effects as favored over the quadratic ones at lower fields.

3.3.4 Air-biased coherent detection

The second method, ABCD [183], uses air as the sensor medium taking advantage of a third-order nonlinear mixing process. The actual measured quantity is the THz-field-induced second harmonic (TFISH) of an near-infrared optical pulse. In the first implementation for the THz detection [185], the process becomes 'coherent' above a certain probe intensity threshold when the laser-induced plasma starts to act as a local oscillator. In these conditions, the intensity of the TFISH becomes approximately proportional to the terahertz field.

Since then, other methods to obtain such local oscillator were proposed [182]. One of them, ABCD, uses a high-voltage bias field applied around the interaction region between THz and infrared pulse (Fig. 3.2) to retrieve the THz phase. The difference between the TFISH measured under a positive and a negative bias of the same magnitude is proportional to the THz electric field. To improve the TFISH, it is possible to purge the detection area with alkane gases instead of nitrogen [186].

This method is particularly useful when employing THz pulses with a large spectral breadth. In fact, many crystals present infrared-active phonon modes in the 1-20 THz range which cause resonant absorption in correspondence of their associated frequencies.

This does not occur in ABCD.

Other measurement methods include photoconductive switches and bolometer detectors [175][187].

3.3.5 Out-of-equilibrium phenomena

In out-of-equilibrium physics, THz fields can be used to excite, probe and monitor low-energy properties of a physical system, such as electron excitations as free-carriers or excitons [188][189][190] and collective modes like coherent phonons and magnons [191][192][193].

The combined use of THz pulses with higher photon energy beams has been exploited for many system in the literature, but it is also possible to explore the ultrafast response by using two THz pulses. Especially in this last case, due the picosecond-duration and comparable field amplitude of the two THz pulses, the role of pump and probe can be alternatively assumed by the two pulses within the same experiment. This distinction is especially loose in two-dimensional terahertz spectroscopy.

Two-dimensional terahertz spectroscopy

This technique is a particular version among the two-dimensional optical spectroscopies [194], where two pulses are employed to study the interplay of characteristic resonances in molecular, biological and solid systems, often by monitoring the resulting nonlinear effects. Two-dimensional terahertz spectroscopy (2D THz) has been performed to study the response among electron, phonons and magnons [195] [196] [197] [198] in solids systems as well as rotational motion in molecular systems [199].

One of the most interesting obtainable quantities in 2D THz measurements is the nonlinear field, derived by collecting the material's response simultaneously and individually with respect to the single THz fields.

During the measurements, the two beams can be chopped at distinct submultiples of the laser system repetition rate. By properly setting the phases, this allows to distinctively record the resulting signal for different field combinations: using both THz pulses (E_t), only one (E_1, E_2) and none (E_b background, subtracted to the fields). The nonlinear signal is then obtained as

$$E_{nl} = E_t - E_1 - E_2 + E_b \tag{3.5}$$

Its value depends on the temporal superposition of the individual fields. The operation refers to the associated fields recorded after the sample when the corresponding THz pulses are applied. In 2D-THz spectroscopy, one obtains matrices of data, thus we will refer to those datasets through their field label. Morever, the reported fields values are meant as the maximum field amplitude for each pulse registered at the sample position before the interaction with it.

We define two time coordinates: the excitation delay t_{ex}, which is the difference between the average time coordinates of E_1 and E_2 and the detection delay t_{del}, set to be zero at the average time coordinate for E_2, that represents the electro-optic sampling delay (Fig. 3.3). The average time coordinate of the terahertz pulse, defined as a time centroid, can be obtained using

$$t_0 = 1/I_t \int_{-\infty}^{\infty} E(t)^2 t dt \tag{3.6}$$

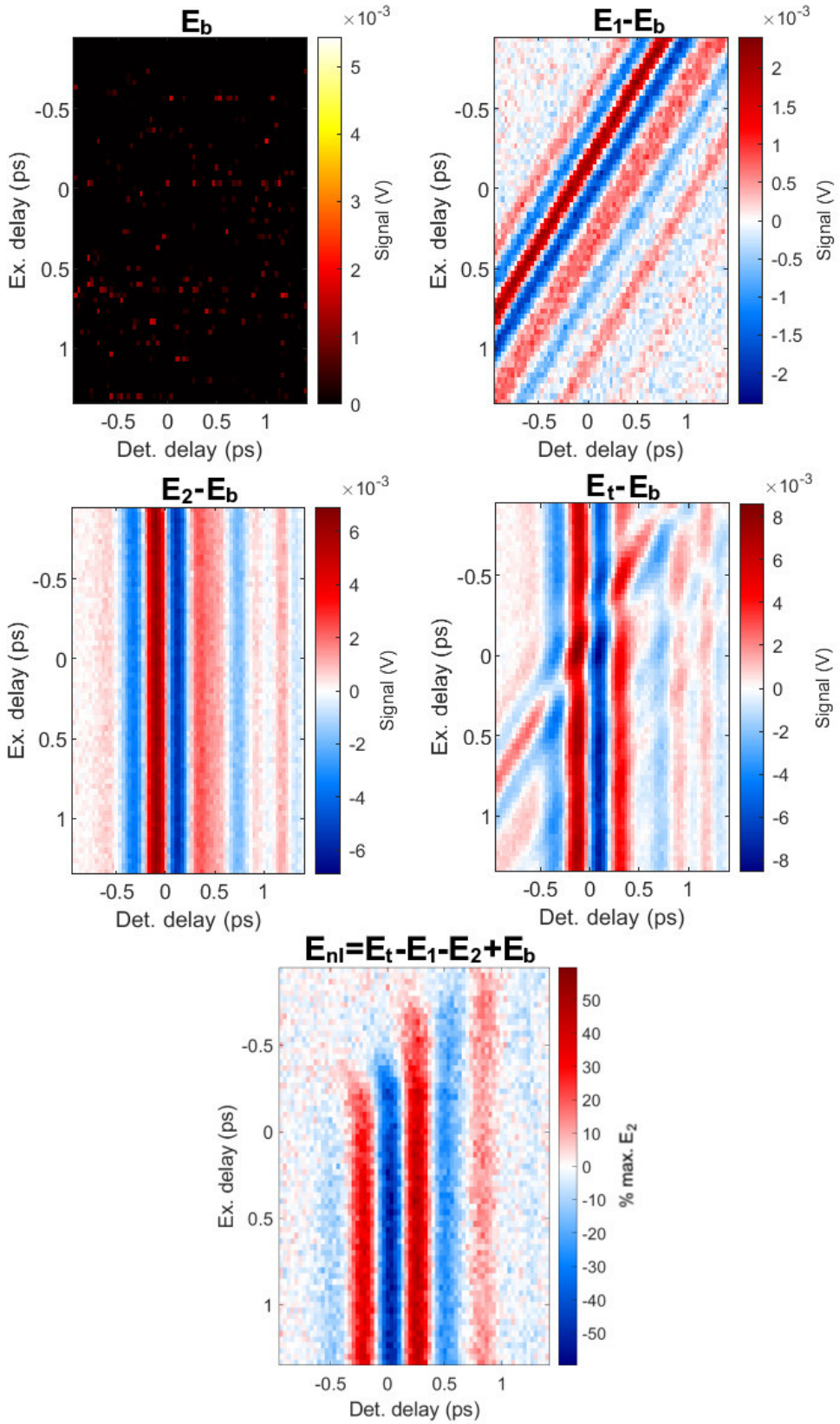

Figure 3.3. Two-dimensional THz maps for $Hg_{0.825}Cd_{0.175}Te$ using E_1 ∼34 kV/cm, E_2 ∼17 kV/cm and T=12 K in the time domain and cross-polarized configuration (see Chapter 8).

where $I_t = \int_{-\infty}^{\infty} E(t)^2 dt$ [175]. This bidimensional description leads to data maps in which E_2 is centered at $t_{del} = 0$, regardless of t_{ex}, while the centroid for E_1 follows a diagonal path such that $t_{ex} + t_{del} = 0$. This behavior is a simple consequence of the fact that varying t_{ex} corresponds to a change in the t_{del} at which E_1 is detected, since E_2 is fixed in t_{del}.

Furthermore, we distinguish between odd and even nonlinearities based on the parity of the nonlinear signal with respect to E_1 [200]. For this purpose, two equivalent data sets must be acquired, labeled '+' and '−', by varying the E_1 electric field direction by 180 degrees, *e.g.* through the combined used of two wire grid polarizers. Summing and subtracting the sets, one obtains

$$E_{odd} = E_{nl+} - E_{nl-} \quad E_{even} = E_{nl+} + E_{nl-} \tag{3.7}$$

As a remark, it is important to highlight that while a definition for the central position of the terahertz pulses is given, only differences between time positions are important. These are the key ingredient for the Fourier-transformed analysis of the nonlinear features. In the frequency domain, the coordinates at which nonlinear contributions appear give information regarding their identities, as well as the order of the electrical susceptibility terms involved, that can be rationalized in terms of the Liouville-space pathway theory [201].

In Chapters 7 and 8 we will present our two-dimensional THz studies on Weyl and Kane semimetals. For some considerations, we will refer to the Drude-Lorentz model for the dielectric function [59]. In general, this is a complex quantity comprehending terms connected to optical transitions (intraband and direct/indirect interband) as well as phononic resonances. In metallic or semimetallic systems, the contribution connected to quasi-free electrons can be semiclassically expressed by the Drude term in the frequency domain as

$$\epsilon_D(\omega) = \epsilon_\infty \left(1 - \sum_i \frac{\omega_{pi}^2}{\omega^2 + i\gamma_{pi}\omega}\right) \tag{3.8}$$

where ϵ_∞ is the high-frequency dielectric constant and ω_{pi} is the plasma (angular) frequency for the carrier population i with associated damping γ_{pi}, inversely connected to the scattering times of the different scattering channels.

In semimetals, the number of terms in the sum depends on the details of the electronic structure, *e.g.* the presence of multiple electron and hole pockets. For example, in WTe_2, two separate terms are used to represent the electron and hole carriers [202], while for HgTe a single one was shown to be sufficient [129]. The (angular) plasma frequency can be expressed in terms of the carrier density as [200]

$$\omega_{pi} = \sqrt{n_i e^2/(\epsilon_0 \epsilon_\infty m_i^*)} \tag{3.9}$$

where n_i is the carrier volumetric concentration, ϵ_0 is the vacuum dielectric constant and m_i^* is the effective mass of the carriers.

CHAPTER 4

Computational methods for ground and excited states

Theoretical and experimental studies are two complementary aspects of physics that must support each other in order to obtain a faithful description of a physical system. However, as research advanced, people gradually started to focus on more complex structures, requiring more elaborate models and challenging experiments. As the number of degrees of freedom (DOF) became enormous, this resulted in increasing difficulties to compare ab-initio theory and experiment. Moreover, many theories do not provide analytical solutions for the investigated systems or are too intricate to be of any use.

Fortunately, the simultaneous and quick development of computers allowed to develop alternative strategies surpass these limitations, at least from a practical point of view. In chemistry, biology and condensed matter physics, this encouraged the development of codes and pathways to simulate physical systems considering the atomic DOF [203]. Nevertheless, real samples are constituted by an immense number of particles, which can become same order or the Avogadro constant ($\sim 10^{24}$), making any numerical simulation virtually unfeasible.

To overcome this issue, two approaches can be used to simplify the system under study: grouping DOF to create functional groups or making it periodic. The first method is often employed in systems where the fundamental unit components are already too complex themselves, *e.g.* proteins, and studying their mutual interactions and together with the response from the solvent is too computationally demanding. Usually these are implemented using semiclassical equations of motion to study equilibrium properties, together with the aid of thermal baths and further constraints to simulate the experimental conditions. The second method is exploited for structures where a long-range order is present. In this case, the simulation cells can become very small, even composed by single atoms in elemental solids. The presence of the surrounding unit cells is taken into account through the Born-von Karman periodic boundary conditions (PBC), instead of open boundary conditions (OBC). In principle, the two strategies are not in opposition

and they can be integrated in the same code if needed.

These approximations, just as experiments, are subjected to limitations which give to the obtained values a certain degree of accuracy and comparability for the analyzed systems.

In condensed matter systems, electronic and lattice DOF are of crucial importance. Here, the spatial and spin variables of the particles not only characterize the individual objects of the simulations, but also their interactions. Generally, when simulating a solid system in equilibrium or quasi-equilibrium conditions, a first approximation comes from the separation among electronic and ionic DOF in the wavefunctions through the Born-Oppenheimer adiabatic approximation. This allows to treat the lattice coordinates as parametric conditions for the electronic ensemble.

While a numerical solution is in principle obtainable, taking into account all of the many-body interactions among the particles becomes a formidable task for complex unit cells.

4.1 Density functional theory

When treating ground-state configurations, an alternative formulation of the problem is available, thanks to the two Hohenberg-Kohn theorems [204]. The first one established a bijective map between electron density and external potential, which usually consists of the interaction between electrons and nuclei although it can be generalized. The same proof shows that analogous relations exist for the ground state wavefunction which acts as an intermediate link between electron density and external potential. The second one says that the ground-state energy is found by minimizing the expectation energy, now a functional of the electron density

$$E_{V_{ext}}[n(\boldsymbol{x})] = \langle \Psi[n(\boldsymbol{x})] | \, \hat{H}_{V_{ext}} \, | \Psi[n(\boldsymbol{x})] \rangle \tag{4.1}$$

where $n(\boldsymbol{x})$ is the electron density, $\Psi[n(\boldsymbol{x})]$ is the many-mody wavefunction and $\hat{H}_{V_{ext}}$ is the Hamiltonian operator for a given external potential V_{ext}, by varying the electron density towards the ground state, in the spirit of the Rayleigh-Ritz variational principle.

$$E_0 = \min_{n(\boldsymbol{x}) \to n_0(\boldsymbol{x})} E_{V_{ext}}[n(\boldsymbol{x})] \tag{4.2}$$

In the original formulation, the last part was only valid for non-degenerate states, but multiple extensions of the required conditions allowed to broaden even more the applicability of these two theorems.

The possibility to determine the ground state through a energy functional of the electron density is a central point as it allows to recast the many-body problem to a functional along the spatial coordinates of the system. Aside from a reformulation of the observables through the density, it is of fundamental importance to simplify the structure of simulations.

However, it is essential to know how to appropriately include the electron-electron interactions. An important step forward was given by the Kohn-Sham scheme, where the interacting electronic system is recasted into a non-interacting one, with the kinetic term given by the one for non-interacting particles and a potential term, assuming that the ground state is representable through such auxiliary system. This leads to the eigenvalue problem

$$\hat{H}_{ks}^{m_s}\phi_{\lambda m_s}(\boldsymbol{x}) = \epsilon_{\lambda m_s}\phi_{\lambda m_s}(\boldsymbol{x}) \tag{4.3}$$

where m_s is the spin channel and λm_s represents the quantum numbers for a specific solution. The Hamiltonian is

$$\hat{H}_{ks}^{m_s} = -\frac{\hbar^2}{2m}\nabla^2 + V_{ks}^{m_s}(\boldsymbol{x}) \tag{4.4}$$

with

$$V_{ks}^{m_s}(\boldsymbol{x}) = V_{ext}(\boldsymbol{x}) + V_h(\boldsymbol{x}) + V_{xc}^{m_s}(\boldsymbol{x}) \tag{4.5}$$

being the potential term which includes the external potential, Hartree potential and the exchange-correlation potential, also containing the correction to the kinetic term to make it consistent with the interacting picture. Further terms need to be added when considering a non-collinear spin configuration with a non-null magnetization density.

Nevertheless, while the problem is concentrated in the exchange-correlation potential, an analytical expression still lacks. This can be solved through approximated forms, often starting from simpler systems, *e.g.* homogenous electron gas in a jellium. Depending on how the density dependence is taken into account, exchange-correlation can be considered in the local density or (generalized) gradient approximations, LDA and GGA in short respectively.

To improve their performance, some of the developed codes for electronic structure approximate the atomic potentials with pseudopotentials. This form substitutes the ionic potential with a smoother form using pseudo-wavefunctions, especially in the inner core region where the all-electron wavefunctions present multiple nodes. Such description is appropriate when we can view the atoms as composed by valence and core electrons where only the first group intervene in the chemical bonding. This distinction can become blurry when considering elements of the d-block, having orbitals with orbital angular momentum $l = 2$ at least partially filled which may play a role in bonding, even when they are not the uppermost energy levels.

Even though several recipes were created during the years, there is not a universal path to generate a pseudopotential. Several choices and compromises modify the final result such as which electrons are included in the 'pseudodization', the 'hardness' (*i.e.* the variability of the pseudopotential along the spatial coordinates), the normalization of the pseudo-wavefunctions and the mathematical method used to generate them. All these conditions impact the transferability and adequacy of a pseudopotential in different environments. Vast comparative studies have been performed [205], most of these are focussed on elemental solids. Thanks to the diffusion of the internet, groups started to collect the results and data coming from the different computational studies and created online platforms to share the information, including the pseudopotentials used [206][207].

Nevertheless, research often requires working with new systems and/or unexplored properties for which appropriate comparisons do not exist. For this reason, one tries to compare the results of different pseudopotential flavors, when possible, to find the most adequate description.

In this thesis, two flavors of pseudopotentials were used: norm-conserving (NC) [208] and based on projected augmented wave method (PAW) [209]. In both cases, the exchange-correlation functional obtained the generalized gradient approximation (GGA) in the Perdew-Burke-Ernzerhof (PBE) [210] parametrization. Depending on the observable under study, partially (scalar, [211]) or fully relativistic pseudopotentials were employed from different libraries [212][213].

4.1.1 Electronic structure simulations

The DFT-based codes for the electronic structure usually employ a similar strategy to solve the Kohn-Sham equations and to derive associated quantities. When treating periodic system, *e.g.* chains, slabs or crystals, it is common practice to use PBC for the simulation cell as well as to express the derived quantities, *e.g.* wavefunctions and electron density, in terms of bases with periodic terms, as for example the complete plane-waves set, similarly to a superposition of the Bloch functions. This encourages to compute coefficients and observables directly in the reciprocal space. However, just as in the direct space, to perform an accurate discretized integration, one needs to finely sample the integrand. In the reciprocal space, this means to calculate eigenfunction and eigenvectors for selected coordinates expressed as k wavevectors. In the reduced-zone picture, this corresponds to a sampling of the Brillouin zone and/or summing over the energy levels given by the diagonalization of the Hamiltonian, marked by the 'band index' n_b.

At the core of electronic structure codes, there is the diagonalization of the Kohn-Sham Hamiltonian to find eigenvalues and eigenvectors. The energy minimum corresponding to the ground state configuration is found through an iterative cycle to obtain a self-consistent solution of the Kohn-Sham equation, starting for example from the atomic and/or random wavefunctions. The cycle ends once the results are consistent under a certain threshold.

The wavefunctions, charge density and potential are expressed in a convenient basis, *e.g.* plane-waves, although the number of terms in the expansion is limited by a cut-off, which may be given as an energy, to reduce the size of coefficient matrices. To calculate accurate coefficients and expectation values, one must introduce a fine sampling of the Brillouin zone, usually as a regular grid whose details depend on the studied system [214].

This is one of the origin of numerical inaccuracies even for an exact theory, together with the discretization of integrals, pseudopotentials, thresholds for convergence and limited number of numerical figures.

Having obtained the ground state parameters, it is possible to derive numerous quantities for the configuration. Immediate results are the electronic band structure and density of states (DOS). For all these quantities, the absolute energy scale does not hold a special significance and it depends on the pseudopotentials used. Instead, energy differences are physically meaningful. For electronic structure calculations, usually one sets as zero energy value the Fermi energy, which separates unoccupied from occupied orbitals at T=0 K. The constant-energy surface in the Brillouin zone at the Fermi energy is called Fermi surface and can be used to understand, for example, the k-coordinates where states involved in transport properties are present and characterize their volume [215].

The band structure is a collective term to comprehend the eigenvalues of the orbitals and their dependence on k and n_b. If a finer study of the dispersion is required, a single diagonalization iteration cycle can be performed again starting from the results obtained at the end of the self-consistent procedure. It is plotted through energy-momentum graphs by choosing a certain path in the Brillouin zone. It can reveal information regarding the electronic structure, electronic velocity, effective masses, the presence of band gaps and the identification of electronic transitions. The DOS is the integrated version of the band structure in the reciprocal space, usually for the whole Brillouin zone, which is given as the number of states per energy unit. Possible indications one may extract from it are the presence/lack of carriers around the Fermi level, which influence the transport properties, and the effects of functional groups on the electronic properties of a solid system (*e*.g. molecules on a solid surface).

A concept similar to the DOS is the projected density of states (PDOS). This quantity represents the projection of the atomic orbitals of the individual atoms in the unit cell on the wavefunctions of the full system and, similarly to the DOS, it is usually expressed a states per energy unit. It may be exploited to understand which orbitals are mostly involved in states in particular energy and momentum ranges of the electronic structure, *e.g.* valence states involved in the bonding between atoms.

This description was based on the strategy used in the open-source suite QUANTUM ESPRESSO [216], a plane-wave-based code employing the pseudopotential approximation used in this thesis as the core package.

4.1.2 Phonons from perturbation theory

To derive quantities like the phonon spectrum using a perturbative approach, it is important for simulated structure to be in a structural equilibrium at a certain given pressure [217]. In other words, it is necessary to adopt an algorithm that leads the system towards a minimization of the interatomic forces among the nuclei and the most energy favorable configuration. A popular strategy is the Broyden–Fletcher–Goldfarb–Shanno (BFGS), a quasi Newton method, for which a force and an energy threshold must be specified to end the iterative minimization cycle.

While this minimization process may seem relatively straightforward, one must examine the final results to understand if the obtained structure correctly represents the experimental counterpart. Regarding the algorithm, its objective is to find the minima starting from a set of initial positions. Even though BFGS is more elaborate than a simple gradient descent, the system may fall in a local minimum for which the force and energy minimization conditions are also satisfied. The final configuration is also influenced by the choice of pseudopotential, additional correction terms to simulate van der Waals interactions and cut-offs/thresholds for the self-consistent calculation.

There are two main approaches to calculate the phonon eigenvectors and eigenvalues (*i.e.* their frequencies) [217]. The first one is the 'frozen-phonon' method which requires the construction of a simulation supercell, whose dimensions have to be at least $2\pi/|\boldsymbol{q}|$, with $\boldsymbol{q}$ being the phonon wavevector for which the solutions are sought. The main advantage of this approach is its simple implementation as it is based on displacing some atomic positions starting from the equilibrium configuration. However, calculating the required interplanar force constants, considering forces perpendicular to $\boldsymbol{q}$, can become increasingly computationally heavy as the supercell size is increased, which is required when considering small $\boldsymbol{q}$ vectors.

A different approach comes from the density functional perturbation theory [217]. Based on the linear response theory and adiabatic approximation, it is applicabile for small perturbations of the external potential which in turn lead to variations of the electronic density and wavefunctions. The phonon frequencies and eigenvectors are derived from the diagonalization of the dynamical matrix, *i.e.* the matrix of the interatomic force constants in the reciprocal space. The dynamical matrix is written as

$$\tilde{C}_{ab}^{\alpha\beta}(\boldsymbol{q}) = \sum_{\tilde{\boldsymbol{R}}} e^{i\boldsymbol{q}\cdot\tilde{\boldsymbol{R}}} C_{ab}^{\alpha\beta}(\tilde{\boldsymbol{R}}) = \frac{1}{N_c} \frac{\partial^2 E}{\partial u_a^{*\alpha}(\boldsymbol{q}) \partial u_b^{\beta}(\boldsymbol{q})} \tag{4.6}$$

where $u_a^{\alpha}(\boldsymbol{q})$ are the lattice distortions of wave vector $\boldsymbol{q}$ for the atom a and α is the Cartesian component, N_c is the number of unit cells forming the studied system, $\tilde{\boldsymbol{R}}$ represents the difference between the coordinates of a pair of atoms and E is the Born-Oppenheimer energy surface. The last term is present in the Born-Oppeheimer equation

for the nuclei

$$\left(-\sum_I \frac{\hbar^2}{2M_I}\nabla^2_{\boldsymbol{R_I}} + E(\boldsymbol{R})\right)\Phi(\boldsymbol{R}) = \mathcal{E}\Phi(\boldsymbol{R}) \tag{4.7}$$

with M_I mass of the I-th nucleus, $\boldsymbol{R}_I$ the position of the I-th nucleus and $\boldsymbol{R}$ collectively represents the atomic configuration. Thus, $E(\boldsymbol{R})$ corresponds to the ground-state energy of the system with 'clamped' nuclei whose associated Hamitonian is

$$H_{bo} = -\sum_i \frac{\hbar^2}{2m_e}\nabla^2_{\boldsymbol{r_i}} + \sum_{i\neq j}\frac{e^2}{2}\frac{1}{|\boldsymbol{r}_i - \boldsymbol{r}_j|} - \sum_{iI}\frac{Z_I e^2}{2}\frac{1}{|\boldsymbol{r}_i - \boldsymbol{R}_I|} + \sum_{I\neq J}\frac{Z_I Z_J e^2}{2}\frac{1}{|\boldsymbol{R}_i - \boldsymbol{R}_I|} \tag{4.8}$$

where m_e is the electron rest mass, $\boldsymbol{r}_i$ is the position vector for the i-th electron, Z_I is the charge for the I-th nucleus and e is the fundamental charge. The perturbative approach intervenes in the calculation scheme of the second derivatives of $E(\boldsymbol{R})$ in (4.6), as described in [217].

The phonon frequencies $\omega(\boldsymbol{q})$ are then solutions of the secular equation

$$det\left|\frac{1}{\sqrt{M_a M_b}}\tilde{C}^{\alpha\beta}_{ab}(\boldsymbol{q}) - \omega^2(\boldsymbol{q})\right| = 0 \tag{4.9}$$

From the phononic calculations, one expects 3·N phonon modes for each $\boldsymbol{q}$ wavevector [1], where N is the number of atoms in the primitive unit cell. Three of them are acoustic modes for which $\lim_{\boldsymbol{q}\to\boldsymbol{0}}\omega(\boldsymbol{q}) = 0$, while the rest are optical modes. Depending of how many symmetries are maintained by phononic shifts, the phonon modes can be cataloged based on the irreducible symmetry representations of the unit cell's point group. The totally-symmetric representation, treated in the thesis, is the one for which the symmetry elements of the point group are all preserved.

In the thesis, we concentrate on the phonon modes for $\boldsymbol{q} \to \boldsymbol{0}$, also called zone-center phonon modes as $\Gamma = \boldsymbol{0}$ is the center of the Brillouin zone, for metallic systems. Due to computational inaccuracies caused by *e.g.* cut-offs and thresholds, it may happen that the computational output of the diagonalization of the dynamical matrices gives non-null eigenvalues for the acoustic modes as $\boldsymbol{q} \to \boldsymbol{0}$. This issue can be mitigated by imposing acoustic sum rules, linked to the translational invariance of the crystal, that introduce slight corrections in the dynamical matrices. These changes may also affect the other phonon modes, although usually their impact is significant only for the first few optical eigenvalues and eigenvectors.

When trying to explore the effects of small distortions along the phonon eigenvectors, it is important to take into account the different masses of the atoms in the non-elemental solids to correctly predict the ratio between the actual shifts. One can obtain this information from the eigenvectors $\boldsymbol{\zeta}_{I,n}(\boldsymbol{q})$ via

$$\boldsymbol{\eta}_{I,n}(\boldsymbol{q}) \equiv \frac{1}{\sqrt{M_I}}\boldsymbol{\zeta}_{I,n}(\boldsymbol{q}) \tag{4.10}$$

where I indicates the I-th atom in the unit cell and n represents the index of the solution under consideration. $\boldsymbol{\eta}_{I,n}(\boldsymbol{q})$ are called eigendisplacements, which are also directly present in formulas regarding the optical properties [218].

4.1.3 Optical properties

As for the lattice normal modes, linear response theory can be employed to derive expressions for quantities sensitive to charge variations, *e.g.* due to an externally applied

electric field. A similar perturbation, albeit varying in time, occurs when studying the response of the system to light fields to measure its reflectivity, absorption or transmission properties.

All these observables critically depend on the dielectric tensor, although its complexity may be mitigated by exploiting the symmetries of the crystal system [219]. In the orthorhombic case, such as for WTe_2, the dielectric tensor is diagonal on its standard axes, although with three distinct eigenvalues, which lead to anisotropic equilibrium optical properties.

The influence of an external electric field is described through a scalar external potential ϕ that couples to the charge density giving a perturbative contribution to the Hamiltonian [220]. In the Coulomb gauge, it can be expressed as

$$\delta\hat{H} \equiv -\frac{e}{V}\sum_{\boldsymbol{q}\neq\boldsymbol{0}}\phi(\boldsymbol{q},t)\hat{\rho}(-\boldsymbol{q}) \tag{4.11}$$

with

$$\phi(\boldsymbol{q},t) = \frac{4\pi e}{q^2}\rho_{ext}(\boldsymbol{q},t) \tag{4.12}$$

where $e\rho_{ext}(\boldsymbol{q},t)$ is the $\boldsymbol{q}$ component of the external charge density, $\hat{\rho}$ the electron density operator and V is the sample volume. Its connection with the electromagnetic fields can be expressed through the Gauss equation for the electric displacement field $\boldsymbol{D}$ and electric field $\boldsymbol{E}$. In the reciprocal space, the relations become

$$\begin{aligned} i\boldsymbol{q}\cdot\boldsymbol{D}(\boldsymbol{q},\omega) \equiv i\boldsymbol{q}\epsilon(\boldsymbol{q},\omega)\boldsymbol{E}(\boldsymbol{q},\omega) = 4\pi e\rho_{ext}(\boldsymbol{q},\omega) \\ i\boldsymbol{q}\cdot\boldsymbol{E}(\boldsymbol{q},\omega) = 4\pi e(\rho_{ext}(\boldsymbol{q},\omega) - \rho_{ind}(\boldsymbol{q},\omega)) \end{aligned} \tag{4.13}$$

with $\epsilon(\boldsymbol{q},\omega)$ being the (longitudinal) dielectric function (in the general case, it is a tensor), $\rho_{ind}(\boldsymbol{q},\omega)$ is the induced charge density defined through $e\rho_{ind}(\boldsymbol{x},t) = e\langle\hat{\rho}(\boldsymbol{x})\rangle - en$, where the first term is the thermal and quantum average with respect to the electron density operator and n is the unperturbed electron density value, supposed to be uniform over the considered scale. In the reciprocal space, this last relation is given by $e\rho_{ind}(\boldsymbol{q},t) = e\langle\hat{\rho}(\boldsymbol{q})\rangle$ for $\boldsymbol{q}\neq\boldsymbol{0}$ as $\rho_{ind}(\boldsymbol{q}=\boldsymbol{0}) = 0$ for charge neutrality.

In the linear response theory, the induced charge density can be written as

$$\rho_{ind}(\boldsymbol{q},\omega) = -e\chi(\boldsymbol{q},\omega)\phi(\boldsymbol{q},\omega) = -\frac{4\pi e^2}{q^2}\chi(\boldsymbol{q},\omega)\rho_{ext}(\boldsymbol{q},\omega) \tag{4.14}$$

where

$$\chi(\boldsymbol{q},\omega) = \frac{1}{V}\int_{-\infty}^{\infty} dt\, e^{i\omega t}(-i\theta(t)\langle[\hat{\rho}(\boldsymbol{q},t),\hat{\rho}(-\boldsymbol{q})]\rangle) \tag{4.15}$$

is the 'improper' density-density linear response function with $\theta(t)$ being the step function, which can also be viewed as a retarded correlation function or as a two-operator Green's function [220][221]. The 'proper' density-density linear response function is instead defined by the equation

$$\rho_{ind}(\boldsymbol{q},\omega) = -\frac{4\pi e^2}{q^2}\tilde{\chi}(\boldsymbol{q},\omega)(\rho_{ext}(\boldsymbol{q},\omega) - \rho_{ind}(\boldsymbol{q},\omega)) \tag{4.16}$$

Combining the right-hand sides of the formulas reported in (4.13) gives the relation

$$\epsilon(\boldsymbol{q},\omega)(\rho_{ext}(\boldsymbol{q},\omega) - \rho_{ind}(\boldsymbol{q},\omega)) = \rho_{ext}(\boldsymbol{q},\omega) \tag{4.17}$$

The expression above allows to connect the dielectric function with the response functions leading to

$$\frac{1}{\epsilon(\boldsymbol{q},\omega)} = 1 + \frac{4\pi e^2}{q^2}\chi(\boldsymbol{q},\omega) \tag{4.18}$$

$$\epsilon(\boldsymbol{q},\omega) = 1 - \frac{4\pi e^2}{q^2}\tilde{\chi}(\boldsymbol{q},\omega) \tag{4.19}$$

In the Yambo code [222][223], used to calculate the near-infrared/visible optical properties for WTe_2 (see next section), $\chi(\boldsymbol{q},\omega)$ can be calculated in the space of reciprocal vectors $\boldsymbol{G}$, which is convenient starting from the ground-state databases obtained from plane-wave codes like QUANTUM ESPRESSO (QE) [216][224] or ABINIT [225]. Being yambo a many-body perturbation theory code, its capabilities extended far beyond the independent-particle (IP) approximation we used. The response function can in general be calculated including many-body corrections in the framework of the Dyson equation with the inclusion of local-field effects.

The noninteracting (IP) 'improper' density-density response function may be expressed as [223]

$$\chi^0_{\boldsymbol{GG'}}(\boldsymbol{q},\omega) = \frac{f_s}{N_{\boldsymbol{k}}\Omega}\sum_{nm\boldsymbol{k}} \rho_{nm\boldsymbol{k}}(\boldsymbol{q},\boldsymbol{G})\rho^*_{nm\boldsymbol{k}}(\boldsymbol{q},\boldsymbol{G'})\times \\ \times \lim_{\eta\to 0^+}\left[\frac{f_{m\boldsymbol{k}}(1-f_{n\boldsymbol{k}-\boldsymbol{q}})}{\omega-(\varepsilon_{m\boldsymbol{k}}-\varepsilon_{n\boldsymbol{k}-\boldsymbol{q}})-i\eta} - \frac{f_{m\boldsymbol{k}}(1-f_{n\boldsymbol{k}-\boldsymbol{q}})}{\omega-(\varepsilon_{n\boldsymbol{k}-\boldsymbol{q}}-\varepsilon_{m\boldsymbol{k}})+i\eta}\right] \tag{4.20}$$

where Ω is the unit cell volume, $N_{\boldsymbol{k}}$ is the number of $\boldsymbol{k}$ points along the polarization direction, n and m refer, in general, to two different combinations of spinors (in this thesis, these indices can be reduced to the band and spin indices, since they we treated a spin-collinear case), $f_{m\boldsymbol{k}}$ is the occupation of the corresponding Kohn-Sham state (1 for spin-polarized calculations, 2 in the spin-unpolarized case) whose eigenvalue is $\varepsilon_{m\boldsymbol{k}}$ and matrix elements $\rho_{nm\boldsymbol{k}}(\boldsymbol{q},\boldsymbol{G})$ such that

$$\rho_{nm\boldsymbol{k}}(\boldsymbol{q},\boldsymbol{G}) = \langle n\boldsymbol{k}|\, e^{i(\boldsymbol{q}+\boldsymbol{G})\cdot\boldsymbol{r}}\, |m\boldsymbol{k}-\boldsymbol{q}\rangle \tag{4.21}$$

The microscopic dielectric tensor in the reciprocal space can be then expressed by the relation [222]

$$\epsilon^{-1}_{\boldsymbol{GG'}}(\boldsymbol{q},\omega) = \delta_{\boldsymbol{GG'}} + v(\boldsymbol{q}+\boldsymbol{G})\chi^0_{\boldsymbol{GG'}}(\boldsymbol{q},\omega) \tag{4.22}$$

where

$$v(\boldsymbol{q}+\boldsymbol{G}) = \frac{4\pi}{|\boldsymbol{q}+\boldsymbol{G}|^2} \tag{4.23}$$

is the Coulomb interaction in the reciprocal space.

In the limit $\boldsymbol{q}\to\boldsymbol{0}$ one obtains the macroscopic dielectric tensor as

$$\epsilon_M(\omega) = \lim_{\boldsymbol{q}\to\boldsymbol{0}} \frac{1}{\epsilon^{-1}_{\boldsymbol{G}=\boldsymbol{0},\boldsymbol{G'}=\boldsymbol{0}}(\boldsymbol{q},\omega)} \tag{4.24}$$

The macroscopic tensor is indeed the one that should be considered when comparing the numerical predictions to the macroscopic experimental results [204].

Finally, the macroscopic dielectric tensor components are exploited to calculate the reflectivity for the individual α Cartesian directions. For an orthorhombic crystal like

the examined tungsten ditelluride and approximating the refractive index of air to the unitary value, the reflectivity in quasi-normal incidence conditions is [59]

$$R_\alpha = \frac{(n_\alpha - 1)^2 + k_\alpha^2}{(n_\alpha + 1)^2 + k_\alpha^2} \tag{4.25}$$

where n_α and k_α are the real and imaginary parts of the refractive index for α such that

$$\begin{aligned} n_\alpha &= \{\tfrac{1}{2}[(\epsilon_{\alpha,1}^2 + \epsilon_{\alpha,2}^2)^{1/2} + \epsilon_{\alpha,1}]\}^{1/2} \\ k_\alpha &= \{\tfrac{1}{2}[(\epsilon_{\alpha,1}^2 + \epsilon_{\alpha,2}^2)^{1/2} - \epsilon_{\alpha,1}]\}^{1/2} \end{aligned} \tag{4.26}$$

where $\epsilon_{\alpha,1}$ and $\epsilon_{\alpha,2}$ are the real and imaginary parts of the diagonal components $\epsilon_{\alpha\alpha}$ of the dielectric tensor.

The IP approximation is usually reasonable to describe the optical spectra of metallic compounds like WTe_2 as screening effects are expected to lead to minor corrections in the response function due to the static electron-hole interactions. However, even for certain metallic systems, dynamical electron-hole interactions may give relevant deviations from the IP formulas [226]. Naturally, as the electron-hole interactions are added, the computational workload becomes increasingly large. Thus their inclusion and the level of approximation may be decided when comparing the results to the experimental optical data.

To correctly reproduce the full spectrum of the dielectric tensor of metallic systems, it is important to introduce the Drude term to account for the intraband transitions. While it is possible to calculate this term *ab initio*, it usually requires a very-high sampling of the reciprocal space around the Fermi level, in particular for the region where the Fermi surface intersects the metallic bands, to reach a satisfying convergence [227].

To speed-up the simulation, the Yambo code gives the opportunity to the user to introduce the Drude term as an empirical, anisotropic in the general case, correction to the dielectric function. In this thesis, this was done by comparing the experimental results from [68] with our simulations. Nevertheless, our focus was the near-infrared/visible range, while the plasma edge connected to the Drude contribution is found in the far-infrared for this material (Fig. 2.3). Moreover, to accurately reproduce the far-infrared region of the spectrum, the spin-orbit contribution should be included under a fully-relativistic framework as well, as it was shown to be important for WTe_2. As for QE, the Yambo code calculations include settable convergence parameters in this scripts, such as the considered number of bands for the response function and cut-offs of plane-wave expansions, but the final results also depend on the starting databases derived from QE and, indirectly, from their convergence parameters.

4.2 Density functional theory and many-body codes

4.2.1 Quantum Espresso

QUANTUM ESPRESSO [216][224][228] is an open-source density functional theory suite of codes for electronic structure calculations, mainly written in Fortran and C languages. The atomic potential of the atoms is described through pseudopotentials, under various schemes (*e.g.* norm-conserving, ultrasoft and projector-augmented wave). The electron eigenfunctions and charge density are described through bases of plane waves, which allow a shorter computation time as well as good adaptability when multiple atoms

are present in the unit cell. Ground state properties such as the relaxed configuration, electronic band structure, electronic density of state and charge density can be calculated. Moreover, using density functional perturbation theory, it is possible to obtain the dynamical matrix coefficients for an arbitrary momentum and derive related quantities such as the eigenvalues and eigenvectors for the phonon modes. Other tools permit molecular dynamics calculations and multiple post-processing analysis. In this thesis, QUANTUM ESPRESSO is employed to calculate the electronic ground-state properties of tungsten ditelluride (WTe_2) and its zone-center phonons by making use of the core PWscf, PHonon and Post-Processing packages.

4.2.2 Yambo

The Yambo code [222][223] is an open-source project aimed at describing the excited state properties of various condensed matter systems of different dimensionality. Primerily written in Fortran and C languages, it also offers python extension modules to facilitate the user experience. As a starting point, it requires the ground state electronic structure (eigenvalues and eigenfunctions) calculated through a density function theory code such as Quantum Espresso. It can be employed to study linear and nonlinear response quantities and include many-body quasi-particle corrections at different approximation levels, going from the independent-particle (IP) framework until the electron-hole interactions (Bethe-Salpeter equation, BSE). Among the most useful applications of the code, there is the simulation of the optical properties. Its numerical algorithms and associated libraries allows a very efficient parallel structure to simulate even materials with large unit-cells or peculiarities which require high-convergence parameters. In this thesis, Yambo was used to derive the reflectivity of WTe_2 in quasi-normal conditions starting from the diagonal components of the macroscopic dielectric tensor and to interpret the out-equilibrium signatures of the optical phonon modes through its modifications.

CHAPTER 5

Broadband NIR and VIS experiments on WTe_2

5.1 Introduction

Several fundamental properties of materials, including the electrical and thermal conductivities, are influenced by lattice vibrations [1]. Recently, the possibility to control such behaviors by resonant coupling of ultrashort light pulses to specific lattice modes has been proved [229][230]. Conversely, coherent phonon spectroscopy has emerged as a powerful method to directly observe, in the time domain, coherent lattice vibrations [231][232][233]. Despite the many studies, coherent phonons have been exploited primarily to characterize ground state properties [153][234][235][236], rather than controlling the material properties. This observation motivates the quest to learn how specific lattice vibrations affect the electronic behavior in the vicinity of the Fermi energy. Structural dynamics experiments, such as time-resolved x-ray diffraction [237] and time-resolved electron diffraction [238], are currently used to measure the amplitude of synchronized collective excitations of the atoms in a solid, *i.e.* coherent phonon modes. Yet, subpicometer displacements in complex materials are very challenging to be resolved.

In time-resolved reflectivity experiments, such modes appear as ultrafast oscillations of the probe signal [152][239]. Their amplitude has been related to the atomic shifts for single-element materials [240][241] by using single-frequency measurements. In materials with complex unit cells, a larger number of phonon modes is present and a method that avoids correlations in the estimation of individual amplitudes is required. In this chapter, we report on a novel approach to estimate the non-equilibrium atomic displacements of coherent optical phonon modes by detecting the modulation induced in a broadband reflectivity probe signal, which is required to obtain reliable signatures of the modes. Density functional theory (DFT) calculations are applied to a displacive model to simulate the time-resolved optical reflectivity signals and to estimate the coherent phonon amplitudes in the tens of femtometers regime.

The method is applied to the orthorhombic semimetallic (Td) phase of tungsten ditelluride (WTe_2), a transition metal dichalcogenide that has recently gained interest for showing an unusually high and non-saturating magnetoresistance [65] along with a possible type-II Weyl semimetal character [6]. WTe_2 has a layered structure belonging to the space group $Pmn2_1$ [242] with in-plane covalent bonding and weaker van der Waals interplanar interactions helping to hold together the individual layers. Furthermore, it has been shown that its electronic, optical and topological properties are influenced by strain forces [6][243], which can be induced through non-equilibrium perturbations [35] allowing an ultrafast control of the functionalities of this material.

We focus on two A_1 coherent optical phonon modes at $\sim$8 cm^{-1} and $\sim$80 cm^{-1}. They are comprised of non-equilibrium displacements of the atoms along the **y** and **z** crystallographic directions. The $\sim$8 cm^{-1} optical phonon is a uniform in-plane shift of the atoms, estimated to be $\sim$350 fm using a $\sim$230 $\mu J/cm^2$ absorbed pump fluence, while the $\sim$80 cm^{-1} mode corresponds to atomic displacements of few tens of femtometers which depend on the specific atom.

The majority of the results presented in this chapter can be also found in reference [106]. All the error intervals are expressed and displayed as $\pm\sigma$, one standard deviation.

5.2 Sample

High-quality tungsten ditelluride samples were grown as reported in [65]. The presence of defects was previously studied in [65][244]. In order to identify the in-plane crystallographic axes, low-energy electron diffraction (LEED) images were acquired under ultra-high vacuum conditions. In Fig. 5.1, ball-and-stick projections of the crystal structure of the layered orthorhombic phase of tungsten ditelluride (WTe_2) are shown. The crystallographic data ware taken from [242]. All the crystallographic representations were generated using the XCrySDen [245] software.

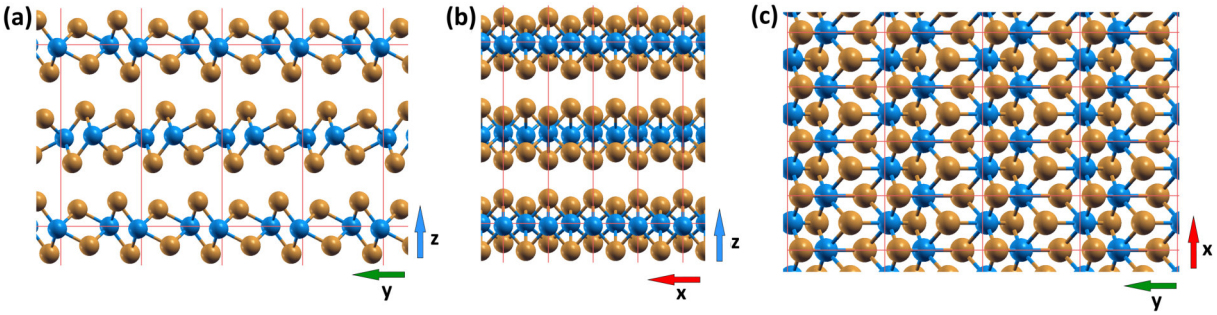

Figure 5.1. Projections of WTe_2 crystal structure perpendicular to the (a) **x**, (b) **y** and (c) **z** (only a single layer is shown) axes; **x** and **y** are the perpendicular in-plane directions, while the **z** axis is perpendicular to the layers; tungsten atoms in blue, tellurium atoms in orange; the unit cells are delimited by red lines.

5.3 Experimental setups

5.3.1 Broadband setup

The time-resolved broadband optical (TRBO) reflectivity setup used in this thesis work allows one to perform measurements in reflection or transmission geometry, over an ultra-

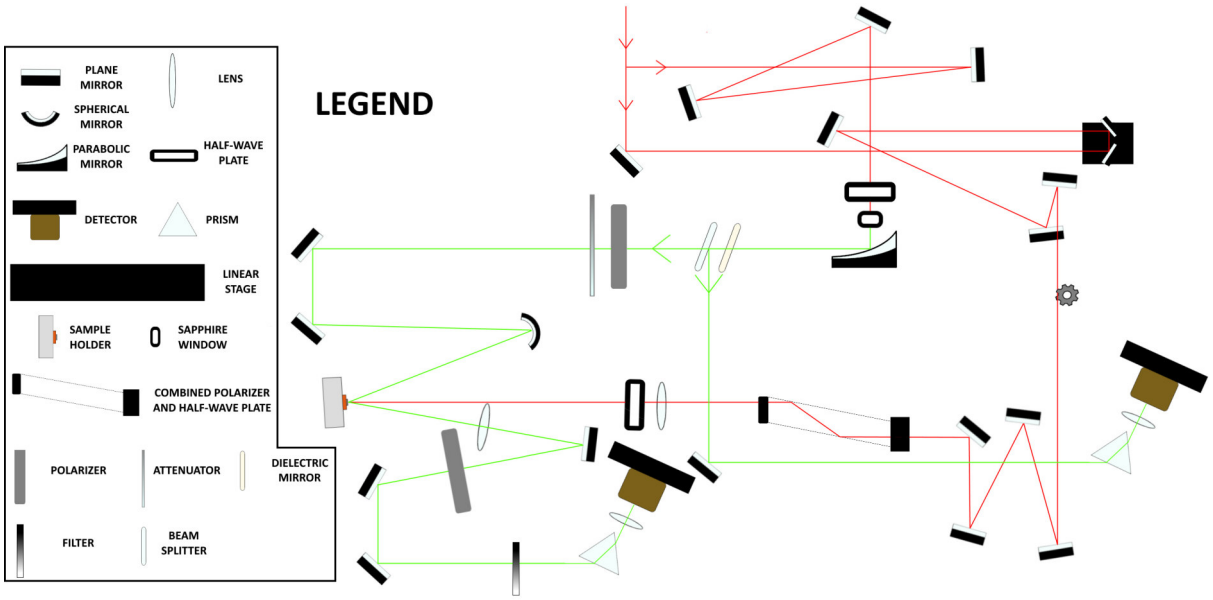

Figure 5.2. Sketch of the optical layout of the setup for broadband time-resolved optical spectroscopy setup used. The path for reflectivity experiments is shown. Adapted from [246].

broadband spectral range (~500-1600 nm, 0.77-2.48 eV). This unique possibility is obtained thanks to a careful optimization of the supercontinuum generation in a sapphire window and to special InGaAs linear array detectors allowing for the simultaneous acquisition of data in this wide spectral range.

The laser system exploited, the RegA (Coherent ®), is made by two laser cavities working in conjunction: an ultrafast oscillator (Mira 900F, working at 80 MHz) and a regenerative amplifier (RegA 9050), based on a chirped pulse amplification scheme. Each laser cavity is 'pumped' by a Verdi G (Coherent ®) which constitutes the primary laser source. The outcoming beam, possessing temporal and spatial coherence, has an almost Gaussian line shape frequency-wise with a central value of ~800 nm and a full width at half maximum (FWHM) value of ~35 nm. Time-wise, the system produces ~50 fs pulses with an energy per pulse of 6 µJ at 250 kHz. This corresponds to an average power of 1.5 W.

In Fig. 5.2 the basic layout and the main components found in the optical setup are presented. The beam arrives to the experimental setup with horizontal polarization. Then, it is split into two paths (pump and probe) by a beam splitter. Through mirrors, the two pulsed beams follow then different paths overlapping again at the sample position.

The pump beam is directed using mirrors, among which two of them are mounted on a linear motorized stage. Next, the ray is modulated through a chopper to impose the pumped and unpumped conditions. Its fluence can be modified using a device consisting in a double Brewster-window polarizer preceded by a rotatable half-wave plate. The s-polarized component is chosen and focused on the sample.

On the other hand, the probe beam is tightly focused in a 3-mm-thick sapphire window, to broaden its frequency spectrum. This is achieved thanks to nonlinear optical processes, the main one being the 'self-phase modulation'. Next, the supercontinuum beam is collimated with a parabolic mirror and impinges on a dielectric mirror to reduce the intensity in the spectral region of the original seed beam. A small portion of the beam is taken through a different path to be used as a reference signal and directed to one of the

two detectors. The main probe beam passes through a polarizer and a disc attenuator, before arriving to the sample.

The sample is placed in the focus of both the pump and probe beams. The spot size can be measured either through knife-edge profiling or using a beam profiler. In general, it is desirable to have a pump spot size larger than the probe one, in order to measure the transient optical properties in a region of the sample that can be considered uniformly excited.

To measure the out-of-equilibrium reflectivity, the samples are positioned on the frontal part of a sample holder with adjustable translational and angular degrees of freedoms.

The experimental data are plotted as

$$\frac{DR}{R}(\omega, t) = \frac{R_{pumped}(\omega, t) - R_{unpumped}(\omega)}{R_{unpumped}(\omega)} \tag{5.1}$$

where $R(\omega)=S_1(\omega)/S_2(\omega)$ with

- S_1, vector of signals collected by the individual photodiode pixels coming from the InGaAs detector after the sample;
- S_2, vector of signals collected by the individual photodiode pixels coming from the InGaAs detector relative to the reference beam, used to reduce the noise arising from fluctuations in the supercontinuum spectrum.

A polarizer is present in the detection path to extinguish the scattering from the pump beam. Nonetheless, a small part often survives. This is mainly due to the roughness of the sample surface provoking a pump scattering in a large cone, making it difficult to fully stop it with an iris, and minor residual perpendicular component, together with the finite extinction ratio of the polarizer.

The outcoming beam goes through a neutral-density filter to avoid the saturation of the detectors. Finally, the spectral components are separated by an equilateral prism (Flint glass) and focused on the sensible area of the InGaAs linear photodiode array detector, particularly sensible in the near-infrared region.

The reflectivity was measured in a near-normal incidence geometry. On the sample, the pump spot diameter was estimated to be $\sim$160 μm, while the average spot diameter for the various spectral components of the probe beam was $\sim$110 μm. Modifying the pump polarization direction produced no significant variation of the main spectral features. For this reason, all measurements were performed by keeping the pump beam polarization perpendicular to the probe one, in order to minimize the residual pump scattering by using a polarizer inserted before the detectors.

5.3.2 Single-color setup at T-ReX

The measurements were performed on the same laser system employed for the broadband optical experiments. When the experiment requires pump and probe to have different photon energy, it is possible to use an optical parametric amplifier (OPA) to generate near infrared light with longer wavelengths or one can simply filter the supercontinuum light using band-pass filters at the desired wavelength. Recently, the setup was upgraded allowing also the possibility to acquire broadband and single-color data without changing the sample position by using a foldable mirror mounted in the path.

Complementary results were obtained using two pump photon energies of 1.0 eV and 3.1 eV, generated from the fundamental 1.55 eV beam. The former is produced through an

optical parametric amplifier (OPA), while the latter is obtained using a nonlinear crystal (barium borate, BBO) to generate its second harmonic and removing the remaining 1.55 eV seed pulse with a filter.

The data was collected by a single photodetector a treated using a lock-in amplifier to improve the signal to noise ratio.

5.4 Computational details

Density functional theory (DFT) simulations were carried out using norm-conserving (NC) [208] scalar relativistic [211] pseudopotentials with the generalized gradient approximation (GGA) in the Perdew-Burke-Ernzerhof (PBE) parametrization for the exchange-correlation functional [210] chosen from the PseudoDojo database [212][247]. An orthorhombic simulation cell (Figs. 5.1(a)-(c)), with lattice constants a=3.477 Å, b=6.249 Å and c=14.018 Å along the **x**, **y** and **z** directions respectively, taken from the crystallographic data in [242], was used. It contains four tungsten and eight tellurium atoms, with 14 and 16 valence electrons respectively, for a total number of 184 electrons per unit cell.

Structural optimizations and zone-center phonon calculations in the framework of density functional perturbation theory (DFPT) were performed using the Quantum Espresso (QE) [216] suite of codes with a plane wave kinetic energy cutoff of 70 Rydberg for the wavefunctions and a 12×10×6 uniform k-point mesh for integrations over the Brillouin zone. Van der Waals contributions were not included, since, although in general relevant to describe layered compounds, in this specific case they do not improve the description of structural and electronic/optical properties of the system. Td-WTe_2 presents 33 zone-center optical phonon modes with four possible symmetry representations given by the C_{2v} point group [242]. In the following sections, we will focus on the two lowest energy A_1 modes.

We calculated the diagonal macroscopic dielectric tensor components through the Yambo code [222] starting from the wavefunctions and eigenvalues obtained through the PW package of QE using the same kinetic energy cut-off and a 16×14×10 k-grid. Convergence tests showed that the parameters used in QE and Yambo ensure the numerical accuracy needed to appreciate the relative effects of subpicometer atomic displacements on the electronic states in the near-infrared and visible spectral regions. As computational resources allowed it, we decided to keep the whole set of G-vectors for the expansion of the wavefunctions derived from the QE calculation. The number of polarization function bands to be considered in the calculations was also determined to be 119 (see section 5.5.6). The reflectance curves were derived at the independent-particle (IP) level using a linear response approach for different atomic configurations for each of the two in-plane investigated probe polarizations separately, setting the electric field along the **x** and **y** axes respectively (Fig. 5.1).

5.5 Results

5.5.1 Broadband reflectivity with a 1.55 eV pump

The normalized time-resolved differential reflectivity (DR/R) revealed a large anisotropy consistent with the two-fold in-plane symmetry of WTe_2 (Fig. 5.3) also reported for equilibrium electrodynamics [68].

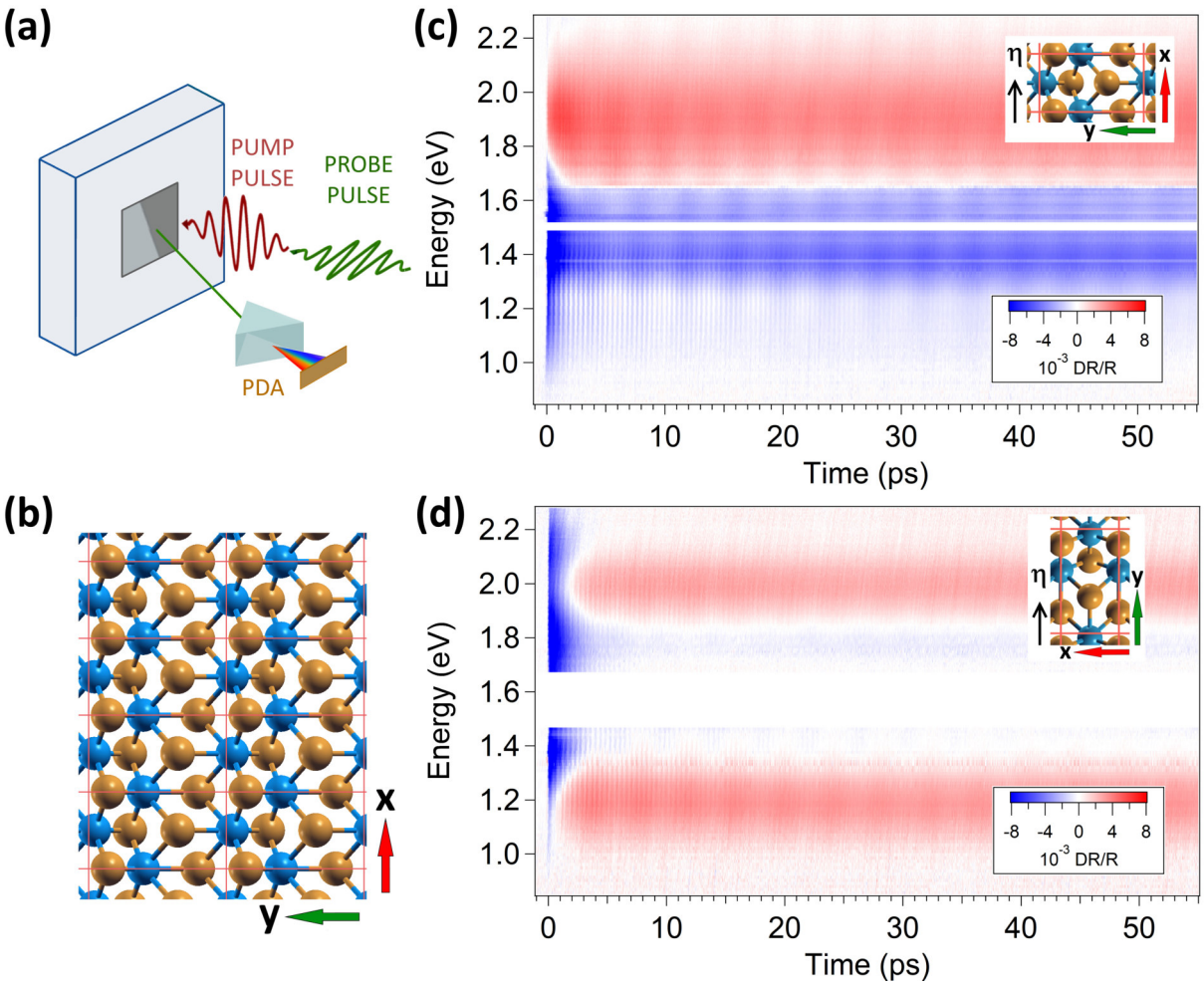

Figure 5.3. (a) Sketch of the time-resolved broadband reflectivity experiment: the reflected probe beam is dispersed through a glass prism and detected by a photodiode array (PDA) detector. (b) Projection of a WTe_2 layer on the xy plane with blue tungsten and orange tellurium atoms showing multiple unit cells delimited by red lines; other projections are reported in Fig. 5.1. (c),(d) Ultrafast broadband DR/R images for WTe_2 with the probe beam polarization along (c) **x** and (d) **y**, both taken at ∼710 μJ/cm^2 absorbed pump fluence and 1.55 eV pump photon energy at T=295 K.

In Figs. 5.3(c),(d), the broadband probe beam polarization was set parallel to the **x** ($\eta||\mathbf{x}$) and **y** ($\eta||\mathbf{y}$) crystallographic axes respectively with pump beam polarization kept perpendicular to the probe one. Measurements were acquired with a ∼710 μJ/cm^2 absorbed pump fluence and 1.55 eV pump photon energy at T=295 K. A region of the spectrum was disturbed by the scattering of pump beam photons from the sample, so it was removed.

The temporal evolution of the reflectivity is directly related to the electronic and ionic degrees of freedom [152][231][239]. In general, the DR/R is a superposition of signals due to transient variations of electronic density of the states and population. We empirically describe the temporal evolution after the perturbation (time-zero, t=0) as

$$DR/R(t,h\nu) = G(t)*\Big[\sum_i A_i(h\nu)e^{-t/\tau_{Ri}} + B(h\nu)e^{-t/\tau_{heat}} + \sum_j C_j(h\nu)cos(\omega_j t+\phi_j)e^{-t/\tau_{Pj}}\Big] \tag{5.2}$$

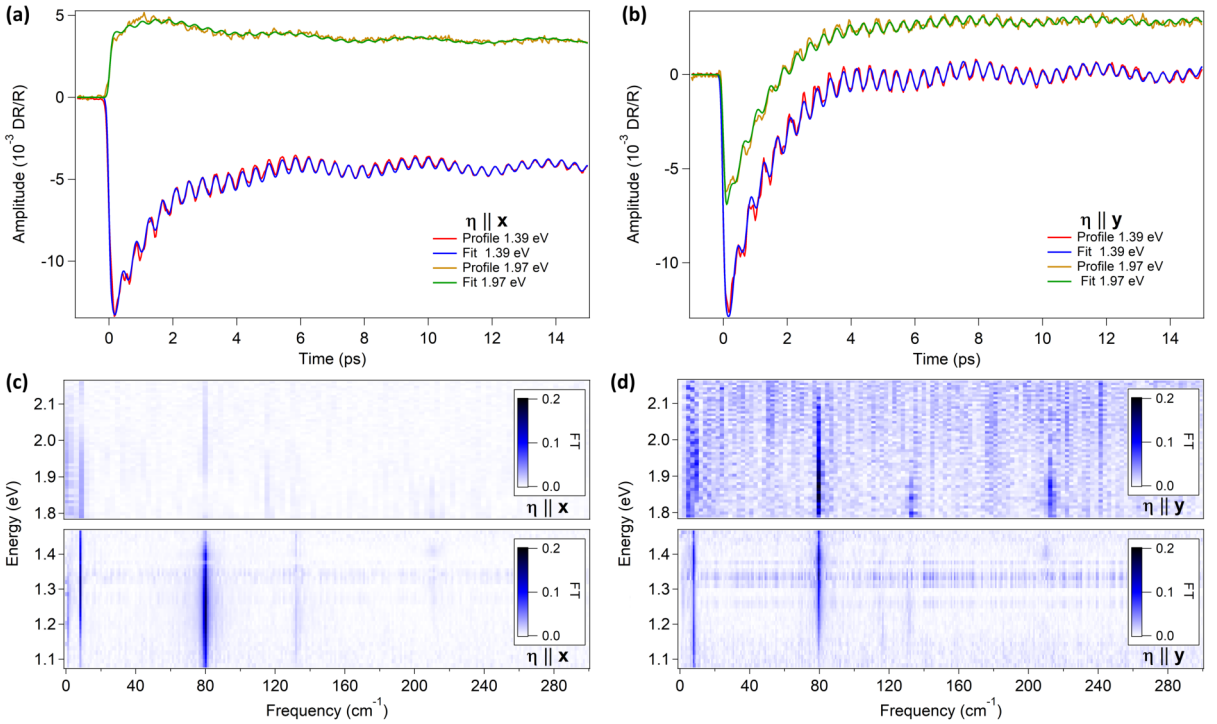

Figure 5.4. Profiles at 1.39 eV and 1.97 eV photon energy for probe beam polarization (a) $\eta||\mathbf{x}$ and (b) $\eta||\mathbf{y}$, at ∼710 µJ/cm^2 absorbed pump fluence and T=295 K. Fourier transform images performed across a few picoseconds after time zero for (c) $\eta||\mathbf{x}$ and (d) $\eta||\mathbf{y}$ after subtracting from the data a purely exponential fit based on Eq. (5.2) for various probe photon energies.

where $G(t)$ represents the pump and probe pulses cross-correlation and $A_i(h\nu)$, $B(h\nu)$ and $C_j(h\nu)$ denote the amplitudes of three different phenomena: i) electronic relaxation phenomena with time constants τ_{Ri}, ii) heating contribution with a characteristic time τ_{heat} and iii) oscillations due to coherent phonons with angular frequency ω_j, initial phase ϕ_j and decay time τ_{Pj}.

After the pump pulse excitation, electron-electron and electron-phonon scattering processes constitute the main incoherent relaxation phenomena in the first hundreds of femtoseconds, as it commonly found for metallic samples [148], and are responsible for the initial exponential decay of the DR/R signal [104]. The coherent phonon effects are empirically added through damped cosine waves, which are approximations of the general DECP result [154].

After a few picoseconds where the main thermalization of the electronic system with the lattice occurs, the differential reflectivity DR/R reaches a plateau, showcasing an offset with respect to the equilibrium value.

The temporal profiles are very well fitted by using Eq. (5.2). Their sign and magnitude vary with the photon energy, while the main relaxation presents a time constant which is almost the same and equal to ∼1 ps with only small differences, as previously found in [104] at hν=1.55 eV and assigned to electron-phonon thermalization.

In Fig. 5.4 we report selected profiles extracted at two photon energies from the datasets reported in Figs. 5.3(c),(d), alongside with the Fourier transform (FT) of the oscillatory signal in most of the investigated range. The most prominent features are at 7.9±0.4 cm^{-1} and 79.7±0.4 cm^{-1}. For notation purposes, we refer to these modes with the labels 8 cm^{-1} and 80 cm^{-1}. These modes give the largest contribution to the coherent

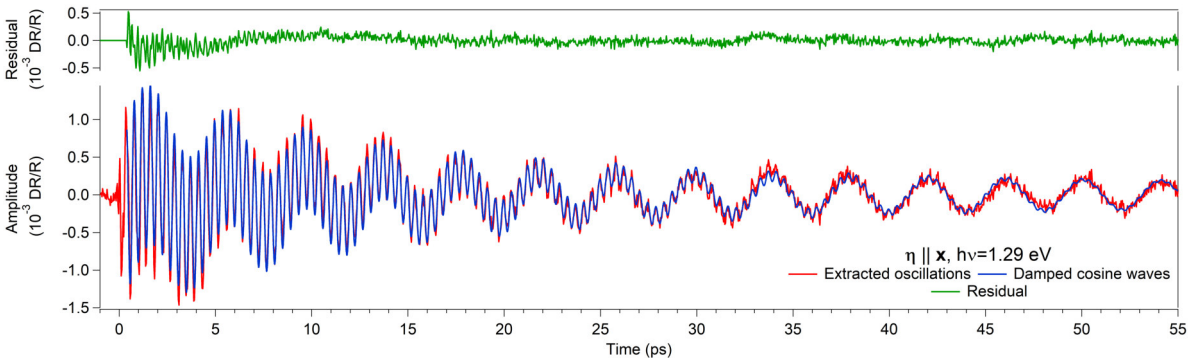

Figure 5.5. Oscillatory component of the DR/R signal, obtained by subtracting an exponential fit (see Eq. (5.2)) from the temporal profile at 1.29 eV acquired at ∼710 µJ/cm^2 absorbed pump fluence and T=295 K for $\eta||\mathbf{x}$.

component of the DR/R signal as shown in Fig. 5.5, where two damped cosine waves fit the oscillatory signal. Minor contributions at higher frequencies are detected at 116.5±0.4 cm^{-1}, 132.2±0.4 cm^{-1} and 210.2±0.4 cm^{-1} and appear as beats in the DR/R signal in the first hundreds of femtoseconds. Together with a blue shift of the 8 cm^{-1} shear mode [246], the phonon effects become more pronounced as the temperature is reduced (Fig. 5.6).

While it is not the focus of the experiment, we can try to infer the origin of the enhanced response from the literature. Such behavior is not only due to a likely reduced dephasing rate at lower temperatures (in Fig. 5.6, this would be especially evident for the modes with a small damping time at room temperature compared to the time window), similar to what was observed in elemental semimetals [248], which would depend on the anharmonic decay of the phonons as well as the defect concentration, but also connected to the excitation process. In [105] (Supplementary Figure 5), it was shown that the temperature dependence of the shear phonon amplitude in WTe_2 closely follows that of the main relaxation peak after time-zero, giving an almost constant ratio between the two. This suggests a common origin for the two. An analogous relation was observed in [249] for transition metals leading to the conclusion that in both cases the temperature dependence of the response is dominated by the change of the dielectric function related to the photoinduced carrier density. In [249], the photoinduced carrier density, a key term in the simple DECP model [154] described in section 3.1.1, is connected to the temperature change occurring in the electronic system at low temperature which is larger under the same fluence, due to the increase of the electronic heat capacity as the temperature grows [1]. Nevertheless, to accurately explain the relative behavior between the coherent phonons amplitude at different temperatures in WTe_2 requires a more advanced analysis, *e.g.* based on the detailed excitation models such as [156], as well as a dedicated experimental study.

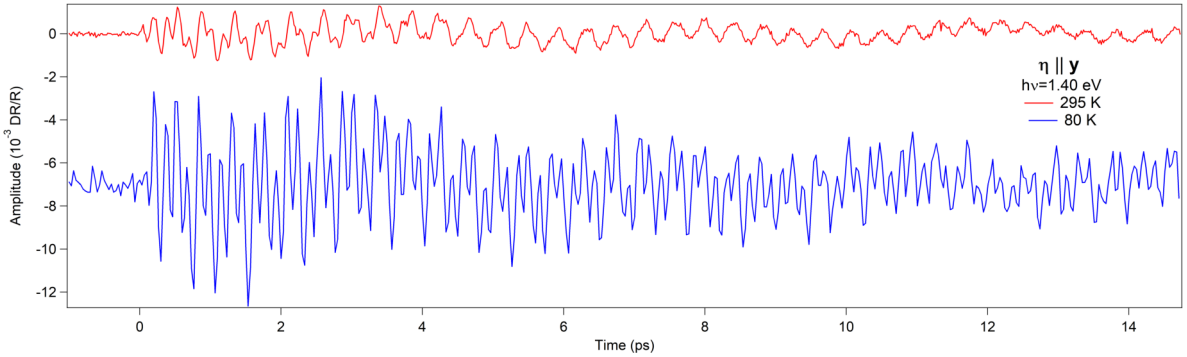

Figure 5.6. Phonon modulation of DR/R, obtained by subtracting an exponential fit (see Eq. (5.2)) from the temporal profiles at 1.40 eV acquired at ∼710 µJ/cm^2 absorbed pump fluence, T=80 K (Fig. 5.14(a)) and T=295 K (Fig. 5.3(a)) and for $\eta||\mathbf{y}$; the beats are due to phonon modes with frequency higher than 80 cm^{-1}.

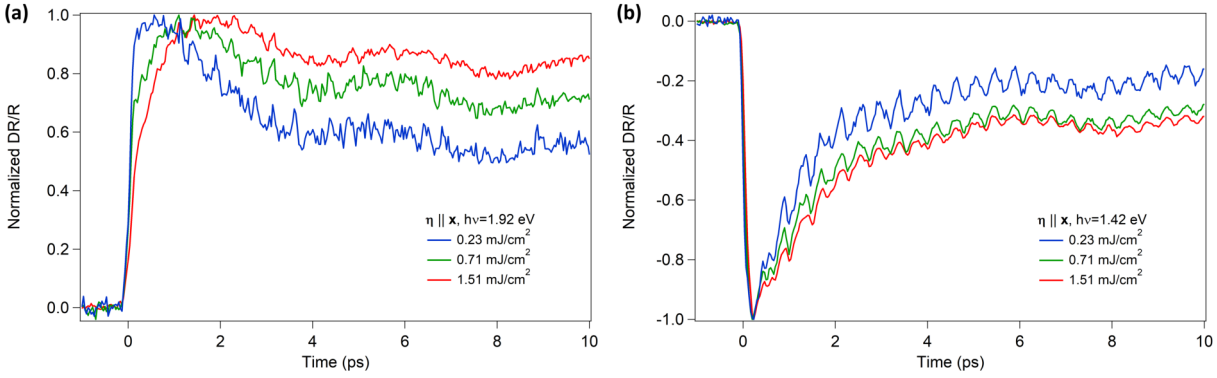

Figure 5.7. DR/R profiles obtained from 1.55 eV pump photon energy-broadband supercontinuum probe beam experiments at different fluences and T=295 K for probe polarization $\eta||\mathbf{x}$; the profiles in (a) at 1.92 eV show a fluence-dependent position of the main out-of-equilibrium peak, while the profiles in (b) at 1.42 eV do not present such behavior.

In the visible spectral region from 1.70 to 2.10 eV, the DR/R cannot be fitted by a single exponential decay (Eq. (5.2)) for probe polarization $\eta||\mathbf{x}$. In presence of spectral contributions with opposite sign and comparable time constants, the DR/R reaches its maximum value at longer delay, analogously to the case in Fig. 5.4(a). This delay can be as large as 1 ps, alongside with a slower decay of the signal. Investigating the dependence on fluence, we learned that (Fig. 5.7) the delay increases with the deposited pump energy. At variance, in the infrared the peak position of DR/R is independent on the fluence. For this reason, for example, it is not possible to effectively describe the behavior of this material with just a single Drude-Lorentz term [59] in the dielectric tensor for the measured spectral range. For $\eta||\mathbf{y}$, we do not observe such phenomenon. This may be connected to different matrix elements for the involved transitions in the two distinct linear probe polarizations. The origin of the shift of the peak is likely connected to the increasing energy inserted in the electron system, which could lead to a longer time required for the electrons to thermalize. The reason why this is not observed for some of the probe photon energies (for example at 1.42 eV in panel (b)) may be related to the different electronic transitions involved in the reflectivity spectrum at the different wavelengths, comprehending energy levels which are more influenced by the increase in the deposited energy (*e.g.* quasi-free electrons around the Fermi level). As fluence is increased beyond the values reached in this experiment (see Chapter 6), we observe that this shift delay starts to appear also at previously (almost) unaffected wavelengths, as shown in Fig. 6.11. This difficulty in redistributing the larger deposited energy to reach a thermal equilibrium is possibly also the cause of the peculiar increase of the non-oscillating diffracted intensity for the $(\bar{1}63)$ Bragg peak in the fluence dependences studied in sections 6.4 and 6.6.

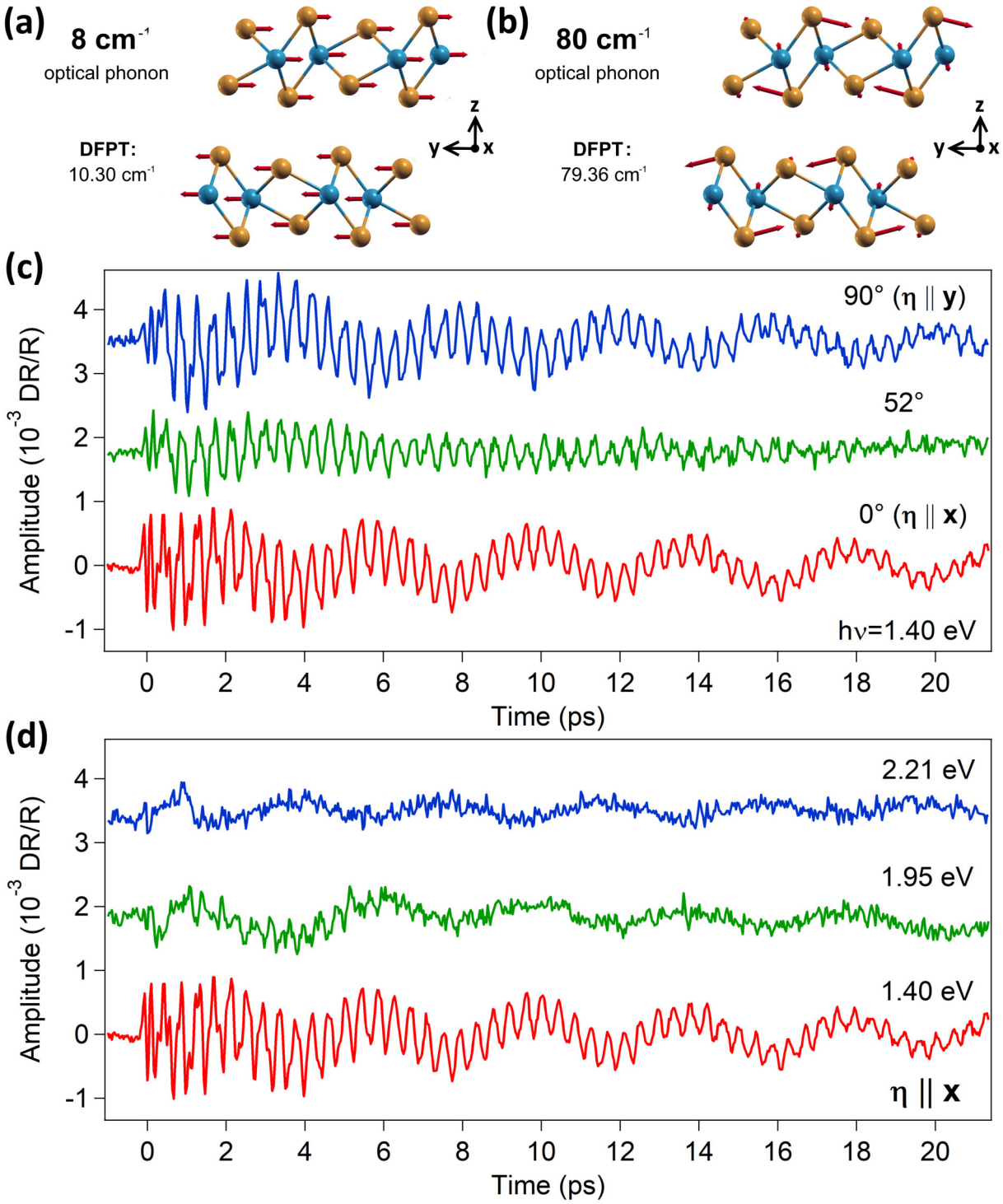

Figure 5.8. DFPT eigendisplacements and frequencies for the (a) 8 cm^{-1} and (b) 80 cm^{-1} optical modes; the tungsten atoms are depicted in blue, whereas the tellurium ones in orange. (c),(d) Oscillatory signal due to coherent phonons (the two upper curves are shifted from the central DR/R=0) (c) at 1.40 eV photon energy for different probe beam polarization angles, showing a π phase shift for 8 cm^{-1} mode between the two perpendicular configurations while the 80 cm^{-1} mode appears to be unaffected and (d) for $\eta||\mathbf{x}$ as a function of the photon energy, evidencing a π phase shift for 8 cm^{-1} mode when comparing the infrared (1.40 eV) to the visible (2.21 eV) spectral region.

Subtracting an exponential fit function from the experimental signals allows the extraction of the coherent component of the DR/R signal. The resulting signal displays marked periodic modulations in the time domain, arising from the excitation of coherent phonon modes. The most prominent oscillating features, as detected by FT and in [104], are the 8 cm^{-1} and 80 cm^{-1}. The associated time-decay constants, derived by fitting the modulations with two exponentially-damped cosine waves, are τ_{P1}=77±4 ps for the 8 cm^{-1} mode and τ_{P2}=12.1±0.2 ps for the 80 cm^{-1} mode. DFPT results indicate that these frequencies are linked to A_1 zone-center optical phonon modes, represented in Fig. 5.8(a),(b). The 8 cm^{-1} mode can be pictured as adjacent layers moving in antiphase, while the 80 cm^{-1} involves more complex in-plane and out-of-plane movements. The smaller value of the experimental frequency for the 8 cm^{-1} mode with respect to the DFPT result (10.30 cm^{-1}) can be attributed to a redshift as temperature or fluence are increased [105]. The marked difference between the time constants of the two modes could be linked to the different type of perturbation of the interatomic bonds induced by the associated displacements. The 8 cm^{-1} mode (Fig. 5.8(a)) only alters the weaker interplanar interactions. Differently, the 80 cm^{-1} mode (Fig. 5.8(b)) induces a modification of the in-plane covalent bonds.

When switching the probed direction from $\eta||\mathbf{x}$ to $\eta||\mathbf{y}$, a π phase change for the 8 cm^{-1} mode (Fig. 5.8(c)) was clearly registered for most of the probe photon energies. Analogous π phase changes were found by comparing the temporal profiles taken at different probe photon energies using the same polarization for the same mode (Fig. 5.8(d)). These phase differences can be explained in terms of the peculiar anisotropy of the dielectric function and were reproduced by our numerical simulations (see discussion for Fig. 5.11).

5.5.2 Equilibrium reflectance

We report the calculated reflectance curves along the two perpendicular polarization directions in Fig. 5.9, compared with the reflectance data found in [68]. We included 119 bands for the response function to reproduce the experimental data with a very good quantitative agreement. Although the experimental data were measured at 10 K and DFT results were obtained at T=0 K, they can be still considered adequate for our DR/R comparisons at T=295 K in good approximation, since the optical properties in this spectral region are only slightly affected by temperature [202].

In order to model the effects of the coherent phonons on the reflectivity, we first calculated the wavefunctions and eigenvalues for the equilibrium configuration using QE and the macroscopic dielectric tensor diagonal components and the reflectivity curves through YAMBO. Then, we considered four out-of-equilibrium configurations labeled as 0 and π phases, corresponding to displacements in opposite directions, for each of the coherent phonon modes, using the eigendisplacements obtained through DFPT with respect to the equilibrium positions.

For each configuration we calculated the associated reflectivity and DR/R with respect to the equilibrium configuration. These curves describe the effect of the optical phonons on a quasi-equilibrium adiabatic system. Indeed, a few picoseconds after time-zero, the system has relaxed through electron-phonon scattering processes and the incoherent part of the DR/R signal reaches a plateau having a decay time much larger than the coherent phonon period and damping timescale.

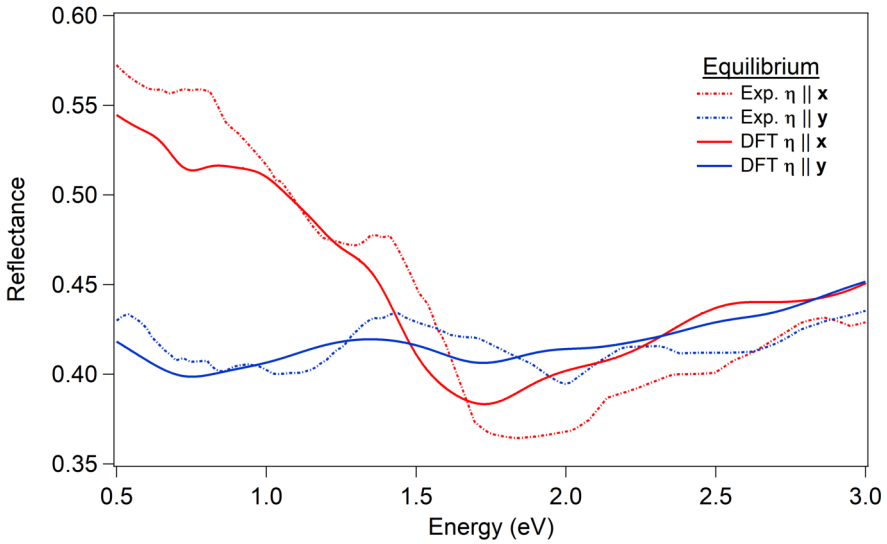

Figure 5.9. Equilibrium reflectance curves for the two perpendicular probe polarizations calculated at the IP level; the experimental curves were derived from the data reported in [68], measured at 10 K.

5.5.3 Experiment - theory comparison

Experimentally, the effects of each single optical phonon mode on the DR/R were isolated with the following procedure. For the 8 cm^{-1} phonon, we took the mean value over one period of the 80 cm^{-1} modulation around two consecutive 8 cm^{-1} extrema (Fig. 5.10). For the 80 cm^{-1} oscillation, we directly used the spectral profiles at the extrema, considering that the period of the slower phonon is about ten times larger. The spectral profiles were collected after the main relaxation peak, as precisely indicated in the insets. The difference between the spectral profiles at the maximum (0 phase) and minimum (π phase) of the coherent phonons, named with respect to the $\eta||\mathbf{x}$ DR/R, gives an unique signature of the phonon mode (Fig. 5.11).

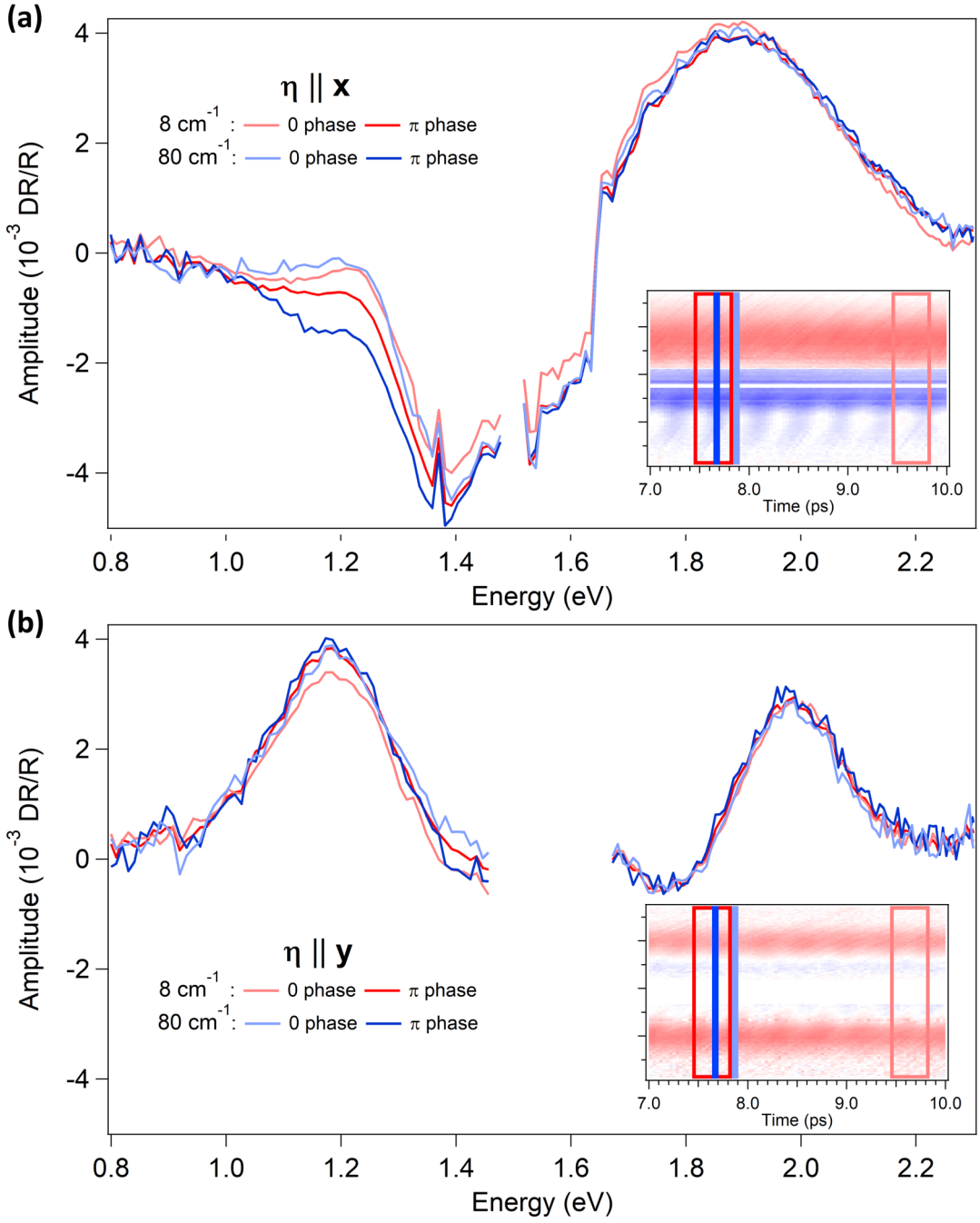

Figure 5.10. Experimental spectral profiles extracted from the DR/R (t,hν) maps reported in Figs. 5.3(c),(d). The linearly polarized probe is oriented for (a) $\eta||\mathbf{x}$ and (b) $\eta||\mathbf{y}$. The 0 and π phases are referred to the maximum and minimum of the oscillation in the DR/R signal for $\eta||\mathbf{x}$ in the infrared spectral region; the insets show the time delays at which the curves were extracted. The vertical axis and color scale of the insets are the same as for Figs. 5.3(c),(d).

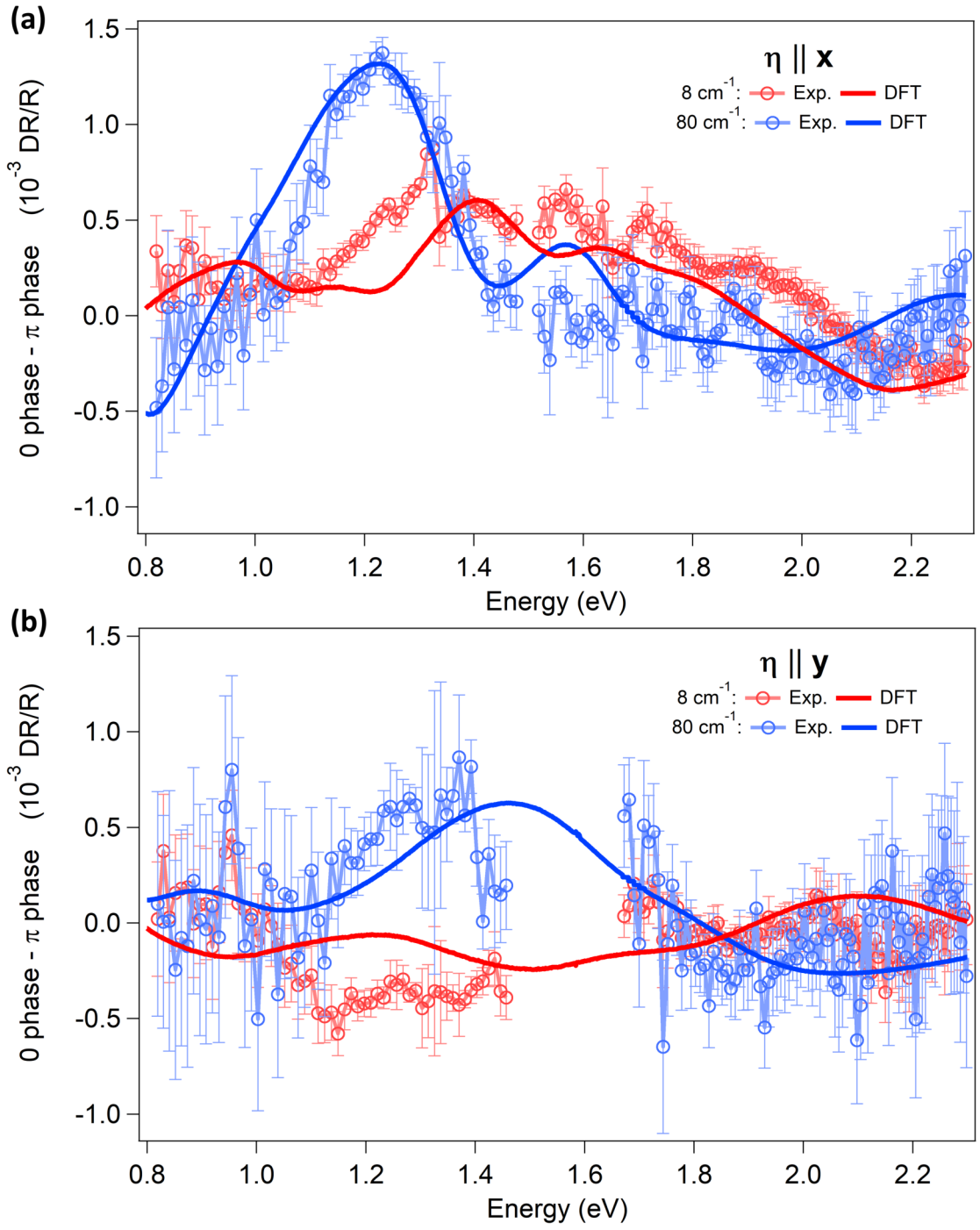

Figure 5.11. Comparisons between the experimental and DFT-based (IP approximation) calculated DR/R difference between the 0 and π phases, showcasing the effects of the 8 cm^{-1} and 80 cm^{-1} optical phonons for (a) $\eta||\mathbf{x}$ and (b) $\eta||\mathbf{y}$ using a $\sim$710 $\mu J/cm^2$ absorbed pump fluence and T=295 K.

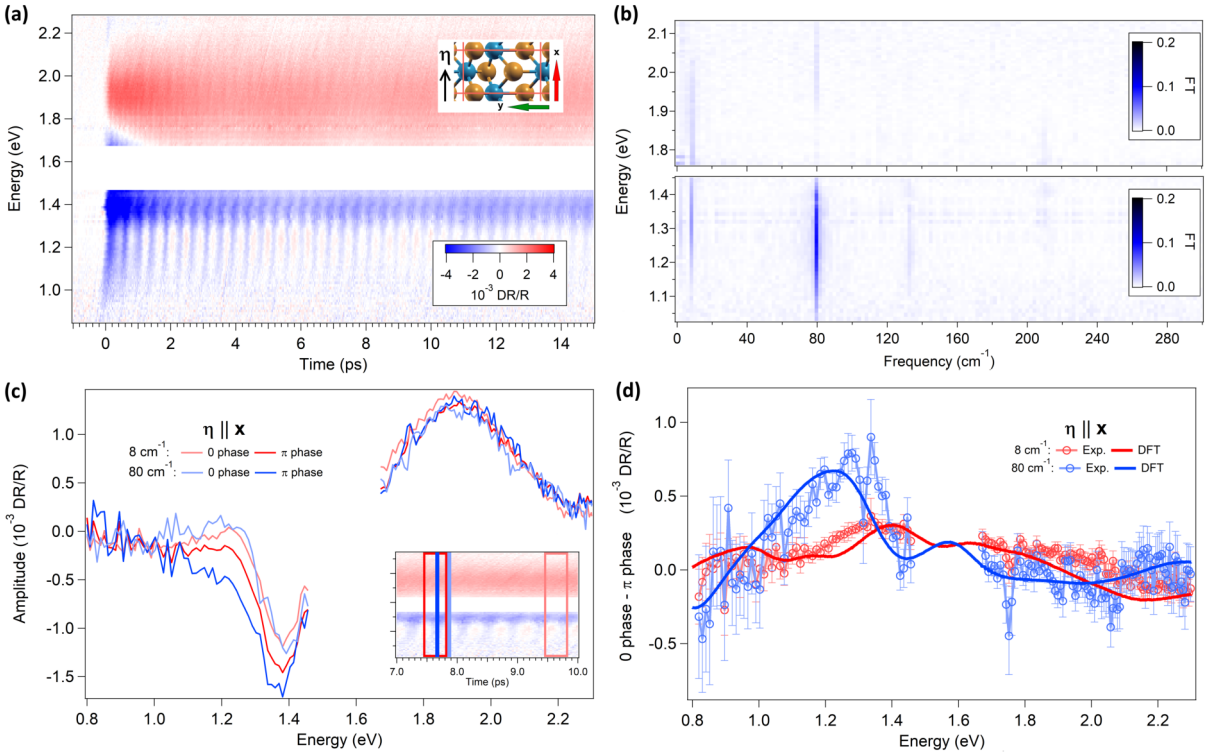

Figure 5.12. (a) Ultrafast broadband DR/R image for WTe_2 for probe polarization $\eta||\mathbf{x}$ taken at ∼230 μJ/cm^2 absorbed pump fluence and T=295 K. (b) Fourier transform images performed across a few picoseconds after time zero after subtracting from the data a purely exponential fit based on Eq. (5.2). (c) Spectral profiles taken at selected time delays for maxima and minima of the 8 cm^{-1} and 80 cm^{-1} optical phonon effects; the inset, with the same vertical axis and color scale as panel (a), shows the exact temporal positions. (d) Comparisons between the experimental and DFT-based (IP approximation) calculated DR/R difference between the 0 and π phases displayed in (c), showcasing the effects of the 8 cm^{-1} and 80 cm^{-1} optical phonons for $\eta||\mathbf{x}$.

Similar fingerprints are obtained when the absorbed pump fluence is lowered at ∼230 μJ/cm^2 at T=295 K, as shown in Fig. 5.12.

Analogous effects can be also extracted at T=80 K, where phonons exhibit a blueshift in their frequencies with respect to T=295 K, as previously reported in [105][246][250]. Compared to T=295 K, the contribution from coherent phonons with frequency higher than 80 cm^{-1} becomes more prominent in the DR/R maps measured at ∼710 μJ/cm^2 (Figs. 5.13, 5.14) and ∼230 μJ/cm^2 (Fig. 5.15) absorbed pump fluence. The phonon effects for $\eta||\mathbf{x}$ shown in Fig. 5.16 are analogous to the room temperature results reported in Figs. 5.12(d), although it becomes harder to separate them using the same method. This becomes especially challenging for $\eta||\mathbf{y}$, where the amplitude of phonons with frequency higher than 80 cm^{-1} is comparable to the lower modes (Fig. 5.6) throughout the investigated spectral region. In this case, a more advanced procedure involving a time-weighted average over multiple 0 or π phase profiles to determine the initial amplitudes of the atomic shifts could be employed.

Such features are also well captured by *ab initio* results obtained with properly rescaled eigendisplacements.

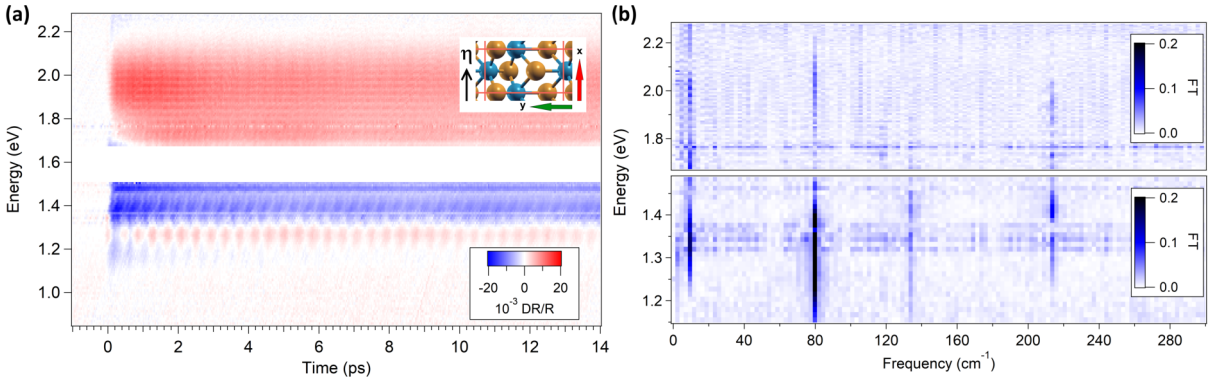

Figure 5.13. (a) Ultrafast broadband DR/R image for WTe_2 for probe polarization $\eta||\mathbf{x}$ taken at ∼710 μJ/cm^2 absorbed pump fluence and T=80 K. (b) Fourier transform images performed across a few picoseconds after time zero after subtracting from the data a purely exponential fit based on Eq. (5.2) for various probe photon energies.

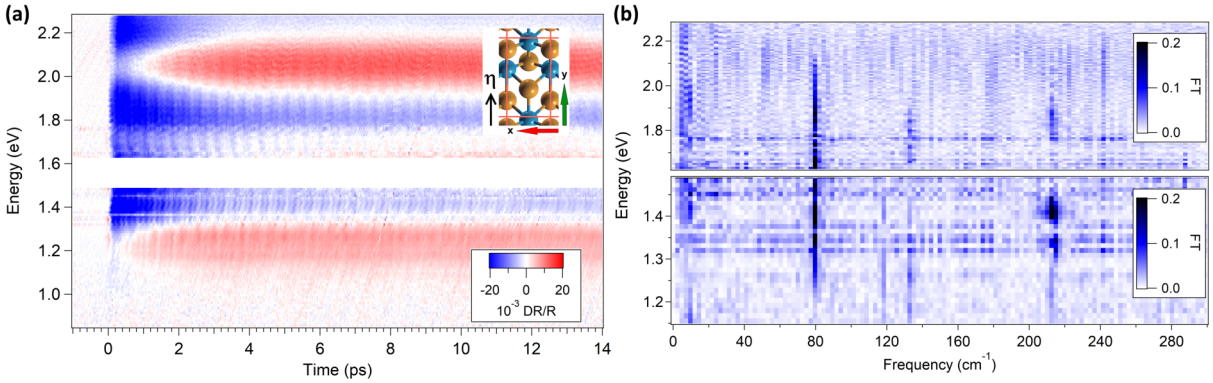

Figure 5.14. (a) Ultrafast broadband DR/R image for WTe_2 for probe polarization $\eta||\mathbf{y}$ taken at ∼710 μJ/cm^2 absorbed pump fluence and T=80 K. (b) Fourier transform images performed across a few picoseconds after time zero after subtracting from the data a purely exponential fit based on Eq. (5.2) for various probe photon energies.

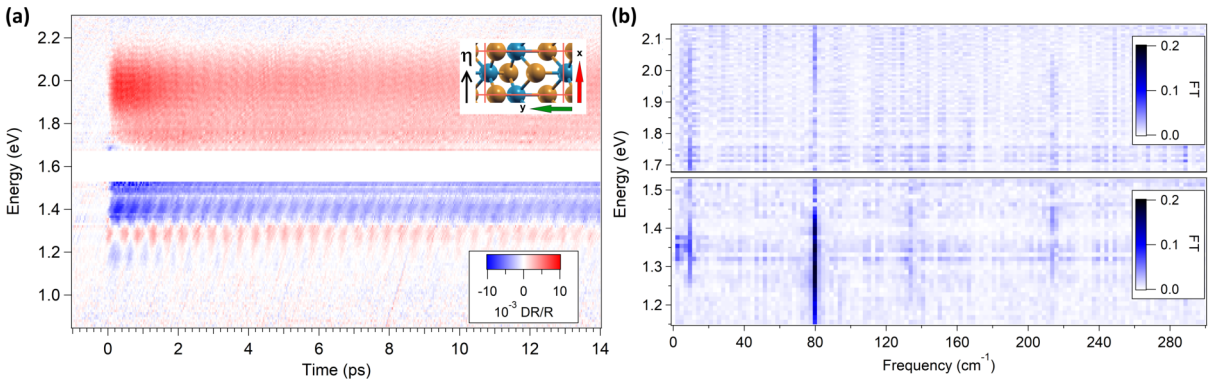

Figure 5.15. (a) Ultrafast broadband DR/R image for WTe_2 for probe polarization $\eta||\mathbf{x}$ taken at ∼230 μJ/cm^2 absorbed pump fluence and T=80 K. (b) Fourier transform images performed across a few picoseconds after time zero after subtracting from the data a purely exponential fit based on Eq. (5.2) for various probe photon energies.

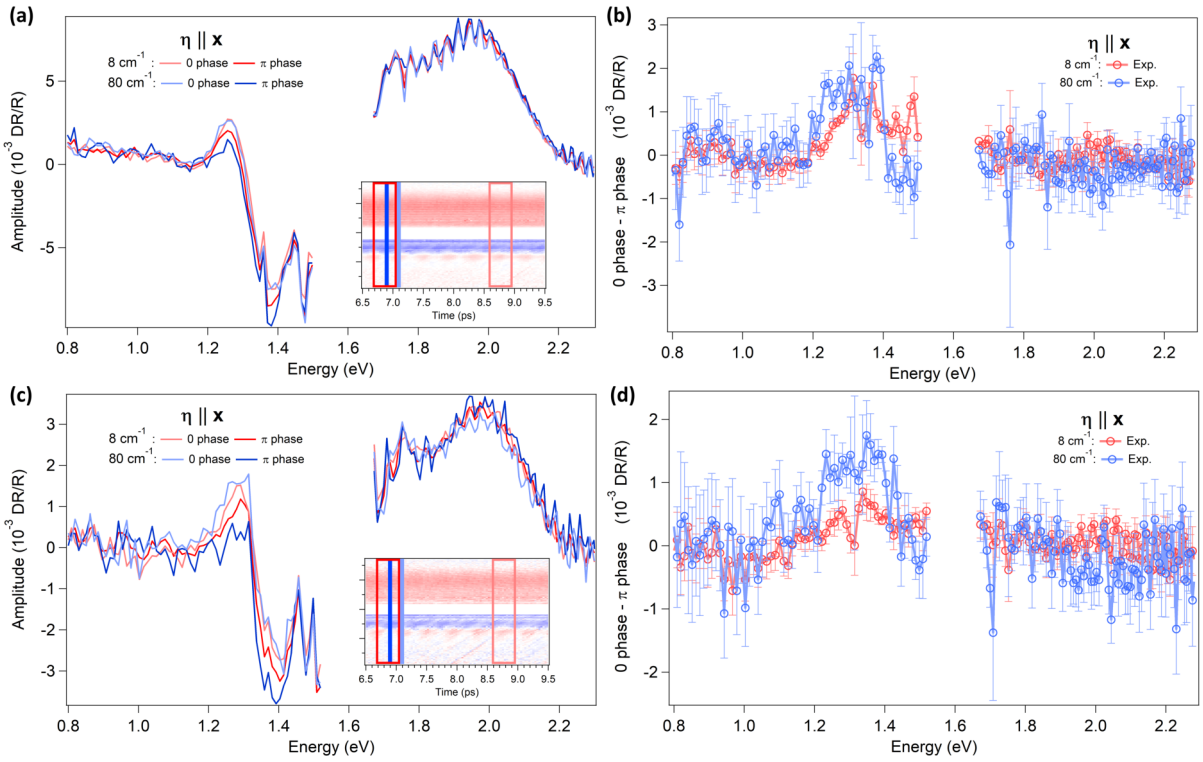

Figure 5.16. Spectral profiles taken at selected time delays for maxima and minima of the 8 cm^{-1} and 80 cm^{-1} optical phonon effects taken at a) ∼710 $\mu J/cm^2$, c) ∼230 $\mu J/cm^2$ absorbed pump fluence and T=80 K; the inset, with the same vertical axis and color scale as the corresponding graphs in Figs. 5.13, 5.15, shows the exact temporal positions. (b),(d) Experimental DR/R difference between the 0 and π phases displayed in respectively (a) and (c), showcasing the effects of the 8 cm^{-1} and 80 cm^{-1} optical phonons for $\eta||\mathbf{x}$.

We considered the difference between the DFT-based (IP approximation) calculated DR/R curves at 0 and π, multiplied by an exponential factor derived from the experimental data, to account for the damping of the optical modulation.

The DFT predictions closely match the experimental results for both the 8 cm^{-1} and 80 cm^{-1} modes by rescaling the atomic displacements, whose relative amplitude is given by DFPT, with a global multiplicative factor, common to both polarizations (Fig. 5.11). The agreement is particularly good for $\eta||\mathbf{x}$ where the phonon effects are most prominent. Peculiar features, such as their trend and change of sign, are maintained throughout the relaxation process as previously illustrated in Fig. 5.8(c),(d).

From this comparison we can quantify the magnitude of the ionic displacements right after the perturbation, when the atoms of different unit cells move uniformly in the probed region. The estimated displacements have to be regarded as average displacements over the probed volume and photon energies. The penetration depth, derived from the optical data in [68] (Appendix A), is almost constant and similar for the two perpendicular polarizations in the probed spectral region, with minor deviations towards the infrared for $\mathbf{y}$ direction.

In order to evaluate very small atomic displacements, we focus on the experiments at lower fluence (∼230 $\mu J/cm^2$), where we showed that the phonon effects can be considered linear with the deposited energy (Fig. 5.18). This is not the case for ∼710 $\mu J/cm^2$, since the phonon effects measured at that fluence are only twice those at ∼230 $\mu J/cm^2$.

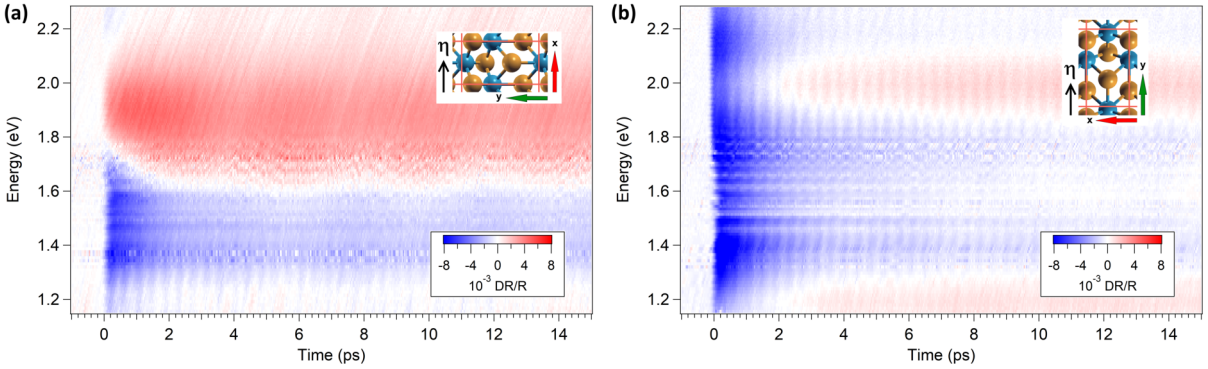

Figure 5.17. (a),(b) Data obtained using 1.0 eV pump photon energy, taken at ∼490 μJ/cm^2 absorbed pump fluence and T=295 K respectively for $\eta||\mathbf{x}$ and $\eta||\mathbf{y}$.

At ∼230 μJ/cm^2, the comparison between experimental and computational results (Fig. 5.12(d)) gives for the 8 cm^{-1} mode initial positions shifts of ∼350 fm along the **y** direction. For the 80 cm^{-1} mode, the displacements are quite distinct for the twelve atoms in the basis cell. The four tungsten atoms remain almost fixed (displacements smaller than 10 fm) along the **y** direction whereas they shift by ∼40 fm along the interlayer **z** direction. Four tellurium atoms are displaced by ∼90 fm along the **y** direction and by ∼25 fm along **z**. The remaining four tellurium atoms are displaced by ∼15 fm along the **y** direction and by ∼30 fm along **z**. None of these modes involves movements along the **x** crystallographic direction. The phononic shift can also be expressed in terms of the normal mode amplitude $Q(t)$ in units of $\sqrt{\mu}$Å, where μ is the atomic mass unit [251]. Their relation is given by $\boldsymbol{d}_n = \boldsymbol{e}_n Q(t)/\sqrt{M_n}$, with $\boldsymbol{d}_n$ is the displacement vector for atom n, $\boldsymbol{e}_n$ eigenvector for atom n and M_n is the ionic mass for atom n [252]. In the case of the 8 cm^{-1} mode, the initial amplitude is 0.15 $\sqrt{\mu}$Å, while for the 80 cm^{-1} mode it is 0.025 $\sqrt{\mu}$Å.

5.5.4 Changing pump photon energy

1.0 eV pump

In order to check that the reflectivity variation DR/R is independent from the pump photon energy, we repeated part of the measurements by pumping at 1.0 eV photon energy (Fig. 5.17), obtained thanks to an optical parametric amplifier (OPA). We verified that the DR/R is qualitatively similar to the results obtained with the 1.55 eV (800 nm) excitation. Moreover, since in this experimental condition the pump lies at the edge of the measured spectral range, the spectral region around 1.55 eV is not covered by scattered pump photons. This allowed us to confirm that no structured features are present in this range, that was hidden in the datasets acquired with 1.55 eV pump photon energy (Figs. 5.3(c),(d)).

To systematically investigate the response of the material as a function of the fluence, we performed a series of pump-probe reflectivity experiments at 1.0 eV pump and 1.55 eV probe photon energies. The results are summarized in Fig. 5.18. From Figs. 5.18(c),(f), it can be inferred that the amplitude of the main peak and of the phonon effects can be considered a linear function of the absorbed pump fluence in the whole investigated range within a very good approximation. Compared to the time-resolved broadband optical experiments, the 80 cm^{-1} oscillations are quenched because of the following effect. The probe pulse (1.55 eV, 800 nm) produced by the amplifier has a wide bandwidth (>40 nm)

with a finite residual chirp. This chirp cannot be resolved when the full bandwidth of the pulse is measured with a single photodiode, as it happens with lock-in acquisition, leading to a smearing of the fast oscillatory signal. We also want to stress the fact that only the DR/R as measured by broadband spectroscopy can be considered as quantitative. The DR/R magnitude measured through lock-in acquisition is smaller by a given factor, arising from the signal treatment introduced by the lock-in device.

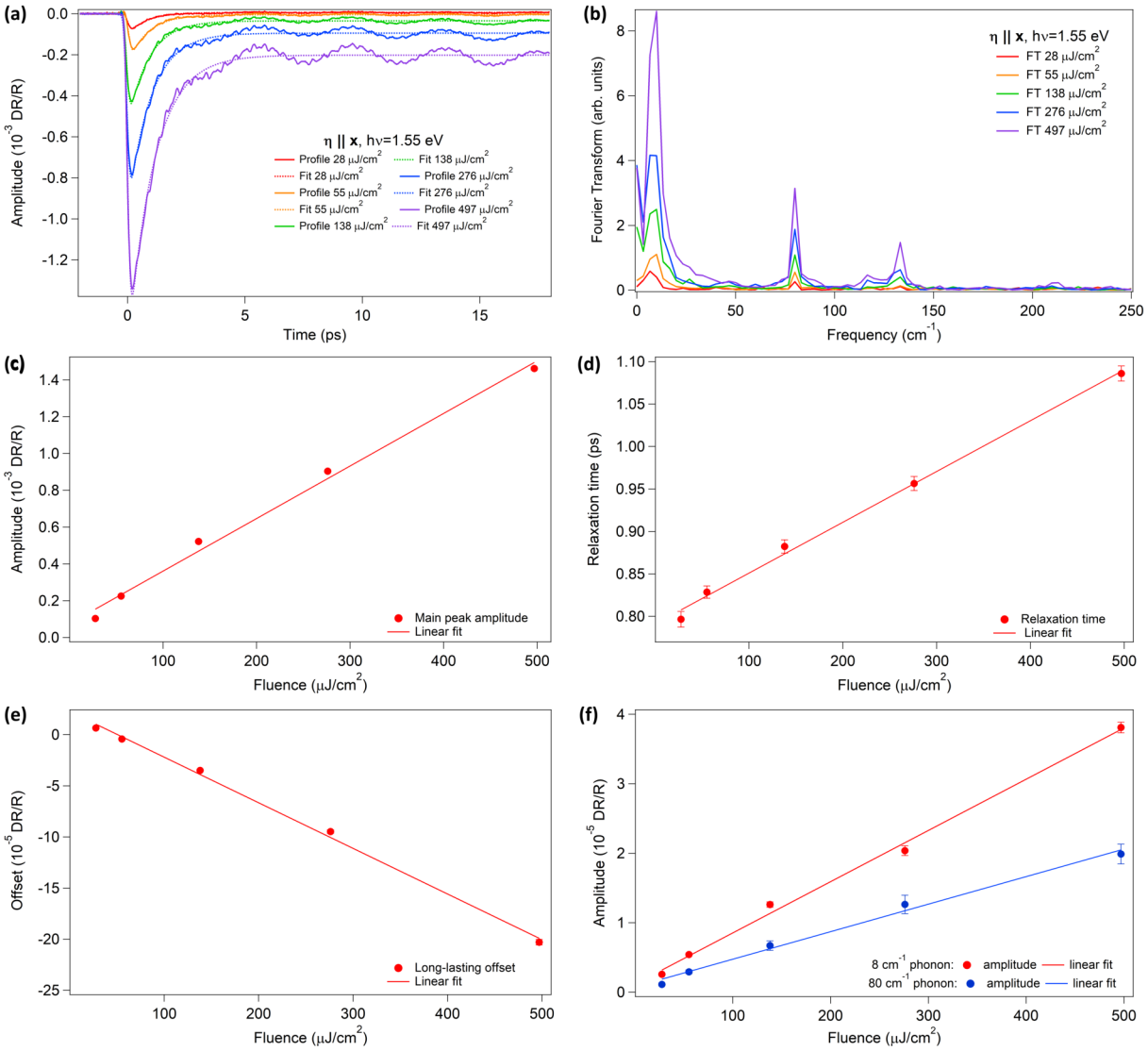

Figure 5.18. (a) Absorbed fluence dependence on the out-of-equilibrium profiles performed with 1.0 eV pump and 1.55 eV single-color probe with $\eta||\mathbf{x}$, at T=295 K, where a single-exponential decay model was used to fit the curves; see Eq. (5.2) for details. (b) Fast Fourier transform (FFT) transform of the residual signals after subtracting to the profiles the fit function. Fit parameters of the single-exponential decay model obtained from the curves reported in panel (a) respectively for (c) amplitude and (d) relaxation time of the main peak, (e) offset and (f) amplitudes of the phonon effects related to the 8 cm^{-1} and 80 cm^{-1} modes. These last values represent the amplitude of two damped cosine waves fitted to the residual signals.

Furthermore, it is possible to determine the timescale of the long-lasting offset observed in the time-resolved profiles. As shown in Fig. 5.19, the signal survives for hundreds of picoseconds. Its timescale reminds of similar long-lasting non-equilibrium signals observed

in time-resolved x-ray diffraction and time-resolved electron diffraction for transition metals, ascribed to the transient lattice heating [151].

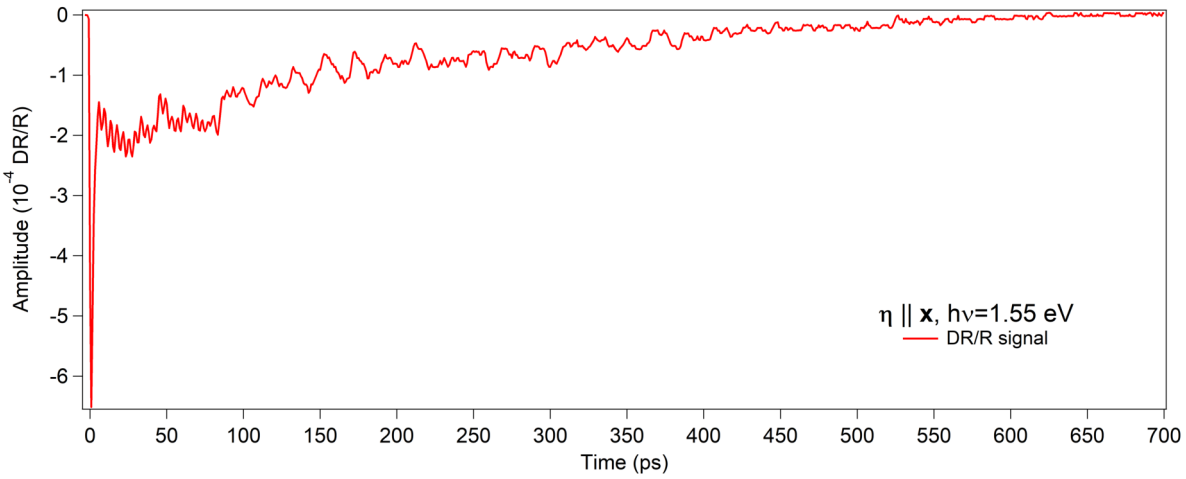

Figure 5.19. Single-color DR/R curve obtained at 1.0 eV pump photon energy and a perpendicularly polarized 1.55 eV probe beam polarized along $\eta||\mathbf{x}$ at ∼500 μJ/cm^2 absorbed pump fluence and T=295 K, showing that the material returns to equilibrium in about 700 ps.

Due to its timescale, this effect is likely to be associated with local lattice heating, as described in [151] for transition metals. For our purposes, we can consider the offset as a constant over the temporal range explored in Figs. 5.3(c),(d).

3.1 eV pump

The broadband experiment was also repeated with a 3.1 eV pump (Fig. 5.20), obtained using a BBO crystal to produce the second harmonic of the 1.55 eV original pump. We verified that the DR/R is qualitatively similar to the results obtained with the 1.55 eV (800 nm) excitation. In this experimental condition, the pump lies completely outside the probed specral range and thus not only the spectral region around 1.55 eV is not covered by scattered pump photons, but it can be also extended towards the infrared, whereas in Fig. 5.17 is limited by the 1.0 eV pump.

Comparison

The DR/R broadband images share very similar spectral features independently from the pump photon energies used (1.0 eV, 1.55 eV and 3.1 eV). This suggests that the interband optical transitions that mainly determine the dielectric function at the wavelengths studied through the white probe do not have a final state with energy higher than 1.0 eV from the Fermi level, as its occupation would be perturbed differently depending on its photon energy. At room temperature, this condition should be less strict than in a frozen picture due to phonon-assisted transitions. Nonetheless, the final state and its k-space neighborhood should be affected. WTe_2 is a semimetal with various bands around the Fermi level in a-few-eV range (Fig. 6.19(d)), thus there exist, in principle, many quasi-vertical transitions that could satisfy such energy condition for the final state. However, from Fig. 6.19(d), we see that aside from the electron and hole pockets region, elsewhere, initial and final states are separated more than 0.6 eV. Thus a pump photon energy below

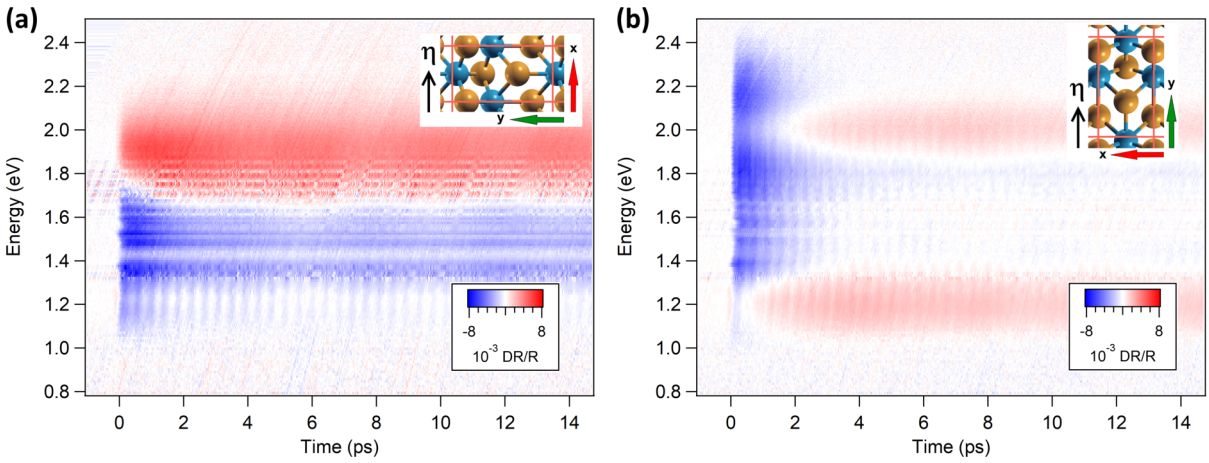

Figure 5.20. (a),(b) Data obtained at a 3.1 eV pump photon energy, taken at ∼0.29 μJ/cm^2 absorbed pump fluence and T=295 K respectively for $\eta||\mathbf{x}$ and $\eta||\mathbf{y}$.

such threshold would further reduce the number of perturbed final states, which should help in the identification of the transitions. From the theoretical point of view, an analysis of the k-dependent joint density of states together with the occupation function would support the assignment.

5.5.5 Coherent optical phonon effects on the energy levels

The subpicometer atomic displacements in the out-of-equilibrium structural configurations lead to modifications of the electronic band structure (Fig. 5.21) of the order of a few meV.

Although such variations are small, they are above our relative numerical accuracy. Furthermore, we checked that these effects are almost linear with the displacements if we increase them by a factor up to twenty. We focus on the extrema of the electron and hole bands along Γ-X. In Fig. 5.22, we show the results corresponding to the displacements estimated from the low (∼230 μJ/cm^2) fluence measurements. The effects (doubled in the graph for clarity) depend on the band and phonon mode. For the 8 cm^{-1} mode, the bottom (top) of the electron (hole) band at -80 meV (60 meV) under (above) the Fermi energy experiences a ∼0.7 (1.5) meV difference between the two oscillation phases (0 and π, represented in Fig. 5.23), while for the 80 cm^{-1} modes the difference becomes ∼1.7 (0) meV. By properly tuning the Fermi level, these variations, although small, could have an impact on the extremely high magnetoresistance in WTe_2 [65], which is ascribed to a delicate balance between electron and hole carriers. Additional contributions may come from carrier mobility and the magnetic field [253] [254]. We caution the reader that we used scalar relativistic pseudopotentials. The inclusion of spin-orbit coupling (SOC) using fully relativistic pseudopotentials would provide a more accurate description of these effects, since it is known that SOC plays an important role on the electronic bands around the Fermi level in WTe_2 [6]. This description will be developed and reported in the computational analysis for the time-resolved x-ray experiment on the same material (Chapter 6).

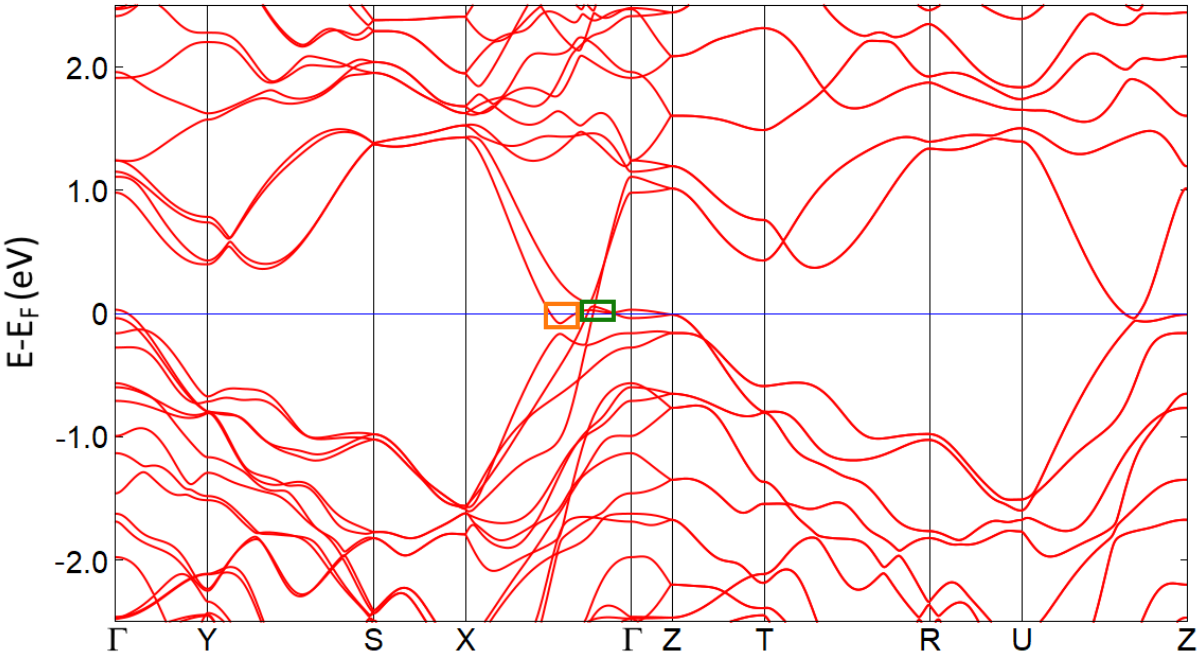

Figure 5.21. Electronic band structure of WTe_2 in the equilibrium configuration; the orange and green rectangles highlight respectively the electron and hole pockets; the energy values are referred to the Fermi energy (E_F).

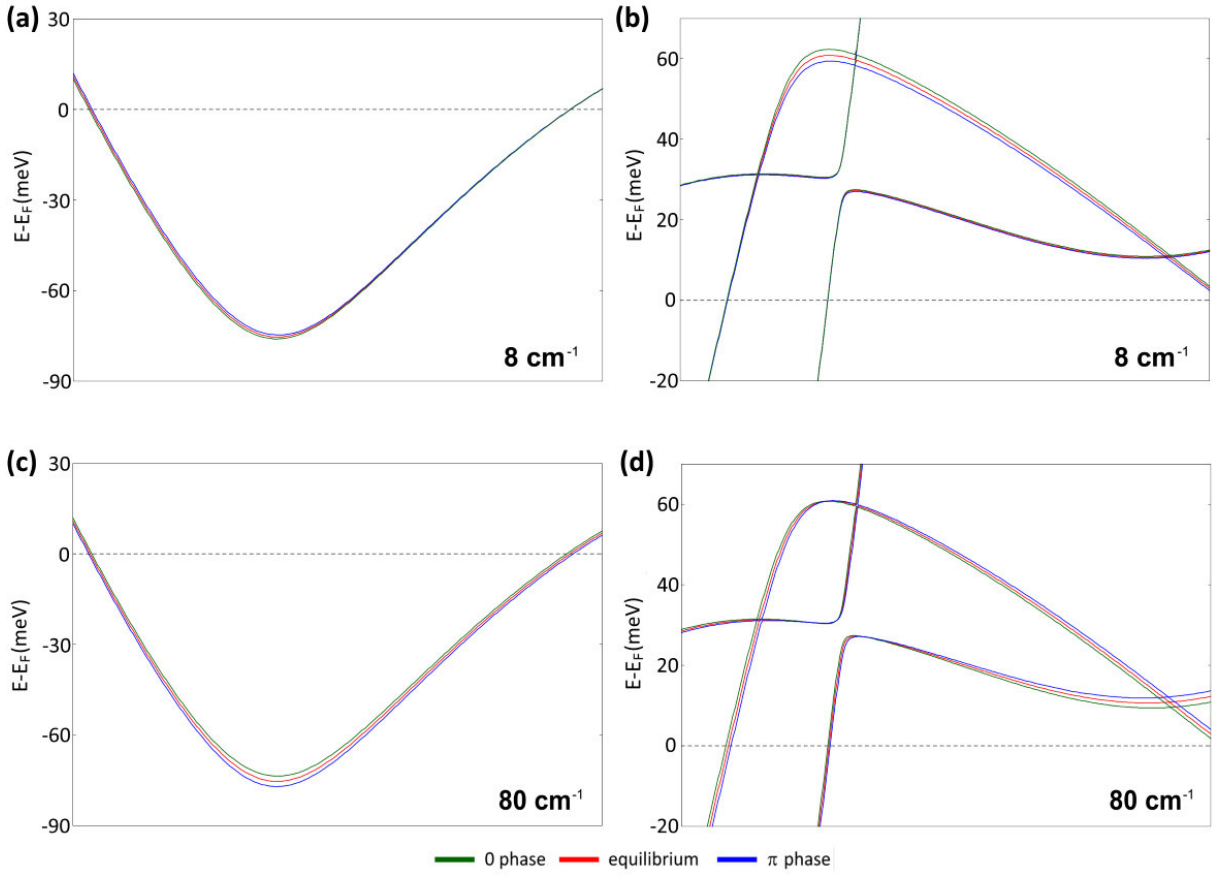

Figure 5.22. Effect of the phonon displacements on electron- and hole-like bands cut by the Fermi level along Γ-X. (a),(b) Magnified views of the regions delimited by the orange and green rectangles in Fig. 5.21 for the 8 cm^{-1} optical phonon mode; (c),(d) as (a),(b), but for the 80 cm^{-1} phonon mode; the 0 and π phases are labeled taking as a reference the $\eta||\mathbf{x}$ polarization; the displacements used for the graphs are doubled with respect to the low fluence values to highlight the phonon effects.

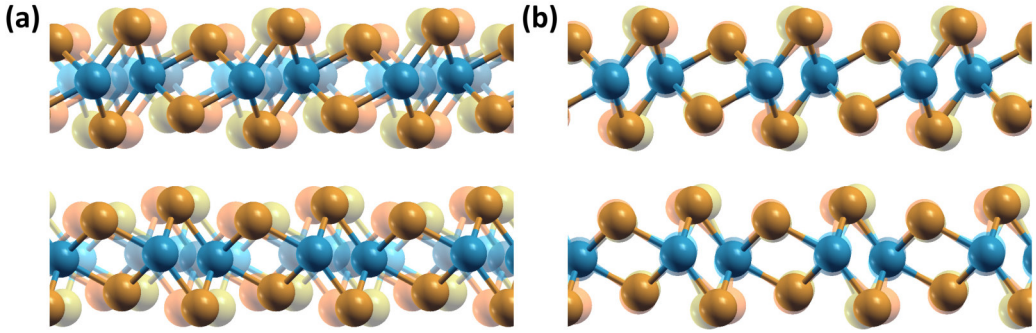

Figure 5.23. The 0 and π phases of the phonon oscillations for the (a) 8 cm^{-1} mode and (b) 80 cm^{-1} mode. The 0 phase is represented by transparent yellow Te atoms and light blue W atoms, while the π phase is reported with transparent orange Te atoms and dark blue W atoms. Opaque colors describe the atoms in their equilibrium positions. The displacements are exaggerated for a better visualization.

5.5.6 Bands contribution to the response function

To accurately describe the effects induced by the optical phonons, it is necessary to include in the response function an appropriate number of bands around the Fermi level. The "converged" curves shown in Fig. 5.24 were obtained including 119 bands, which is safe enough compared with the 184 electrons per unit cell and the spectral range under consideration for the transitions. In the same figure, we show the effect of varying the number of "conduction bands", *i.e.* the totally unoccupied bands above the Fermi level. We notice that the main features of the DR/R profile are quickly captured even using fewer conduction bands, while to correctly compare the DFT amplitudes with the experimental data and give a reasonable estimate of the ionic displacements, more than 15 conduction bands have to be included.

However, since the major features are still retained by including only the first conduction band in the response function, we deduce that transitions having final states that belong to bands crossing the Fermi level are involved. This supports the claim that for this material the phonon effects cannot be attributed to single transition in k-space, but to multiple contributions.

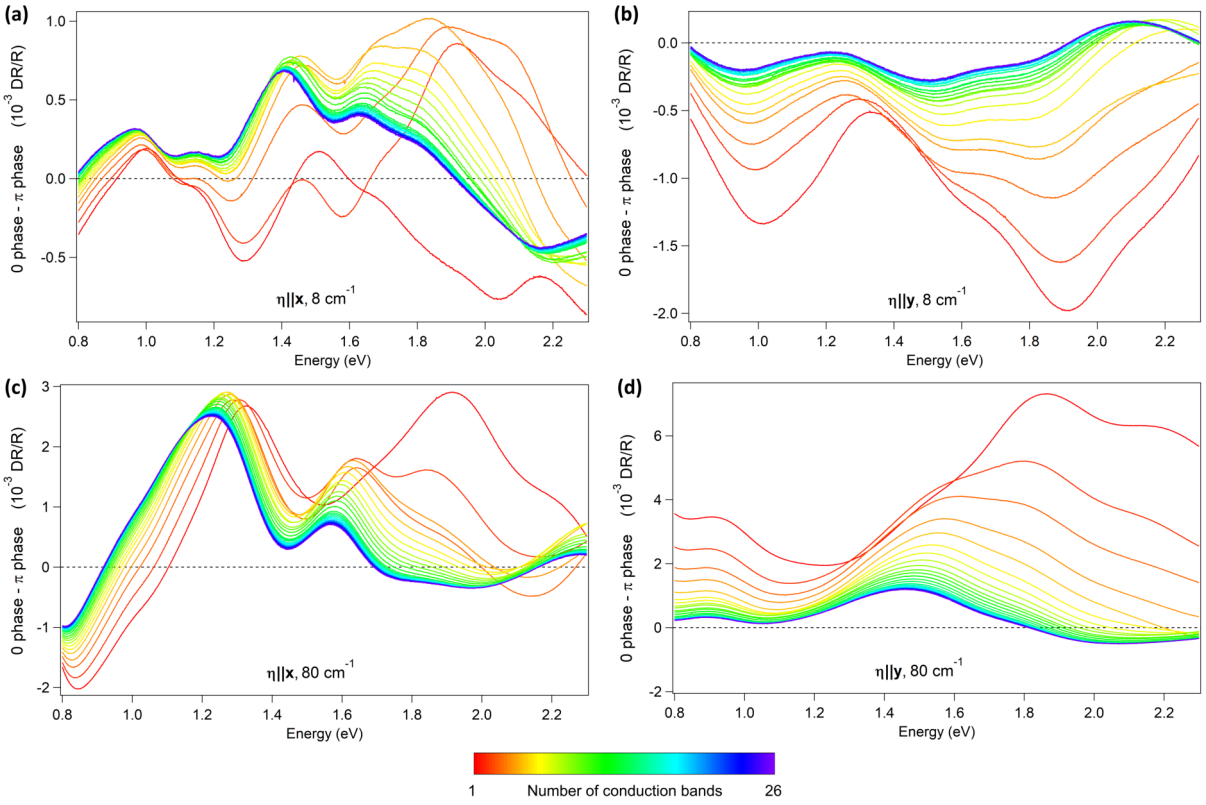

Figure 5.24. Phonon effects on the DR/R profiles obtained from the differences between the 0 and π phases with an increasing number of conduction bands inserted in the response function; (a) 8 cm^{-1} $\eta||\mathbf{x}$; (b) 8 cm^{-1} $\eta||\mathbf{y}$; (c) 80 cm^{-1} $\eta||\mathbf{x}$; (d) 80 cm^{-1} $\eta||\mathbf{y}$.

5.5.7 Linearity of the DR/R effects on the shifts

Similarly to the modification of the energy levels shown in Fig. 5.22, also the DFT-based (IP approximation) calculated DR/R effects are linear with the chosen displacement. This is depicted in Figs. 5.25, 5.26, where the profiles are compared with an increasing shift

of the atomic coordinates along the corresponding atomic displacements. Here they are reported as the DR/R between the 0 phase and the equilibrium, which is basically equal to half of the overall effect in our operating conditions. As a reference, we label the values used to obtain the theoretical curves in Fig. 5.12(d) as 'x1'.

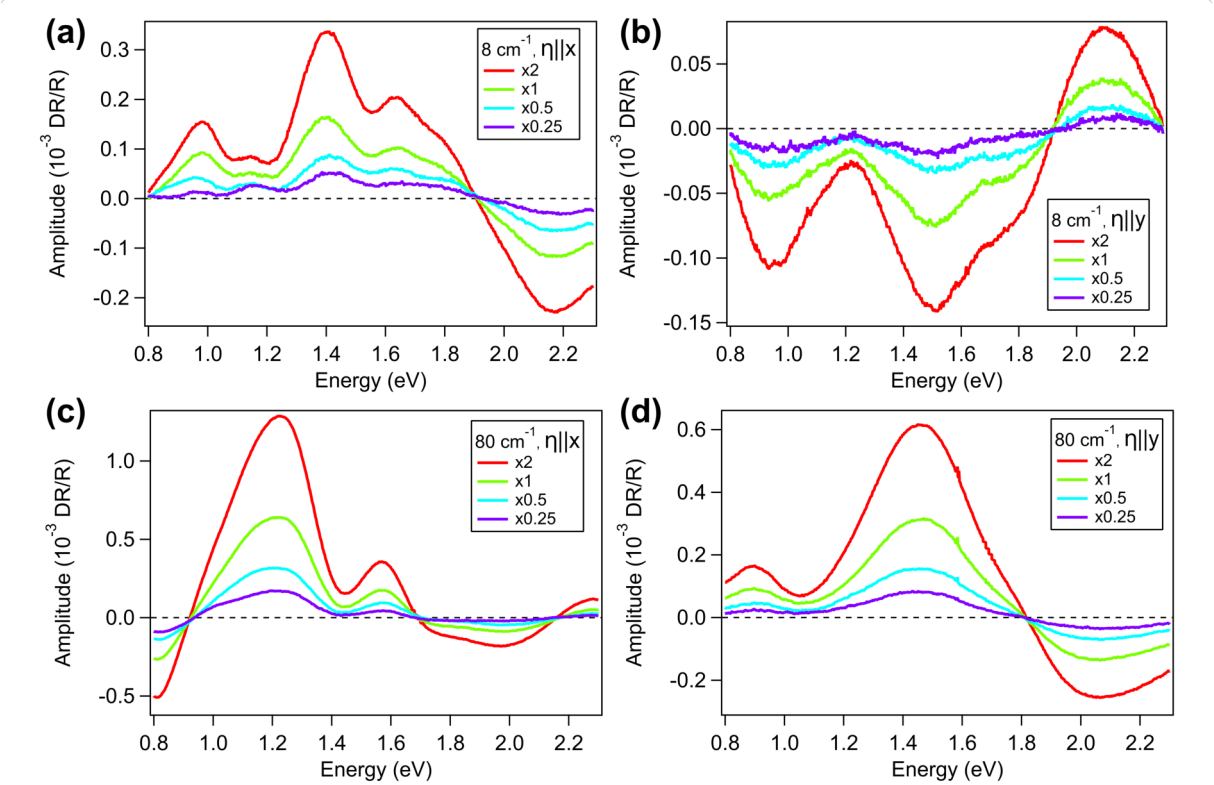

Figure 5.25. Phonon effects on the DR/R profiles obtained from the differences between the 0 ad the equilibrium phases with an increasing shift along the corresponding eigendisplacements; (a) 8 cm^{-1} $\eta||\mathbf{x}$; (b) 8 cm^{-1} $\eta||\mathbf{y}$; (c) 80 cm^{-1} $\eta||\mathbf{x}$; (d) 80 cm^{-1} $\eta||\mathbf{y}$. The 'x1' corresponds to the undamped values used for the DFT curve in Fig. 5.12(d).

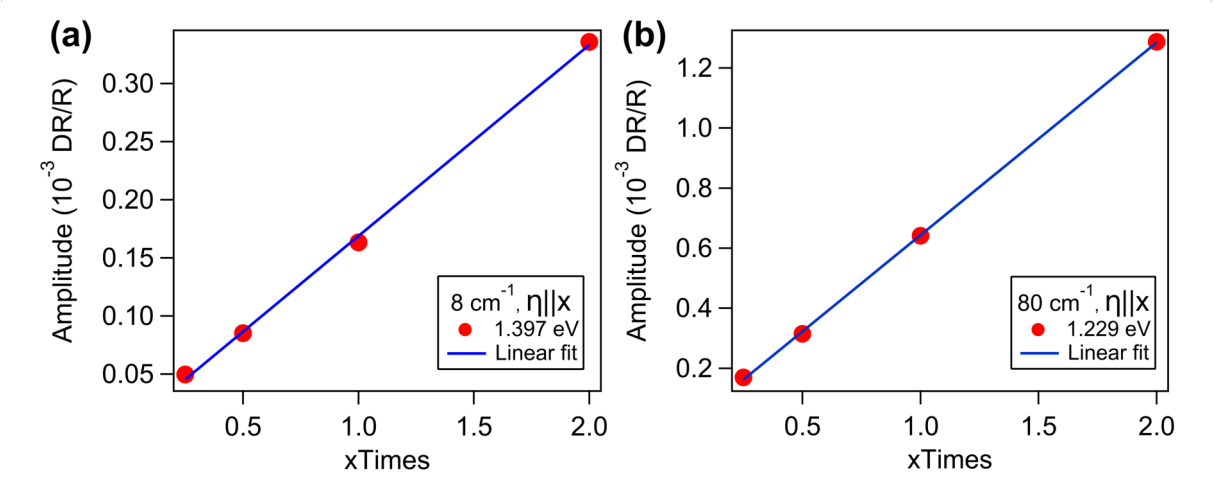

Figure 5.26. Dependence of the phonon effects on the DR/R profile obtained from (a) Fig. 5.25(a); (b) Fig. 5.25(c).

5.6 Conclusions

The main achievement of the work is the evaluation of the atomic displacements with a precision of a few femtometers without free tuning parameters, except a scaling factor determined by an overall comparison between experimental data and numerical simulations of the broadband DR/R signal. Concerning WTe_2, a good agreement between the measured and calculated phonon effects on the optical properties for both in-plane crystal axes has been obtained. This finding confirms that the macroscopic lattice distortions excited in WTe_2 at 8 cm^{-1} and 80 cm^{-1} can be entirely mimicked by the coherent population of selected zone-center A_1 lattice modes. We stress that the possibility to measure the optical properties on a wide spectral range is fundamental to obtain reliable quantitative results about the magnitude of eigendisplacements of multiple and intertwined phonon modes. Finally, we mention that the method described here is not system-specific and in principle can be extended to any crystalline material, provided that its high-energy optical properties are affected by the coherent motion of atoms. In perspective, our findings can pave the way to the design of tailored devices in which the coherent lattice motion (at selected frequencies and up to large displacements) is exploited to finely tune the functional properties of semiconducting and metallic systems.

CHAPTER 6

Time-resolved x-ray diffraction on WTe_2

6.1 Introduction

In periodic crystals, monitoring the collective vibrational modes is an important method to characterize a system at equilibrium [153][234][235][236]. Their frequency, amplitude and linewidth are sensitive to temperature, pressure and dimensionality of the investigated samples and their variations can be exploited as fingerprints of an undergoing change in the material [63][250][255]. Using ultrashort laser pulses, it is possible to coherently excite zone-center optical phonons such that macroscopic regions of the material are subjected to an in-phase collective ionic motion. In nonequilibrium observables, *e.g.* optical properties and diffraction, they appear as short-lived oscillations which are damped in a few picoseconds, due to phase decoherence and decay into acoustic modes [231][232][233]. For this reason, the experimental studies often use them as a mean to learn about the excited state of the system, although rarely focusing on their direct impact on the properties of the excited state of the crystal.

In layered transition metal dichalcogenides (TMDCs), coherent optical modes like the shear modes, *i.e.* antiphase uniform movement of consecutive layers, have been shown to last for several tens of picoseconds (Chapter 5 and [105]), encompassing multiple oscillation periods with similar amplitude. Moreover, in tungsten ditelluride (WTe_2), the out-of-equilibrium structural evolution along the shear coordinate was reported to provide a pathway to modify the topological properties of the system varying the number and type of Weyl points as its electronic, optical and topological properties are influenced by strain forces [6][35][36][243].

In WTe_2, the coherent optical phonon modes perturb the electronic structure periodically in time (Chapter 5 and [256]). The associated modifications of the band structure impact a particularly interesting region of the Brillouin zone where the electron and hole pockets of the semimetal are located. These are central in the proposed explanation for

the extremely high magnetoresistance in WTe_2 [65] and host the predicted type-II Weyl points [6].

Structural dynamics techniques allow to reconstruct the ionic motion triggered by a pump excitation by monitoring the intensity and scattering geometry of a suitable probe, such as x-ray, electron or neutron diffraction. Coherent phonons are detected as periodic wiggling of the diffracted intensity [237], which can be used to obtain information regarding frequency, eigenvectors and displacement amplitude of the modes. Hard x-ray free electron laser (FEL) provide high-brilliance, coherence and short pulses, which can be employed to resolve the ionic motion right after the perturbation [257].

In this chapter, we explore the lattice dynamics of WTe_2, perturbed using a near-infrared pump pulse to gain insight on its optical phonons and cell dynamics using time-resolved x-ray diffraction (Fig. 6.1). We support our findings with additional time-resolved optical measurements, a displacive model and density functional theory (DFT) calculations. Under our experimental conditions, the maximum phononic displacements reach values of $\sim$3 picometers that directly affect the semimetallic pockets, leading to a periodic change of the energy levels as well as their associated effective mass. In particular, this last property is a key ingredient in the magnetotrasport properties of the materials and in the theoretical models for the extremely high magnetoresistance in WTe_2 [65] through the electron and hole mobilities.

Moreover, the observed amplitudes of the coherent phonon effects show an opposite dependence among the modes with the pump fluence. Finally, we observe a long-lasting behavior which we attribute to a reorganization of the atomic positions, a change in the Debye-Waller factors connected to an increase of the thermal motion and a cell expansion due to the deposited energy. Overall, these modifications arecompatible with the proposed out-of-equilibrium 1T'(*) centrosymmetric intermediate structure, first proposed in [35].

6.2 Sample

Tungsten ditelluride is a TMDC with in-plane covalent bonding and weaker van der Waals interplanar interactions helping to hold together the individual layers (Figs. 6.1(b),(c)). At equilibrium, its structure is described by the orthorhombic space group $Pmn2_1$ (Td) [61], aside from high temperature [62] and high pressure conditions [63], where the material exhibits its monoclinic phase 1T', with space group $P2_1/m$. In this experiment, WTe_2, grown by HQ Graphene [258], was a $\sim$3.5x3 mm^2, few-hundreds µm thick, freshly-cleaved sample measured in air environment. Bulk WTe_2 is stable in such conditions, although flakes may present a thin oxidation layer at the surface, much smaller than the penetration depth of the beams in our experiment [68][76][259] (see also Appendix A). The sample crystallographic axes were pre-oriented using Fourier transform infrared (FTIR) spectroscopy (see Appendix B) and verified in-situ by comparing the necessary angular settings to observe specific Bragg peaks with the expected ones through [260].

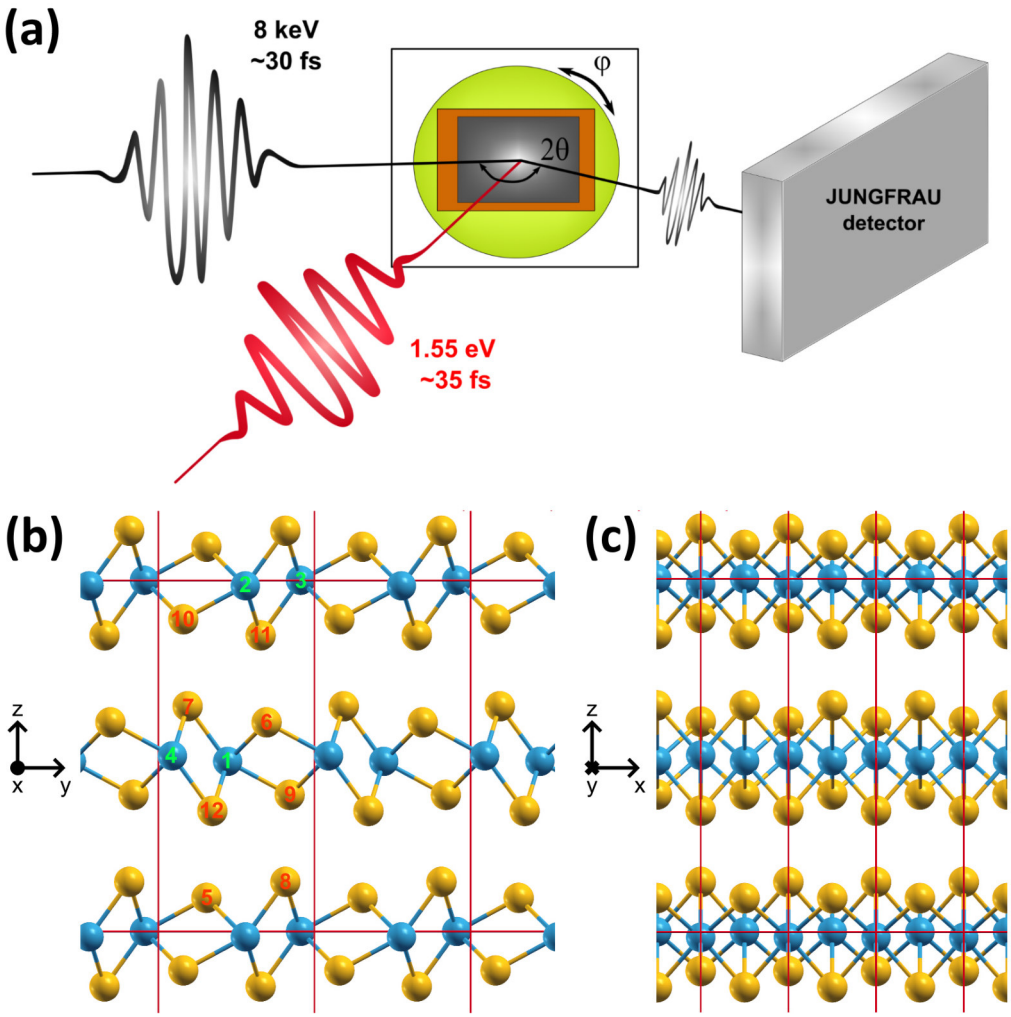

Figure 6.1. (a) Scheme of the time-resolved x-ray diffraction experiment. The optical pump (1.55 eV) arrives at the sample with a 10 degree angle with respect to the surface while the x-ray beam arrives at grazing incidence. The Bragg conditions are obtained by rotating the sample along φ and a JUNGFRAU areal detector is used to collect the diffracted photons. (b), (c) Projections of the WTe_2 crystal structure on the yz and xz planes, with blue tungsten and orange tellurium atoms showing multiple unit cells delimited by red lines. The numbering in (b) is used later in the chapter.

6.3 Experimental details

6.3.1 Time-resolved x-ray diffraction

The time-resolved x-ray diffraction experiment was performed at the Bernina beamline at SwissFEL, Paul Scherrer Institute, in Villigen (Switzerland)[257]. The x-ray beam was generated by the FEL with a 50 Hz repetition rate and pulse duration shorter than 30 fs (rms). It was then monochromatized at 8 keV through a Si (111) crystal and arrived at the sample at grazing incidence with a ~5x50 μm^2 normal section.

To excite the system, a near-infrared (800 nm) pump laser beam was employed, presenting a temporal pulse width shorter than 35 fs (FWHM) and 100 Hz repetition rate. It arrived at the sample at ~10 degrees incidence with respect to the sample surface with a ~200x200 μm^2 normal section. The jitter between the near-infrared and x-ray beams was

corrected through the beamline 'timing tool'. The diffracted x-ray beams were collected by a 1.5 Megapixels JUNGFRAU detector, set 760 mm far from the sample. The diffracted intensities were then obtained by integrating the values registered by each pixel over a region of interest (ROI). The experiment was performed at room temperature and normal pressure conditions without a vacuum chamber. Rocking-curve scans were acquired by modifying the azimuthal angle φ around the value at which the maximum of the peak intensity occurred.

6.3.2 Geometrical predictions

The coherent x-ray diffraction intensity is directly related to the distribution of the atoms in the unit cell [157].

The angular conditions fulfilling the diffraction conditions to observe a certain Bragg reflection (hkl), with h, k, l Miller indices, depend on the geometry of the crystal's unit cell as well as on the degrees of freedom of the manipulator and detector [260]. In this thesis, they were obtained through scripts written in the C-like language of Igor Pro (Wavemetrics Inc.) as well as in MATLAB (Mathworks ®).

The output consists of tables with the angular conditions for the different peaks as a function of the wavelength and crystal geometry [157]. Using the general triclinic formula [261], which can be written in the matrix form, the inverse of the square of the interplanar distance is obtained as

$$\frac{1}{d_{hkl}^2} = \frac{\left(h/a \begin{vmatrix} h/a & cos\gamma & cos\beta \\ k/b & 1 & cos\alpha \\ l/c & cos\alpha & 1 \end{vmatrix} + k/b \begin{vmatrix} 1 & h/a & cos\beta \\ cos\gamma & k/b & cos\alpha \\ cos\beta & l/c & 1 \end{vmatrix} + l/c \begin{vmatrix} 1 & cos\gamma & h/a \\ cos\gamma & 1 & k/b \\ cos\beta & cos\alpha & l/c \end{vmatrix} \right)}{\begin{vmatrix} 1 & cos\gamma & cos\beta \\ cos\gamma & 1 & cos\alpha \\ cos\beta & cos\alpha & 1 \end{vmatrix}} \tag{6.1}$$

with a, b and c lattice and α, β and γ angular constants of the unit cell. From it, one can calculate the modulus square of the reciprocal lattice vector $\boldsymbol{G}_{hkl}$ as $|\boldsymbol{G}_{hkl}|^2 = 4\pi^2/d_{hkl}^2$. This value is necessary to derive the atomic form factor $f_X(q)$ of an atomic species X at the vector modulus $q = |\boldsymbol{G}_{hkl}|$ [262]

$$f_X(q) = \sum_{i=1}^{4} a_{Xi} exp\left[-b_{Xi}\left(q/4\pi\right)^2\right] + c_X \tag{6.2}$$

where a_{Xi}, b_{Xi} and c_X are tabulated coefficients derived from comparisons with the atomic scattering curve. This expansion is usually effective unless a value $q > 4\text{Å}^{-1}$ is needed or an absorption edge is present in close proximity of the chosen x-ray wavelength [262][263]. The atomic form factors can be obtained from data found in [262][263], also including the first-order anomalous scattering corrections due to x-ray photon energy dependence [157]. The diffracted intensity is then proportional to the absolute square of the structure factor $S(G_{hkl}, \lambda)$, calculated as

$$S(G_{hkl}, \lambda) = \sum_j f_j(G_{hkl}, \lambda) e^{2\pi i(hu_{xj} + ku_{yj} + hu_{zj})} \tag{6.3}$$

where G_{hkl} is the modulus of the reciprocal lattice vector, λ is the x-ray wavelength, $f_j(G_{hkl}, \lambda)$ is the atomic form factor and u_{xj}, u_{yj}, u_{zj} are the coordinates in the unit cell for the j-th atom of the base normalized by the corresponding lattice parameter.

Using this data, we predicted which Bragg peaks were affected more by the optical phonon modes, with particular regard for the lower energy modes (∼0.25 THz and ∼2.5 THz) which are the most prominent at ambient as well as at lower temperatures, as shown in Chapter 5 (there indicated as ∼8 cm^{-1} and ∼80 cm^{-1} respectively). The ratio between the 0.25 THz and 2.5 THz modes as well as their predicted peak-to-peak amplitudes were obtained based on the optical quantification found in Chapter 5. Thanks to the order of magnitude difference between their periods, their dynamics can be clearly distinguished in the time-resolved traces and can thus be used as an indication of the adequacy of the model *a posteriori*.

Fig. 6.2 shows (a) the Ewald sphere together with reciprocal lattice points as a graphical representation of the diffraction condition (their intersection by rotating the crystal) and (b) a collective graph capturing the angular conditions at which the detector must be set for all the h±8, k±8, l±8 peaks considering a polar tilt of the sample of 0.7 degrees and 8 keV photons for the diffraction probe. Two solutions can in principle be obtained, although with different azimuthal rotations φ of the crystal. Gamma (γ) and delta (δ) are the azimuthal and polar degrees of freedom of the detector respectively [260].

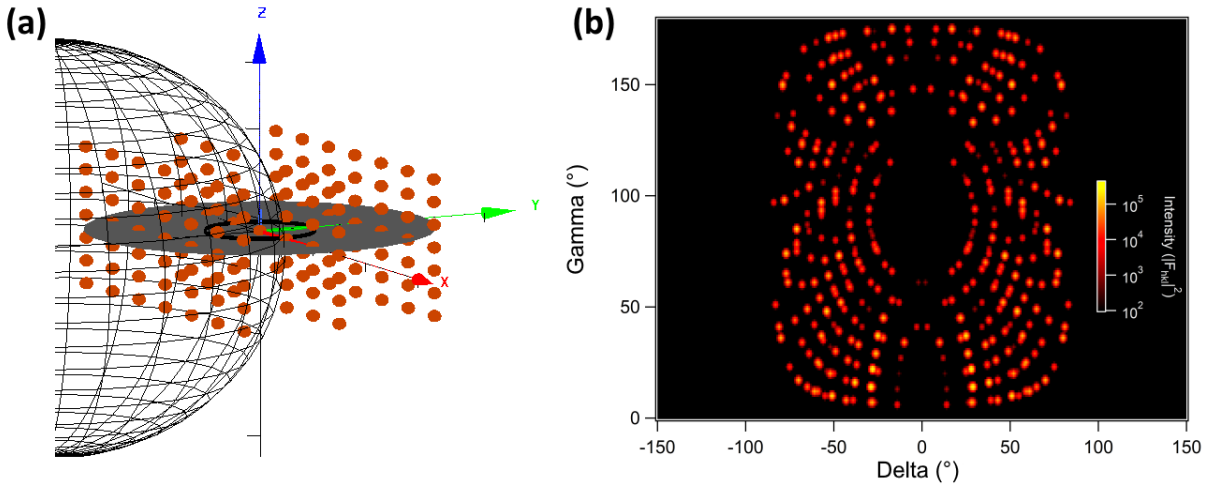

Figure 6.2. Prediction code for the angular coordinates. (a) Scheme of Ewald sphere and reciprocal lattice points. (b) Collective results for the angular conditions for the detector for all the peaks with h±8, k±8, l±8.

6.3.3 Single-color time-resolved reflectivity at T-ReX

The experiment utilizes the same setup employed for the single-color measurements and described in the 'Experimental details' section of Chapter 5, although with some differences. To compare our x-ray results, we performed fully-optical time-resolved measurements using a Ti:sapphire amplifier which produces ∼50 fs and 800 nm pulses with 250 kHz repetition rate. Divided by a beam splitter, part of the outcoming beam was directed in a 3-mm sapphire window to generate a supercontinuum of wavelengths between 550 and 1550 nm. The resulting light was directed to the sample to be used as a probe beam,

together with the 800 nm pump, in a quasi-normal incidence configuration. The reflected beam was then filtered at 950 nm using a bandpass filter when acquiring single-color measurements. We measured the reflectivity signal as a function of the pump-probe delay and pump fluence conditions. The choice of the probe wavelength was made in order to observe a significant contribution of, at least, the two most prominent modes (∼0.25 and ∼2.5 THz) based on previous results obtained on WTe_2 by probing the coherent phonons with white light (Chapter 5). Additional measurements were also performed using the full spectrum of the white light, as it was described in Chapter 5.

6.3.4 Single-color time-resolved reflectivity at UDG

The experiments were conducted using a Legend Elite Duo laser system (Coherent ®), a Ti:sapphire amplifier which produces ∼100 fs and 800 nm pulses at 1 kHz repetition rate. An optical parametric amplifier (TOPAS-white, Coherent ®) was set to generate ∼950 nm, ∼16 fs radiation. Part of the original 800 nm beam was utilized as a pump beam (∼90 µm spot diameter), while the OPA output was employed as a probe beam (∼30 µm spot diameter). The experiment was performed in a quasi-normal incidence configuration. We measured the reflectivity signal as a function of the pump-probe delay and pump fluence conditions and plotted it as DR/R (Eq. (5.1)). In this chapter, we report the evolution of the reflectivity signal at the point where a fluence-induced 'damage' sets in, for the case of a high repetition rate laser source.

6.4 Experimental results

In Fig. 6.3 we report the dynamics of the intensity of selected Bragg peaks. The intensity variation is represented as ΔI/I, defined as the difference between the diffraction intensity with and without the optical pump laser, divided by the one without it. To improve the signal to noise ratio, each intensity value was divided by a reference intensity value coming from a portion of the incoming FEL beam, measured before the interaction of the beam with the sample. The datasets were collected using a ∼3.2 mJ/cm^2 absorbed pump fluence. In terms of reflectivity coefficients, some small differences are present due to the polarization dependence of the in-plane reflectivity [68] (see Appendix A), although we can consider the reported fluence as an average value comprehending the maximum and minimum values in a 6% interval. After time-zero (t=0), where pump and probe are superimposed in time, the peak intensity starts to deviate from the equilibrium value with the clear appearance of a sharp slow modulation.

Close to time-zero and using a ten times smaller delay step (Fig. 6.4(a)) for peak $(\bar{1}63)$, we observe that not only a ∼0.25 THz mode is present, but also higher frequency modes emerge. The slower mode frequency, which is clearly distinct from the others, is found to be 0.240±0.001 THz from a fitting of the profile using a cosine wave. Subtracting it from the raw data allows to extract more clearly the higher frequency phonons (Fig. 6.4(b),(c)). From the resulting residual curve, its Fourier transform (Fig. 6.4(d)), taken between 1 and 6 ps, shows their frequencies: prominent contributions are found at 2.39±0.07 THz, 3.38±0.07 THz and 6.20±0.07 THz. These frequencies correspond to A_1 zone-center optical phonon modes as we confirmed through density functional perturbation theory

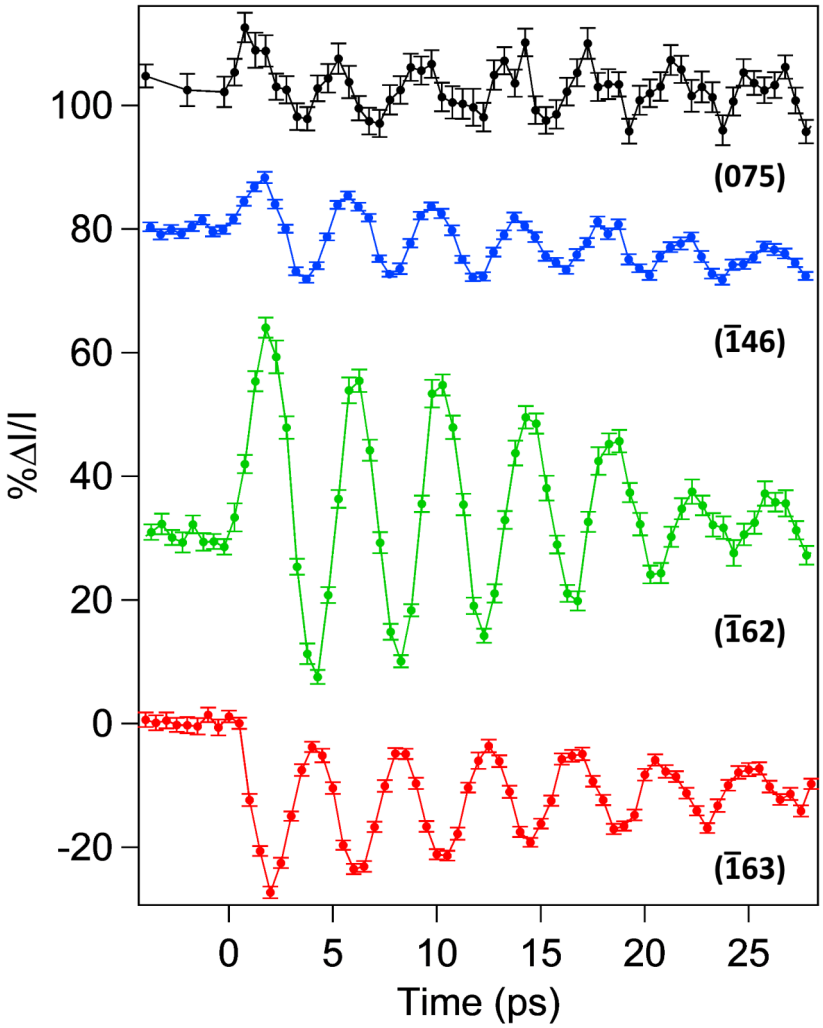

Figure 6.3. Time-resolved modification of the diffraction intensity ΔI/I for the (075), ($\bar{1}$46), ($\bar{1}$62) and ($\bar{1}$63) diffraction peaks taken at ∼3.2 mJ/cm^2 incidence fluence and 1.55 eV pump photon energy at T=295 K. The upper profiles were vertically shifted for clarity.

(DFPT) calculations (Fig. 6.5), whose computational details are found later on in this chapter.

All the A_1 modes involve displacements in the yz plane, while no shift along the x direction is present due to the mirror symmetry element (C_{2v} point group [61]) perpendicular to x. Around the frequencies at which the last two peaks are resolved, multiple eigenvalues are present. This, together with the spectral breadth of those peaks, may be an indication that a higher number of modes is actually excited.

In Fig. 6.6, we report additional time windows for the ΔI/I signal for the ($\bar{1}$46), ($\bar{1}$62) and ($\bar{1}$63) Bragg peaks taken with different temporal samplings.

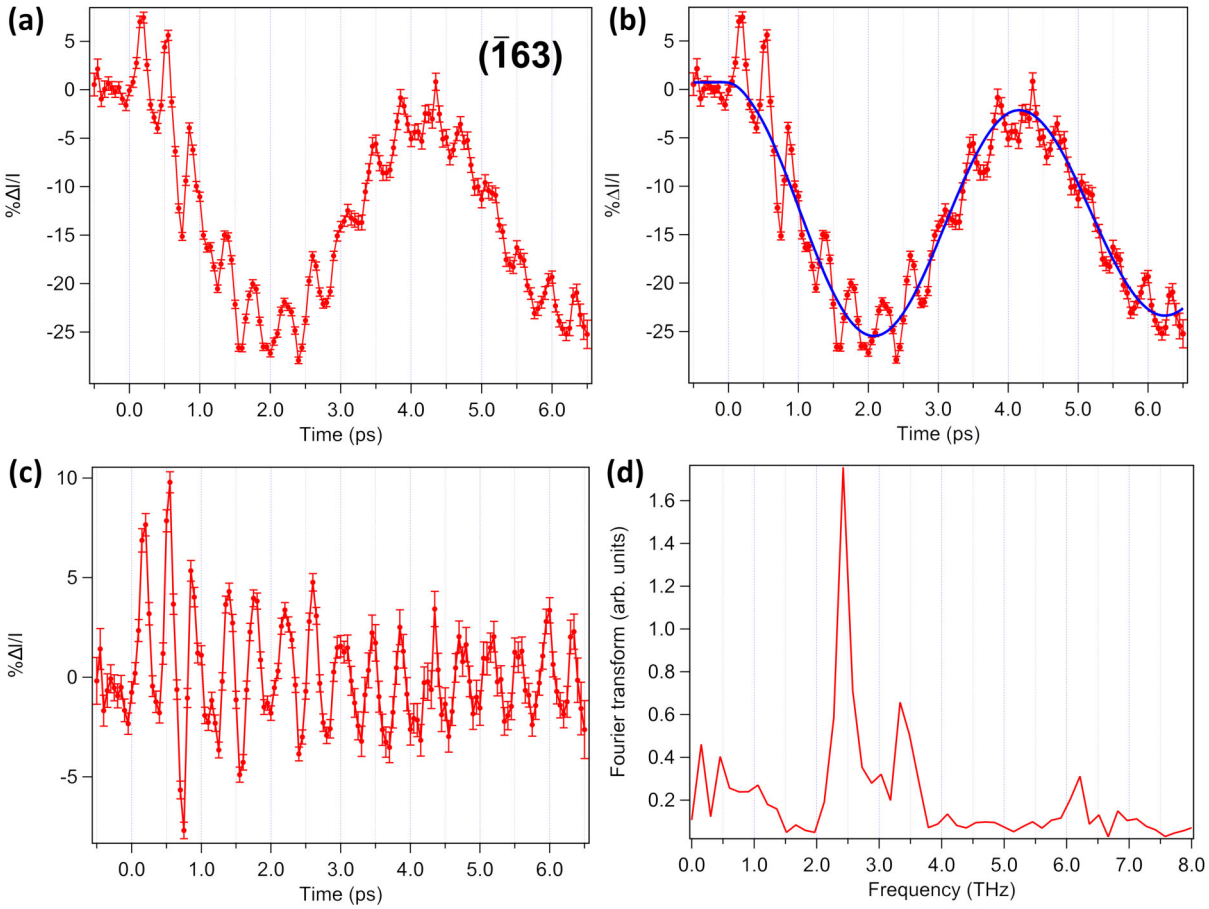

Figure 6.4. (a) ΔI/I profiles for Bragg peak ($\bar{1}63$) in the first picoseconds. (b) Panel (a) using a cosine wave to fit the shear contribution to the experimental data. (c) Coherent phonon response for frequencies higher than the shear mode after subtracting from (a) the fit curve shown in (b). (d) Fourier transform of (c) taken at room temperature and ∼3.2 mJ/cm^2 absorbed fluence.

At later time delays the time-traces reach quasi-equilibrium values for the diffraction intensities in 80-100 ps. The time scale and the peak intensity behavior showcased by the phenomenon are comparable with the transient lattice heating effects observed in transition metals-based materials [150][151].

In Fig. 6.7, the fluence dependence of the ($\bar{1}63$) diffraction peak is reported for multiple time windows and steps. In the first hundreds of femtoseconds, the optical phonons modes with frequency higher than 0.25 THz dominate the ΔI/I with a quasi-linear dependence of the initial amplitudes on fluence. Their signal decays faster as the fluence is increased. Differently, the slow mode exhibits an amplitude decrease with the deposited energy. This is highlighted in Fig. 6.8, where the oscillations are shown in different time ranges, separating the high-frequency modes from the shear mode.

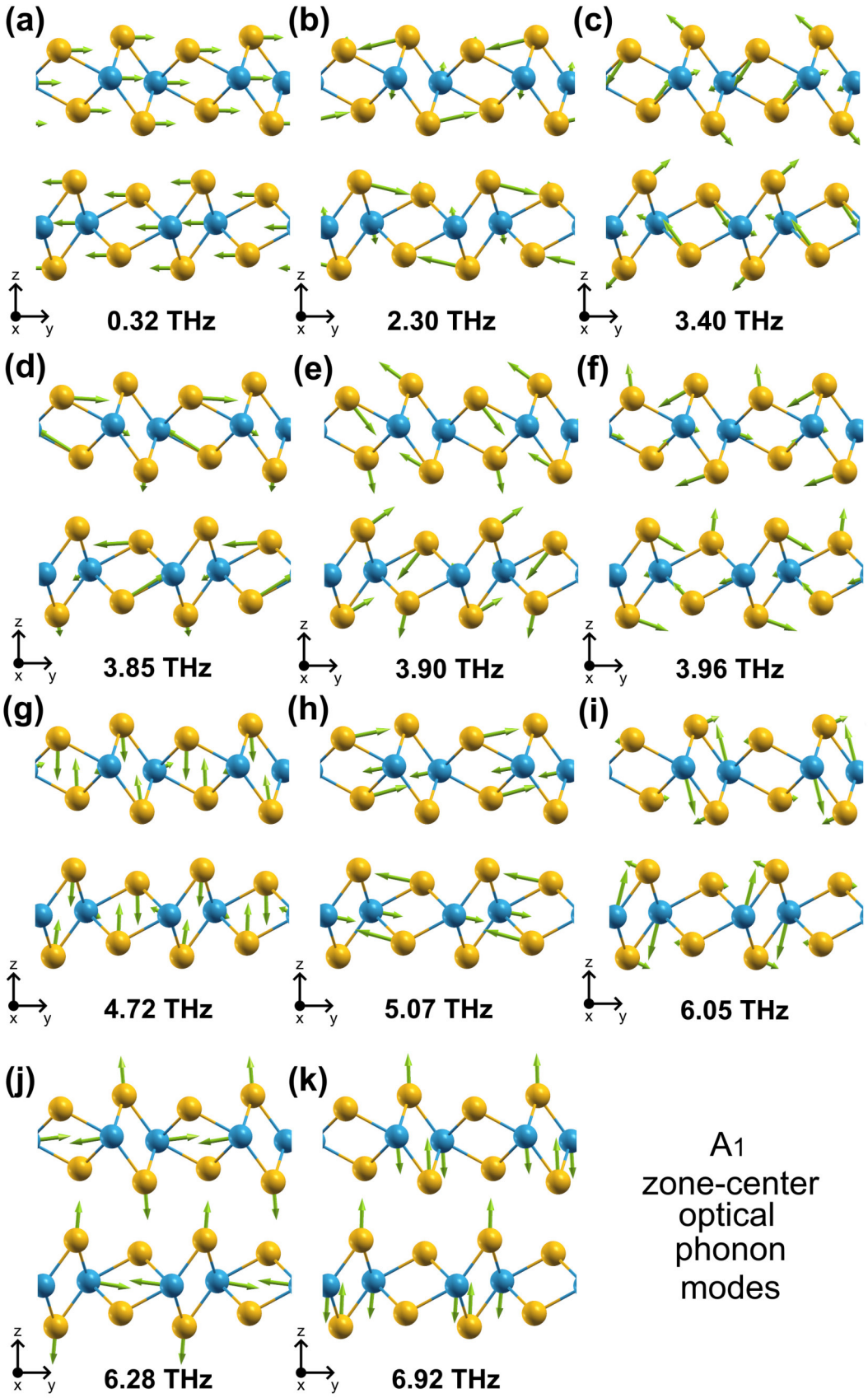

Figure 6.5. Zone-center A_1 optical phonon eigendisplacements resulting from the DFPT calculations.

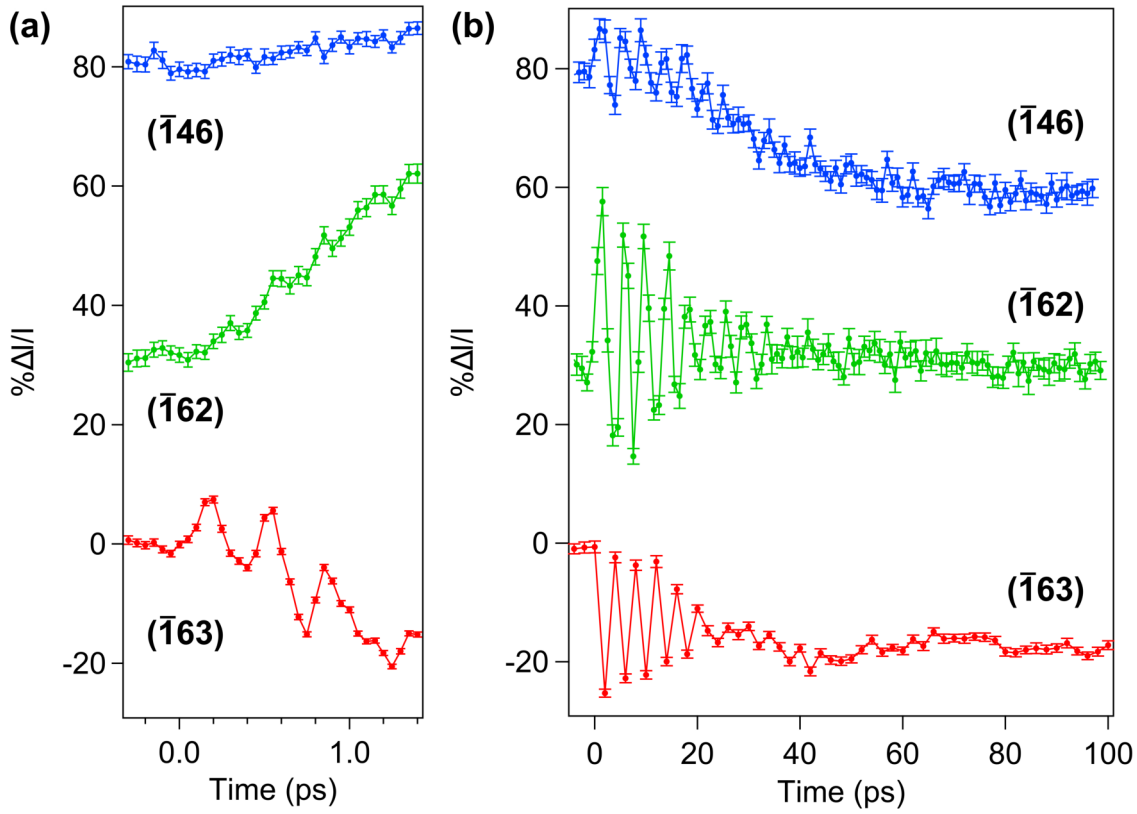

Figure 6.6. (a) ΔI/I profiles for the (1̄46), (1̄62), (1̄63) Bragg peaks (a) around time-zero and (b) in an extended time window taken at room temperature and ∼3.2 mJ/cm^2 absorbed fluence. The upper profiles were vertically shifted for clarity.

The long-delay dynamics was also probed through rocking-curve scans varying the azimuthal angle φ of the sample goniometer keeping the detector fixed (Fig. 6.1(a)). Figs. 6.9 (a)-(d) present the dependence of the diffracted intensity difference ΔI between pumped and unpumped conditions as a function of φ for the (075), (1̄46), (1̄62) and (1̄63) Bragg peaks for selected time delays using a ∼3.2 mJ/cm^2 fluence. The correspondence of the rocking curves to the time dynamics can be understood using the profiles in Figs. 6.3, 6.6 (see also Appendix C). During the first picoseconds, the rocking curves are heavily affected by the sensitivity of the examined Bragg peak to the coherent optical phonons and they follow their maxima/minima trend.

At longer time delays, we observe a gradual shift of the maximum of the (1̄46) and (1̄63) peaks, together with an overall decrease of their diffraction intensity. Differently, (075) and (1̄62), while showing a similar shift, present an almost null and small increase in the integrated ΔI respectively. The modifications are compatible with a change of the structure towards the proposed centrosymmetric 1T'(*) phase [35][36]. This aspect is treated in more detail in the discussion section. The variation of the angular position of the peaks is consistent with an expansion of the material which reduces the φ required to meet the diffraction conditions.

As the deposited energy increases, the effect is enhanced as expected due to its positive thermal capacity [264]. Fig. 6.10 showcases a comparison between the rocking curves varying the azimuthal angle φ at two different absorbed fluences at (a)∼3.2 mJ/cm^2 and (b)∼9.5 mJ/cm^2. For panel (b) we observe a more pronounced shift of the peak at later time delays compatible with a larger expansion of the crystal cell.

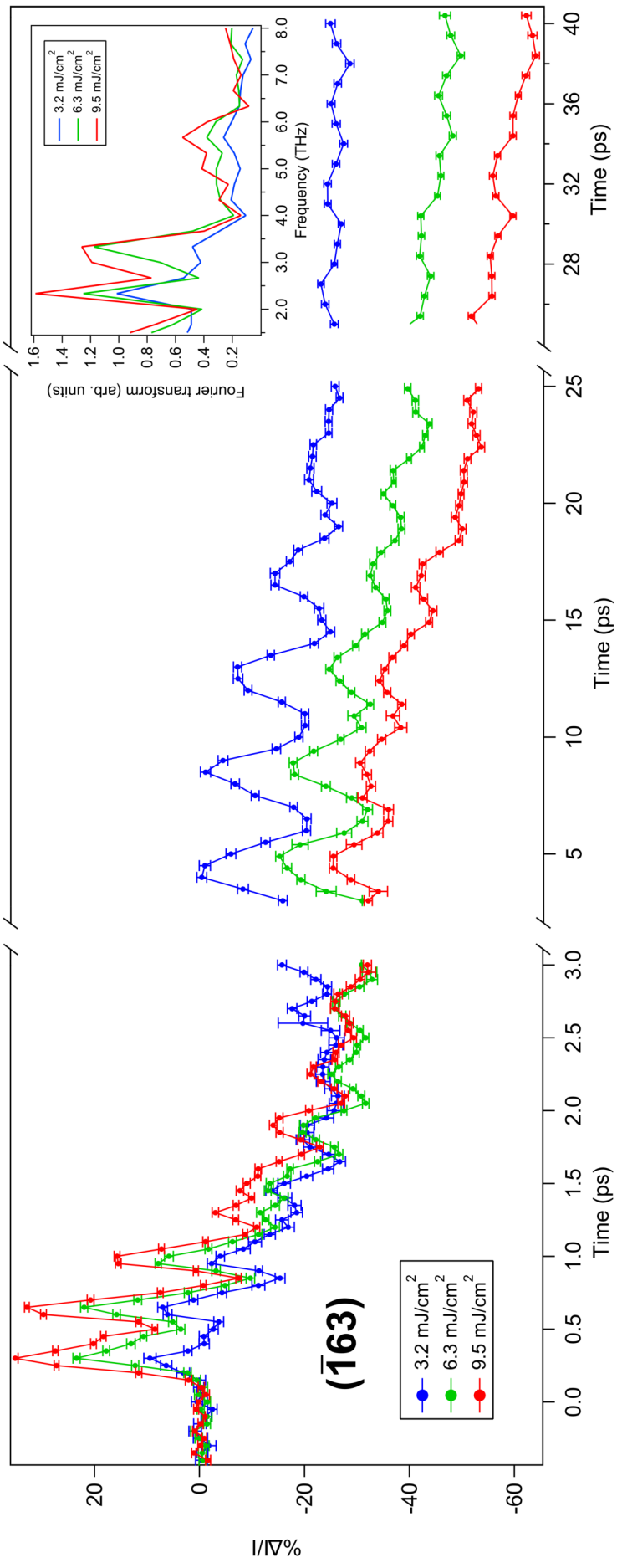

Figure 6.7. Time-resolved modification of the diffraction intensity $\Delta I/I$ for the $(\bar{1}63)$ taken at different absorbed pump fluences and 1.55 eV pump photon energy at T=295 K. The inset shows the Fourier transform in the 1.5-8 THz range taken in the interval 0-3 ps for the different fluence profiles.

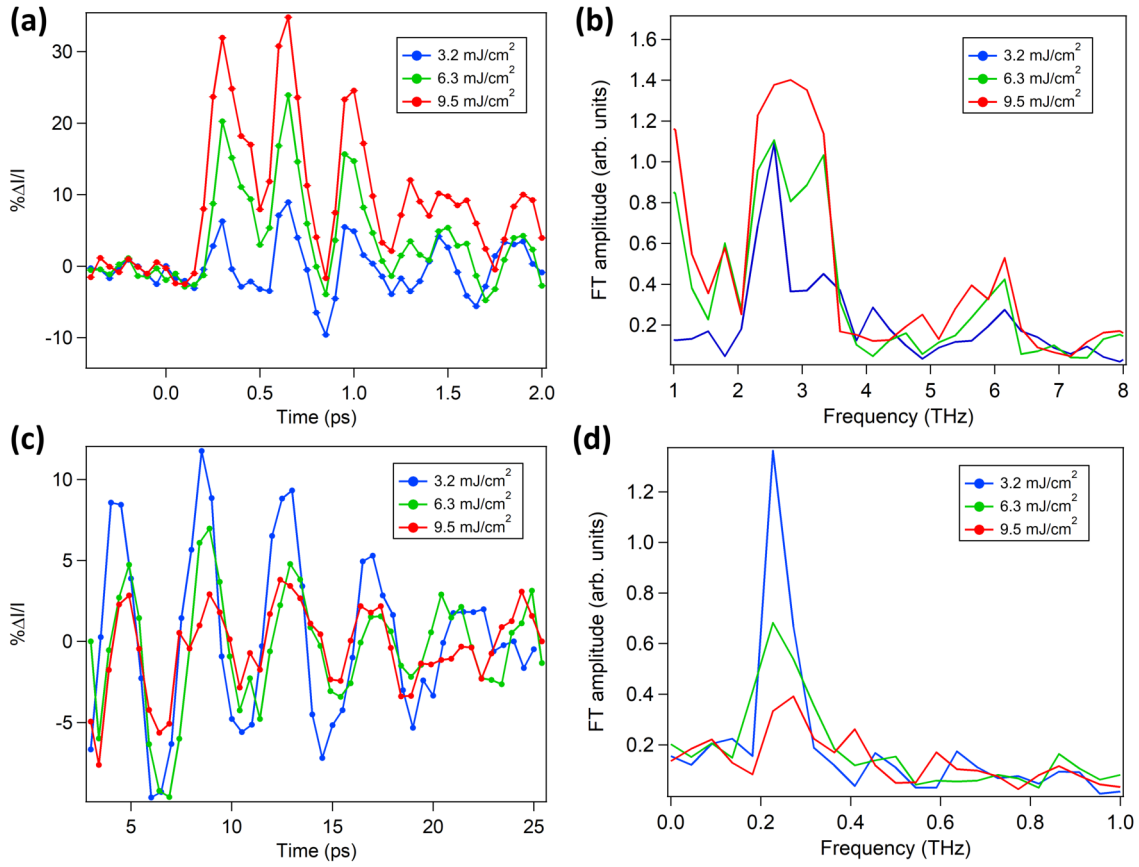

Figure 6.8. Extraction of the phonon modes from the fluence dependence data of Fig. 6.7 for the $(\bar{1}63)$ peak. (a) First time window, where a common curve, deriving from the fitting of the shear mode with a cosine wave fine, was subtracted from the profiles at different fluence; the corresponding Fourier transforms are reported in panel (b). (c) Second time window, where the experimental data was fitted using a second-order polynomial curve for each profile which was then subtracted from it; the corresponding Fourier transforms are reported in panel (d).

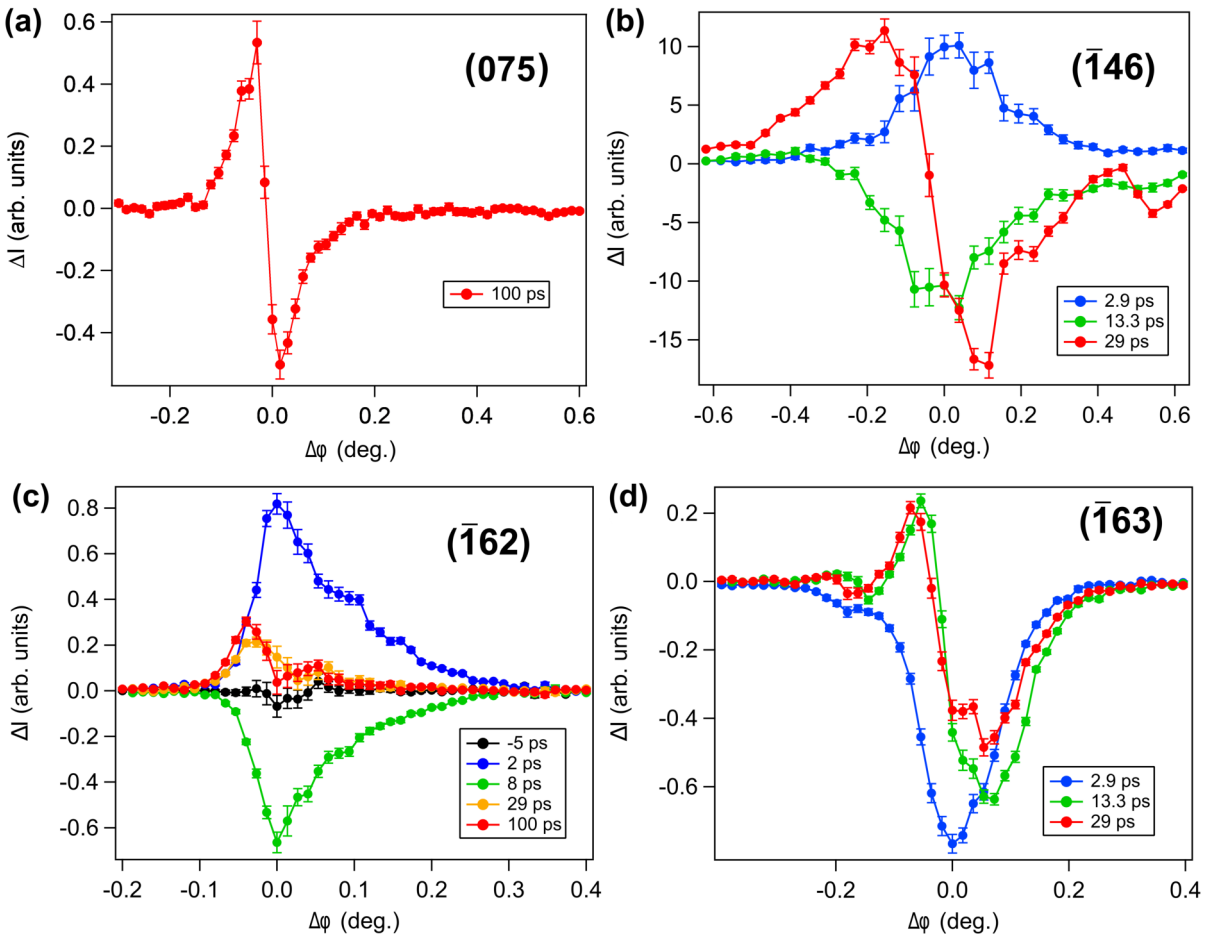

Figure 6.9. Rocking curves obtained by modifying the goniometer azimuthal angle φ showing the diffraction intensity difference ΔI for the (a) (075) (b) ($\bar{1}46$) (c) ($\bar{1}62$) and (d) ($\bar{1}63$) taken at $\sim$3.2 mJ/cm^2.

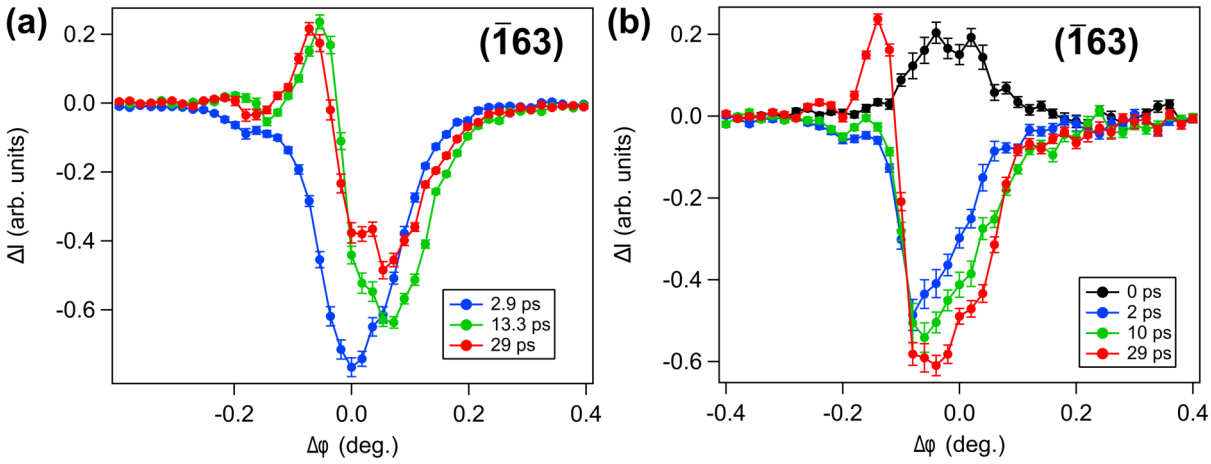

Figure 6.10. φ-scans for the ($\bar{1}63$) Bragg peak at (a)$\sim$3.2 mJ/cm^2 (b)$\sim$9.5 mJ/cm^2 absorbed fluence.

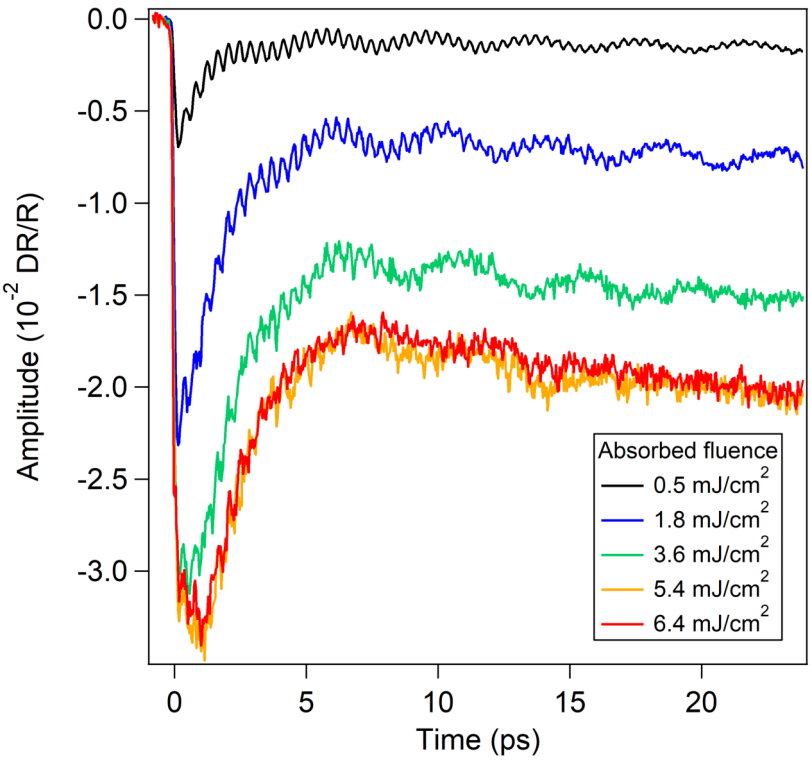

Figure 6.11. Fluence dependence of time-resolved reflectivity measurements in quasi-normal incidence taken at 250 kHz. A 800 nm pump beam and a 950 nm probe are linearly polarized along the y and x directions respectively.

6.4.1 Time-resolved optical measurements

The time-resolved traces are reported in Fig. 6.11 for selected fluence values. Here the non-equilibrium reflectivity is expressed in terms of DR/R, *i.e.* the ratio between the reflectivity difference due to the presence of the pump pulse and the equilibrium value. At time-zero (t=0), the DR/R quickly decreases due to carrier excitation. Subsequently, carrier relaxation occurs, involving electron-electron and electron-phonon scattering processes, with a time constant of about ∼1 ps at low fluence. As already reported in Chapter 5 (see Eq. (5.2)), the decay follows single-exponential law; the signal then reaches a quasi-equilibrium value a few ps afterwards.

As the fluence is increased, fitting the time-resolved reflectivity profiles using a decaying-exponential fit becomes less adequate. A subtraction of such fit leads to a relevant quasi-zero frequency contribution in the analysis of the coherent phonon effects, which interferes with the 0.25 THz mode even when using a double-decaying exponential. For this reason, while low-fluence data can be very well fitted in terms of a single decaying-exponential fit with a ∼1 ps decay time, a single decay-time constant cannot be obtained for the higher fluences using this model.

Nevertheless, it is possible to analyze the fluence dependence by normalizing the time-resolved profiles to -1 (Fig. 6.12). It becomes clear that as the fluence is increased, the relaxation time of the main non-equilibrium peak grows, reaching a saturation at the highest fluence values. Moreover, the main peak reaches its maximum further from time-zero, which we interpret as both a saturation in the excitable carriers together with the

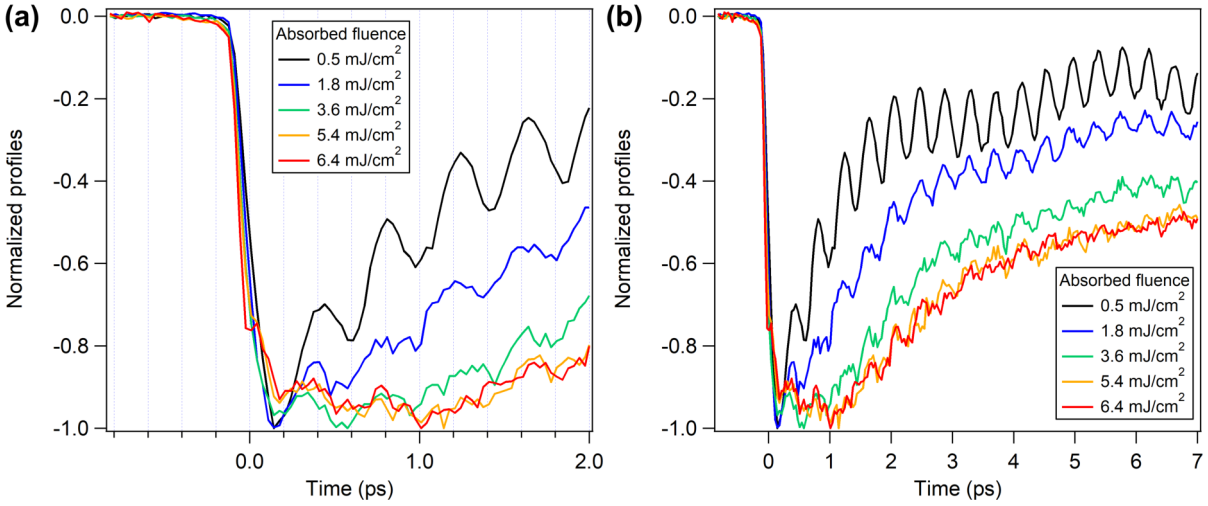

Figure 6.12. Normalized optical profiles from Fig. 6.11 in two different time windows taken at room temperature.

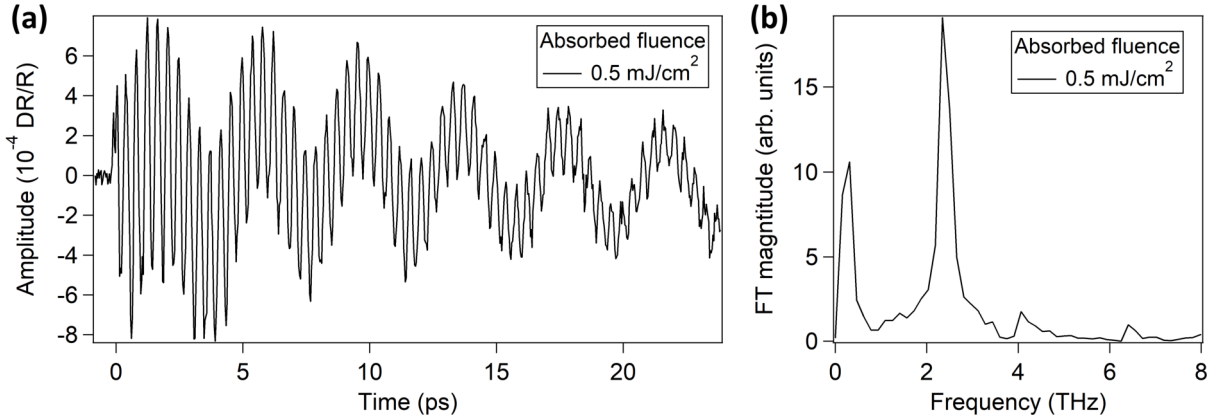

Figure 6.13. (a) Coherent oscillatory response extracted from Fig. 6.11 subtracting a decaying-exponentional fit. (b) Fourier transform of (a) taken at room temperature and $\sim$0.5 mJ/cm^2 absorbed fluence.

difficulty of the electronic system to redistribute the absorbed energy to reach a thermal equilibrium. This observation, together with a further slower reduction of the DR/R after a few picoseconds, is an indication that the system struggles to quickly redistribute the large energy introduced by the pump pulse in the electronic and lattice subsystems.

Superimposed to these energy redistribution mechanisms, coherent phonons are clearly distinguishable. In Fig. 6.13 we examine the coherent phonon response for the lowest measured fluence. In this case, the oscillatory component was derived by subtracting a single decaying-exponential fit, as described in Eq. (5.2). It shows two prominent peaks around 0.25 and 2.5 THz as well as higher frequency contributions similarly to the Fourier transform of the ($\bar{1}63$) dynamics (Fig. 6.4(d)), when analyzed in an analogous time range, as depicted in panel (b).

Initially, as the fluence increases, the initial amplitudes of both the 0.25 and 2.5 THz modes grow in the selected temporal window. However, a visible reduction of the damping

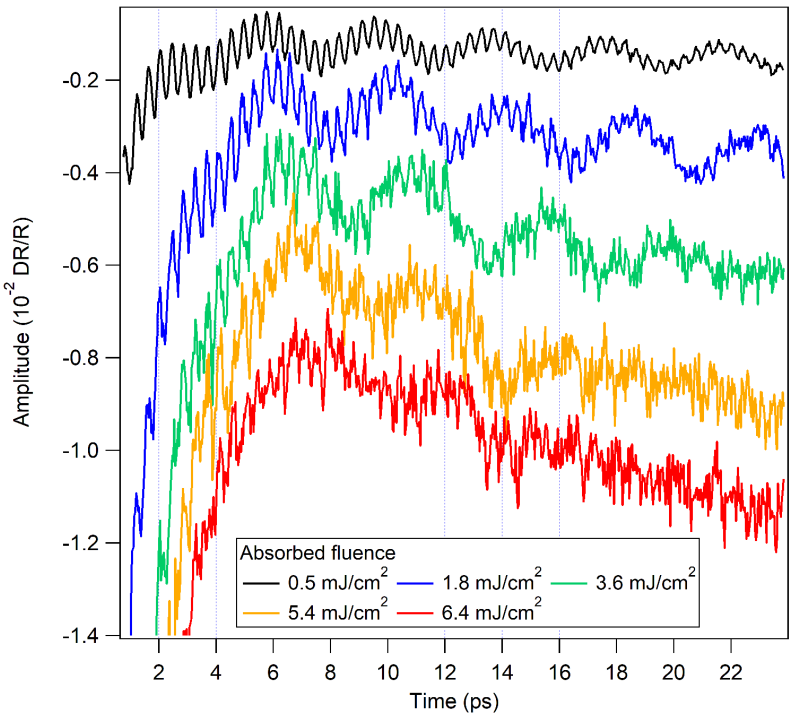

Figure 6.14. Particular of time-resolved profiles focusing on the coherent response shown in Fig. 6.11. The profiles are shifted close to each other as an aid to the eye to observe the frequency redshift of the phonons.

times for the two phonons occurs together with a redshift of the shear mode frequency, depicted in Fig. 6.14 where the profiles were shifted to better highlight the phenomenon. The redshift was already reported in [105][246], albeit at lower fluences, and proposed to be connected to lattice anharmonicity induced by the increasing excitation. Above 5.4 mJ/cm^2, the time-profiles reach saturation together with a partial reduction of the shear mode related effects.

Increasing even more the deposited energy, the system slowly breaks down under exposition to the pump pulse. The fluence at which this phenomenon appears to be spot-dependent ranges from 6.4 to 9.1 mJ/cm^2 absorbed fluence using high-repetition rate systems.

It is worth noting that employing a 1-kHz Ti:sapphire laser system with a ∼100 fs 800 nm pump pulse and a OPA-generated ∼16 fs 950 nm probe pulse, it is also possible to monitor the process (Fig. 6.15), which, however, requires about 40 minutes to reach a stationary situation; the data was continuously acquired during the process. Moreover, if one examines the aftermath of the over-exposure using a white light probe pulse (Fig. 6.16), clear difference emerge in the reflectivity response in both the two polarization directions.

The reason why we did not observe such analogous breakdown during the x-ray experiment is likely connected to the much lower repetition rate (50 Hz). As shown in Fig. 6.15, this process takes tens of minutes to occur at 1 kHz under continuous exposure to the pump beam, pointing towards a mechanism which does not only depend on the peak fluence, but also on the total exposure involving a slower local atomic reorganization.

Due to the time-scale on which the transformation occurs and the occurrence only using high-repetition rate sources, we attribute the phenomenon to a superficial melting of the system. In fact, the temperature increase calculated using the formula used reported in [105] for the higher used absorbed fluences is compatible with the reported 1020-1300 K melting point [265][266].

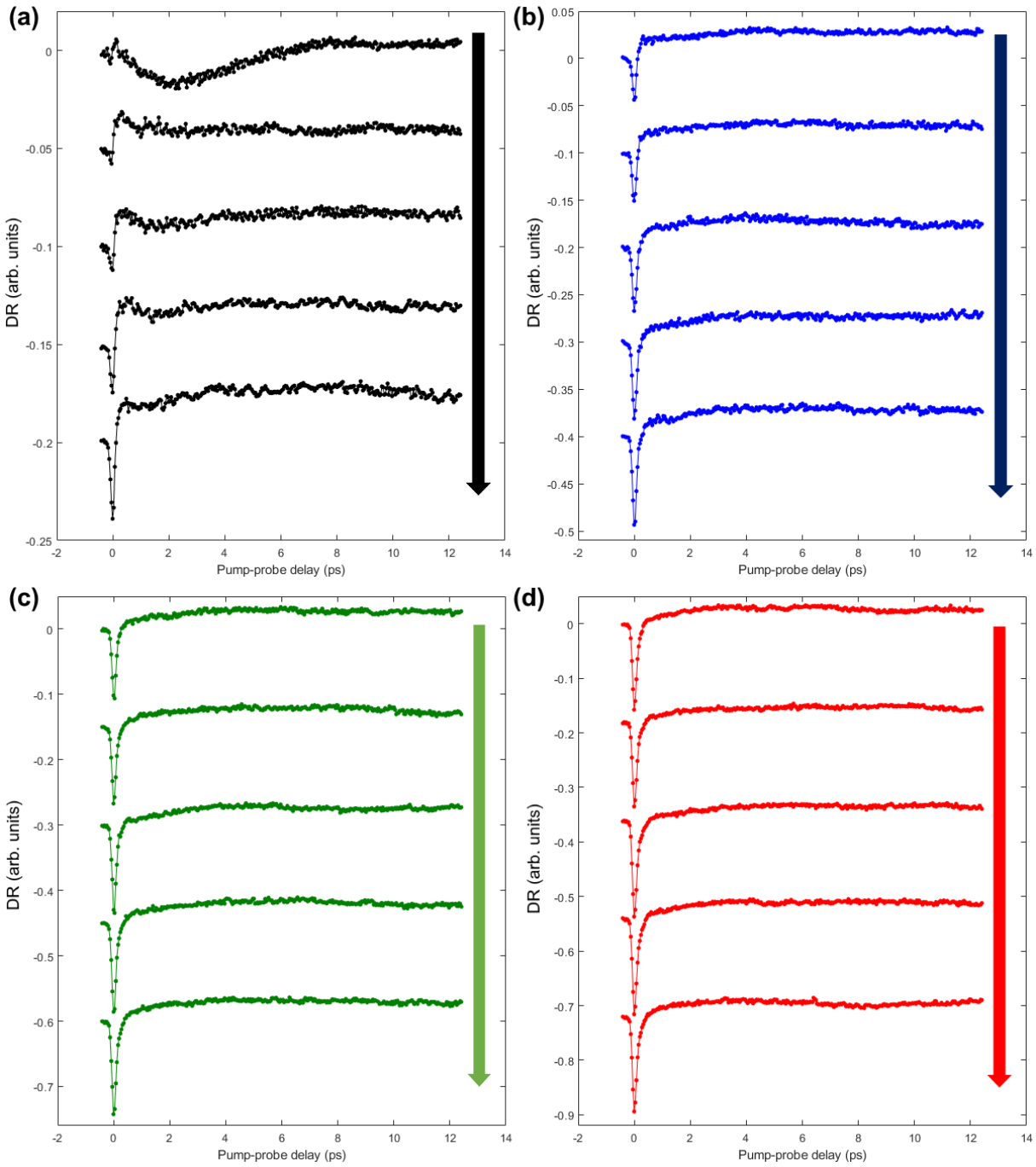

Figure 6.15. Gradual change in the sample at high fluences as irreversible changes occur. The profiles are time-ordered from top to bottom from panel (a) to panel (d). The total acquisition time was ∼42 minutes. The data was acquired at room temperature and ∼6.4 mJ/cm^2 absorbed fluence albeit using a different laser system at 1 kHz and a different sample spot compared to the rest of the reported optical measurements. The lower profiles were vertically shifted for clarity in each panel.

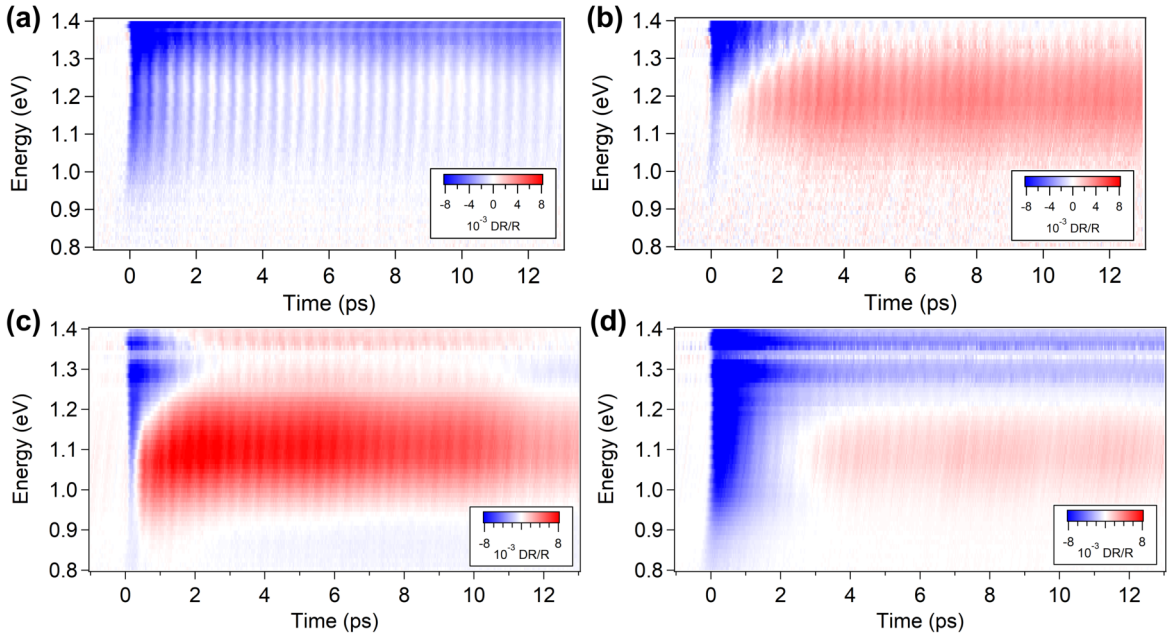

Figure 6.16. DR/R comparison between under-exposed (a),(b) taken at ∼0.7 mJ/cm^2 absorbed fluence as shown in Chapter 5 and over-exposed (c),(d) taken at ∼0.5 mJ/cm^2 using a 250 kHz laser system at room temperature. (a) and (c) were taken having the white probe polarized along the x crystallographic direction, while it was directed along y for (b) and (d); the pump beam, linearly polarized, was kept perpendicular to the probe.

6.5 Numerical simulations

6.5.1 Technical details

To support our results, density functional theory (DFT) simulations were carried out using the Quantum Espresso (QE) [216] suite of codes. Pseudopotentials based on the projected augmented wave method (PAW) [209] with the generalized gradient approximation (GGA) in the Perdew-Burke-Ernzerhof (PBE) parametrization for the exchange-correlation functional [210] from the pslibrary 1.0.0 [213] were employed, choosing the most stringent versions. The equilibrium configuration was obtained starting from an orthorhombic simulation cell with lattice constants a=3.496 Å, b=6.282 Å and c=14.073 Å crystallographic coordinates at room temperature [61]. The electronic density and band structure was obtained using a 80 Rydberg plane wave kinetic energy cut-off for the wavefunctions and uniform 14×12×8 k-point mesh for integrations over the Brillouin zone under a fully-relativistic description including spin-orbit coupling. Van der Waals contributions were not included, since, although in general relevant to describe layered compounds, in this specific case they do not improve the structural description of the system. For consistency, we follow this prescription for all the simulations. Crystal structure representations were plotted using XCrySDen [245]. The charge density planes, the Brillouin-zone-integrated density of states and projected density of states were calculated through a subsequent non-self consistent step with an increased 20×16×10 k-point mesh.

Compared to Chapter 5, the inclusion of spin-orbit coupling was necessary to more accurately describe the electronic band structure close to the Fermi level [6], which is of central interest in this chapter in the description of the impact of the coherent phonons on the electron and hole pockets.

The starting coordinates and lattice parameters were obtained from [61] instead of [242], previously used in Chapter 5. From the conceptual point of view, the experimental data in [242] was previously used in Chapter 5 to calculate, at the end, the optical properties to be compared with the literature data at 10 K [68]. This decision was taken as it is the dataset at the lowest temperature between the two. Differently, for this chapter, we chose the dataset which better represented our working conditions (room temperature). Moreover, we compared the experimental $\Delta I/I$ coherent phonon effects among the Bragg peaks to each of the two models, finding a much better agreement for the one based on [61].

6.5.2 Charge density distribution

In the equilibrium structure, the distortion of the octahedral coordination for tungsten is influenced by the interaction between the tungsten atoms through bonding, which has been also observed for other tungsten-based compounds [267]. Although an inversion center is absent among its space group elements [61], two subsequent layers are almost connected by it, leading to similar features shared by more atoms than simply the Wyckoff equivalents. This particular, together with other symmetry elements, are revealed through electron density surfaces (Figs. 6.17, 6.18); the charge density is plotted as numerical density in $(\text{bohr radius})^{-3}$. While the charge is primarily confined close to the individual atoms (Figs. 6.17(a),(b), 6.18(a)), in-layer directional W-Te and W-W bonds formation is clearly visible when we consider the difference between the electron density of the system and the superposition of the atomic electron densities (Figs. 6.17(c),(d), 6.18(b)). Focusing on atoms having the same x coordinate, we observe that all the tungsten atoms

present an analogous octahedral configuration, the tellurium atoms can be separated in two groups where the electronic density close to the atoms shows similar features. Taking as reference Fig. 6.1(b), we see that the Te atoms can be grouped as numbers #5, 6, 9, 10 and #7, 8, 11, 12, which constitute two different tellurium chains when observed in the xy plane. This fact emerges in various properties such as the projected density of states.

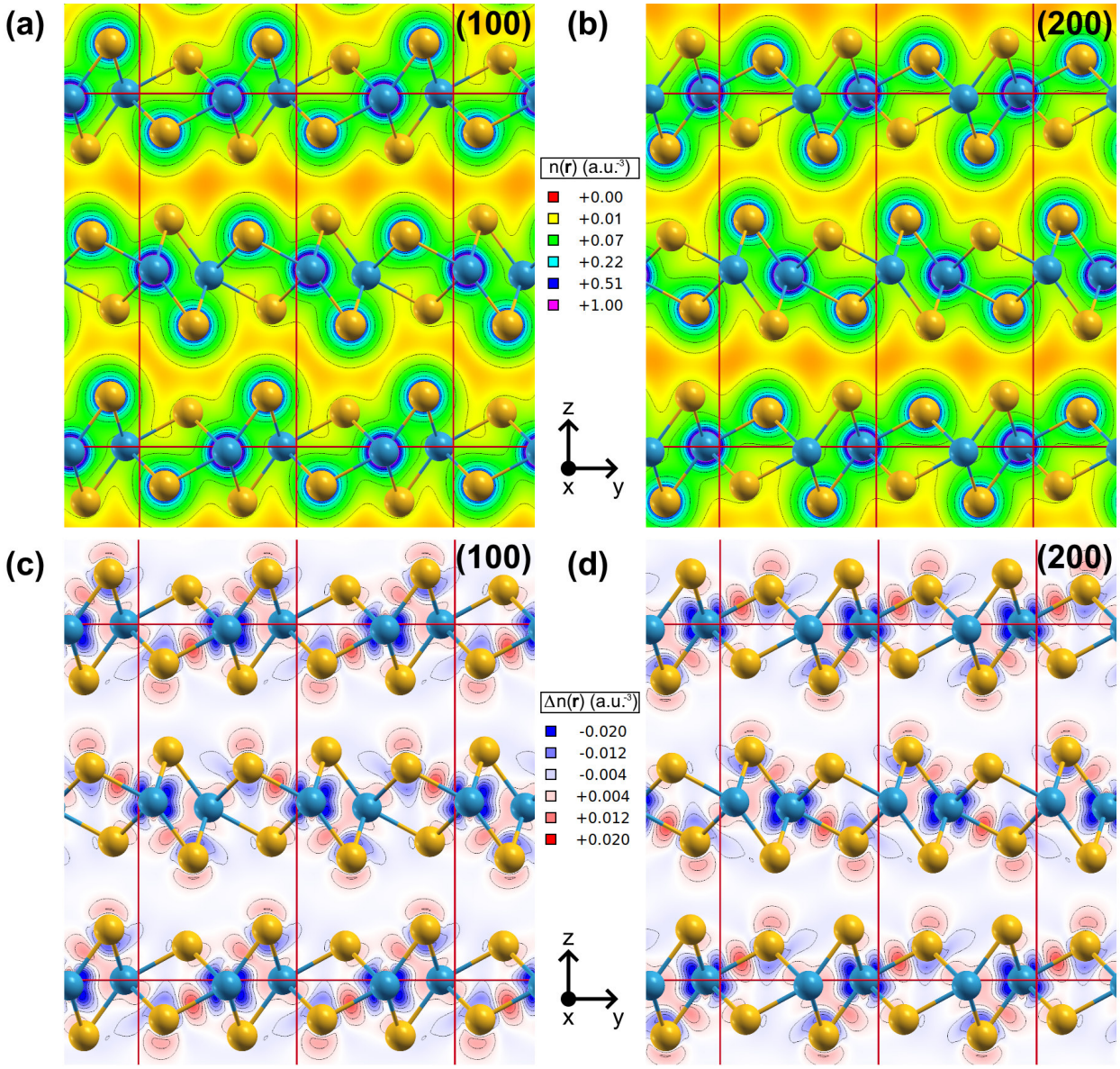

Figure 6.17. Electron density planes of WTe_2 for the (a) (100) surface (b) (200) surface. Electron density difference between the compound and the superposition of atomic electron densities are reported for the (c) (100) surface (d) (200) surface. Black isolines are reported as a guide for the eye. The unit cell is demarcated by red lines.

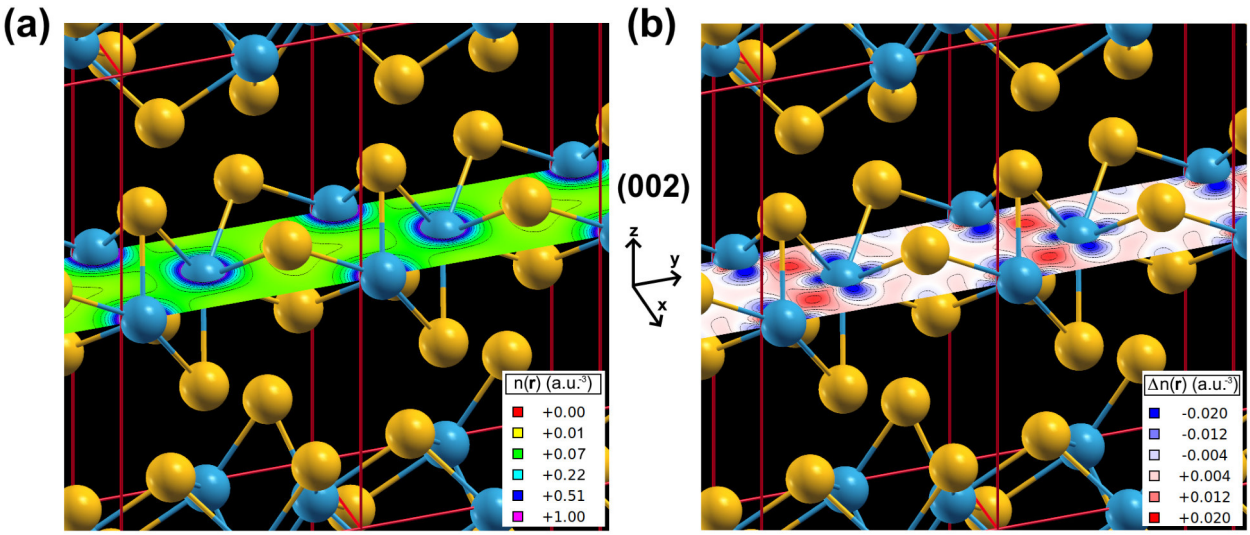

Figure 6.18. (a) Electron density of WTe_2 for the (002) surface. (b) Electron density difference between the compound and the superposition of atomic electron densities for the (002) surface. Black isolines are reported as a guide for the eye. The unit cell is demarcated by red lines.

6.5.3 Electronic structure

Tungsten ditelluride presents an orthorhombic Brillouin zone with semimetallic electron and hole pockets centered around Γ-X, which influence several of its properties [6][65]. The spin-orbit interaction gives a relevant contribution to the energy levels, especially around the Fermi level [6].

In Fig. 6.19(a) we report the Fermi surface of Td-WTe_2 in the relaxed configuration, plotted using a color map proportional to the modulus of the Fermi velocity at each point [215]. The symmetry lines connecting two points, one of them being Γ, sharing two null k-coordinates present $mm2$ point group symmetry for the points along them, as observed in the selected sections in Figs. 6.19(b),(c). The hole pockets are the closest to Γ, while the electron pockets are the closest to X; both of them are constituted by two bands. The relative size between electron and hole pockets is closer to the one expected for room-temperature conditions where the electron carriers dominate [13].

In Figs. 6.19(d),(e) we report the electronic band structure of WTe_2 along a selected k-path together with its density of states (DOS) respectively, showing a reduced, although finite, contribution around the Fermi level. The energy levels around the Fermi level are primarily connected to the in-plane bonds among tungsten 5d orbitals and tellurium 5p orbitals with varying contributions depending on k-point, total angular momentum and specific wavefunction.

This can be visualized through the projected density of states (PDOS) which gives an indication of the contribution of the individual atomic orbitals to the energy levels of the crystal. In Figs. 6.20, 6.21, we report the Brillouin-zone-integrated PDOS. While contributions are numerically distinct for each Wyckoff position, the twelve atoms of the unit cell can be divided into three groups with similar values and energy dependence. The first is formed by the four tungsten atoms which present similar PDOS, having the largest

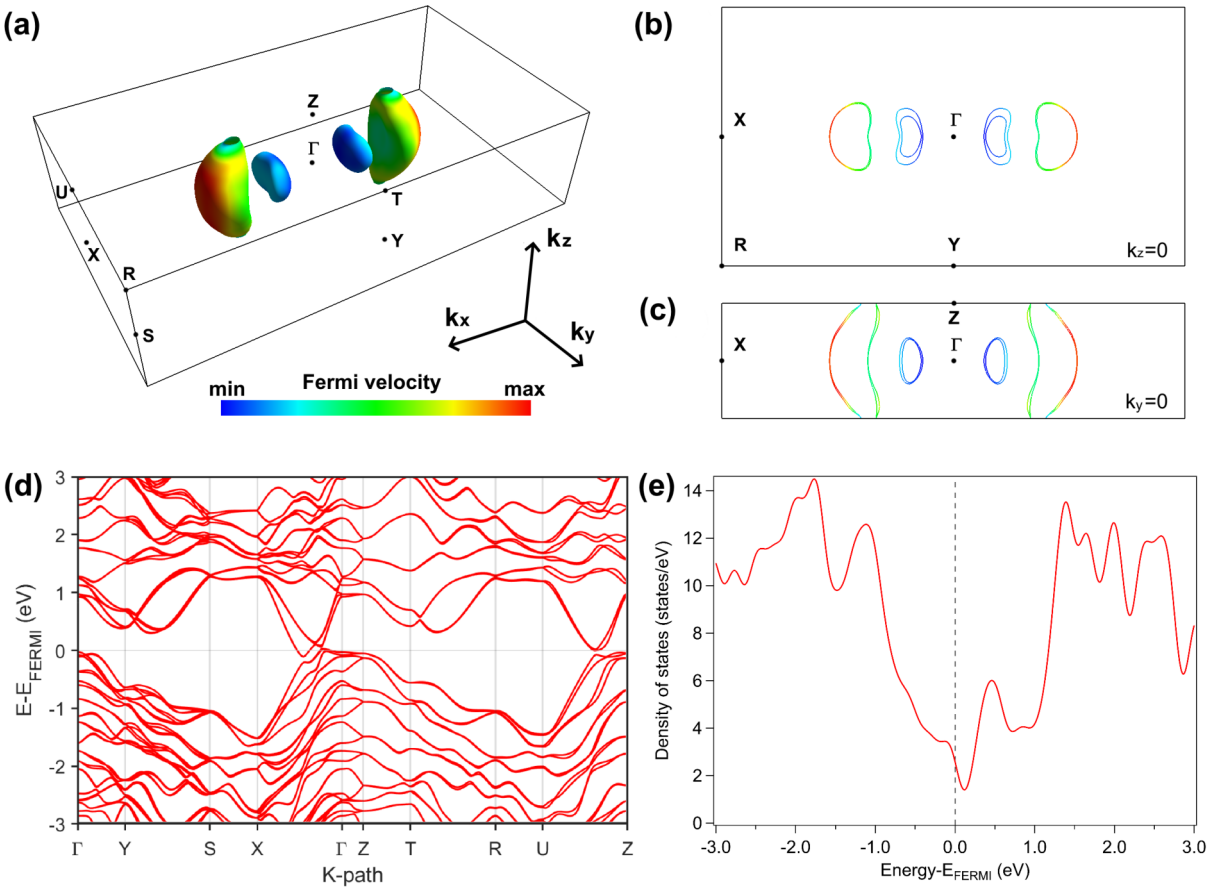

Figure 6.19. (a) Fermi surface of the relaxed system, E-E_{FERMI}=0 surface in the first Brillouin zone. (b) Section of (a), such that k_z=0 .(c) Section of (a), such that k_y=0. The color scale is linearly proportional to the modulus of the Fermi velocity ($|\mathbf{v_F}|$). (d) Electronic band structure along the k-path in the Brillouin zone. (e) Density of states (DOS).

contributions for the 5d, j=3/2 and 5d, j=5/2 subshells (Fig. 6.20(a)). The eight tellurium atoms can be instead separated into two four-atom subgroups, although their PDOS is dominated by the 5p, j=1/2 and 5p, j=3/2 subshells in both cases (Figs. 6.21(a),(b)). This grouping can be directly understood from the atomic crystal configuration, as described in the previous section.

Using the same k-path followed for the electronic band structure, we mapped the k-resolved contributions to the PDOS (Figs. 6.22, 6.23). Here we report the projections with the highest contributions around the Fermi level, summed over the wavefunctions and averaged over their degeneracy to use the same color scale in each case. We observe that the tungsten wavefunctions exhibit large projections for states which are far from the pockets region, along Γ-X, aside from small values for 5d, j=5/2 around Γ. Most of the highest occupied bands have a prominent 5p, j=3/2 character belonging to one of the two subgroups of tellurium atoms, while the rest of the examined projections is less relevant.

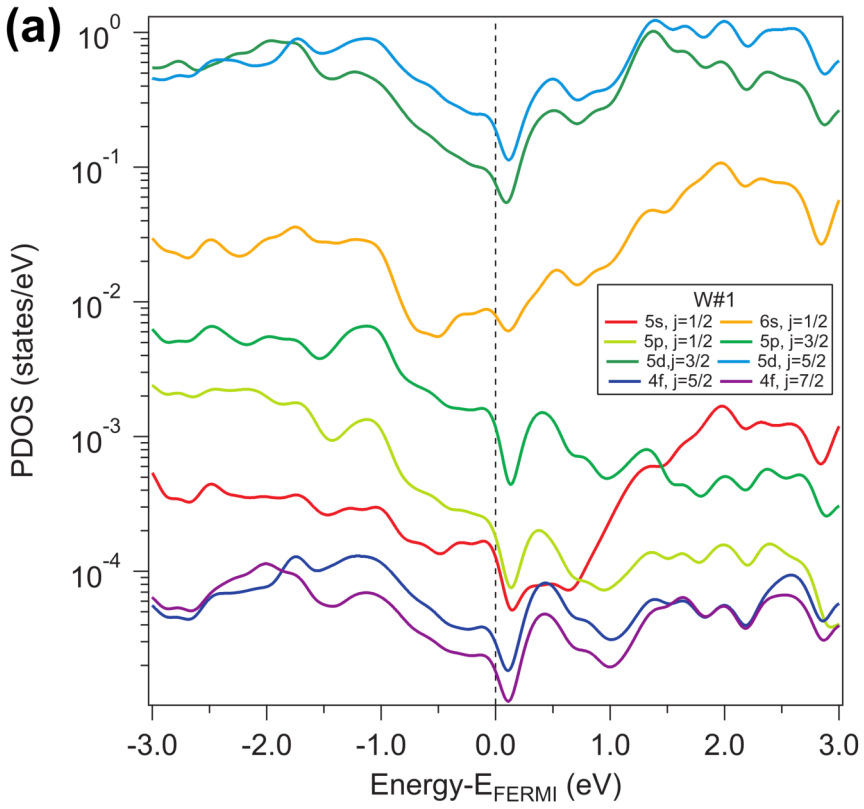

Figure 6.20. Brillouin zone integrated PDOS. (a) Projections for atom W#1. (b) Projections for atom Te#5. See Fig. 6.1(b) for reference.

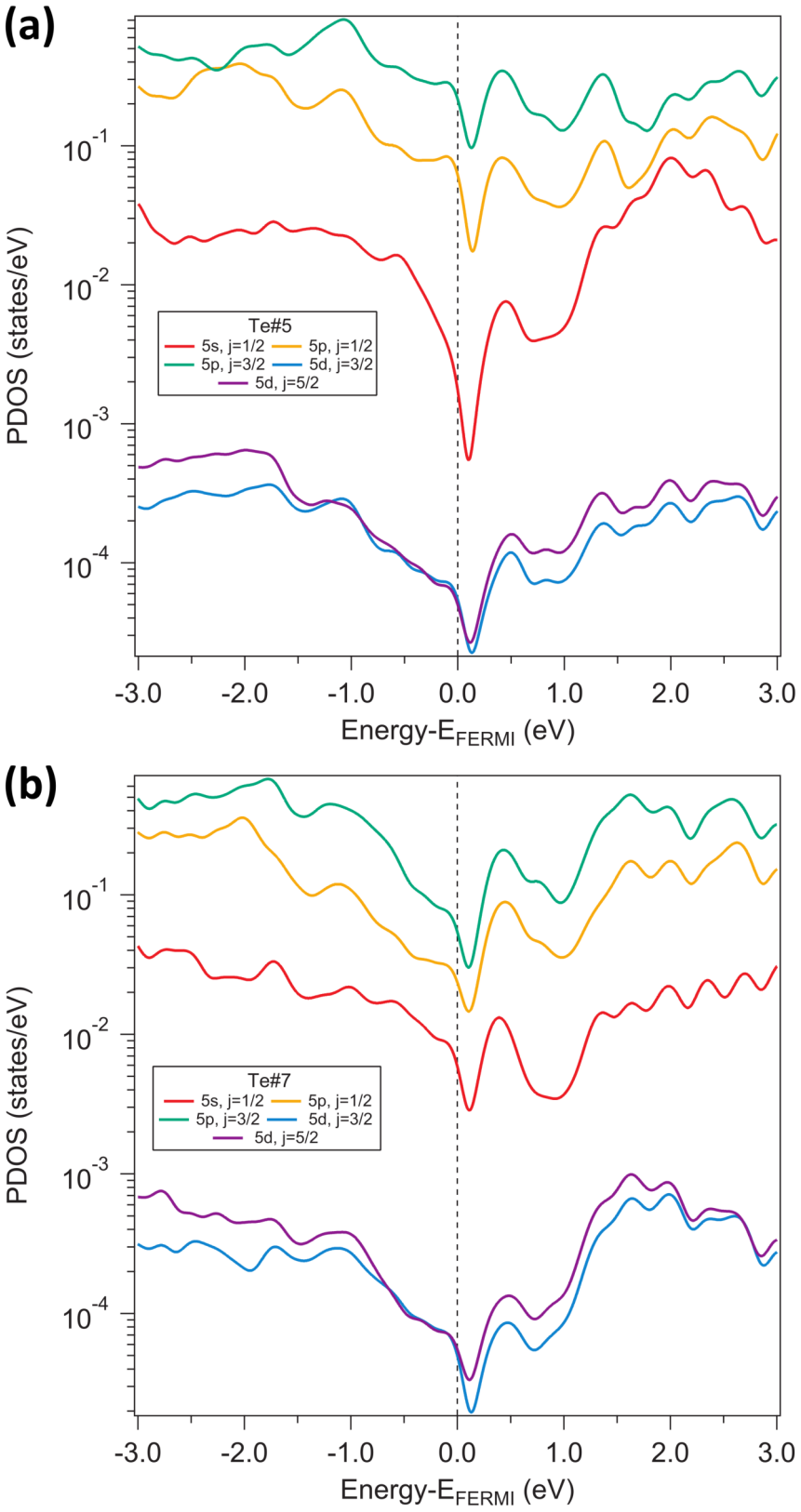

Figure 6.21. Brillouin zone integrated PDOS. (a) Projections for atom Te#7. See Fig. 6.1(b) for reference.

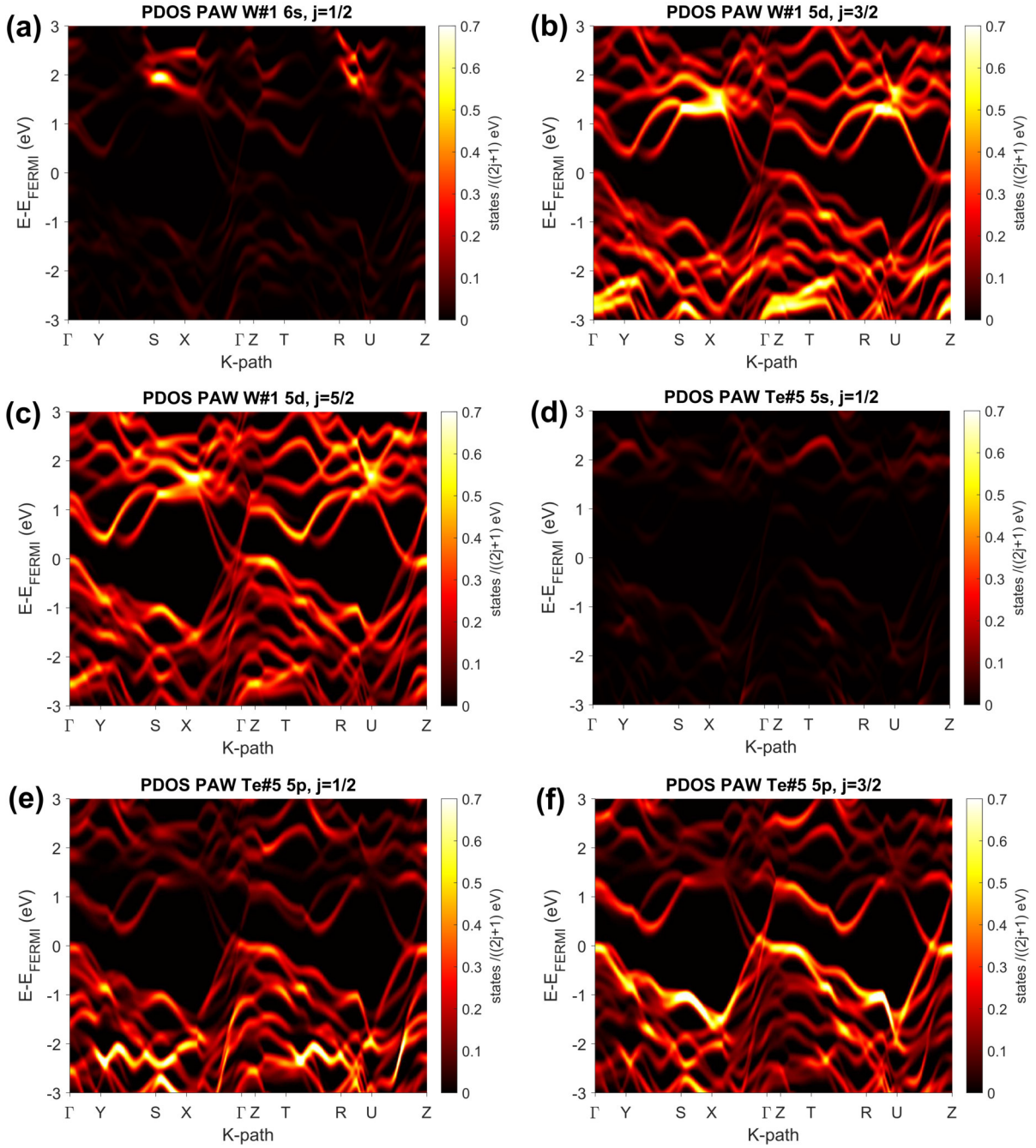

Figure 6.22. Part 1 - K-resolved PDOS along the same reciprocal space path used in Fig. 6.19(a) for the electronic band structure: atom W#1 (a) 6s, j=1/2 (b) 5d, j=3/2 (c) 5d, j=5/2; atom Te#5 (d) 5s, j=1/2 (e) 5p, j=1/2 (f) 5p, j=3/2 atom. See Fig 6.1(b) for reference. The results were obtained using (a-f) PAW pseudopotentials [213].

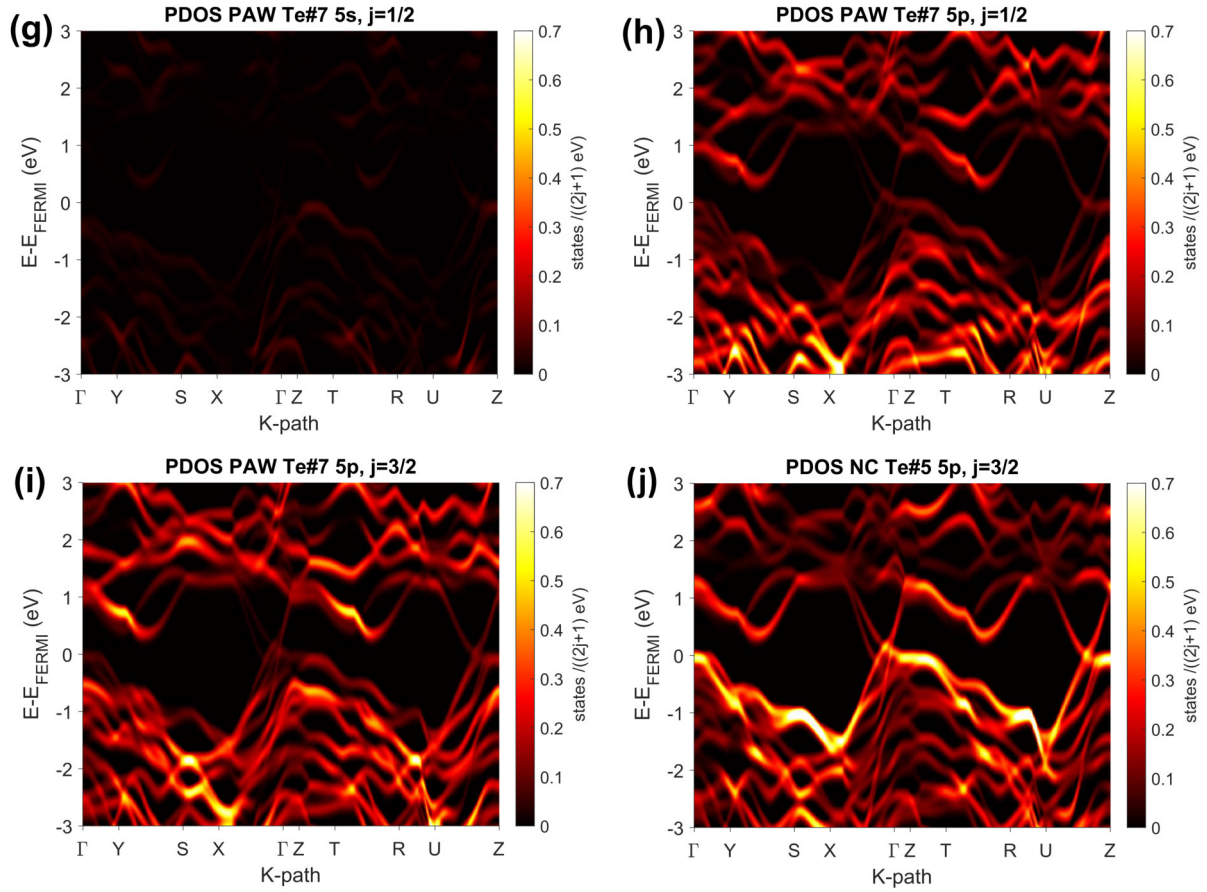

Figure 6.23. Part 2 - K-resolved PDOS along the same reciprocal space path used in Fig. 6.19(a) for the electronic band structure: atom Te#7 (g) 5s, j=1/2 (h) 5p, j=1/2 (i) 5p, j=3/2 atom (j) Te#5 5p, j=3/2. The results were obtained using (g-i) PAW and (j) NC pseudopotentials [213][212]. See Fig 6.1(b) for reference.

Note that to compare PDOS values between different k-points and energies, one has to take into account possible band degeneracies and the smearing of the energy levels [268], here equal to the one used for the electronic density derivation and DOS for consistency. Almost identical results were obtained using a norm-conserving (NC) [208] fully relativistic [211] pseudopotentials with the generalized gradient approximation (GGA) in the Perdew-Burke-Ernzerhof (PBE) parametrization for the exchange-correlation functional [210] chosen from the PseudoDojo database [212][247]. This is understood by comparing Figs. 6.22(f), 6.23(j).

6.5.4 Coherent phonon effects

The coherent phonon effects in WTe_2 have a direct impact on the optical properties of the material; we demonstrated that spectral dependence of their effects can be accurately reproduced through a displacive model starting from the relaxed equilibrium configuration using DFT (Chapter 5). From the time-resolved optical experiments reported in the previous section, we show that analogous characteristics are maintained at higher fluences around which the time-resolved x-ray measurements were acquired. Hence, we followed

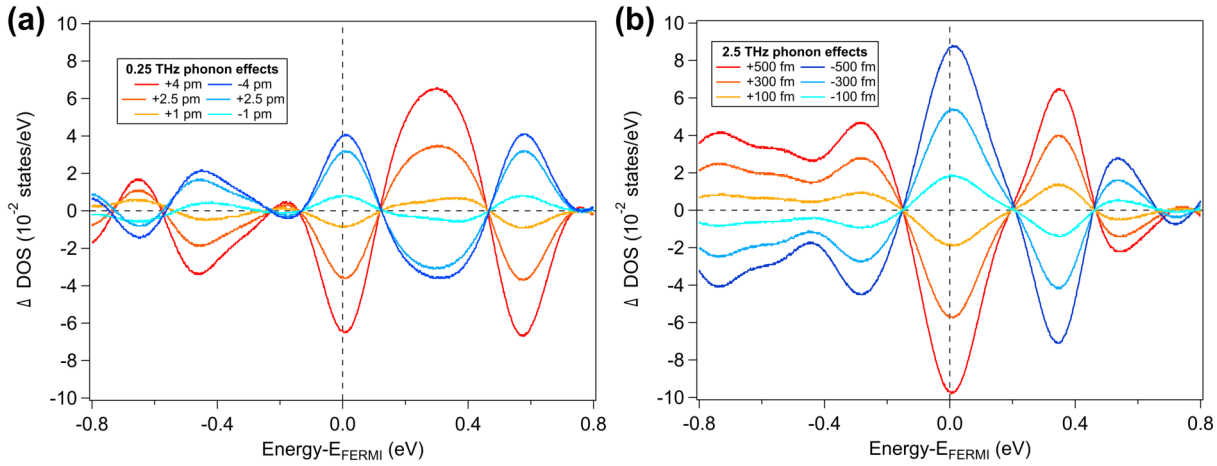

Figure 6.24. Variations of the DOS induced by displacements along the (a) 0.25 THz (y-shifts) (b) 2.5 THz (z-shifts) zone-center phonons.

a similar approach, including the previously neglected spin-orbit correction to study in detail the electronic structure modifications.

To obtain the zone-center phonon eigenvalues and eigenvectors, the dynamical matrix was calculated and diagonalized in a density functional perturbation theory (DFPT) [217] approach under the scalar relativistic approximation [211], a kinetic energy cutoff of 50 Rydberg for the wavefunctions and a 8×6×4 k-point mesh.

The phonon eigendisplacements for the zone-center A_1 modes are reported in Fig. 6.5 and ordered by increasing eigenvalue. Shifts along the x-axis are forbidden by the point group symmetry elements for such representation, forcing them to stay on the yz plane. In the following, we focus on the two most prominent modes, which we keep calling 0.25 and 2.5 THz for simplicity, as their experimental (Fig. 6.4) and simulated frequencies, albeit with some differences, are clearly distinct from those of the other A_1 modes.

In terms of Brillouin-zone-integrated properties, the two phonon modes lead to a different impact on the electronic density of states (Figs. 6.24(a),(b), see Fig. 6.19(e) for comparison). To avoid confusion, we report the shear mode displacements in terms of the average y-coordinate shift, while the 2.5 THz modifications are reported in terms of their tungsten z-shift, which is ∼2.44 times smaller than the maximum y-shift due to such mode. The DOS variations connected to the 2.5 THz phonon are larger compared to the corresponding values of the largest y-shifts among their atoms. Differently from the shear mode, the 2.5 THz phonon involves non-uniform y- and z-shifts, which perturb the in-layer covalent bonds between the atoms, varying their relative distances (see also Appendix D). As the displacements are increased, the effects become more asymmetric between + or - variations, which also suggests the failure of a symmetric potential picture, *e.g.* a harmonic oscillator.

Moreover, the k-resolved mapping of these effects shows that they result in distinct contributions and modifications to the energy levels. Figs. 6.25, 6.26 illustrate how the modes affect for increasingly high atomic atomic shifts, selected specific maxima and minima of the band structure which are relevant for the transport properties.

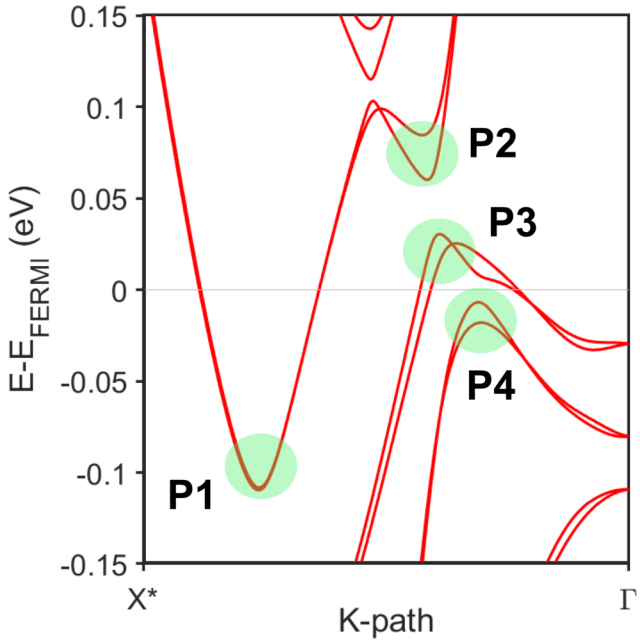

Figure 6.25. Band dispersion along X* (0.3 0 0) - Γ (0 0 0) (reciprocal lattice units) around the Fermi level. Selected interested regions are highlighted for the following analysis.

Displacing the structure along the phonon eigendisplacements leads to a quasi-symmetric 'oscillation' of the bands, which is not a simple rigid energy shift, but it also leads to a change in the band curvature. Around the regions of interest marked in Fig. 6.25, the bands along the $\mathbf{k_x}$ direction wiggle as shown in Fig. 6.26. However, while the band extremum remains close to the equilibrium position for the P1 region, this does not apply for most of the other investigated cases. This is relevant if one wants to obtain the band curvature in other k-paths passing through the extremum.

We express these variations in terms of the effective mass, which we define as [1].

$$[\mathbf{M}(\mathbf{k})^{-1}]_{ij} = \pm\frac{1}{\hbar^2}\frac{\partial^2\varepsilon(\mathbf{k})}{\partial k_i \partial k_j} = (m^*_{ij})^{-1} \tag{6.4}$$

where + and - are respectively used for electron-like and hole-like band respectively and $\varepsilon(\mathbf{k})$ is the energy-momentum dispersion relation. Each electronic dispersion was fitted using a 6th-order polynomial expression

$$\varepsilon(\boldsymbol{k}) = \sum_{q=0}^{6} a_q \boldsymbol{k}^q \tag{6.5}$$

around the extrema and the diagonal effective mass values were extracted as the curvature (second derivative) at the point where the first derivative is zero.

$$(m^*_{ii})^{-1} = \left.\frac{\partial^2\varepsilon(\boldsymbol{k})}{\partial {k_i}^2}\right|_{\boldsymbol{k}=\boldsymbol{k_0}}, \quad \boldsymbol{k_0} \,|\, \left.\frac{\partial\varepsilon(\boldsymbol{k})}{\partial k_i}\right|_{\boldsymbol{k}=\boldsymbol{k_0}} = 0 \tag{6.6}$$

In Table 6.1 we list the effective mass equilibrium values, while in Fig. 6.27 we report the variations due to the coherent phonon modes. We tag the different bands by a number which expresses their energy order.

The electron-like bands in P1 and P2 are oppositely affected by the two phonon modes in the examined shift ranges. In P1, where electron pocket has its minimum, the bands are almost unaffected by the shear mode, while they are uniformly modified by the 2.5 THz mode. In P2, their roles are almost inverted as the higher lying electron-like bands are mostly impacted by the slow mode. For the hole-like bands in P3 and P4, the effects on the band curvature in the depicted range are similar in magnitude albeit with an opposite sign.

The electronic dispersion along the $\mathbf{k_y}$ and $\mathbf{k_z}$ directions is generally much flatter than in $\mathbf{k_x}$ leading to higher effective masses around the examined k-points in such directions, limiting the electron/hole mobility [269][270].

At equilibrium (Fig. 6.28), m^*_{yy} assumes the following values: 3.55 and 3.46 m_o at P1 for bands 5 and 6; 2.09 and 2.23 m_o at P2 for bands 5 and 6; 0.62 m_o at P3 for band 4; 1.82 and 1.44 m_o at P4 for bands 1 and 2. For m^*_{zz} the dispersion is even more flat giving 26.60 and 16.26 m_o at P1 for bands 5 and 6 and 9.79 m_o at P3 for band 4.

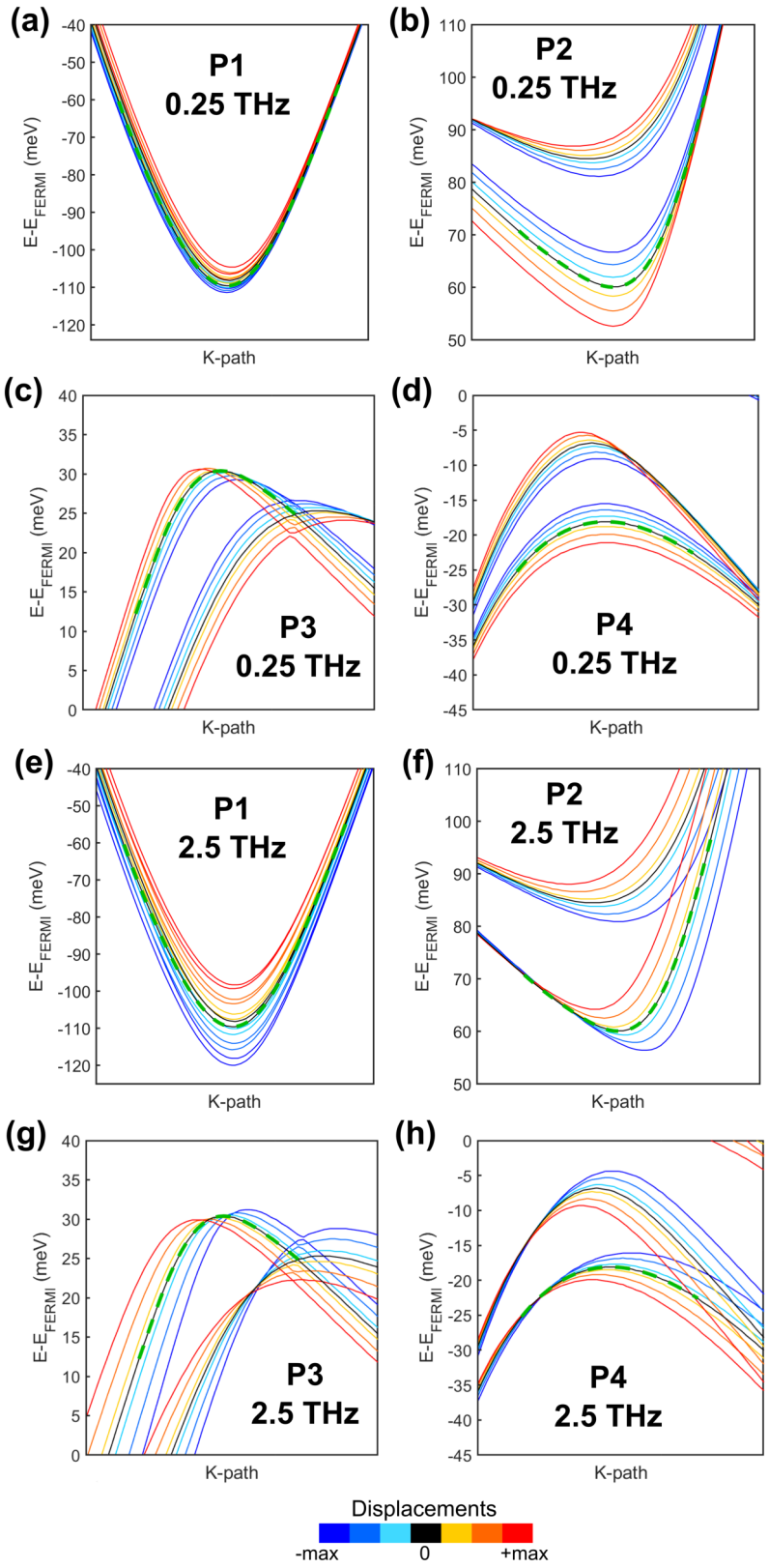

Figure 6.26. Band wigglings displacing the structure along the phonon eigendisplacements. Displacements are considered positive when they follow the same directions as in Fig. 6.5. Band dispersions along the $\mathbf{k_x}$ direction around the P1 (0.228 0 0), P2 (0.123 0 0), P3 (0.117 0 0), P4 (0.093 0 0) k points (reciprocal lattice units) for the (a)-(d) 0.25 THz and (e)-(h) 2.5 THz phonon effects. As an example, selected equilibrium bands are fitted: (a),(b),(e),(f) band 5 (c),(g) band 4 (d),(h) band 1. The various displacements correspond to the data points reported in Fig. 6.27.

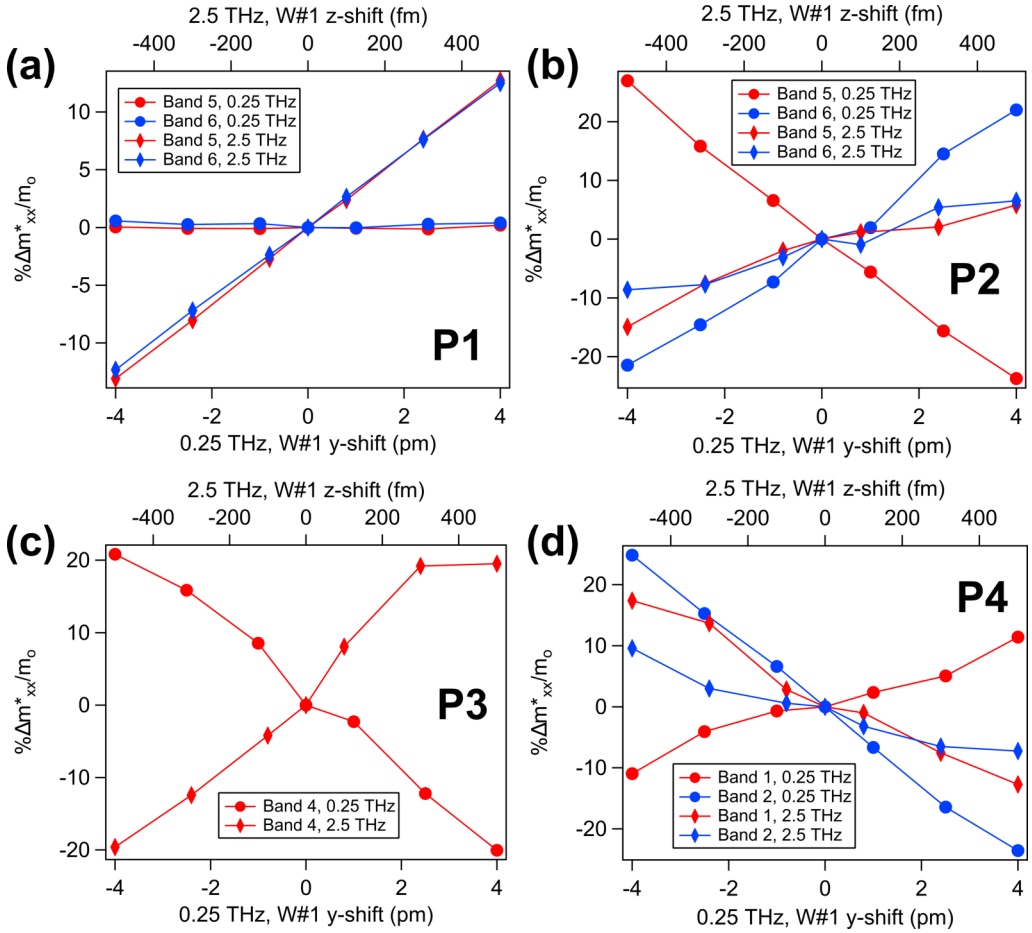

Figure 6.27. Band curvature variation along $\mathbf{k_x}$ showing the dependence on the phononic shifts around (a) P1 (0.228 0 0) (b) P2 (0.123 0 0) (c) P3 (0.117 0 0) (d) P4 (0.093 0 0) (reciprocal lattice units).

Region	P1	P2	P3	P4
Effective mass m^*_{xx}/m_o	0.531 (Band 5) 0.527 (Band 6)	0.384 (Band 5) 1.049 (Band 6)	0.433 (Band 4) \	1.653 (Band 1) 0.774 (Band 2)

Table 6.1: Equilibrium effective masses m^*_{xx} at the band extrema in the regions highlighted in Fig. 6.25.

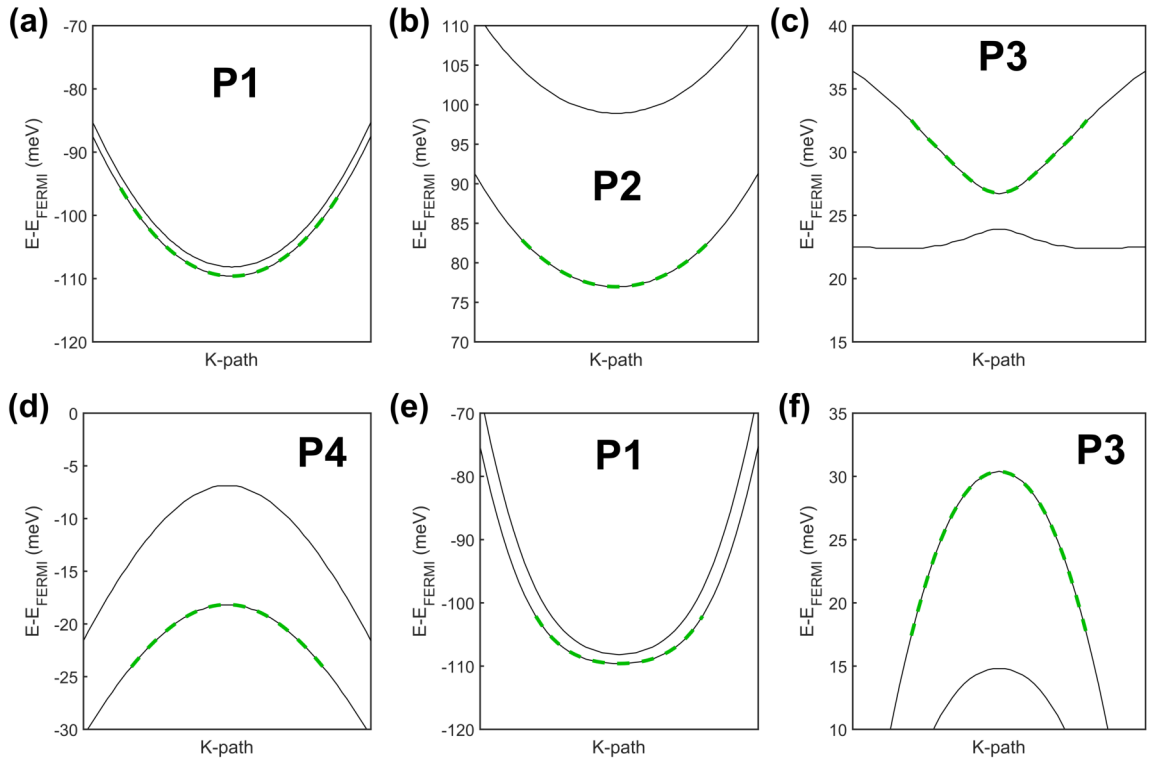

Figure 6.28. Band dispersions along $\mathbf{k_y}$ around (a) P1 (0.228 0 0) (b) P2 (0.123 0 0) (c) P3 (0.117 0 0) (d) P4 (0.093 0 0) and $\mathbf{k_z}$ around (e) P1 (0.228 0 0) (f) P3 (0.117 0 0) (reciprocal lattice units).

6.6 Discussion

6.6.1 Displacive model

The x-ray diffraction dynamics was fitted using the most general version of displacive excitation of coherent phonons (DECP) model [154] (section 3.1.1), where the amplitude of each phonon mode is proportional to the time coordinate:

$$Q(t) = \frac{\omega_0^2 k \rho \varepsilon_{pump}}{\omega_0^2 + \beta^2 - 2\gamma\beta} \int_{-\infty}^{\infty} g(t-\tau)[e^{-\beta\tau} + e^{-\gamma\tau}(cos(\Omega\tau) - \frac{\beta'}{\Omega} sin(\Omega\tau))]d\tau \qquad (6.7)$$

where $\omega_0 = 2\pi f_0$ is the angular frequency, k is a proportionality constant, ρ and β are constants related to the rate of carrier generation and return to the ground state respectively, ε_{pump} is the pump fluence, γ is the damping factor, $\Omega = \sqrt{\omega_0^2 - \gamma^2}$ and $\beta' = \beta - \gamma$.

The coordinate $Q(t)$ can be regarded as a multiplicative factor for the phonon eigendisplacements obtained through DFPT and can be separated into two types of contributions within the integrand (Eq. (6.7)). The first one is an exponentially-decaying term related to the electron relaxation which gives the initial offset to the $\Delta I/I$ profile, while the second one is composed by oscillatory contributions giving the periodic modulations. As the system is brought out-of-equilibrium, the excitation of the electrons from their ground state configuration drives the system into a new transient configuration which involves a reorganization of the interatomic distances. The diffraction intensity is very sensitive to

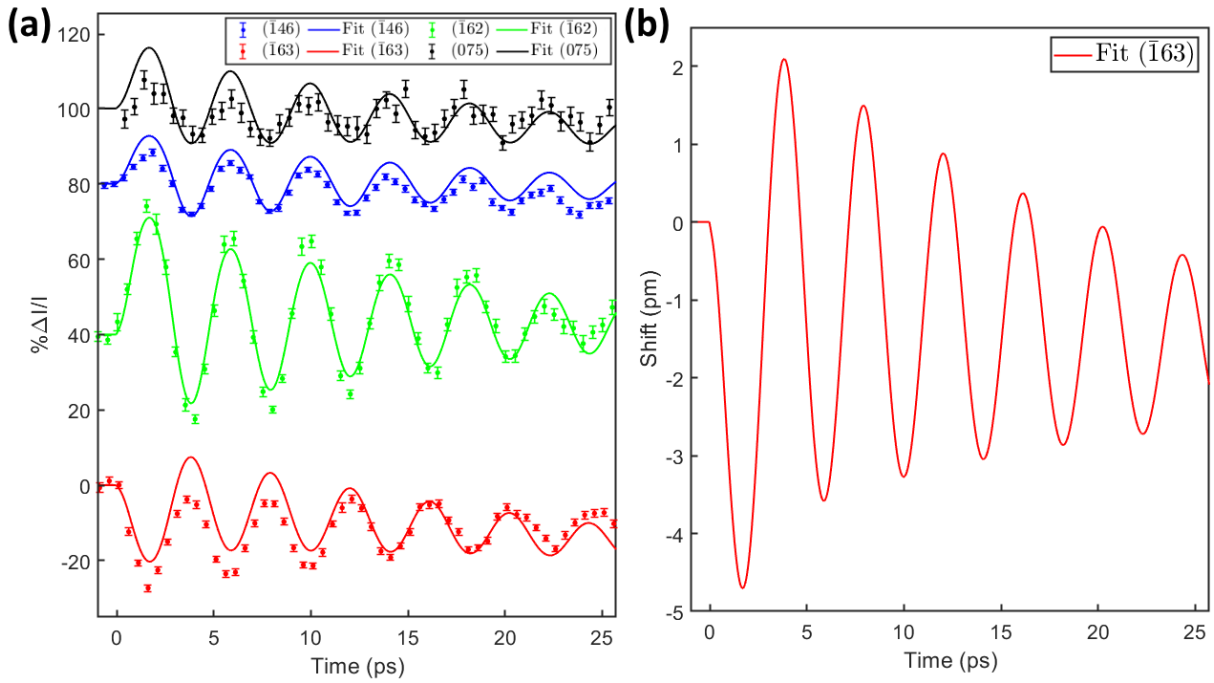

Figure 6.29. DECP model fitting in the intermediate time-range. (a) Comparison among experimental data and their simultaneous global fit. The upper profiles and fit curves were vertically shifted for clarity. (b) y-shift of the W#1 position extracted from the results shown in panel (a).

the atomic configuration and its accurate description based on computer simulations can rapidly become very challenging as the number of atoms involved in the unit cell grows.

Nevertheless, in the neighborhood of a few picometers of the actual atomic coordinates along the shear mode, the ΔI/I oscillation due to the phonon modes keeps an almost constant value (Fig. 6.31, the coordinate along the shear mode is indicated by the x axis).

The DECP model [154] in its most general form can be used to fit the x-ray data in a nonequilibrium configuration of the system. While extensions are possible, its use in describing the transient x-ray intensity in the form (6.7) fails when lattice thermalization and expansion occur, as well as when the transient equilibrium state is markedly different from the initial one, *e.g.* at very high fluences. It is thus only appropriate close to time-zero when the described phenomena have not significantly perturbed the initial configuration yet.

To take into account the effect of thermalization, we implemented a three temperature model using an isotropic average, in first approximation, Debye-Waller factor through a system of three coupled equations as described in [150] to which we added a slow thermal drain to take into account the $\sim$ 700 ps relaxation timescale reported in Chapter 5. The isotropic average Debye-Waller factor can be written as [150][157]

$$W(G_{hkl}) = \frac{1}{2} G_{hkl}^2 \langle u^2 \rangle \tag{6.8}$$

where G_{hkl} is the modulus of the reciprocal lattice vector for (hkl) reflection under consideration and $\langle u^2 \rangle$ is the isotropic average displacement

$$\langle u^2 \rangle = \frac{9\hbar^2 T_l}{M k_B \Theta_D^2} \tag{6.9}$$

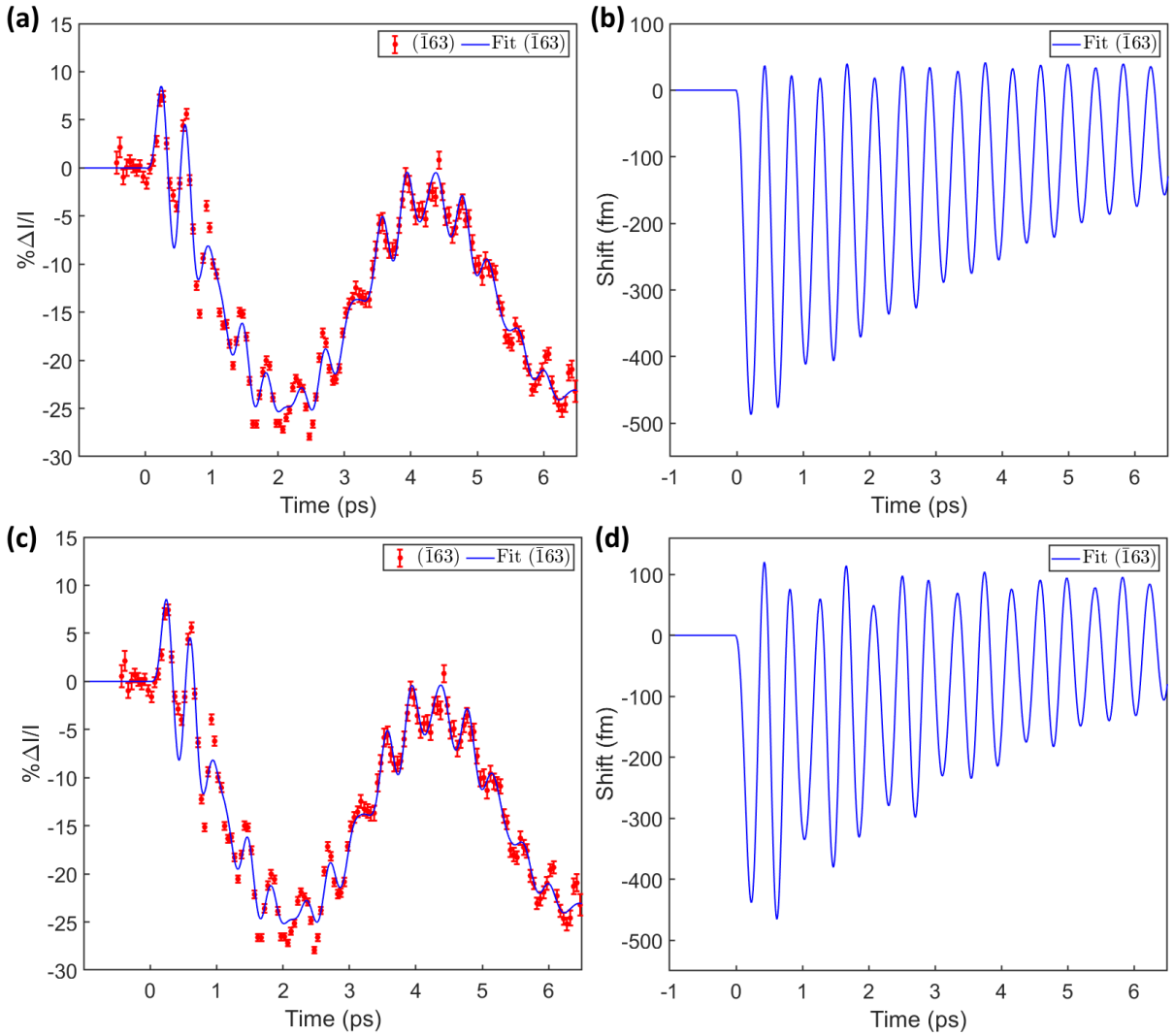

Figure 6.30. DECP model fitting in the initial time-range, reported in Fig. 6.4. (a) Comparison among experimental and a fit of the curve using as third phonon mode (d) from Fig. 6.5; (b) z-shift of the W#1 position extracted from the results shown in panel (a); (c) Comparison among experimental and a fit of the curve using as third phonon mode (e) from Fig. 6.5; (d) z-shift of the W#1 position extracted from the results shown in panel (c).

where T_l is the lattice, M is the unit cell mass, k_B is the Boltzmann constant and Θ_D is the Debye temperature.

The Debye-Waller factor is then implemented in the formula for the diffracted intensity as

$$I(G_{hkl}) = I_0(G_{hkl})exp(-2W(G_{hkl})) \tag{6.10}$$

where $I_0(G_{hkl})$ is the diffracted intensity in the $T_l \to 0$ K limit. The system of three coupled equations for the thermalization is [150]

$$2C_e\frac{\partial T_e}{\partial t} = \frac{2(1-R)}{l_{dep}}I_L(t) - g(T_e - T_h)$$

$$\alpha C_l\frac{\partial T_h}{\partial t} = g(T_e - T_h) - g_c(T_h - T_c)$$

$$(1-\alpha)C_l\frac{\partial T_c}{\partial t} = g_c(T_h - T_c) - g_r(T_c - T_r) \tag{6.11}$$

where

- C_e, C_l are the electronic and lattice thermal capacities;
- T_e, T_h, T_c, T_r=295 K are the electronic, 'hot' lattice, 'cold' lattice and room temperatures;
- R is the sample reflectivity at the pump wavelength;
- l_{dep} is the pump penetration depth;
- I_L is the pump intensity;
- α is the fraction of phonon modes efficiently-coupled to the electron system ('hot' lattice);
- g, g_c, g_r are the coupling parameters between electrons and 'hot' lattice, 'hot' and 'cold' lattices and 'cold' lattice and sample mount respectively.

Finally the effective lattice temperature is given by

$$T_l = \alpha T_h + (1-\alpha)T_c \tag{6.12}$$

While the Debye temperature, thermal capacities and penetration depth data are available in the literature [68][264](see also Appendix A), we treated the fraction of 'hot' phonons and couplings as fitting parameters. However, since the Debye-Waller factor reduces the diffracted intensity due to the thermal motion of the ions, it cannot take into account the increase of the integrated diffraction at long time-delays resolved for $(\bar{1}62)$ and (075). In WTe_2, the removal of electrons near the Fermi level is thought to be the driving mechanism triggering the shear mode, along whose coordinate the system evolves towards a monoclinic-1T'-like phase 1T'(*) [35][36][271]. We thus added the possibility for a gradual shift of the structure along the shear coordinate as proposed in [35][36], then the fit agreement becomes satisfying.

The results of the global fit are reported in Fig. 6.29 for intermediate time delays. The results are $\beta_{0.25THz}$=(1.3±0.5) ps, $f_{0.25THz}$=(0.2342±0.0008) THz and $\gamma_{0.25THz}$=(22±3) ps. The shear mode displacement is initially $d_{0.25THz}$ ∼3.4 pm (taken as a peak-to-peak variation over the first period), while the gradual shift of the structure along the shear coordinate (y-axis) is ∼1.7 pm at the end of the examined range, during which the sample temperature ('cold phonons') has risen to ∼450 K at 3.2 mJ/cm^2 absorbed fluence. As shown in Fig. 6.29(a), just after time-zero there is a discrepancy between the $(\bar{1}63)$ peak and the global fit, which may be due to differences between our relaxed configuration and the experimental atomic positions as well as to a fluence anisotropy due to the different penetration depth calculated from the data in [68] (Appendix A), which we estimate to be give a 6% variation around the presented value.

We considered now the fine-sampled delay interval after time-zero for $(\bar{1}63)$ (Fig. 6.4) and we focus on the higher frequency modes (Fig. 6.30). In order to fit the single profile, we allowed the shear mode $\beta_{0.25THz}$ to change, in contrast to the other parameters reported above. This was required to obtain a reliable fit of the higher frequency modes due to the presence of the initial discrepancy between data and global fit (Fig. 6.29(a)). Nonetheless,

as shown in Fig. 6.31, the phononic oscillations for $(\bar{1}63)$ remained quasi-constant in few-picometer range along the shear coordinate. While the assignment of the two lower A_1 modes was straightforward and supported by the complementary optical studies as well as from Chapter 5, the assignment of the third mode at ∼3.4 THz was more laborious. Together with the fitting results, we exploited Figs. 6.6, 6.31. From Fig. 6.5, we note that the phonons (c)-(f) are the ones which are the closest in frequency to the third peak shown in Fig. 6.4(c).

As shown in the experimental data in Fig. 6.6(a) and, the most sensitive to the higher frequency modes among the $(\bar{1}46)$, $(\bar{1}62)$ and $(\bar{1}63)$ Bragg peaks is the last one. Therefore, one expect the phonons (d) and (e) to be responsible for the most prominent effects at such frequency. This is motivated by the fact that, as shown in Fig. 6.31, the ratio amongst the phononic ΔI/I, there expressed as a peak-to-peak variation induced by shifts in opposite directions along the phononic coordinates, shows a preponderant effect for $(\bar{1}63)$. This is also supported by the fitting, where the phononic displacements are linearly combined, to study the evolution of the system through the DECP model. Considering the first two modes and one of the four possible choices for the third mode, we obtain that only the two modes (d) or (e) give an appreciable improvement of the fit curve. Choosing one of the other two possibilities, (c) or (f), no real change from a two-phonon model, using just (a) and (b), is observed. However, these two modes, (d) and (e), appear indistinguishable among the examined peaks, thus it is not possible to determine which of the two contributes more or even to separate them in a possible four-phonon model. Nonetheless, their separation is in principle possible measuring additional peaks in which their contribution can be clearly resolved.

Regarding the last peak around 6.2 THz in Fig. 6.4(c), with similar considerations we would attribute it to the (g) phonon in Figs. 6.5, 6.31. Unfortunately, due to its low contribution in the acquired data, it does not give clear-cut effects as the other two. For this reason, when left free, the fitting procedure tries to use it as a way to introduce an initial shift of the structure (through a very small β) to better fit the data rather than a contribution in the oscillatory motion. The values for the 2.5 THz phonon modes obtained from the second examined range are then $\beta_{2.5THz}$=(6.4±1.6) ps, $f_{2.5THz}$=(2.404±0.005) THz and $\gamma_{2.5THz}$=(6.5±1.5) ps. For atom W#1 (see Fig. 6.1(b)) the z-shift is ∼260 fm (peak-to-peak variation) from the equilibrium position.

Finally, we conclude this section with a remark about Fig. 6.7, where the fluence dependence for $(\bar{1}63)$ is reported. The initial shift of the ΔI/I curve with respect to the zero value in the first hundreds of femtoseconds, aside from the phonon modulations, is possibly linked to the struggle of the electronic system to thermalize due to the increasing deposited energy as discussed in section 6.4. From the point of view of the DECP model, when β is reduced (longer relaxation time for the associated electrons), the non-oscillating part of the $Q(t)$ expression (eq. 6.7) presents a longer decay time and, thus, longer discrepancy of the curve from ΔI/I=0 as average value. However, when multiple phonon modes are present, the fitting procedure cannot unambiguously associate this effect to one of the 2.5 or 3.4 THz modes, as it does not depend on the frequency of the mode, therefore the two separate β values would be as accurate as at the lowest fluence.

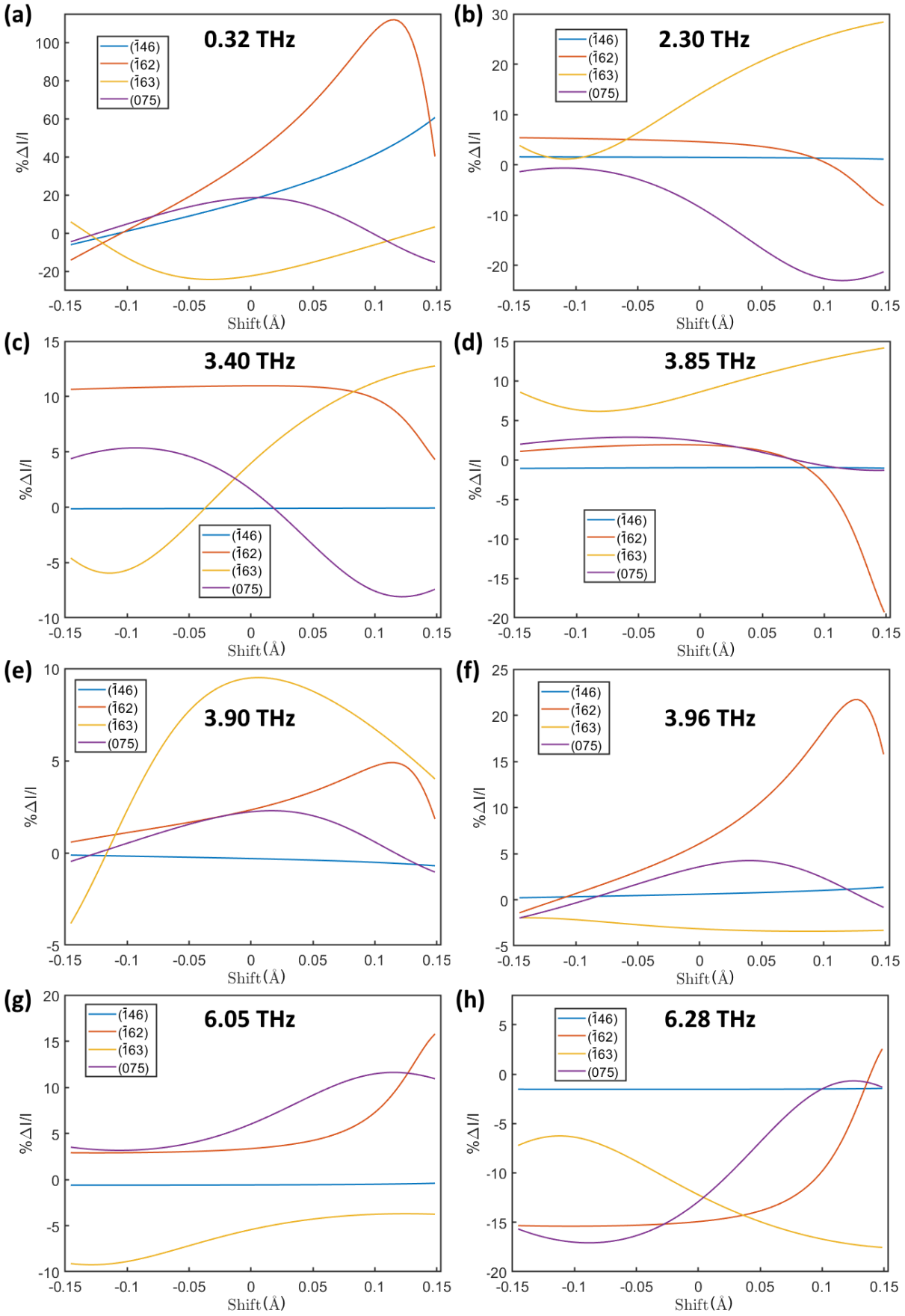

Figure 6.31. ΔI/I variation for the four examined peaks calculated as symmetric peak-to-peak phonon oscillations around the corresponding position along the shear coordinate (referred to the y-shift of W#1) represented by the horizontal axis, referred to the equilibrium configuration. The set displacements are (a) 2.5 pm along y (average) (b)-(h) 300 fm along z (maximum value among the atoms).

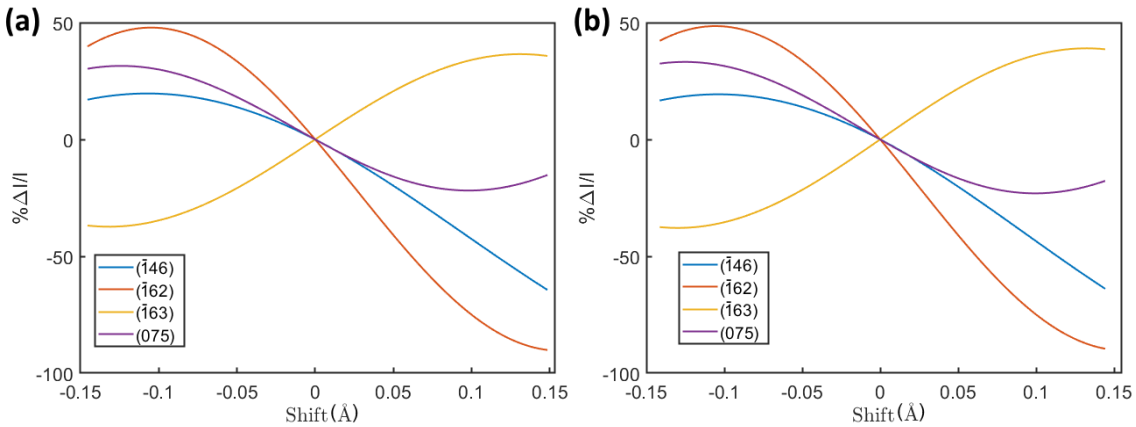

Figure 6.32. ΔI/I variation for the four examined peaks with respect to the equilibrium configuration (shift=0) for a shift along the shear mode coordinates, referred to W#1. (a) Using the DFPT output for the shear mode (b) Employing a uniform shift magnitude along y for all the atoms.

6.6.2 Long-delay evolution

As shown in the inset of Fig. 6.7, the contribution of the coherent optical modes faster than 0.25 THz becomes more prominent with respect to the 2.5 THz mode as fluence grows.

The different fluence dependence shown between the shear mode and the higher frequency modes may be caused by two factors. The first one is due to the change of the surrounding potential for the oscillation as the quasi-equilibrium average position changes along the shear mode. As shown in [36], the modification of the center of oscillation requires the shear displacement to reach its maximum which takes a few hundred femtoseconds, which is longer than the temporal region where we observe the highest increase for the fast modes in panel Fig. 6.7. The second reason is a geometrical argument: as shown in Fig. 6.32, as we move towards the 1T'(*) configuration [35], since negative y-shift of W#1 starting from our relaxed configuration lead to such geometry, the ΔI/I connected to the phononic shear oscillation becomes smaller when considering the same displacement amplitude after a few picometers. The two panels in Fig. 6.32 show that the small numerical differences from a completely uniform y shift when considering the shear mode from DFPT have a minor impact for our diffraction change considerations.

This geometrical evolution is also supported by the collected rocking curves (Fig. 6.9). The angular position of the Bragg peaks is determined by the cell parameters and their variation is compatible with an expansion of the unit cell due to the increase of the lattice temperature due to the deposited energy [264][272]. The temperature variation also leads to a reduction of the peak intensity due to a change of the Debye-Waller factor connected to the ionic thermal motion [150][151][157]. However, the thermal expansion is not just a simple renormalization of the atomic positions in complex unit cells such as WTe_2's, the overall intensity is also affected by the reorganization of the ions within the unit cell through the atomic form factors phase weighted combination (Eq. (6.3)). We tend to exclude penetration depth variability between the pump and probe beams during the experiment as the cause of the overall sign differences of the integrated ΔI at long delays (Fig. 6.9). In fact, we notice that the ratio between the ΔI/I oscillations, connected to

the phonon modes, among the measured Bragg peaks is compatible with the prediction of the model described in the previous section.

Since the ($\bar{1}62$) and (075) peaks are both sensitive to the antiphase displacement of the layers (Fig. 6.32) with an opposite sign ΔI/I contributions with respect to the ($\bar{1}63$) peak approaching the 1T'(*) state as the inversion symmetry is obtained around ∼-8 pm comparing the atomic positions, we interpret the almost stable intensity value of (075) and small increase of ($\bar{1}62$) as the combination between the increased thermal motion and a quasi-equilibrium distortion of the lattice with similar characteristics to the shift studied in Fig. 6.32. This modification is also supported by time-dependent density functional theory - molecular dynamics (TDDFT-MD) simulations evolution of the out-of-equilibrium structure [36] and its behavior is compatible with the change of the structure towards the 1T'(*) structure proposed in [35], *i.e.* towards a centrosymmetric non-equilibrium phase.

6.6.3 Role of the effective mass

The effective mass is a crucial parameter for various transport properties. In particular, for WTe_2, it directly enters in the formula for the carrier mobility using a deformation potential based model [78] as $\mu^{bulk} \propto (m^*)^{-5/2}$. Due to the -5/2 exponent, even smaller changes in the effective mass would have a large impact on the carrier mobility, which is a fundamental parameter for the material large and non-saturating magnetoresistance [65]. In case of perfect electron and hole carrier compensation, the magnetoresistance is such that $MR = \mu_e^{bulk}\mu_h^{bulk}B^2$, where 'e' and 'h' refer to the electron and hole species and B is the magnetic field amplitude. It has been experimentally and theoretically shown that strain can directly impact the electronic band structure and vary the magnetoresistance of the material (Chapter 5 and [77]). This, together with temperature and carrier doping [13][81], suggests that the fast modification of the band curvature and, thus, effective mass, could be employed to build a modulator of the magnetoresistance in the material across the GHz and THz frequencies. As the Fermi velocity was predicted to be ∼2· 10^5 m/s [87], the carriers in the system are expected to travel for several tens of nanometers experiencing a similar effective mass while the coherent phonon oscillations are affecting the system, provided that the sample quality and excitation lead to an adequate coherence for the collective modes.

Thanks to their distinct fluence dependence, it is possible to select their amplitude ratio and thus effects on the electronic band structure, although this also impacts their damping time, which is still quite long, especially for the shear mode. In particular, the long survival of the coherent phonon modes can be exploited to set away from the main carrier relaxation peak (Fig. 6.11(a)), which involves incoherent carrier-carrier and carrier-phonon scattering after which the carriers enter a quasi-equilibrium state.

Furthermore, as it was reported in multiple works [81][88], the material presents a very high magnetoresistance even down to the thickness of the intensity penetration depth at 800 nm in WTe_2, at ∼30 nanometers (see Appendix A), which would ensure a uniform excitation of the system by the pump pulse. The thickness limitation could be lifted further by employing a lower photon energy pump which was shown to be effective [35][36] as well in order to drive the shear mode, albeit above the plasma edge frequency in order to avoid the high reflection from the sample.

Its exfoliability and growth control make it a promising candidate for implementation in nanometric two-dimensional devices, also within more complex heterostructures to exploit its functionalities.

6.7 Conclusions

We examined the structural response of WTe_2 to a 1.55 eV light excitation with particular focus on its coherent phonon modes. This collective motion has a significant impact on the electronic properties of the material leading to measurable changes in the optical properties and energy levels. In particular, the electronic band structure is perturbed in such a way that eigenvalues are subjected to a non-uniform change which modifies the band curvature for the bands involved in the electrical transport through a variation in the effective masses. Based on previous experimental and theoretical results, the impact of the coherent phonon oscillations should lead to consequences for various transport properties such as electrical transport through a fast modification of its extremely high magnetoresistance [65][78] and thermoelectric performance [273] which are of particular interest for low effective mass systems. Such variations could be implemented as modulators, simple function generators and test devices for high frequency application which are expected to become relevant for fast big data transfer and telecommunications [274].

Finally, as a comparison, we remind that the displacements obtained in Chapter 5 at an absorbed fluence of $\sim$0.23 mJ/cm^2 were $\sim$350 fm for the shear mode motion along the y axis and $\sim$40 fm for the z-shift of the tungsten atoms. While the relation between fluence and phonon amplitude is initially linear (see Chapter 5, results section), between the $\sim$0.23 mJ/cm^2 and $\sim$0.71 mJ/cm^2 fluences, the factor is only $\sim$2. We thus would expect a value close, but smaller due to a possible saturation of the effects, when extrapolating this last relation to $\sim$3.2 mJ/cm^2. In fact one obtains $\sim$3.2 pm for the shear mode motion along the y axis and $\sim$370 fm for the z-shift of the tungsten atoms, which are in reasonable agreement with the $\sim$3.4 pm value for the shear mode motion along the y axis and $\sim$260 fm for the z-shift of the tungsten atoms obtained from the x-ray diffraction experiment. Moreover, we remind that the shear mode amplitude was obtained as a simultaneous fit of multiple Bragg peaks, making it a more reliable representation of the behavior at $\sim$3.2 mJ/cm^2, whereas some small correlation between the parameters of the 2.4 and 3.4 THz modes may affect the estimate of the amplitude of the second-most prominent mode having only a single profile to analyze an extended time-window.

CHAPTER 7

Two-dimensional terahertz experiments on Weyl semimetals

7.1 Introduction

Materials with small Fermi surfaces are often associated with a small number of carriers and a semimetallic character. Examples are compounds displaying double-cone dispersions close to the Fermi level. Tantalum arsenide (TaAs) and tungsten ditelluride (WTe_2) were recognized as Weyl semimetals [4][5][6], although with distinct Fermi surfaces. TaAs exhibits a quasi-point-like Fermi surface, while electron and hole pockets lead to multiple pockets in the Fermi surface of WTe_2 [13][103].

The use of broadband THz pulses allows to monitor simultaneously a wide range of frequencies which help to recognize and quantify the characteristic electronic and vibrational resonances of the system under investigation. Sampling the electric field after the interaction with the sample through time-domain spectroscopy allows to analyze the response in both the time and frequency domains giving complementary information to understand the phenomena.

Measurements can be performed through time-domain spectroscopy (TDS) at equilibrium conditions or through pump-probe schemes to examine the effects of an excitation.

Depending on the characteristics of the eigenstates connected to unfilled bands and on the Fermi level, different carrier densities and favored scattering channels are present [275]. When excited by low-energy perturbations such as THz pulses, these properties can be transiently modified by coherent phononic motion and the generation and acceleration of carriers.

A time-dependent electric field accelerates the electrons in the material and may be responsible for a variety of peculiar effects, such as ballistic transport [200], impact ionization [276], intervalley scattering [277] and Zener tunneling [190][278]. Although they have different origins, they can all contribute in determining the response of the material.

Especially with high field amplitudes, these phenomena may lead to appreciable non-

linear effects of the optical properties with respect to the THz electric field amplitude. Typically, this is caused by the sensitivity of the carriers on the band structure curvature (*i.e.* different effective mass), changes in the quasi-free carrier density and electron-phonon interactions.

Two-dimensional terahertz spectroscopy (2D THz) gives the opportunity to study the response of the system to low photon-energy excitations through a mapping of the nonlinearities. These emerge by considering the response of the simultaneous application of two THz pulses, with separate polarization and amplitude characteristics, with respect to the sum of individual responses when they are applied singularly.

The experimental data and discussion are organized as follows. We first consider the response from the type-I Weyl semimetal TaAs and then analyze the results for the type-II Weyl semimetal WTe_2. For both we detect nonlinearities in the response in correspondence of the plasma edge, which we examine as a function of the temperature and impinging field amplitude.

In each section, the nonlinear signal is reported and characterized both in the time and frequency domains as a function of temperature and impinging THz field amplitude. The interpretation of the experimental results follows together with the comparison of the responses from the different materials.

7.2 Experimental details

The experiments on the Weyl semimetals were performed in a reflectivity configuration using a broadband 2D THz setup with air-biased coherent detection (ABCD) [183] (see Chapter 3).

7.2.1 Ti:sapphire laser system

The 2D THz setup relies on a Ti:sapphire amplifier which produces ∼100 fs, 800 nm pulses with 1 kHz repetition rate. Its main output is then divided and seeds two three-stage optical parametric amplifiers (OPAs), which in turn generate two near-infrared, ∼1.3 and 1.5 µm, beam with phase stability between them. Using the OPAs outputs, two THz beams are produced through different methods, *i.e.* optical rectification and plasma-based generation. The setup employs nitrogen-purged boxes to reduce the water-related THz absorption, taking the relative humidity below 2%.

7.2.2 ABCD-detection setup

The THz radiation is produced using two OPAs-generated infrared beam through two separate methods [200]: i) using an organic crystal (4-N,N-dimethylamino-4'-N'-methyl-stilbazolium 2,4,6-trimethylbenzenesulfonate, DSTMS) through optical rectification and ii) two-color plasma source. The setup allows alternatively reflection (Fig. 7.1) and transmission measurements, using parabolic mirrors and a Si beamsplitter to partially reflect the radiation towards the detection cell. Here the THz electric field is sampled with air-biased coherent detection (ABCD) [183] using a small fraction of one of the two OPA beams, which is delayed using a linear stage.

Although a cryostat is not present in this setup, it is possible to reduce the sample temperature using a cryojet (Oxford Instruments ®) employing a liquid nitrogen dewar

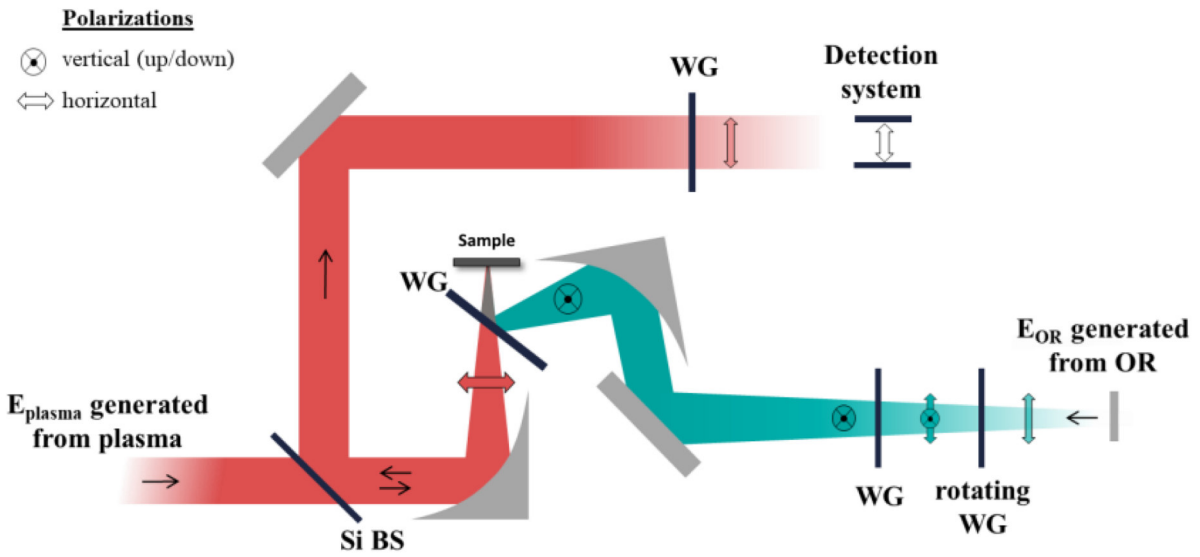

Figure 7.1. Scheme of the ABCD-detection setup employed for two-dimensional THz spectroscopy. The path for reflectivity experiments is shown, albeit transmission geometry is also available. Adapted from [200].

to blow cold nitrogen directly one the sample. The temperature variation was mapped before each experiment depending on the substrate used.

In this series of experiments, the two generated THz fields are named E_1, through optical rectification in DSTMS, and E_2, using the plasma source. While the second source allows to obtain a very broad spectral content (1-17 THz), it is limited to lower field amplitudes. In turn, the DSTMS-based generation can reach even values near 1 MV/cm, but its spectral content is negligible above 5 THz.

As described in the following sections, E_1 was employed as a pump pulse to drive the material out of equilibrium and E_2 to probe the induced changes. Moreover, both the examined samples exhibit plasma edges outside the frequency range attainable through the DSTMS, making the plasma source a key component to examine the field-induced modifications of the carrier density. In fact, these variations may change the plasma frequency of the system leading to nonlinearities around the plasma edge. These variation are monitored by considering the nonlinear signal [188], here defined as

$$E_{nl} = E_t - E_1 - E_2 + E_b \tag{7.1}$$

where E_t is the field recorded when two THz pulses are simultaneously applied to the sample and E_b is the background signal detected in absence of both the THz fields. We remark that the operation refers to the associated fields recorded after the sample when the corresponding THz pulses are applied. In 2D-THz spectroscopy, one measures matrices of data, thus we will refer to those datasets through their field label. In the following, when an estimate of an electric field is given, the value is meant as the maximum field amplitude of the pulse at the sample position.

In this chapter, the two THz pulses are linearly polarized with orthogonal polarizations: E_2 is polarized parallel to the optical table with the ABCD detection optimized for such direction. Conversely, The ABCD detection is nearly insensitive to E_1. However, this is not a problem for the experiments, whose objective is to investigate the effects of E_1 on the sample reflectivity of E_2.

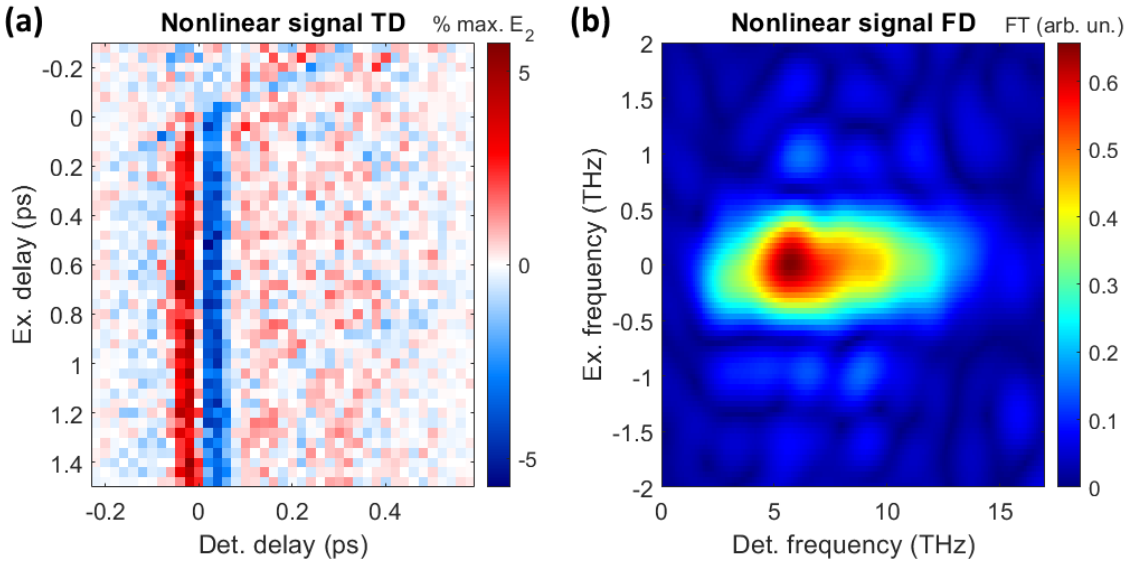

Figure 7.2. Nonlinear signal E_{nl} observed for TaAs. (a) Time domain. (b) Frequency domain with E_1 ∼570 kV/cm, E_2 ∼45 kV/cm and T=110 K.

In the following analysis, some of the plots contain error bars to express the uncertainty value. Unless otherwise stated, they are reported as ±σ, one standard deviation, supposing a normal distribution of the values; when they refer to a calculated quantity they are obtained by using the propagation formulas for independent quantities [279].

7.3 Results

7.3.1 TaAs

In Figs. 7.2, 7.3, the 2D maps for the nonlinear signal and E_2 are shown, both in the time and frequency domains, using (peak) field amplitudes equal to E_1=570 kV/cm and E_2=45 kV/cm at T=110 K. Both signals are normalized to the maximum of the absolute E_2 signal for each excitation delay, *i.e.* horizontal vector of data, and expressed as a percentage with respect to it. This adimensional value is employed to take into account possible minor fluctuations of the E_2 field amplitude during the experiment.

In these experiments, time-zero is more ill-defined compared to experiments where shorter near-infrared or x-ray pluses are employed (Chapters 5 and 6). In those cases, pump and probe are superimposed just for a few sampling points when examining excitation and relaxation phenomena of hundreds of femtoseconds or more. Exploiting THz pulses of a few hundred femtoseconds to study dynamics of the order of picoseconds implies that multiple sampling points are situated within the temporal region where the superposition takes place. This leads to a 'rise time' necessary to reach the plateau in the nonlinear signal when considering pump-probe effects like impact ionization. Nonetheless, the rise time is also influenced by the time it takes for the electrons to exchange energy among themselves, *e.g.* kinetic energy as in impact ionization after the initial acceleration of the primary electrons by the impinging field [280] or after interband excitations. Although this is not the main focus of the thesis, we will discuss this further in Appendix

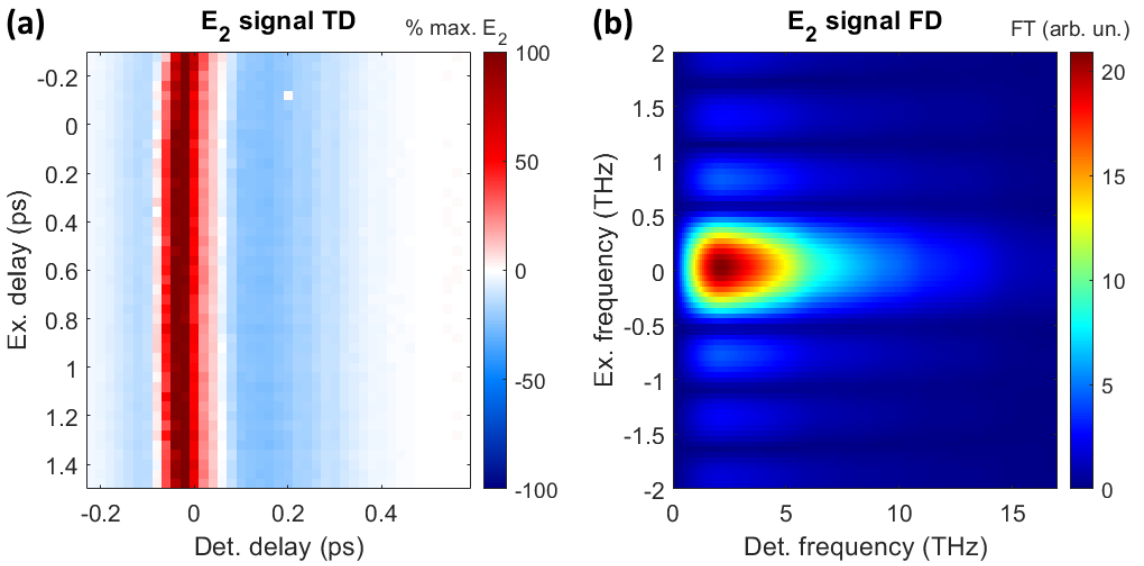

Figure 7.3. E_2 THz signal registered for TaAs. (a) Time domain. (b) Frequency domain with E_1 ∼570 kV/cm, E_2 ∼45 kV/cm and T=110 K.

G, where results from HgCdTe (Chapter 8) are presented alongside with a much more pronounced nonlinear signal.

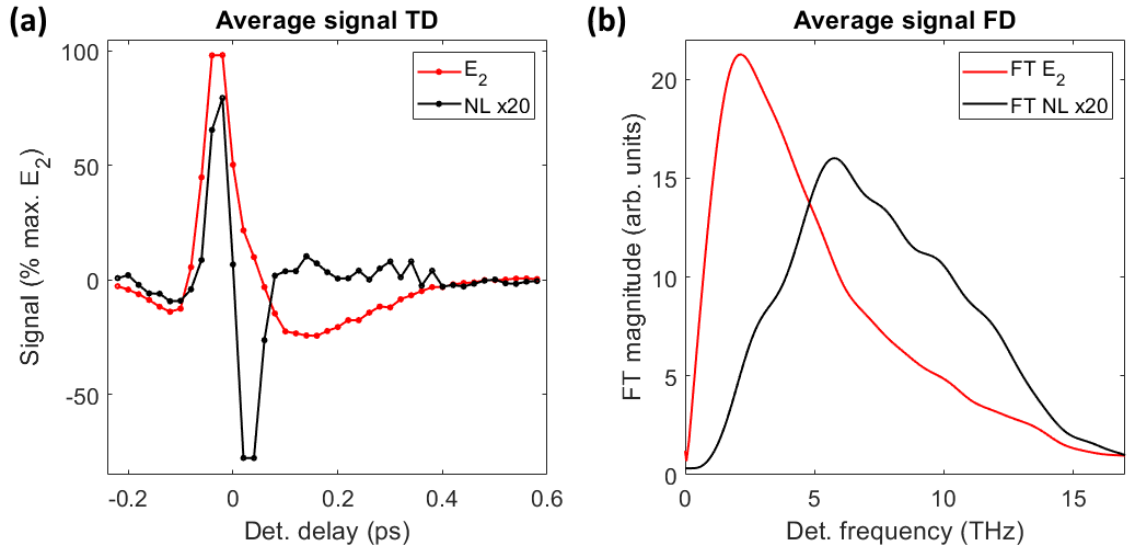

Figure 7.4. Comparison by taking the average profiles between the nonlinear signal E_{nl} and E_2 THz signal registered for TaAs. (a) Time domain (mean profiles 0.3-0.7 ps). (b) Fourier transform of the profiles reported in (a) taken with E_1 ∼570 kV/cm, E_2 ∼45 kV/cm and T=110 K.

Moreover, THz pulses generated by DSTMS and plasma present a very different temporal shape, thus making it hard to find a univocal definition for time-zero. We decide to adopt the conventional definition given by formula Eq. (3.6), where it can be viewed as an expectation value weighted by the field intensity.

Although the detection of the E_1 field, having vertical polarization, is not optimized, because of the anisotropy of the ABCD scheme, the positions of the maxima and minima of the THz wave are still measured and the Eq. (3.6) can be used for the time-zero determination.

In the time domain (Figs. 7.2(a), 7.3(a)), the nonlinear signal becomes prominent after the main peaks (one minimum and one maximum) of E_1 and gradually reaches a plateau in a few hundreds of femtoseconds. The fact that the nonlinear signal persists long after the superposition of the pulses is an indication that the phenomenon that varies the state of the material is provoked by E_1 and can be viewed as a pump-probe effect phenomena.

If this is the case, one would then expect to see similar effects by switching the roles of pump and probe between E_1 and E_2. This corresponds to the portion of the 2D maps where the excitation delay is negative. As one moves away from the superposition of the pulses at zero excitation delay towards negative times, the time separation between E_2 (now pump) and E_1 (now probe) grows. Because of the definition of the two time coordinates (see Chapter 3), this pump-probe signal would appear along the diagonal direction, on which the E_1 field is registered (see Fig. 3.3). Another way to understand this is by considering the 2D maps as a collection of TDS profiles in which the relative time between the pulses is gradually modified.

However, since the field amplitude ratio between E_1 and E_2 is large, only minor effects are expected when E_2 plays the role of the pump. Moreover, such features are expected to be reduced by the spectral range at which the nonlinear effects were detected, which for TaAs, as presented in the next paragraph, at the high-frequency edge of the range for DSTMS-generated THz beam. Finally, if the nonlinear signal comes the reflectivity of vertically-polarized E_1, as in the predicted pump-probe effect, its detection is not optimized in the ABCD scheme. These reasons motivate its absence in the Fig. 7.2(a) map.

In Fig. 7.4(a), a comparison between the temporal shape of E_2 and E_{nl} is shown. Since a very high E_1 field amplitude is required to induce a nonlinear response, we would exclude that nonlinear effects provoked by the E_2 field ($E_1 >> E_2$) in its first hundreds femtoseconds, coming *e.g.* from carrier multiplication effects, would be strong enough to lead to a self-phase modulation for the later portions of the pulse [281]. Therefore, we mainly attribute the difference between the temporal shapes of E_2 and E_{nl} to a non-uniform frequency-dependent change of the dielectric properties of the sample after E_1 is applied, varying the relative spectral content of the reflected E_2 pulse. The spectral shape of the nonlinear signal E_{nl} is then determined by the probed frequencies that are affected the most.

As expected, in the frequency domain (Figs. 7.2(b), 7.3(b)), E_2 and E_{nl} exhibit two very different spectral signatures. While both are centered around the excitation frequency f_{ex}=0 THz, their peaks are located around f_{det}∼2 THz and f_{det}∼6 THz respectively. Moreover, as highlighted by Fig. 7.4(b), the spectral dispersion is distinct. Starting from lower frequencies, the plasma-generated E_2 rapidly grows, peaks at f_{det}∼2 THz and then decreases more gradually with a quasi-exponential tail. Differently, E_{nl} exhibits a less peaked structure, where the rise and decrease of the signal centered at f_{det}∼6 THz show a similar steepness in the probed frequency range. The reported Fourier transform results were smoothened through zero-padding, *i.e.* adding null matrix elements along the directions where both E_2 and E_{nl} decrease to the noise level by the end of the window. We use it only as a graphical aid, while the quantitative results (see below) for the frequency domain quantities and their uncertainties, are calculated only from the measured

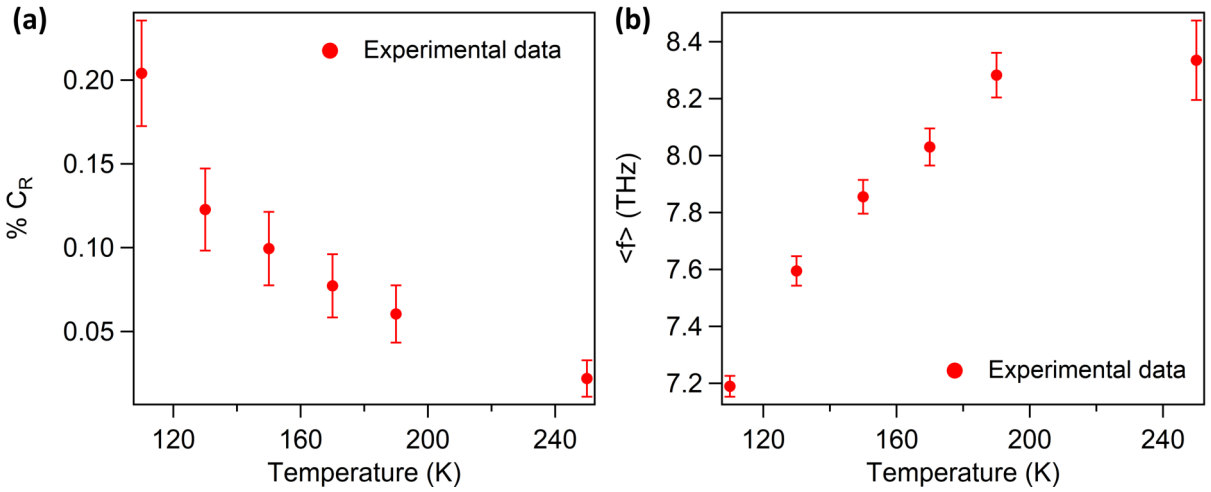

Figure 7.5. Temperature dependence of (a) C_R and $\langle f \rangle$ for TaAs.

databases, without zero-padding.

Keeping the sample under the same impinging field conditions, the overall amplitude of E_{nl} decreases as the temperature increases from T=110 K. At the same time, the peak position of E_{nl} shifts towards higher frequencies. In order to quantify these variations, we calculate the following parameters:

$$C_R = \frac{\int_{-\infty}^{+\infty} |E_{nl}(t)|^2 dt}{\int_{-\infty}^{+\infty} |E_2(t)|^2 dt} \tag{7.2}$$

$$\langle f \rangle = \frac{\int_{-\infty}^{+\infty} |E_{nl}(\nu)|^2 \nu d\nu}{\int_{-\infty}^{+\infty} |E_{nl}(\nu)|^2 d\nu} \tag{7.3}$$

C_R is an adimensional parameter used to quantify the nonlinear signal, while $\langle f \rangle$ is the 'average' frequency of the nonlinearity weighted by the modulus square field of the registered signal in the frequency domain.

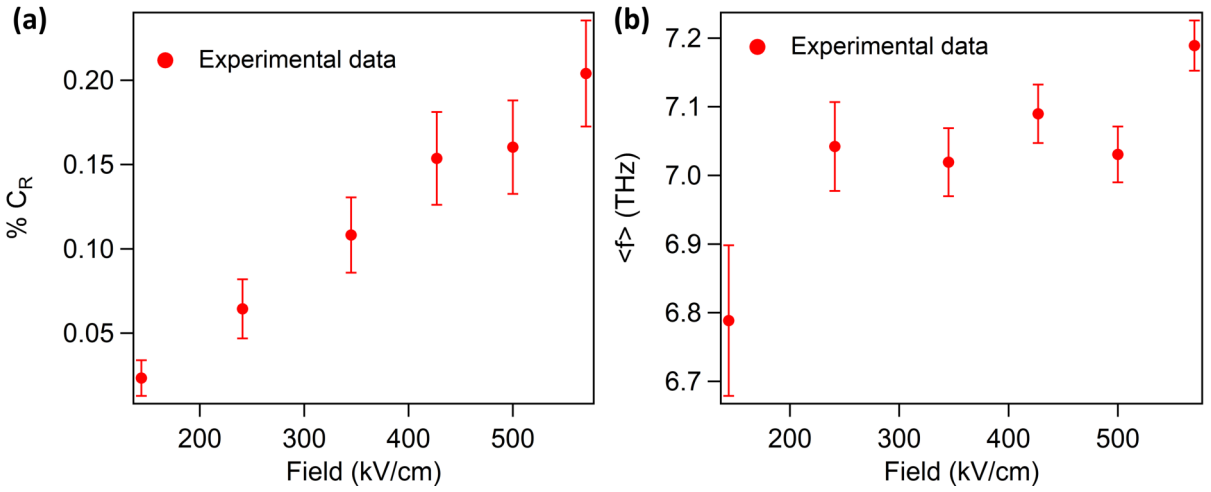

Figure 7.6. E_1 field dependence of (a) C_R and $\langle f \rangle$ for TaAs.

Since the data is taken over a limited and finitely-sampled temporal range, the extrema of (7.2) are approximated to the examined time window as the field goes to zero at its

edges (Fig. 7.4(a)) and the integration is performed through a trapezoidal discretization of the experimental profiles. The finite temporal sampling rate leads to a reduction of the maximum frequency for $\langle f \rangle$ to the Nyquist frequency, while its lower bound can be set to 0 due to the symmetry of the Fourier transform derived from real data. The limited temporal range also leads to a finite set of frequency terms and thus to analogous discretization of the integral in the frequency domain for (7.3).

In Fig. 7.5, the temperature dependence of such parameters is showcased.

In panel (a), C_R follows the previously described decrease of the amplitude of the nonlinear signal. The error intervals associated to the single data points were calculated as the standard deviation of the mean, starting from the individual field values registered for each point, from which the average values were reported. Subsequently, the errors were used, with the standard propagation formula for independent variables [279], to derive the error intervals for C_R and $\langle f \rangle$ by discretizing the integral expressions.

In panel (b), we see that $\langle f \rangle$ shifts toward higher values as the temperature rises.

Using a similar approach, it is possible to analyze the impact of an increasing E_1 field on the nonlinear signal. Fig. 7.6 shows this dependence in the 144-570 kV/cm range. Here C_R grows quasi-linearly with field amplitude. Differently, in this case $\langle f \rangle$ is left almost unchanged, although with a small increase.

A full gallery of the 2D maps in the various temperature and E_1 field amplitude conditions is provided in Appendix E.

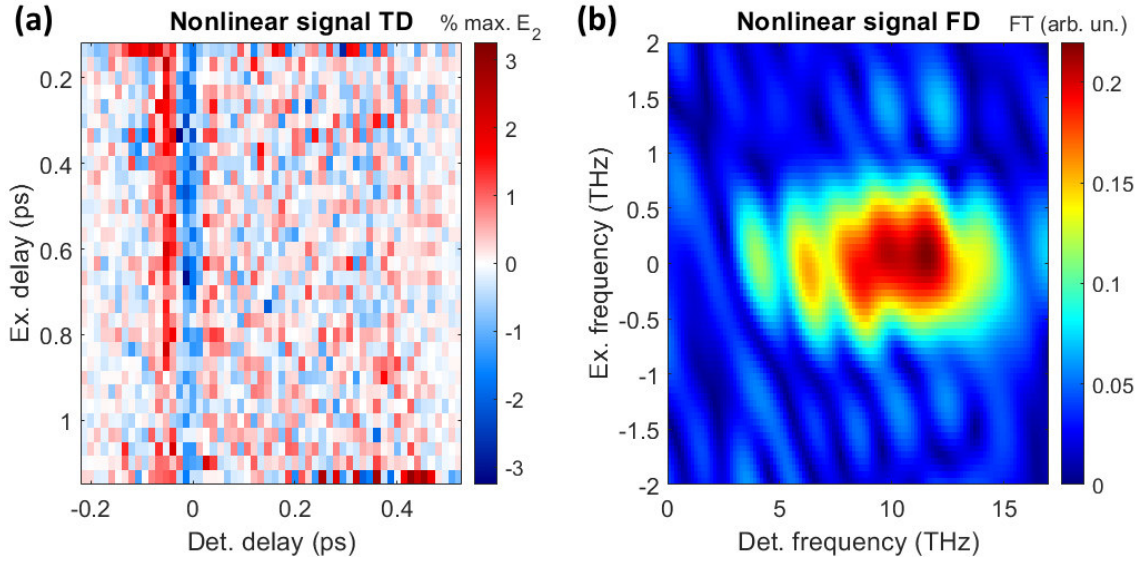

Figure 7.7. Nonlinear signal E_{nl} observed for WTe_2. (a) Time domain. (b) Frequency domain with E_1 ∼675 kV/cm, E_2 ∼55 kV/cm and T=110 K keeping E_2 || x.

7.3.2 WTe_2

For WTe_2, the mapping was performed for two orientations of E_2 with respect to the crystal axes, keeping E_1 perpendicular to E_2: E_2 || x, parallel to the tungsten chains direction and E_2 || y, normal to it. The two directions were selected by rotating the sample. The sample orientation can be readily inferred from the its shape, as it usually resembles a ribbon: the tungsten-chain direction is along the long side of the sample. Nevertheless, we also confirmed this through the Fourier transform infrared (FTIR) spectroscopy results reported in Appendix B.

Compared to TaAs, WTe_2 presents its plasma edge at higher frequencies leading the nonlinearities close to the edge of the spectrum of the plasma-generated E_2 as shown in Fig. 2.3 and in Appendix F, where the anisotropy of the optical properties, including the Drude-like contribution is evident. Moreover, the temperature change does not heavily modify the plasma edge position for both polarization directions, differently from TaAs (Fig. 2.2), while it clearly impacts the spectral width of the tilted region of the reflectivity curves (Fig. 2.3).

Probe || x

We report in Figs. 7.7, 7.8, the 2D maps for the nonlinear signal and E_2 respectively, both in the time and frequency domains, using E_1=675 kV/cm, E_2=55 kV/cm and T=110 K.

In percentage, the observed nonlinear signal is weaker than the one observed for TaAs. In the time domain, they share similar characteristics even though differences can be spotted by looking at their phase correspondence with respect to the E_2 profile (Fig. 7.9(a)), which is an indication of a different spectral content. This clearly emerges in Fig. 7.7(b) and in the average profile shown in Fig. 7.9(b) where the nonlinear signal is centered at higher frequencies, around 12 THz.

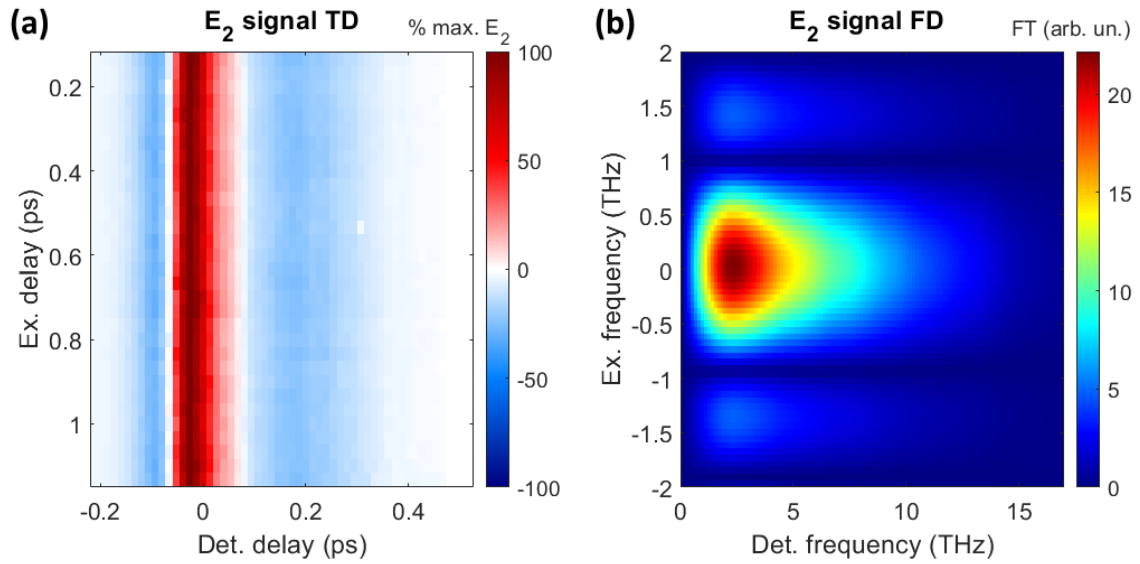

Figure 7.8. E_2 THz signal registered for WTe_2. (a) Time domain. (b) Frequency domain with E_1 ∼675 kV/cm, E_2 ∼55 kV/cm and T=110 K keeping $E_2 \parallel x$.

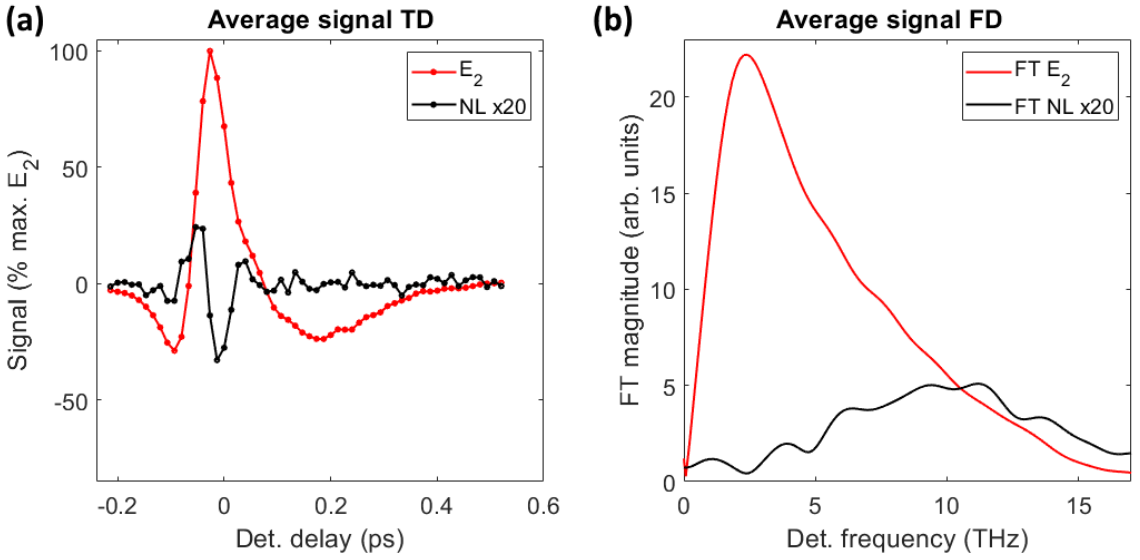

Figure 7.9. Comparison by taking the average profiles between the nonlinear signal E_{nl} and E_2 THz signal registered for WTe_2. (a) Time domain (mean profiles 0.3-0.7 ps). (b) Fourier transform of the profiles reported in (a) taken with E_1 ∼675 kV/cm, E_2 ∼55 kV/cm and T=110 K keeping $E_2 \parallel x$.

As previously done for TaAs, the analysis of the 2D maps is implemented using C_R and $\langle f \rangle$ (Eqs. (7.2), (7.3)).

As the E_1 field amplitude grows, C_R follows a quasi-linear increase (Fig. 7.10).

Moreover, when the plasma edge corresponds to a frequency situated at the limit of the E_2 spectral range, what one may observe is that the nonlinearity spectral content is situated mainly below the plasma edge. As discussed in the TaAs section, this is usually inferior to the change above the plasma edge. This is likely caused by the effect of the

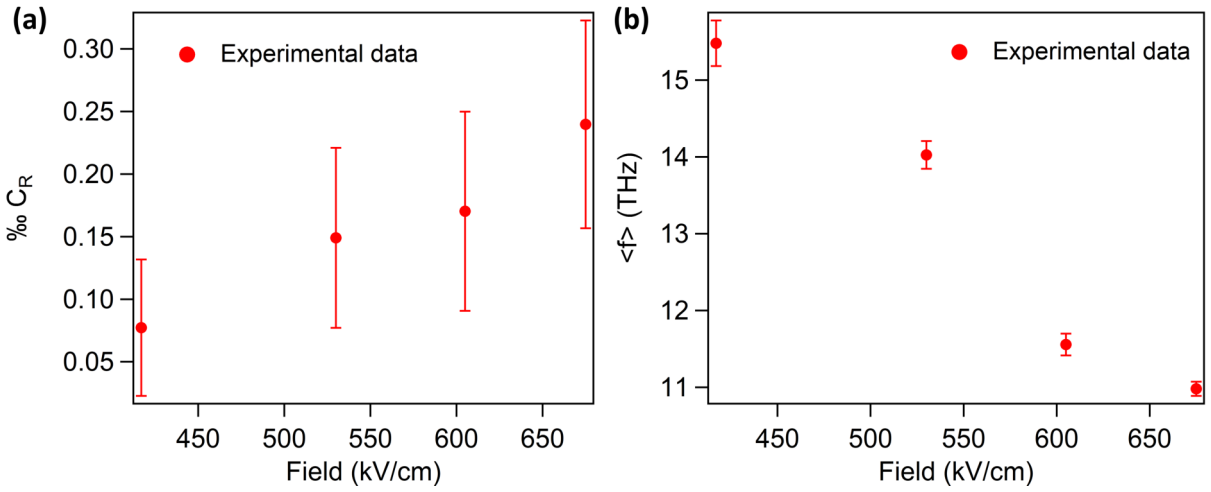

Figure 7.10. E_1 field dependence of (a) C_R and $\langle f \rangle$ for WTe_2 keeping E_2 || x.

low spectral content of E_2 above the plasma edge together with a lower reflectivity from the samble above the plasma edge, which limit its accurate determination. In fact, in this case, based on Fig. 2.3(a) and the data in Appendix F, the plasma edge is centered at 15 THz, which is at the very end of the E_2 spectral window. Moreover, this would explain why we observe a decrease in $\langle f \rangle$ for increasing E_1 fields, differently to what we observed for TaAs where the plasma edge is centered in the explored frequency range and a small increase was obtained.

A full gallery of the measured 2D maps can be found in Appendix F.

Probe || y

In Figs. 7.11, 7.12, the 2D maps for the nonlinear signal and E_2 are displayed, both in the time and frequency domains, using E_1=675 kV/cm, E_2=55 kV/cm and T=110 K. The angle between the polarizations of the two THz beams is $\pi/2$. E_2 is set perpendicular to the tungsten chain direction.

Compared to the tungsten chain direction (E_2 || x), the nonlinear signal is higher for the same field amplitudes. For E_2 || x, the plasma edge appears at lower frequencies, although it remains closer to the limit of our detection range (Figs. 7.13, 2.3(b)). Nevertheless, we once again observe a quasi-linear dependence between C_R and the E_1 field amplitude (Fig. 7.14) which is analogous to what we detected in the past sections in similar field conditions. As for $\langle f \rangle$, aside from its value at the lowest field, it remains stable around 12 THz for most of the observed field range. Based on the reasoning developed in the previous section, this can be attributed to nonlinear effects at the plasma edge which extend above our detection range, with the same low-field increase discussed for E_2 || x. In particular, based on Fig. 2.3(b) and the data in Appendix F, one expects the plasma edge to be centered around 12 THz.

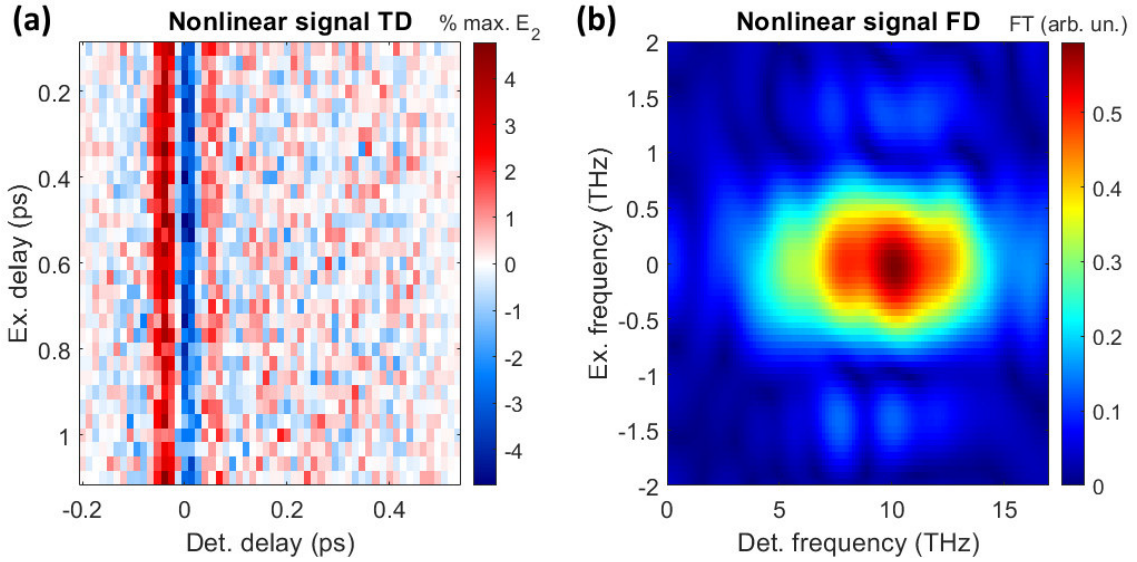

Figure 7.11. Nonlinear signal E_{nl} observed for WTe_2. (a) Time domain. (b) Frequency domain with E_1 ∼675 kV/cm, E_2 ∼55 kV/cm and T=110 K keeping $E_2 \parallel y$.

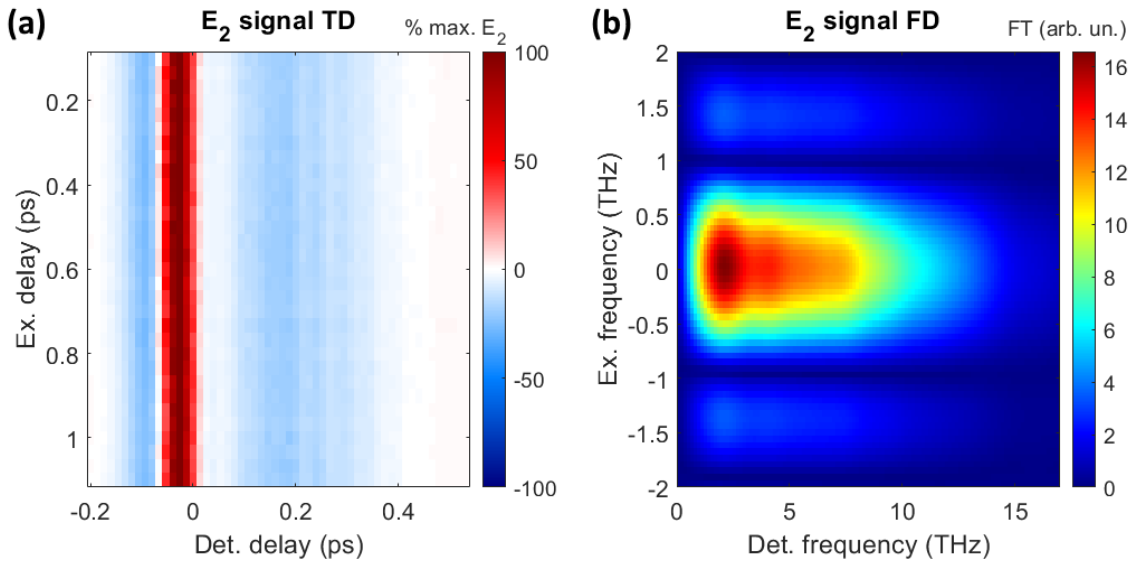

Figure 7.12. E_2 THz signal registered for WTe_2. (a) Time domain. (b) Frequency domain with E_1 ∼675 kV/cm, E_2 ∼55 kV/cm and T=110 K keeping $E_2 \parallel y$.

For this polarization configuration, we also acquired a temperature dependence of the two-dimensional response (Fig. 7.15). While the number of points is small and the error intervals are large, we resolve a similar decrease in C_R as the temperature increases as for TaAs, while $\langle f \rangle$ remains almost constant throughout the temperature range, with a small increase towards the higher temperatures. As shown in 2.3(b), the plasma edge position remains almost fixed throughout the temperature range, which is consistent with our observation.

A full gallery of the measured 2D maps can be found in Appendix F.

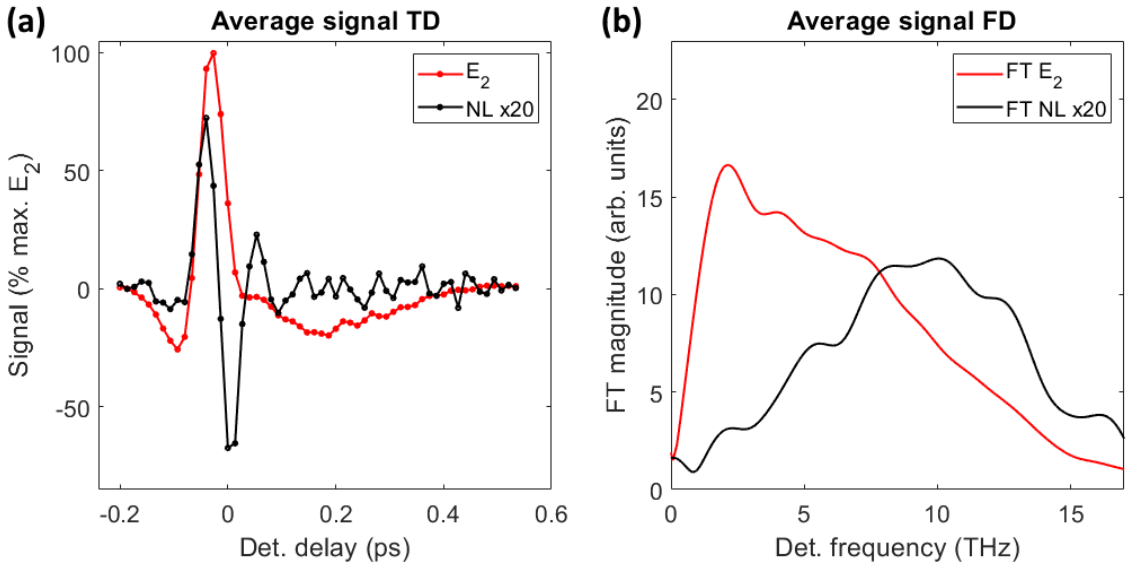

Figure 7.13. Comparison by taking the average profiles between the nonlinear signal E_{nl} and E_2 THz signal registered for WTe_2. (a) Time domain (mean profiles 0.3-0.7 ps). (b) Fourier transform of the profiles reported in (a) taken with E_1 ∼675 kV/cm, E_2 ∼55 kV/cm and T=110 K keeping $E_2 \parallel y$.

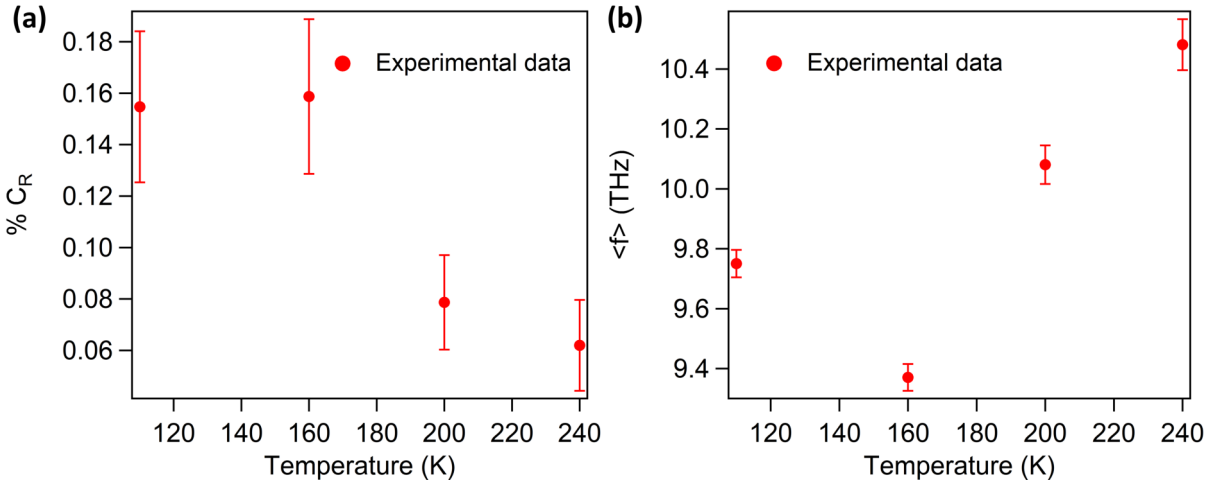

Figure 7.14. Temperature dependence of (a) C_R and $\langle f \rangle$ for WTe_2 keeping $E_2 \parallel y$.

7.4 Discussion

As previously discussed in Chapter 2, TaAs is a semimetal with a characteristic double-cone energy-momentum dispersion in the reciprocal space. When the Fermi level is in close vicinity to the intersection point, a low density of states and thus carrier density are expected.

The contribution of the Drude-like electrons is revealed from reflectance measurements (Fig. 2.2) where at low temperature a plasma edge is formed. As the temperature increases, the plasma edge bends and shifts its frequency position. This can be rationalized in terms of a Drude-Lorentz model, where Drude terms represent the quasi-free carriers [59]. For semimetals like TaAs [282] and WTe_2 [68] various electron-like and hole-like carriers can contribute through different Drude terms to the quasi-free carrier density giving the (screened) plasma frequency and thus plasma edge in the reflectivity spectra

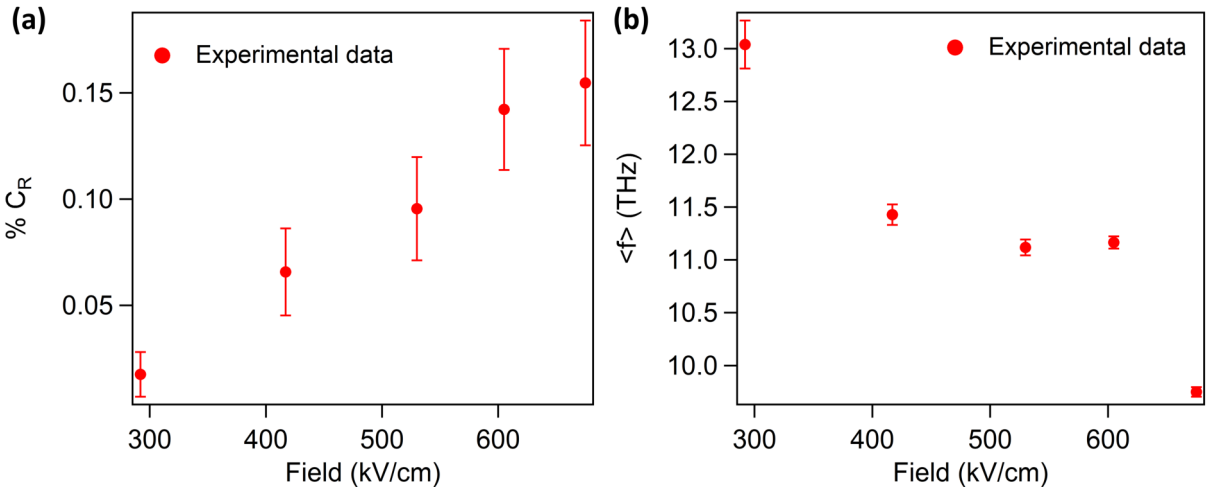

Figure 7.15. E_1 field dependence of (a) C_R and $\langle f \rangle$ for WTe_2 keeping $E_2 \parallel y$.

(Eq. (3.8)). When their individual plasma frequencies vary, either through a change of the carrier density, *e.g* through impact ionization, or effective mass, *e.g* when they are ballistically brought to a different position in the energy-momentum dispersion, they may lead to a change of the plasma edge position as well as of the scattering times [283].

In any case, the modifications are expected close to the plasma frequency, around the tilted region of the plasma edge in the reflectivity curves, in agreement with our experimental results when compared with the equilibrium reflectivity spectrum (Figs. 2.2, 2.3)

At higher temperatures, the change of the Fermi-Dirac distribution allows a higher number of carriers to participate in conduction phenomena. A change in their density has a direct consequence on the plasma frequency since $f_{pl} \propto \sqrt{n}$ with n being the carrier density (Eq. (3.9)). This does not usually severely impact metals having already a large carrier concentration and thus the relative change is minor. However, this becomes important in semimetals with small Fermi surfaces like TaAs [56] or HgTe [129] as well as for low band gap semiconductors. At the same time, an increase in the number of carriers and temperature lead to larger damping factors [1][283], which tilt the plasma edge as shown in [56] for TaAs.

To summarize, when the primary effect of the impinging E_1 electric field is to accelerate electrons and create secondary carriers through impact ionization, one expects to find the peak of the nonlinear signal in correspondence of the plasma edge as the number of the carrier increases, modifying its frequency [1]. The sign of the variation, however, may depend on the material, through its peculiar set of Drude and Lorentz terms to describe its dielectric tensor (Chapter 3 and [59]), in particular through the combination of the plasma frequencies and scattering times leading to competing effects.

The observed temperature dependence of $\langle f \rangle$ can be thus attributed to such shift of the plasma edge.

The described reduction of the nonlinear field C_R is consistent with this picture. The temperature dependence of the impact ionization rates was shown to be critically different depending on the material under analysis. When considering large band gap semiconductor, such rates are almost insensitive to it, while for low-band gap semiconductors, approaching the gapless limit, a reduction in the impact ionization coefficient is usually observed [114][284]. Exceptions can be found among heterostructures when mean free path and energy gap have a competing behavior [285][286].

While many scattering channels, such as from Coulomb, phonon, ionized or neutral impurities and, if it is the case, alloy disorder events, may contribute to the scattering rate of the carriers, the thermal activation of the phononic channels (acoustic and optical) plays the major role in regulating the rate. These processes are influenced by the variation of the phononic occupation number following the Bose-Einstein distribution

$$N_{ph} = \frac{1}{e^{E_{ph}/k_B T} - 1} \tag{7.4}$$

where E_{ph} is the phonon energy and k_B is the Boltzmann constant. In particular, optical phonon scattering processes are expected to give an important contribution when the associated optical phonon energies are found to be comparable with the thermal $k_B T$ denominator. This is true for TaAs and even more for WTe_2 and HgCdTe as later discussed. These processes then limit the kinetic energy the electrons can acquire and thus their impact on the variation of the optical properties. Furthermore, the optical phonon directly can intervene in the modulating the system response [191].

In a semiclassical picture, a higher field amplitude corresponds to a higher carrier acceleration, allowing carriers to acquire more kinetic energy in the same amount of time or unit length. This leads to an increase, until a saturation threshold is reached, of the impact ionization coefficients which generally follow a $\propto exp(-a/E)$ behavior with a and E being a system-dependent parameter and the electric field amplitude respectively [114], leading to higher variations of the reflectivity with respect to the unpumped conditions. However, at high excitations (as shown for graphene [287]), it may occur that impact ionization and its counterpart, named Auger recombination, present asymmetric, *i.e.* unequal, rates for increasingly narrower temporal windows thus leading to a gradual saturation of these effects with respect to the number of photoexcited electrons.

The small increase of $\langle f \rangle$ for higher E_1 field is compatible with an induced increase of the carrier density. As previously discussed, an increment of the number of carrier leads to a larger plasma frequency and a larger damping factor of the associated Drude term (Eq. (3.8)). Aside from the temperature effects on the scattering channels, its impact on the reflectivity is qualitatively similar to the temperature dependence given in Fig. 2.2.

Furthermore, when considering a temperature increase and inducing a shift or a quasi-symmetric tilt of the edge, for frequencies lower than the position of the plasma edge these effects have a smaller relative incidence on the reflectivity value, as the resulting value would remain close to one. For frequencies higher than the edge position at the equilibrium state, a lower reflectivity value is modified thus usually leading to higher relative effects. In other words, nonlinear effects coming from pump-probe effects of carrier multiplication would have a larger spectral spread towards higher frequencies as the field amplitude increases, thus leading to the observed increment, albeit small, of $\langle f \rangle$.

The full quantification of the nonlinear effects, however, requires a detailed model of TaAs's band structure, damping times, scattering rates, ionization rate as well as a clear determination of the chemical potential position which may differ from sample to sample. Moreover, the picture is complicated by the fact that the linear dispersion around the Weyl point maintains such characteristics only in a small energy-momentum window (a few tens of meV), leading to larger effective masses and nonlinear dispersion moving away from the node, requiring a very fine sampling of the reciprocal space to obtain the optical properties [288]. In fact, as shown for graphene, using driving electric field amplitudes for E_1 of the same order of our experiment can cause the electrons occupying states of the linear dispersion to be driven away from the nodes when compared to the few-tens of meV

neighborhood [189]. Larger effective electron masses would reduce the plasma frequency leading to a competing effect.

Regarding WTe_2, although affected by large uncertainties, we observe similar trends for both polarization directions, which are reminiscent of what observed in TaAs in both the temperature and E_1 field dependence. For C_R we observe a quasi-linear increase for growing E_1 field amplitude and a decrease as higher temperatures are reached.

The field dependence of $\langle f \rangle$ is influenced by the low spectral amplitude of E_2 in correspondence of the plasma edge, which is particularly critical for $E_2 \parallel x$ where it is located around 15 THz, as shown in Fig. 2.3 and Appendix F.

7.5 Conclusions

In this section, the results of the 2D THz response of a type-I, TaAs, and a type-II Weyl semimetal, WTe_2 were reported and discussed.

The nonlinear signal was calculated and analyzed in terms of its temperature and pumping-field dependences. While the signal magnitude varies between the two materials, similar characteristics are shared. The nonlinearities are understood as the result of carrier multiplication (impact ionization) occurring due to the acceleration of electrons by the driving E_1 THz pulse. This provokes a change in the nonlinear polarization of the material leading to the nonlinear signal. Due to their position in the frequency maps (Figs. 7.2, 7.7, 7.11), these pump-probe effects are assigned to variations in the third-order susceptibility tensor (see the discussion in Chapter 8).

From the physical point of view, one characteristics that could lead to the smaller nonlinear response in WTe_2 is its higher carrier concentration compared to TaAs, which is related to distinct Fermi surfaces in the type-I and type-II Weyl semimetals [6]. In fact, as the plasma frequency of a Drude-like term depends on the square root of the number of carriers (Eq. (3.9)), it is necessary to generate a larger number of new quasi-free carriers to provoke a comparable change in the edge position. However, an accurate modelization of the scattering terms is necessary to complete the picture.

Nevertheless, this is likely an important factor explaining why the temperature dependence does not visibly affect the plasma edge frequency through the thermal activation of carriers (Fig. 2.3 and Appendix F), even though the electron pockets size in the Fermi surface, connected with low effective mass, is expected to largely grow [13] due to the shift of the chemical potential as the sample is heated.

In order to elaborate more on this point, further experiments, such as a determination of the chemical potential position, may be necessary to obtain the specific parameters for the ionization process of the two different samples. However, their complex band structure and curvature changes in the energy-momentum space pose a hard challenge to unequivocally connect the nonlinear signal to the signature of the high-mobility carriers in the neighborhood of the Weyl points [6][288].

CHAPTER 8

Two-dimensional terahertz experiments on HgCdTe

8.1 Introduction

Mercury cadmium telluride ($Hg_{1-x}Cd_xTe$, MCT) is an alloy compound formed by a semimetal (HgTe) and a semiconductor (CdTe, band gap E_g ∼1.5 eV at room temperature). At particular composition and temperature conditions, its electronic band structure displays a double-cone structure around the Fermi level which resembles type-I Weyl semimetals like TaAs [7][113][289].

However, compared to Weyl semimetals, it does not present monopoles of Berry curvature and its double-cone dispersion is intersected by a flat heavy-hole-like band. Its band structure can be described by a well-known model for semiconductors, the Kane model [108][109]. The peculiar conic intersection occurs as a boundary between the 'normal' and the 'inverted' phases, at which the parametric eigenvalues expressions giving the double-cone dispersion in the Kane model exchange their energy order, and the material presents a point-like intersection between the cones. It was experimentally shown [7][113] that in a small neighborhood of the boundary between the phases, the electron and light-hole bands maintain a linear dispersion. Moreover, magneto-optical experiments have shown that the conduction band dispersion can be effectively considered linear for several hundreds of meV [7][113], in contrast to the previously examined examples of Weyl semimetals.

In this chapter, we present the results of an experimental 2D THz study on a MCT film with composition x∼0.175, which approaches the linear-dispersion configuration at low temperature starting from a normal phase at room temperature. This can be seen already from the temperature-composition diagram based on the empirical formula from [289] in Fig. 8.1, although we will discuss the eaxct values for the measured sample in the experiment discussion. The combined contributions of reducing the band gap and of the sharpening of the Fermi-Dirac distribution as the temperature is lowered allow to

keep the carrier density small throughout the whole temperature range [113] which, at equilibrium, brings the chemical potential close to the bottom of the conduction band. We examine the carrier dynamics under the action of the electromagnetic fields in transmission geometry. We detect large nonlinearities in the response, which we examine as a function of temperature and impinging field amplitude. The results are analyzed both in the time and frequency domains. The latter is obtained as the discrete Fourier transform (DiFT) of the former and gives complementary information regarding the source and dependencies of the underlying phenomena. Following the discussion of Chapter 3, we also divide the nonlinear effects between 'odd' and 'even' contributions with respect to the field E_1.

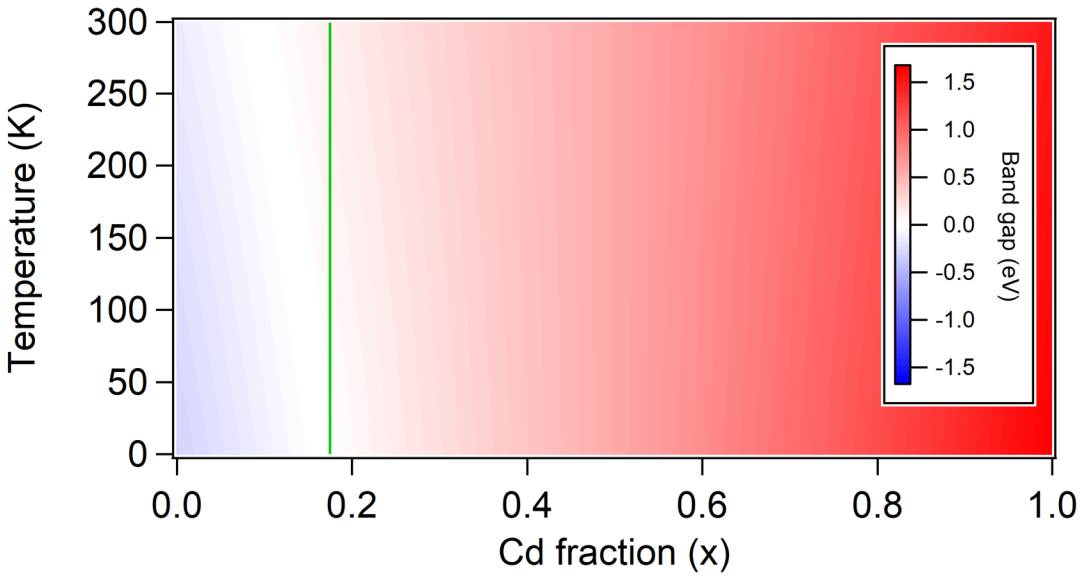

Figure 8.1. Temperature-composition diagram for the band gap of $Hg_{1-x}Cd_xTe$. The map was obtained from the formula found in [289]. The vertical green line highlights the composition of the investigated sample.

8.2 Sample

HgTe, CdTe and their alloys present a zinc blende structure (space group $F\bar{4}3m$) with small lattice mismatch among them [121]. Our MCT sample is a heterostructure grown starting from a GaAs substrate with intermediate CdTe buffer layer (∼40 nm) between the ∼3.2-µm-thick [013]-oriented MCT film with composition x∼0.175 (Fig. 8.2(a)) and finally covered by a CdTe capping layer. Although its main purposes are to reduce the strain of the active layer and protect it, the capping layer serves also as a safety measure for the user to avoid any remote possibility of mercury inhalation. More details regarding the sample growth can be found in [290]. The sample was attached to a copper cold finger and inserted in a helium cryostat (pressure $\sim 10^{-6}$ mbar).

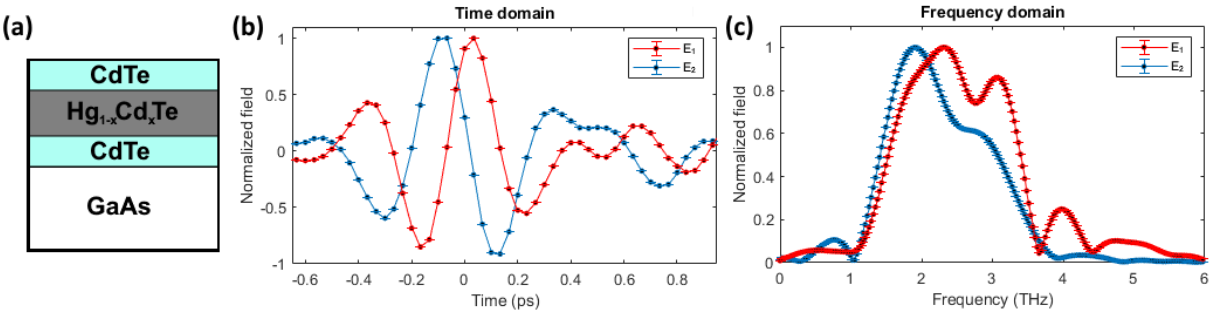

Figure 8.2. (a) Scheme of the $Hg_{1-x}Cd_xTe$ sample. The active layer is protected by a CdTe capping layer and separated from the GaAs substrate through a CdTe buffer layer. Examples of normalized signal: (b) time domain and (c) frequency domain for E_1 and E_2 transmitted through the sample.

8.3 Experimental details

8.3.1 Ti:sapphire laser system

The 2D THz setup relies on the same Ti:sapphire amplifier described in the 'experimental details' of Chapter 7. As for the ABCD-detection setup, it exploits nitrogen-purged boxes to reduce the water-related THz absorption, taking the relative humidity below 2%.

8.3.2 Electro-optic sampling setup

The two infrared beams obtained as the output of the OPAs (see Chapter 7) are used to obtain THz radiation using organic crystals (DSTMS) through optical rectification, which provide broadband quasi-single-cycle THz pulses, whose spectral content is maximum between 1 and 4 THz (Figs. 8.2(b),(c)), with peak values up to ∼1 MV/cm. The electric field amplitude and polarization are controlled through the combined use of two wire-grid polarizers and directed toward the sample using plane and parabolic mirrors. The transmitted radiation was collected and measured through electro-optic sampling using a 300-µm-thick GaP crystal and a remaining fraction of the original 800 nm beam. The experiments were performed at different temperature conditions (12-100 K), using a cryostat employing liquid helium, and electric field amplitudes (11-65 kV/cm). The setup is similar the to scheme reported in Fig. 7.1 for the ABCD setup with the possibility to work either in reflection or transmission geometries.

The two main differences compared to the ABCD setup which impact on our measurements are the possibility to reach lower temperature, but with a more limited spectral range for E_2 compared to the plasma-generated THz beam. Nevertheless, data from the literature [113][121][129] suggest that important features from the active layer such as the plasma frequency and phonon resonances of the alloy should lie in the measured spectral window.

As in the previous chapter, we monitor the nonlinear signal [188], defined as in (7.1). When an estimate of an electric field is given, the value is meant as the maximum field amplitude of the pulse at the sample position. Moreover, following the discussion presented in Chapter 3, we employ the 'odd'-'even' separation of the nonlinear effects [200] based on the response of the signal to a π variation of the THz pulse phase. This requires acquiring the nonlinear signal for the two '+' and '-' data subsets, where the phase of E_1 is changed by π through the combined use of two wire-grid polarizers between the two.

Finally, the odd and even contributions are determined by (Eq. (3.7))

$$E_{odd} = E_{nl+} - E_{nl-} \quad E_{even} = E_{nl+} + E_{nl-} \tag{8.1}$$

Naturally, to get the odd and even contribution per set, one should divide them by two. To analyze the results, however, it is convenient to quantify E_{odd} and E_{even} with respect to the maximum of E_2, which can be expressed as $E_2 = E_{2+} + E_{2-}$ for both the channels. However, since $E_{2+} \simeq E_{2-}$ as the sets are acquired one after the other, the conclusions are expected to be the same. Due to this, one can also take the odd nonlinear signal as

$$\begin{aligned} E_{odd} = E_{nl+} - E_{nl-} &= (E_{t+} - E_{1+} - E_{2+} + E_{b+}) - (E_{t-} - E_{1-} - E_{2-} + E_{b-}) \\ &\simeq (E_{t+} - E_{1+}) - (E_{t-} + E_{1-}) \end{aligned} \tag{8.2}$$

where the last step considers that it is no longer necessary to add background terms as the subtraction $E_t - E_1$ cancels them out.

This simplification is applicable in our analysis and avoids the inclusion of two further data sets E_2 and E_b which add noise, without changing the physical significance of the data. Approximations regarding E_{1+} being $-E_{1-}$, instead were not exploited as the π phase change occurs by modifying the position of a wire grid, which although carefully balanced can lead to minor albeit appreciable differences between E_{1+} and $-E_{1-}$.

8.4 Time domain - parallel configuration

8.4.1 2D maps

The sample was studied under two different configurations, obtained varying the relative angle α between the linearly polarized E_1 and E_2 THz beams: parallel (α=0) and cross-polarized (α=$\pi/2$) geometries.

In Fig. 8.3 we report the nonlinear response in the time domain for (a) odd and (b) even signal using the parallel scheme. Taking Fig. 3.3 as reference, we observe that the most prominent odd nonlinearity exhibits fronts parallel to the $t_{ex} + t_{del} = 0$ direction, akin to E_1; it appears for $t_{ex} < 0$ and disappears around (t_{del}=0, t_{ex}=0). Differently, the even signal behaves similarly to E_2, starting around the superposition region for the two field centroids and reaching a plateau ∼0.5 ps later. The signal then slowly decays in a few tens of picoseconds (shown in Appendix G for the cross-polarized configuration, Fig. G.1(d)).

A faint signal is observed for $t_{ex} > 0$ in the odd channel. Even though it characteristics could correspond to a different physical process (see the discussion of the frequency domain), it is likely a consequence of the minor imbalance for the E_1 values between the two '+' and '-' datasets, leading to small discrepancies in the odd/even channels. These variations also lead to the non-zero 'dot'-like pattern of high values near (0,0), which would not be present for perfectly balanced sets. This association can be visualized when analyzing the individual datasets and looking at the superposition coordinates between the two fields E_1 and E_2.

This imbalance is more evident for the odd signal, where the signal is lower, although it is present in a less pronounced way also in the even channel.

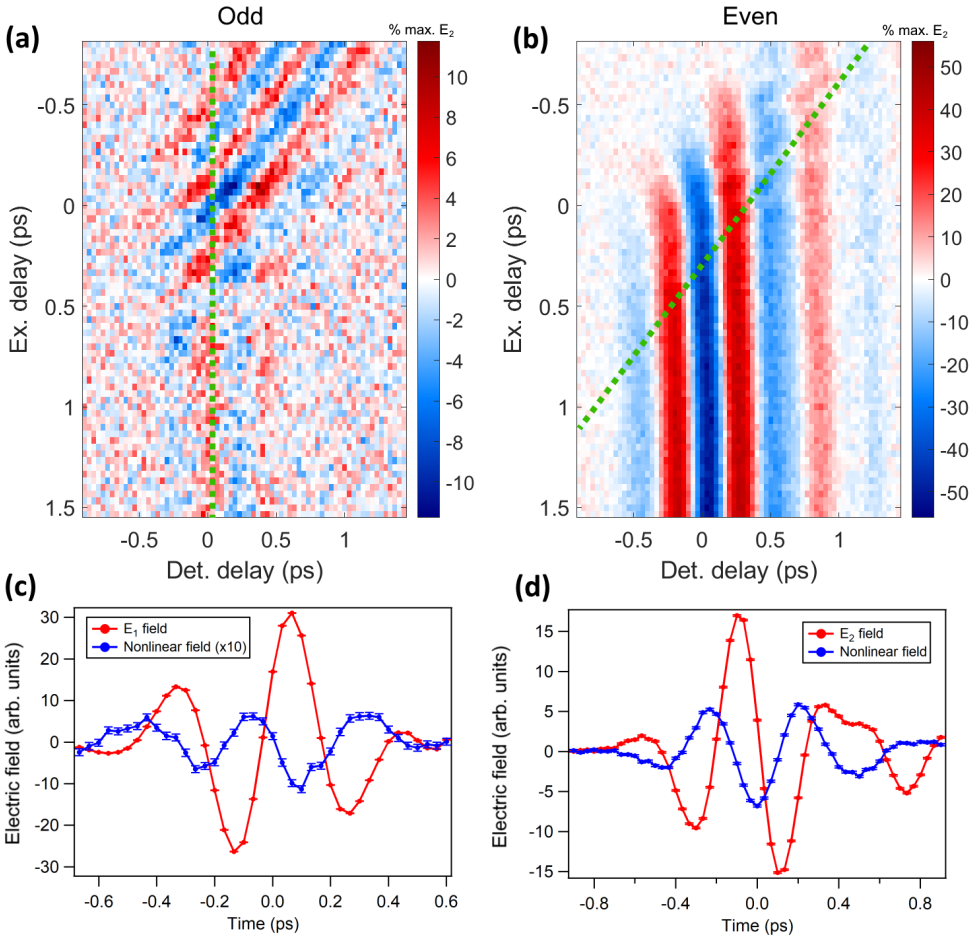

Figure 8.3. Nonlinear signal for $Hg_{0.825}Cd_{0.175}Te$ in the time domain for the parallel configuration reported in panels (a) and (b) for the odd and even channels normalized to the E_2 maximum amplitude. Constant-excitation-delay profiles for the (c) odd, and (d) even nonlinear signals shown together with the E_1 and E_2 electric field respectively, taken along the green dotted lines in (a) and (b) respectively. The experimental conditions were E_1 ∼31 kV/cm, E_2 ∼17 kV/cm and T=12 K.

In Figs. 8.3(c),(d), the temporal structure of the odd and even nonlinear signals is shown and compared with E_1 and E_2. These profiles were taken so that each point of the second-arriving field, with respect to t_{del} coordinate, experiences the same delay from the average time (Eq. (3.6)) of the first pulse. The curves in (c) are thus vertical profiles taken at $t_{del} \sim 0.25$ ps, while the ones in (d) are taken along $t_{ex} + t_{del} \sim 0.3$; their paths are depicted in green dotted lines in the (a),(b) panels respectively (165 fs integration). In both cases, the nonlinear signal exhibits an evident $\sim \pi/2$ phase shift with respect to the corresponding maxima/minima of the fields. Usually, this is indicative of a different spectral content with respect to the compared pulse (Chapter 7), although, as shown later, the precise value of the shift is affected by the impinging field amplitude, which we interpret as a change in the dielectric function.

8.4.2 Temperature and field dependences

The temperature was carried out keeping the field amplitudes constant. When the sample is cooled down, the nonlinear signal amplitude increases for both channels. In Figs. 8.4

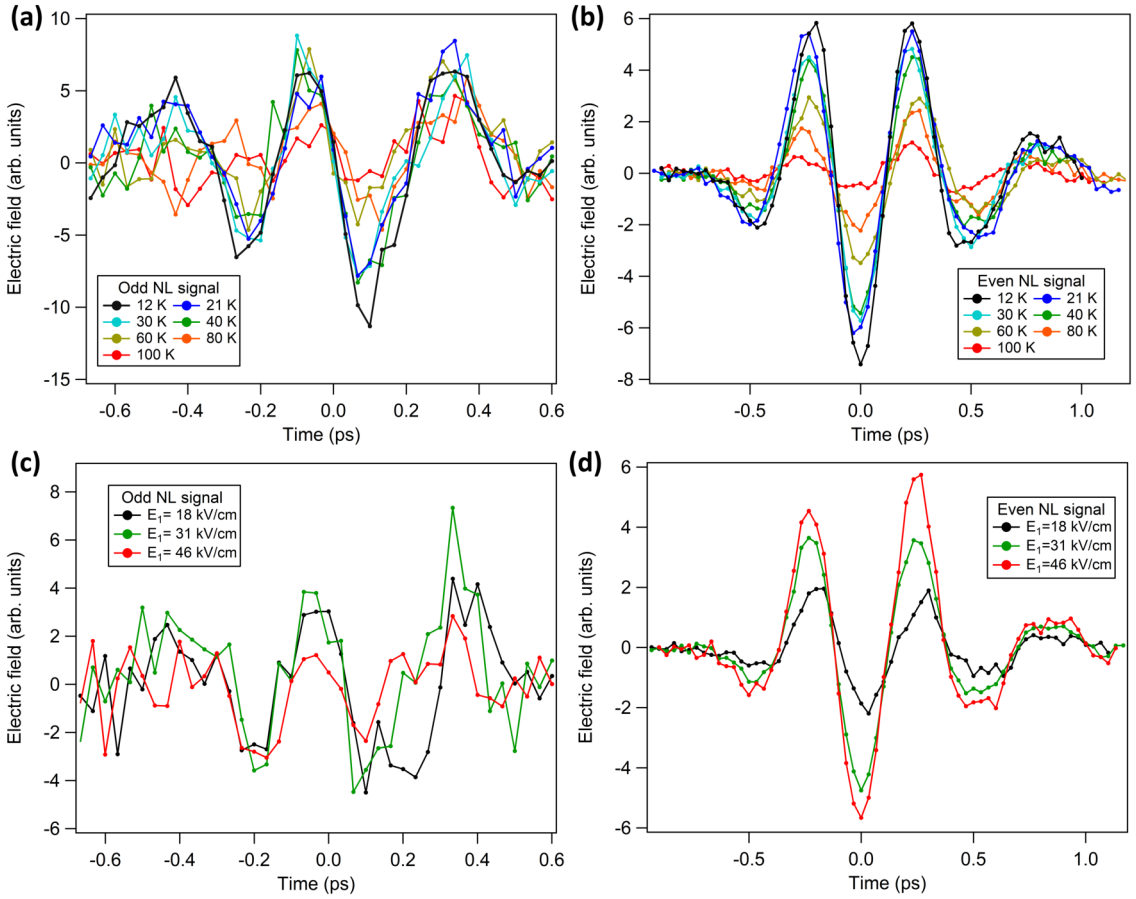

Figure 8.4. Dependencies of the nonlinear signal in the parallel configuration. (a),(b) Temperature dependence with E_1 ∼31 kV/cm, E_2 ∼17 kV/cm for odd and even parities respectively. (c),(d) Field dependence varying E_1 keeping E_2 ∼11 kV/cm and T=21 K constant for odd and even parities respectively.

(a),(b) we report the profiles for the odd and even nonlinearities measured at selected temperatures. Moreover, in both cases, the phase of the nonlinear signal does not change varying the temperature.

Setting the temperature at 21 K and the E_2 amplitude at ∼11 kV/cm, a study on the effect of the E_1 amplitude was performed. Increasing the field amplitude leads to an enhancement of the even nonlinear contribution (Fig. 8.4(d)), while the odd amplitudes (Fig. 8.4(c)) do not vary appreciably with E_1. Regarding the phase, the even signal displays a dependence of its electro-optic delay time as a function of the E_1 field amplitude, as depicted in Fig. 8.4 (d), leading to a global shift of the nonlinearity at earlier t_{del}. This fact becomes more prominent in the cross-polarization scheme using higher fields.

8.5 Time domain - cross-polarized configuration

As a remark, we note that the electro-optic sampling values depend on the THz polarization. Rotating by $\pi/2$ the E_1 polarization direction while keeping every other setup component as it was set for the previously optimized parallel detection, leads to a reduction of its registered signal by a factor ∼7. This is due to the relative geometry between

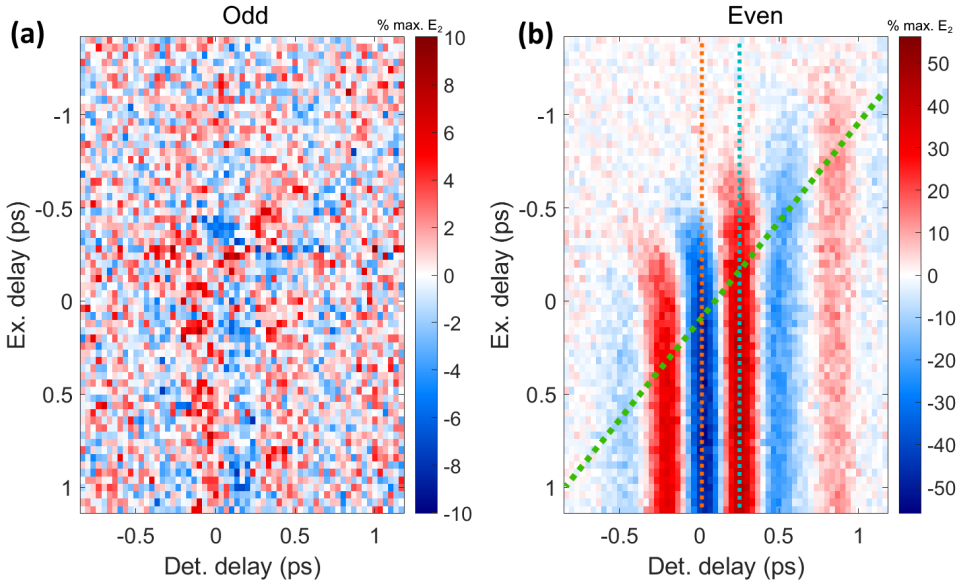

Figure 8.5. Nonlinear signal for $Hg_{0.825}Cd_{0.175}Te$ in the cross-polarized configuration. Time domain responses are reported in panels (a) and (b) for the odd and even parities. Profiles in current chapter taken along the green dotted line in (b), albeit without the odd/even separation. The other two dotted lines indicate profiles discussed in the Appendix G. The experimental conditions were E_1 ∼34 kV/cm, E_2 ∼17 kV/cm and T=21 K.

the THz and the electro-optic sampling pulse for the (110)-cut zinc-blende-type crystals, which depends on their relative orientation as well as with respect to the crystal axes [291].

8.5.1 2D maps

The 2D data sets are reported in Figs. 8.5(a),(b) for the odd and even contributions respectively. No prominent odd contribution is detected (Fig. 8.5(a)). As explained in the discussion section, this absence is likely connected to it being polarized along the same direction as E_1, as the reduction of a factor ∼7 would bring the signal close to the noise floor of the setup. Residual contributions in the odd channel are connected once again to the minor imbalance between the '+' and '-' data sets. Instead, a distinct even contribution is registered (Fig. 8.5(b)), which presents analogous characteristics as the parallel counterpart (Fig. 8.3(b)).

8.5.2 Temperature and field dependences

As for the parallel configuration, a temperature and field dependence was acquired (Figs. 8.6(a),(b)). As no clear odd nonlinearity was detected, we decided to focus only on one set between the '+' and '-' datasets. Hence, the nonlinearities reported, even though effectively reproduce the even nonlinearities, should be regarded as the total nonlinearities. The even nonlinear signal decreases as temperature is increased and as the E_1 amplitude

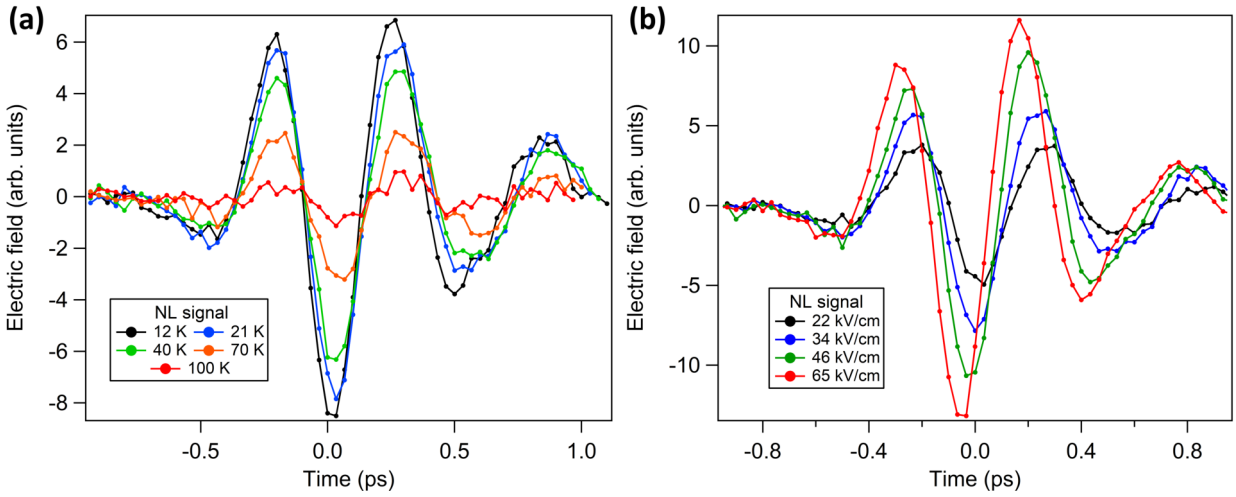

Figure 8.6. Dependencies of the total nonlinear signal in cross-polarized configuration. (a) Temperature dependence with E_1 ∼34 kV/cm, E_2 ∼17 kV/cm. (b) Field dependence varying E_1 while keeping E_2 ∼17 kV/cm and T=21 K constant.

is reduced. The variation of the nonlinear signal phase, seen before in the parallel configuration, is reproduced in the cross-polarized scheme (Fig. 8.6). While the temperature does not seem to lead to significant variations, increasing E_1 shifts the nonlinear profile towards earlier t_{del} values.

The rise time, *e.g.*, the time required to reach the plateau of the nonlinear signal, is discussed in Appendix G.

8.6 Frequency domain results

In the frequency domain, the nonlinear signal can be described employing the Liouville-space pathway theory [201]. In this picture, the location of the nonlinear contributions in the bidimensional frequency maps is viewed as succession of steps linked to the individual E_1 and E_2 electric fields. The number of steps is limited by the order of the susceptibility term involved, which selects the available positions at which signal can be found. The coordinates of such contributions are usually expressed as multiples of the pulse frequency, which gives information about how many times the individual fields contribute in the term.

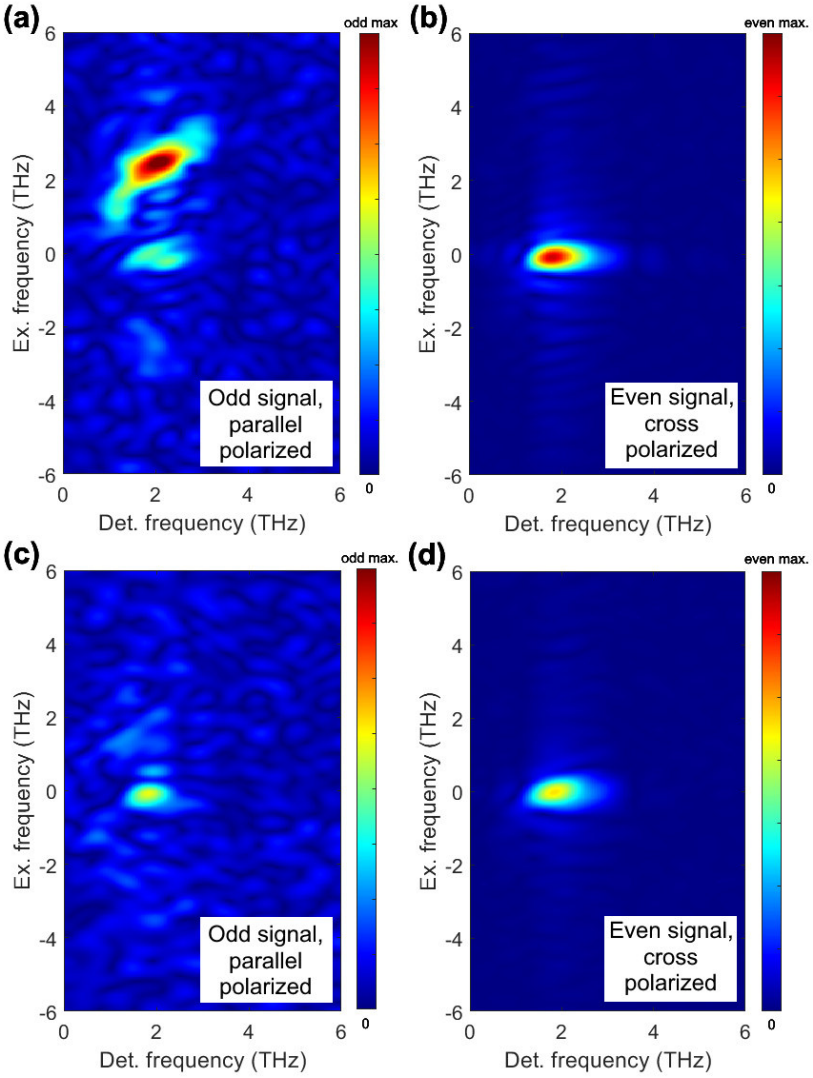

Figure 8.7. Nonlinear signal for $Hg_{0.825}Cd_{0.175}Te$ in the frequency domain. Panels (a) and (b) report the results for the odd and even parities respectively in the parallel-polarized configuration. The experimental conditions were E_1 ∼31 kV/cm, E_2 ∼17 kV/cm and T=12 K. Panels (c) and (d) are the cross-polarized counterparts. The experimental conditions were E_1 ∼34 kV/cm, E_2 ∼17 kV/cm and T=21 K. For each parity, the same colorscale was used for both polarization schemes.

Hence, one can locate the nonlinear contributions using the $(\nu_{del}/\nu_2, \nu_{ex}/\nu_1)$ Cartesian pairs. In our case, having broadband pulses, this description is only approximate, but we

can take as ν_1 and ν_2 the corresponding average frequencies for the two pulses, which we define as $\nu_0 = 1/I_\nu \int_0^\infty E(\nu)^2 \nu d\nu$, where $I_\nu = \int_0^\infty E(\nu)^2 d\nu$ [175]. This leads to ν_1 ∼2.5 THz and ν_2 ∼2.1 THz.

8.6.1 2D maps

In Fig. 8.7 we report the frequency domain maps obtained as discrete Fourier transforms of the time domain results presented in Figs. 8.3(a),(b), for the parallel configuration, and Figs. 8.5(a),(b), for the cross-polarized configuration. When the fields are set parallel, the odd signal shows a prominent contribution at (1,1), which has a large spectral width extending for about one terahertz in each direction, while the even signal is transformed into a single contribution centered around (1,0). Their locations can be explained as primarily linked to third-order polarization contributions (see section 8.7.2). These processes can be described through the Liouville-space pathway theory [201] as a succession of contributions from the fields. The odd signal derives from a pump-probe effect where E_2 plays the role of the pump and E_1 of the probe. The even signal emerges from another pump-probe effect, whereas in this case E_1 is the pump and E_2 is the probe. These frequency positions cannot host even-order nonlinearities as no pathway of such order can reach those coordinates [195]. In principle, higher odd-nonlinearities are not forbidden. However, from the vector-chain representation of the pathways [195] and in the case of fifth-order effects, this is only possible if the polarization contribution depends on the fourth power of one of the two field amplitudes or on the intensity of both. Nevertheless, we have not found evidence of such response in our data: in Fig. 8.4(c) we see that the odd signal (pump E_2, probe E_1) amplitude is almost independent from E_1; later in Fig. 8.11(b) we observe the field dependence for the nonlinear signal registered for the cross-polarized configuration (pump E_1, probe E_2) which, when fitted by an $a + bx^c$ expression, gives c ∼1.7, close to a parabolic behavior of the field amplitude, hence proportional to the E_1 intensity. A finely sampled field dependence of the nonlinearities for both E_1 and E_2 could further reinforce this conclusion.

This assignment is also supported by the time domain behavior. In fact, the odd effects are present for negative t_{ex}, where E_2 arrives before E_1 at the sample, and disappear close to the superposition of the two fields, while the even signal shows a maximum at positive t_{ex}, where E_1 arrives before E_2, and is absent before the temporal superposition.

Minor contributions are present in the odd signal at (1,0) and (1,-1) in the parallel scheme. The former one is due to a small 'leakage' of the even contribution into the odd channel due to a slight imbalance between the values of E_1 in the two '+' and '-' sets, as previously discussed for the time domain. The latter feature is set at frequency coordinates which could be attributed to a four-wave-mixing phenomenon (photon echo) with is absent in other linearly-dispersing systems like graphene [196], although its magnitude varies non-monotonically as temperature changes. This could be an indication of a trivial origin due to the E_1 imbalance between the two sets leading to minor artifacts in the Fourier maps.

8.6.2 Temperature and field dependences

As temperature is increased (Fig. 8.8), both main nonlinear features decrease in amplitude. However, while the even signal shape remains almost unvaried, the shape of the odd feature changes significantly in temperature, with the appearance of a low-frequency tail

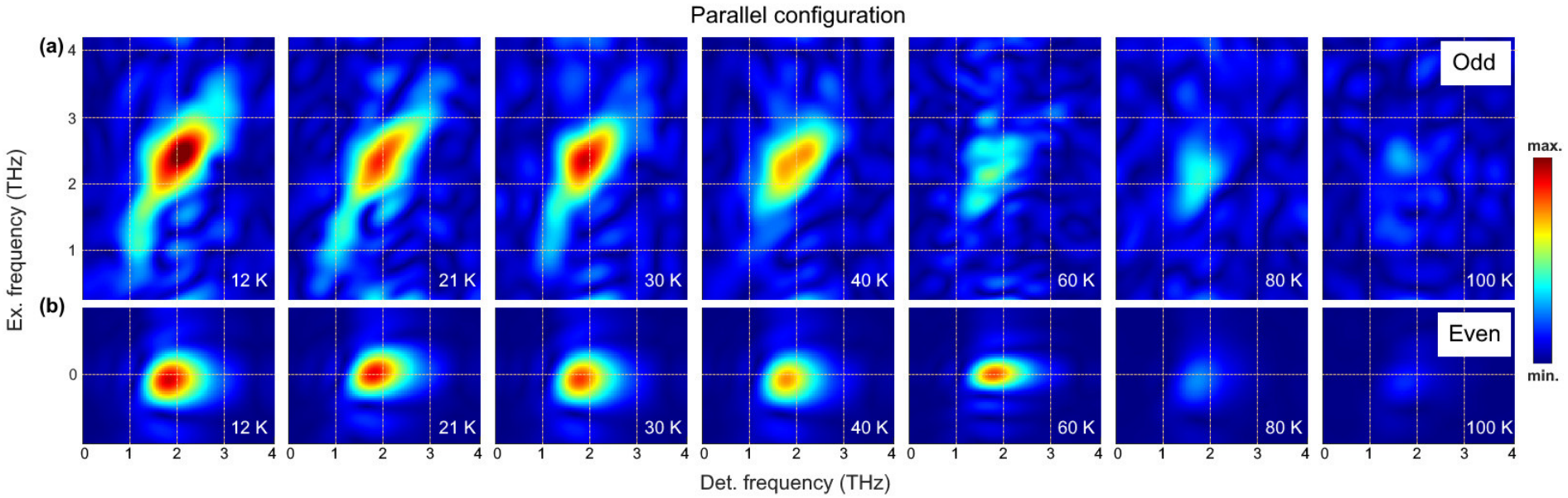

Figure 8.8. Main nonlinearities in frequency domain in parallel configuration shown in the 10-100 K range. (a) Odd contribution at (1,1). (b) Even feature at (1,0). All the measurements were acquired using E_1 ∼31 kV/cm, E_2 ∼17 kV/cm. The color scale range was fixed for all of the maps of a given parity and set between 0 and the maximum of the 12 K signal.

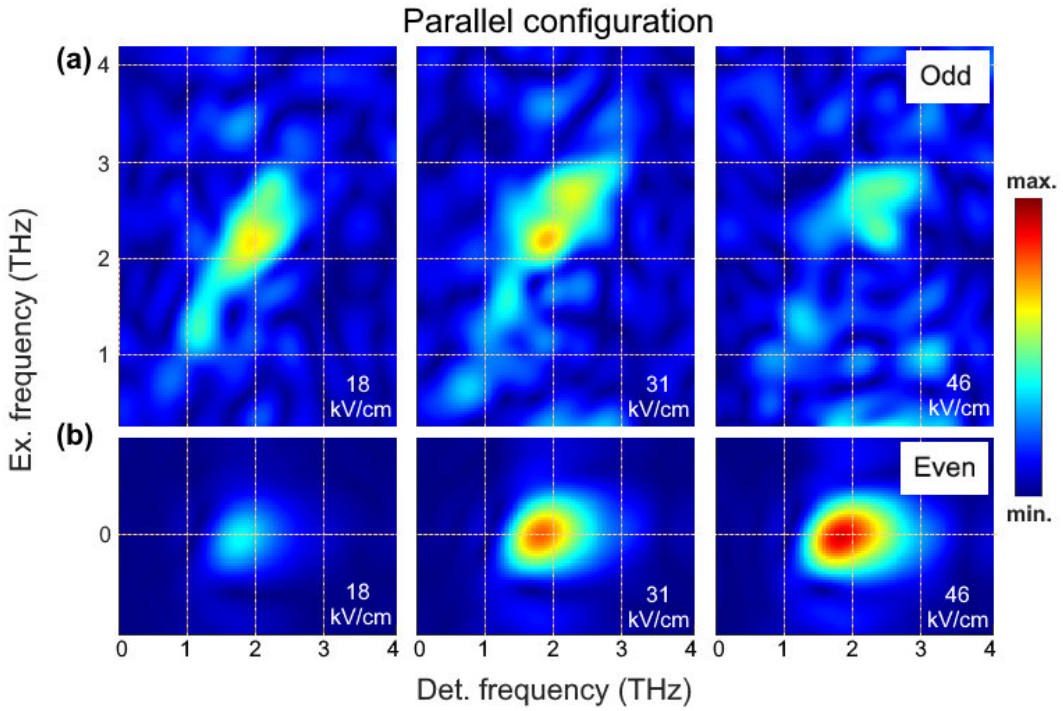

Figure 8.9. Main nonlinearities in frequency domain in parallel configuration shown for the E_1 field dependence in the 18-46 kV/cm range. (a) Odd contribution at (1,1). (b) Even feature at (1,0). All the measurements were acquired using E_2 ∼11 kV/cm and T=21 K. The color scale is the same used in Fig. 8.8 for the two parities.

as the temperature is reduced. When the E_1 field is increased (Fig. 8.9), the nonlinearities behave differently amplitude-wise, as previously described for the time domain and explained in the general discussion for the frequency maps. While the spectral appearance of the even signal remains the same, the odd component exhibits a reduction of the low frequency tail as the field amplitude grows.

The shape of the two nonlinearities at low temperature can be compared to the transmitted spectra of the individual fields. In Fig. 8.10 we schematically show their normalized frequency spectra so that the odd feature (a) is compared with E_1 (b), whereas the even contribution (c) is shown with E_2 (d) underneath. For both parities, the nonlinearities exhibit a small spectral amplitude above 3 THz, whereas the individual transmitted fields show a slower decay. This behavior could be influenced by the close presence of a phonon resonance in the MCT sample, centered around 3.5 THz for x∼0.175 [130] and clearly present in the absorption spectrum [7] , which may limit the extent of the nonlinearity, *e.g.* caused by carrier multiplication, around such frequency as the phonon-related term in the dielectric function gives a very prominent contribution compared to the modification E_1 can induce. While the even channel presents a similar low-frequency shape, the odd contribution shows a more gradual reduction of the spectral amplitude with the emergence of the low-frequency tail when compared with E_1. The slight bending of the tail towards the excitation frequency axis may be due to the higher E_1 spectral amplitude near 1 THz (Fig. 8.2(d)).

In the cross-polarized scheme, the nonlinear signal presents just an even feature centered at (1,0), which has an analogous temperature and field dependence compared to the parallel configuration, with no significant changes in its spectral shape.

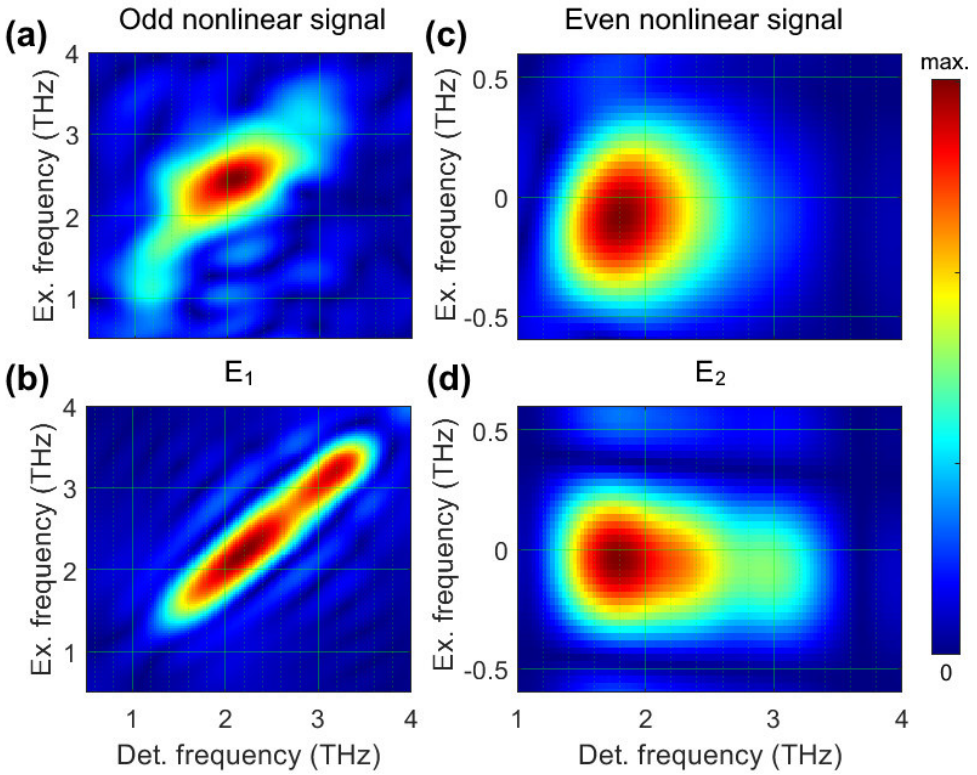

Figure 8.10. Comparison among individual fields and nonlinearities in the frequency domain for the parallel configuration. (a) Odd nonlinear contribution at (1,1) compared with (b) the transmitted E_1 field. (c) Even nonlinear feature at (1,0) compared with (d) the transmitted E_2 field. All the measurements were acquired using E_1 ∼31 kV/cm E_2 ∼17 kV/cm and T=12 K. The colorscale range is normalized for each panel.

8.7 Discussion

8.7.1 Electronic structure

Throughout the examined temperature range, $Hg_{0.825}Cd_{0.175}Te$ remains in the normal phase with a positive band gap [289]. As shown in [113], the gap value varies between 5 and 56 meV in the 2-120 K interval, approaching the linear dispersion at low temperatures. In the neighborhood of that condition, the band structure close to the Fermi level can be described using an isotropic simplified Kane model [109][113]

$$E_\zeta(p) = \zeta^2 \tilde{m}\tilde{c}^2 + (-1)^{1-\theta(\tilde{m})}\zeta\sqrt{\tilde{m}^2c^4 + p^2\tilde{c}^2}, \tag{8.3}$$

$$E_{\zeta=0}(p) = 0$$

where $\zeta = 1, 0, -1$ distinguishes the electron band from the heavy hole and light hole bands respectively, $\tilde{m}$ is the rest-mass, $\tilde{c}$ is the universal velocity, p is the linear momentum and θ is the step function. From this description is then possible to derive an expression for the density of states for the electron band:

$$D(E) = \frac{1}{\pi\tilde{c}^3\hbar^3}(E - \tilde{m}\tilde{c}^2)\sqrt{E^2 - 2\tilde{m}\tilde{c}^2E} \cdot \tilde{\theta}(E - 2\tilde{m}\tilde{c}^2) \tag{8.4}$$

Using the data found in [113], we can estimate the chemical potential (μ) behavior through the carrier concentration integral equation

$$n = \int_{2\tilde{m}\tilde{c}^2}^{+\infty} f(E, \mu, T) D(E) dE \tag{8.5}$$

where $f = 1/exp((E-\mu)/(k_B T)) + 1$ is the Fermi-Dirac distribution with k_B being the Boltzmann constant.

We obtained values of 18.5 to 76 meV moving from 2 K to 120 K. By interpolating the low temperature values, we find that at the lowest examined temperature (12 K), the band gap is ∼9 meV, while the chemical potential resides about 12 meV above the bottom of the electron band. This leads to limitations (Pauli blocking) for direct optical-like interband transitions for photon energies within our terahertz pulses spectral width, although other interband mechanisms may be involved (*e.g.* Zener tunneling [278]).

8.7.2 Nonlinear signal

The induced polarization in a material is connected to its response function in presence of an electromagnetic field. This relation can be expressed as a Taylor expansion based on the n-th power order through which the electric field is involved [201], such that

$$\begin{aligned} P_{\alpha_f}^{(n)}(\mathbf{r}, t) \propto \sum_{\alpha_1, \alpha_2, ..., \alpha_n} \int dV_s^{(n)} e^{\tilde{i}(\mathbf{k_f}\cdot\mathbf{r} - \omega_f t)} \times \chi^{(n)}_{\alpha_1, \alpha_2, ..., \alpha_n, \alpha_f}(\mathbf{k_1}, \omega_1, \mathbf{k_2}, \omega_2, ..., \mathbf{k_n}, \omega_n) \\ \times \tilde{E}_{\alpha_1}(\mathbf{k_1}, \omega_1) \tilde{E}_{\alpha_2}(\mathbf{k_2}, \omega_2) \cdots \tilde{E}_{\alpha_n}(\mathbf{k_n}, \omega_n) \times \delta(\omega_f - \sum_{\eta=1}^{n} \omega_\eta) \delta(\mathbf{k_f} - \sum_{\eta=1}^{n} \mathbf{k}_\eta) \end{aligned} \tag{8.6}$$

where $dV_s^{(n)}$ is the phase space volume element, $\tilde{i}$ is the imaginary unit,

$$\chi^{(n)}(\mathbf{k_1}, \omega_1, \mathbf{k_2}, \omega_2, ..., \mathbf{k_n}, \omega_n) \tag{8.7}$$

is the n-th order electric susceptibility (n+1-th order tensor), $\tilde{E}$ indicates the total electric field, δ represents the delta function, α indices stand for a basis component of the chosen coordinate system, $\mathbf{k}$ and ω represent wavevectors and angular frequencies, which can be either positive or negative.

Knowing the precise waveform of the total electric field, it is possible to simplify the expression. If two or more fields are present, the electric field can be viewed as their sum leading to a series of combinations, as seen from Eq. (8.6). Each of them gives a separate contribution in the multidimensional frequency domain, although distinct contributions may be superimposed.

The nonlinear signal originates from the contributions such that $n > 1$. The frequency coordinates of its features can be viewed in the terms of Liouville-space pathway theory [195][201], which helps to distinguish their origin and the n-th order of the electric susceptibility involved.

Regarding the optical susceptibility, MCT presents a zinc blende structure, whose associated point group ($4\bar{3}m$) does not include inversion among its symmetry elements. Therefore, second-order susceptibility contributions $\chi^{(2)}_{ijk}$, where the indices indicate the crystal axes, are allowed, albeit only for $i \neq j \neq k$. In principle, for our [013]-oriented film and normal pulse incidence, a random in-plane orientation could present components along each crystallographic axis. Moreover, the substitutional character of the alloy may relax strict geometric considerations.

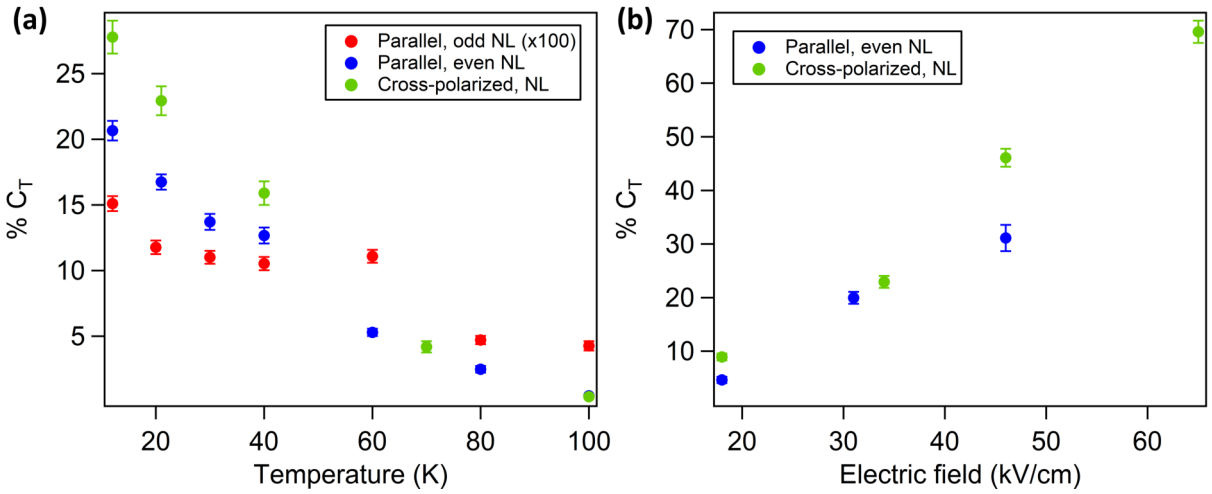

Figure 8.11. C_T ratio for $Hg_{0.825}Cd_{0.175}Te$ in parallel configuration. (a) Temperature dependence with E_1 ∼31 kV/cm, E_2 ∼17 kV/cm. (b) Field dependence varying E_1 and keeping $E_2 \sim 11$ kV/cm T=21 K constant. The values were derived based on Eq. (7.2) using the time domain data along the green dotted lines in Figs. 8.3(a),(b) and 8.5(b). The error bars for the parallel even and cross-polarized contributions are multiplied by a factor 4.

However, in the frequency domain we do not observe any $\chi^{(2)}$-related effect as no Liouville-space pathway of that order can give any contribution at the Cartesian pairs of the observed effects.

For these reasons, we attribute the detected nonlinear features mainly to the third-order $\chi^{(3)}$ electrical susceptibility components which present contributions at the observed locations in the frequency maps.

8.7.3 Role of the electron and holes

As for other small-band gap semiconductors or semimetals, in the presence of an electric field, the carriers are accelerated and can exchange part of their kinetic energy with other carriers at lower energy states creating electron-hole pairs. This phenomenon is known as impact ionization (inverse Auger effect) and has been employed, for example, to enhance small signals in avalanche photodiodes. In MCT, this effect has been widely studied for its applications as infrared detector and its physics differs depending on the stoichiometry [114]. At small band gap values, which depend on the composition variable 'x' and temperature [289], the primary carriers are the electrons in the conduction band. Due to their small masses, linked to the quasi-linear Kane dispersion, the electrons present high mobility, especially at low temperature, together with a weak scattering by optical phonons which let the electrons acquire high kinetic energy. Conversely, the hole bands present smaller mobility due to their heavier effective masses and are subjected to a much more significant optical phonon scattering. This is especially true for the heavy-hole band, the closest in energy to the conduction band, where the effective mass is about two orders of magnitude higher than the electron one. This scheme is experimentally supported by the lack of avalanche breakdown in the gain of MCT diodes [114].

The impact ionization at our sample composition, x∼0.175, is thus mainly connected to the conduction band electron dynamics. A simplified model [114], based on parabolic hole bands and linear Kane dispersion, shows that the ionization rate grows as the band gap is reduced and the electron energy increases. This picture is coherent with the amplitude variation of our nonlinear features both in the temperature and field dependencies.

8.7.4 Temperature and field dependencies

To quantify the temperature and field amplitude dependence of these effects, we make use of the parameter C_R introduced in the previous chapter (Eq. (7.2)), here renamed C_T to highlight the transmission geometry. However, in this case, we substitute E_2 with E_1 for the odd nonlinearities, so that each nonlinear signal is treated together with the corresponding 'probe' pulse.

In Fig. 8.11, C_T was extracted along the same green dotted profiles shown in Figs. 8.3(a),(b) and 8.5(b). The odd C_T temperature trend shows a similar behavior to the even one, where a quasi-parabolic decrease is recognized when considering the entire range.

Reducing the temperature, the band gap is expected to decrease [113][289] as well as the scattering rate attributed to optical phonons [114](depending on the branch), which leads to an increase of the energy the electrons can gain and share with other carriers through impact ionization. Moreover, as the E_1 field amplitude increases, so does the electron energy in the same time or space unit and thus the even nonlinearity, which appears still to be under the saturation limit in our highest-field conditions, as shown when the system is probed by E_2 (Fig. 8.11(b)).

Differently, the E_1 dependence for the odd contribution (Fig. 8.4(c)) exhibits a quasi-constant trend for the amplitude of the odd linearity, which leads to C_T following the denominator trend connected to E_1 itself.

8.7.5 Shape of the nonlinear features

As shown in Fig. 8.8(a), while the position of the peak signal amplitude is almost unchanged throughout the temperature scan, the shape of the (1,1) feature varies with the temperature and assumes a tadpole-like shape at low temperature, with the low-frequency tail becoming more prominent. Comparing these results with the transmitted profiles of the single fields reported in Fig. 8.2(c), we see that the largest frequency content corresponds to the head of the tadpole-like feature. However, the spectral amplitude quickly drops towards 1 THz, where the tail of the nonlinear signal is still present. The origin of such peculiarity may find an explanation in the temperature dependence of the plasma frequency of the sample. Using the carrier concentrations and effective masses reported in [113] and the high-frequency (relative) dielectric constant $\epsilon_\infty \sim 13$ [121], we can estimate the plasma frequency from Eq. (3.9) as

$$f_p = 1/(2\pi)\sqrt{ne^2/(\epsilon_0\epsilon_\infty m^*)} \tag{8.8}$$

where n is the carrier volumetric concentration, ϵ_0 is the vacuum dielectric constant and m^* is the effective mass of the carriers. The resulting plasma frequency shifts from 1.5 THz at 20 K to 2.6 THz at 100 K.

In the 2D frequency maps in the previous chapter and in [200], nonlinearities were registered around the plasma edge, due to the variation in the effective mass or number of carriers after the pump pulse, which may influence the edge position and shape. At higher

temperatures, however, these features tend to be less pronounced due to the increased scattering rate of the active channels (*e.g* phonons and defects). In the present experiment, the combined frequency shift and amplitude reduction of the plasma edge nonlinearities make the low-frequency tail disappear above 40 K. Its low relative spectral amplitude with respect to rest of the signal is likely connected to the low-spectral amplitude around the 'tail' range of the (1,1) odd contribution for the E_1 and E_2 fields (Fig. 8.2(d)).

In the even signal, this particular structure does not seem present. This may be explained by the fact that the pump (E_1) field amplitude is about twice the value for E_2, *i.e.* 31 kV/cm and 17 kV/cm respectively. Far from the saturation, if the plasma frequency is varied due to the increased number of carriers, then one would expect that a higher pump amplitude would lead to a larger shift in the plasma edge position. An additional reduction may be due to the smaller spectral content around 1 THz for E_2 (8.2(c)).

8.7.6 Phase of the nonlinear signal

Regarding the field dependence of the phase of the nonlinear signal shown in Figs. 8.4(d), 8.6(b) for the two polarization schemes, it has been highlighted before that, as the E_1 amplitude is increased, the nonlinear signal peak features shift towards earlier t_{del} values. This can be explained as a consequence of the fact that the polarization state induced by the pump pulse leads to an increase in the propagation speed of the THz pulses in the medium at the observed frequencies. This is more properly depicted in Fig. 8.12 where E_t, E_2, E_t-E_1 and E_{nl} are reported. In particular, if we consider the superposition between E_1 and E_2 to be negligible for the time delays at which the profiles are taken (diagonal profile in Fig. 8.5(b)), panel (c) basically shows the variation of the transmission of E_2 at the different E_1 field amplitudes.

This phenomenon can be related to a reduction of the refraction index (real part) of the medium which decreases with an increase in the number of carriers and thus in the plasma frequency in a Drude-like view (Chapter 3).

8.8 Conclusions

In this chapter, we showed the experimental results of a two-dimensional terahertz study on the mercury cadmium telluride alloy with composition $Hg_{0.825}Cd_{0.175}Te$. The results show large nonlinear response connected to a pump induced change in the polarization of the system which is still non-saturating for the whole field amplitude range explored. The discussion of both the time-domain and frequency-domain effects revealed a modification of the carrier density. This effect can be explained through carrier multiplication via impact ionization, which finds support in the literature [114][292].

Employing different geometries, it is not trivial to directly compare the results obtained in the previous chapter in reflection on the Weyl semimetals with the MCT data in transmission. Moreover, data were acquired in distinct temperature ranges. Nevertheless similar characteristics are shared such as the temperature and field general trends, as well as signatures of nonlinear effects appearing close to the plasma edge. The fact that HgCdTe exhibits larger nonlinearities compared to the ones at analogous temperatures for the Weyl semimetal may be favored by the low, but finite, carrier concentration in the

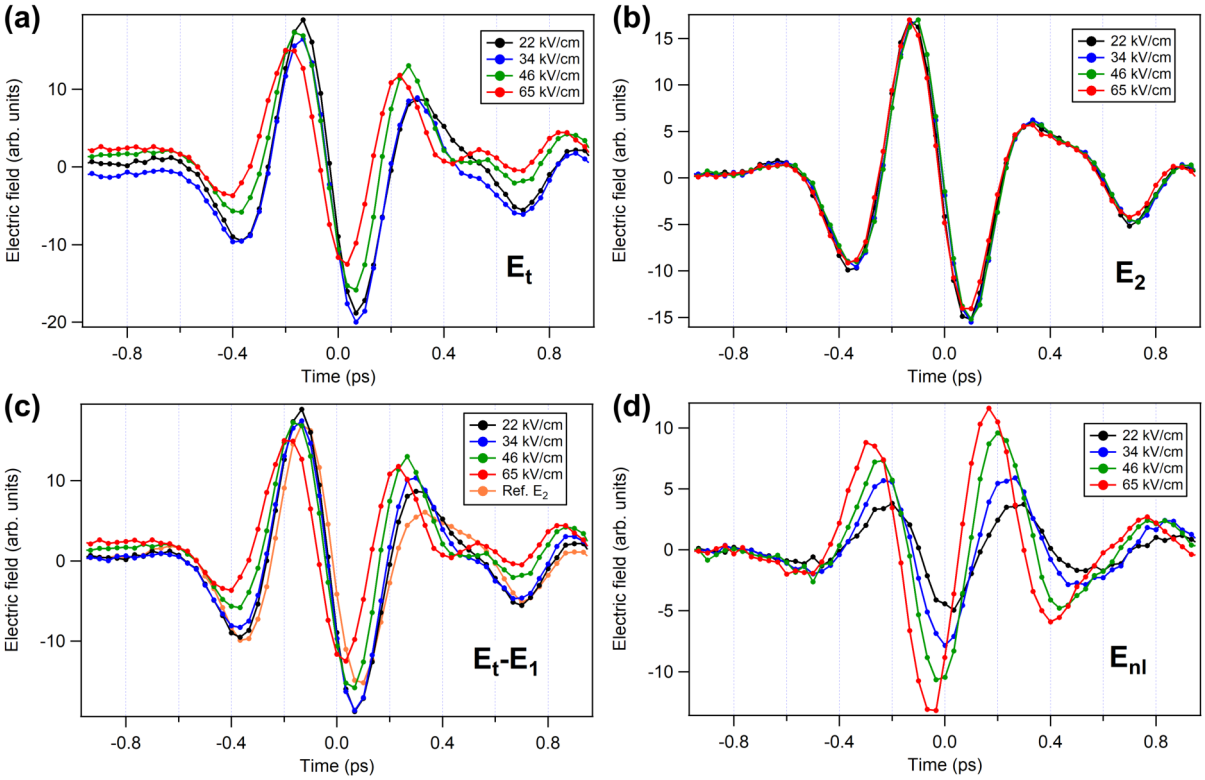

Figure 8.12. (a) Total signal E_t (b) E_2 (c) E_t - E_1 (d) E_{nl} in the same conditions as Fig. 8.6(b).

conduction band which gives a much lower plasma frequency. As this parameter depends on the square root of the carrier density, a smaller number of generated carriers can produce a large change on the dielectric properties, provided that the other parameters are comparable. This would affect both reflectivity and absorption properties of the system. However, it can also be influenced by the highly-extended linear dispersion of the double-cone giving high mobility characteristics also to carriers that are far from the bottom of the conduction band.

CHAPTER 9

Conclusions

The presented PhD project revolved around the ultrafast dynamics of the electronic and lattice degrees of freedom in Weyl and Kane quantum materials, resolving the out-of-equilibrium-response of the investigated systems to ultrashort laser pulses in various photon energy ranges to be particularly sensitive to peculiar features of the response.

In the first experiment in Chapter 5, we focused our attention on the time-resolved broadband reflectivity of WTe_2, analyzing the effects induced by a 800 nm laser pulse on the optical properties of the material in the near-infrared/visible energy ranges. Taking advantage of the broadband character of the probe, it was possible to extract the frequency-dependent effects of the coherent optical phonons on the reflectivity and, employing a strategy based on density functional theory to calculate the optical properties from first principles, to quantify the amplitude of the coherent motion by comparison between experimental and simulated results. Such approach allowed to evaluate the atomic displacements with a precision of a few femtometers and without free tuning parameters, except from a scaling factor determined by a global comparison between experimental data and numerical simulations of the broadband DR/R signal. Regarding WTe_2, we obtained a good agreement between the frequency dependence of the registered and calculated phonon effects on the reflectivity for both in-plane crystal axes. The broadband character is an essential feature of the experiment to reliably derive a quantification of the magnitude of displacements, especially when multiple and intertwined phonon modes are present. Simultaneous acquisition of the reflectivity for an extended range is to be preferred over a series of single-color experiments, where experimental condition may change during the single energy step. The presented method is not system-specific and in principle can be extended to any crystalline material, provided that its optical properties in the broadband range are appreciably perturbed by the coherent lattice motion. This strategy can be also viewed as an alternative route compared to standard structural dynamics methods to derive the amplitude of the oscillations, usually only possible in large scale facilities. However, the wide spread of table-top laser systems allows rapid access to a method which could be employed for the design of peculiar devices where the coherent lattice motion is controlled to carefully tune the functional properties of the material.

The coherent motion was central also in the experiment presented in Chapter 6. Once again, we studied the structural response of WTe_2 to a 800 nm light excitation, although this time we exploited time-resolved x-ray diffraction using hard x-ray pulsed generated by a free electron laser to measure the intensity of selected Bragg peaks. We showed that the collective motion has a significant impact on the electronic band structure properties of the material. The energy levels were found to be not only subjected to a non-uniform change, but also to a modification of the band curvature as well. The electron and hole pockets, at whose intersections Weyl points may be found, are involved in the electrical transport, which is expected to vary due to changes in the effective masses, through the band curvature. The occurrence of such phenomenon is expected to impact on various transport properties such as electrical transport through a fast modification of its extremely high magnetoresistance and thermoelectric performance which are of particular interest for low effective mass systems. Its rapid phonon-induced oscillations could find use as modulators, simple function generators and test devices for high frequency application which are expected to become of high interest given the continuous growth of telecommunications and the necessity of fast big data exchanges. Comparing the estimations of the coherent phonon amplitudes, we found a reasonable agreement between the two experiments reported Chapter 5 and Chapter 6.

The THz experiments were reported in Chapters 7 and 8. In the first chapter, we showcased the results of nonlinear response through the two-dimensional spectroscopy of a type I-, TaAs, and a type II-, WTe_2 Weyl semimetals, which were analyzed through temperature and field amplitude dependence studies. While the level of the nonlinearity depends on the material and, in principle, on the THz polarizations, similar characteristics are shared. The nonlinearities are understood as the result of impact ionization leading to carrier multiplication due to the acceleration of electrons by the driving THz pulse, giving a transient nonlinear polarization for the material. Due to their coordinates in the frequency maps, these pump-probe effects were assigned to variations in the third-order electric susceptibility tensor. Physically speaking, the smaller nonlinear response in WTe_2 could be linked to its high carrier concentration compared to TaAs. In fact, as the plasma frequency of a Drude-like term depends on the square root of the number of carriers, it is necessary to a generate a larger number of new quasi-free carriers to provoke a comparable change in the edge position and tilt. An accurate modelization of the scattering terms, *e.g.* through density functional theory, is required to give quantitative estimations for the change in the parameters. The distinct carrier concentrations are likely important factors in determining why the plasma edge does not appear to vary its frequency position through the thermal activation of carriers, even though the electron pockets size in the Fermi surface is expected to largely grow due to the shift of the chemical potential as the sample is heated up. Additional investigations are necessary to obtain the specific parameters of the ionization process, whose values, in principle, may differ among the samples due to a different position of the Fermi level at equilibrium. Nonetheless, the complex band structure of the Weyl semimetals may pose a computational challenge to map its dispersion in detail, given that it gradually deviates from the quasi-linear Weyl dispersion as one goes further away from the Weyl points. An advanced model and the experimental determination of the Fermi level could help to unequivocally identify the nonlinear signal as a signature of the high-mobility carriers near the Weyl points.

In the second chapter about THz, we presented the experimental results on HgCdTe. The results show large nonlinearities connected to a pump effect leading to a change in the polarization of the system. Focus of the analysis was the discussion of both the time-domain and frequency-domain effects, where characteristics of a carrier density change

were resolved. The effect can be explained through carrier multiplication via impact ionization, studied for the equilibrium properties of HgCdTe-based infrared detectors in the literature. The nonlinear effects in the investigated range are not saturated even for the highest pump field amplitude, in spite of assuming very large nonlinear values.

Exploiting different setting, it is not straightforward to compare the results for the three sampled materials, since they explore different observables (reflectivity and transmission) and separate temperature ranges. Nevertheless, we may identify similar characteristics through the temperature and field general trends, as well as the fact that the signatures of nonlinear effects appear around the frequency position of the plasma edge. HgCdTe exhibits larger nonlinearities compared to the others, even when similar temperature conditions are compared. The phenomenon may be favored by the low, but finite, carrier concentration in the conduction band which gives a much lower plasma frequency. As this parameter depends on the square root of the carrier density, a smaller number of generated carriers can produce a larger change on the dielectric properties, provided that the other parameters are only slightly modified. However, the highly-extended linear dispersion of the double-cone should play an important role giving high mobility characteristics also for carriers that are driven far from the bottom on the conduction band, which in not the case for the examined Weyl semimetals. Even though a Drude model is already used to rationalize the results, a more quantitative model is under work to describe the THz-induced nonlinearities.

To conclude, this thesis work provides not only an experimental characterization of the electronic and lattice dynamics in Weyl and Kane materials in out-of-equilibrium conditions, but also shows the importance of the complementary use of models and numerical simulations to fully understand the physical picture. Moreover, this combination is central to quantitatively calculate the impact of out-of-equilibrium modifications on fundamental observables connected to the most important properties of these materials. The powerful synergy between experiment, theory and simulation is expected to play a key role for the implementation and calibration of nonequilibrium effects in innovative devices, in particular those relying on peculiarities of the electronic band structure.

Appendices

APPENDIX A

Anisotropic optical properties

We report as reference data, the anisotropic optical properties of WTe_2 derived from the data published in [68] for the light polarized along the two in-plane axes (the cell geometry can be found in Chapters 5 and 6).

A polar graph based on Snell's law (Fig. A.1) shows relationship between incident and refracted angles given with respect to the surface normal, assuming an interface between air (n∼1) and WTe_2.

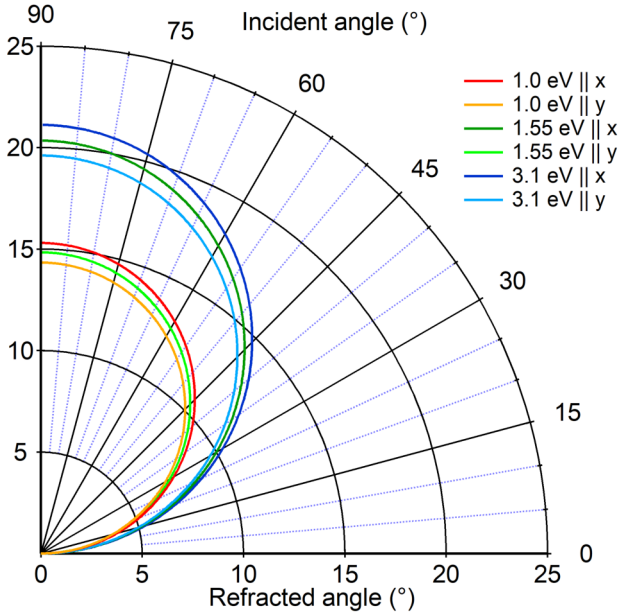

Figure A.1. Polar graph showing the relashionship between incident angle and refracted angle with respect to the surface normal for WTe_2 at the photon energies employed in Chapter 5.

Fig. A.2 showcases graphs reporting the complete frequency-dependence of the real (n) and imaginary (k) parts of refractive index, the reflectance (R) and the intensity penetration depth (IPD) are obtained directly from the dielectric function [59].

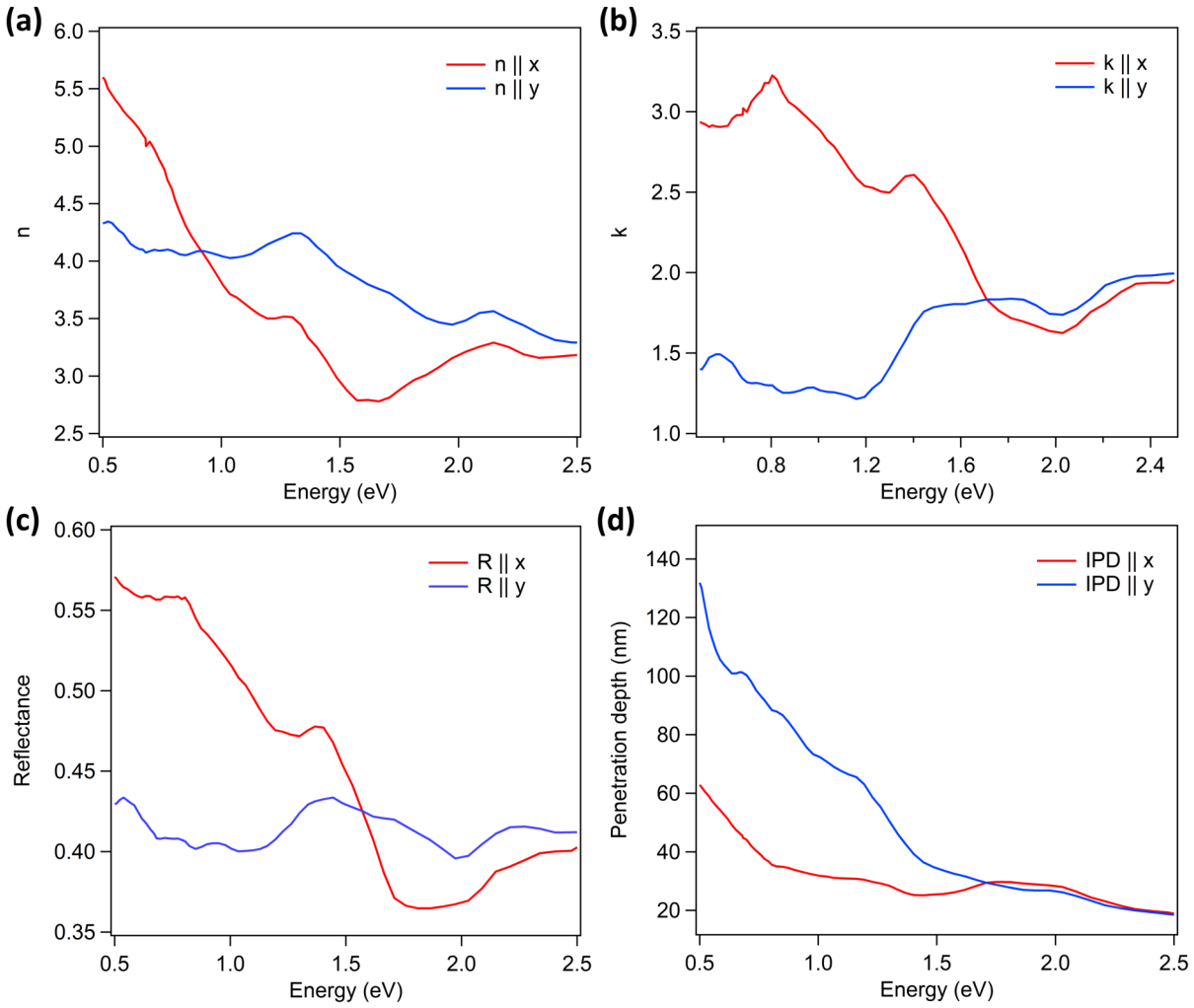

Figure A.2. Optical properties of WTe_2 derived from the data published in [68] for the light polarized along the two in-plane axes. (a) Real part of the refractive index. (b) Imaginary part of the refractive index. (c) Reflectance. (d) Intensity penetration depth.

APPENDIX B

FTIR spectroscopy on WTe_2

To characterize the WTe_2 sample, we performed polarization-resolved Fourier transform infrared spectroscopy (FTIR) using a table-top spectrometer (Bruker ®). Although designed for chemical applications, it can be still employed for an estimation for the reflected or transmitted intensities. Taking this into account, we allow a rescaling of the intensities for the comparison with the literature, while the frequency positions are left untouched. Using distinct beamsplitters, it was possible to select different spectral ranges starting from the far-infrared to the near-infrared spectral ranges coming from the IR source. The samples were glued on a copper plate using silver paste and placed on a cold finger inside the vacuum chamber of the cryostat. To avoid reflected light coming from the sample holder, the bare sample holder and the contour of the sample were masked using black paper. The sample compartment and the vacuum chamber are then pumped and liquid helium was used to cool down the cold finger. The reflected light is then directed in the interferometer section and finally to the MCT detector. The results are reported in Fig. B.1.

The comparison reveals a very good correspondence with the frequency positions of the plasma edges found in the literature [68]. The 'gaps' in the data are due to lack of light between subsequent beamsplitter ranges. The small oscillations are artifacts from the spectrometer.

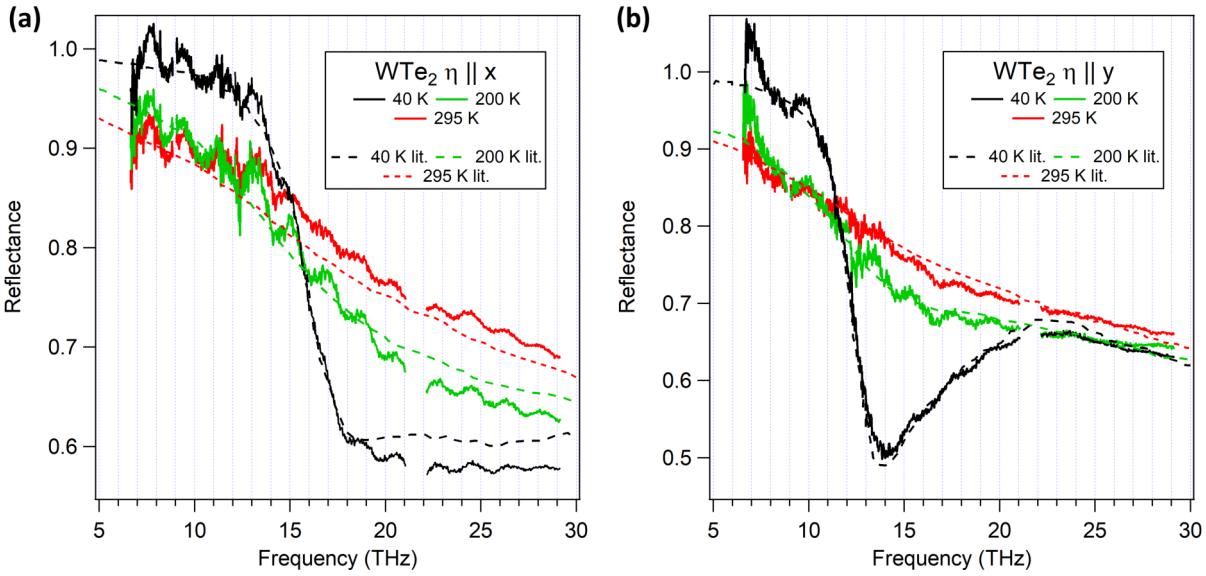

Figure B.1. FTIR spectroscopy on WTe_2 using linearly polarized light. (a) Polarized || x. (b) Polarized || y.

APPENDIX C

Pixel-resolved evolution of the Bragg peaks

In Chapter 6, the time-resolved x-ray experiment results are given in terms of $\Delta I/I$, which represents the ratio between the laser-induced variation in the diffraction intensity and the unpumped value for a certain Bragg peak. These are integrated values over a region of interest, i. e. a certain number of pixels forming an area, of the detector.

Thanks to the large number (1.5 million) and density of pixels in the Jungfrau detector at the Bernina beamline at SwissFEL [257], one can also obtain information regarding the shape of the peak and its time-dependent evolution after a pump pulse.This can be done by considering specific regions of interest (ROIs) and may be also used to monitor the uniformity of the crystal around the probed area. Here we report two examples of this analysis: for the Bragg peaks $(\bar{1}62)$ and $(\bar{1}46)$. In Figs. C.1, framesm146, we showcase four distinct time-delays: before time-zero, at the first maximum of the shear mode, at the first minimum of the shear mode and at long time-delays, where the shift of the peak appears (red area is where it migrated). An alternative way to plot this data is to take 'slices' of the pixels and and collect them for all the time frames. Examples are shown in Figs. C.2, Fig. C.3 and Fig. C.5. Even though it was not the main objective of the performed study, this analysis gives a possible indication of an additional acoustic phenomena occurring as the system is pumped. This particular was resolved for peak $(\bar{1}46)$ and it is presented in Fig. C.5. Differently, we could not resolve a similar phenomenon for the other Bragg peaks, which might be an indication that the $(\bar{1}62)$ peak is particularly sensitive to it through the change in the atomic position. In [35], where thin films ($\sim$50 nm) were used, acoustic breathing mode oscillations were resolved. In our case, the sample is much thicker (a few hundreds of microns). The acoustic propagation in bulk metallic compounds is connected to the presence of a temperature gradient along the perpendicular direction with respect to the surface, generated by the energy deposition given by the pump pulse. The density of 'hot electrons' and the couplings between the electronic and lattice subsystems is what determines the type of response and its timescale

[293][294][295].A reciprocal space to direct space mapping could provide more information regarding its particular pixel-resolved behavior in our thicker sample.

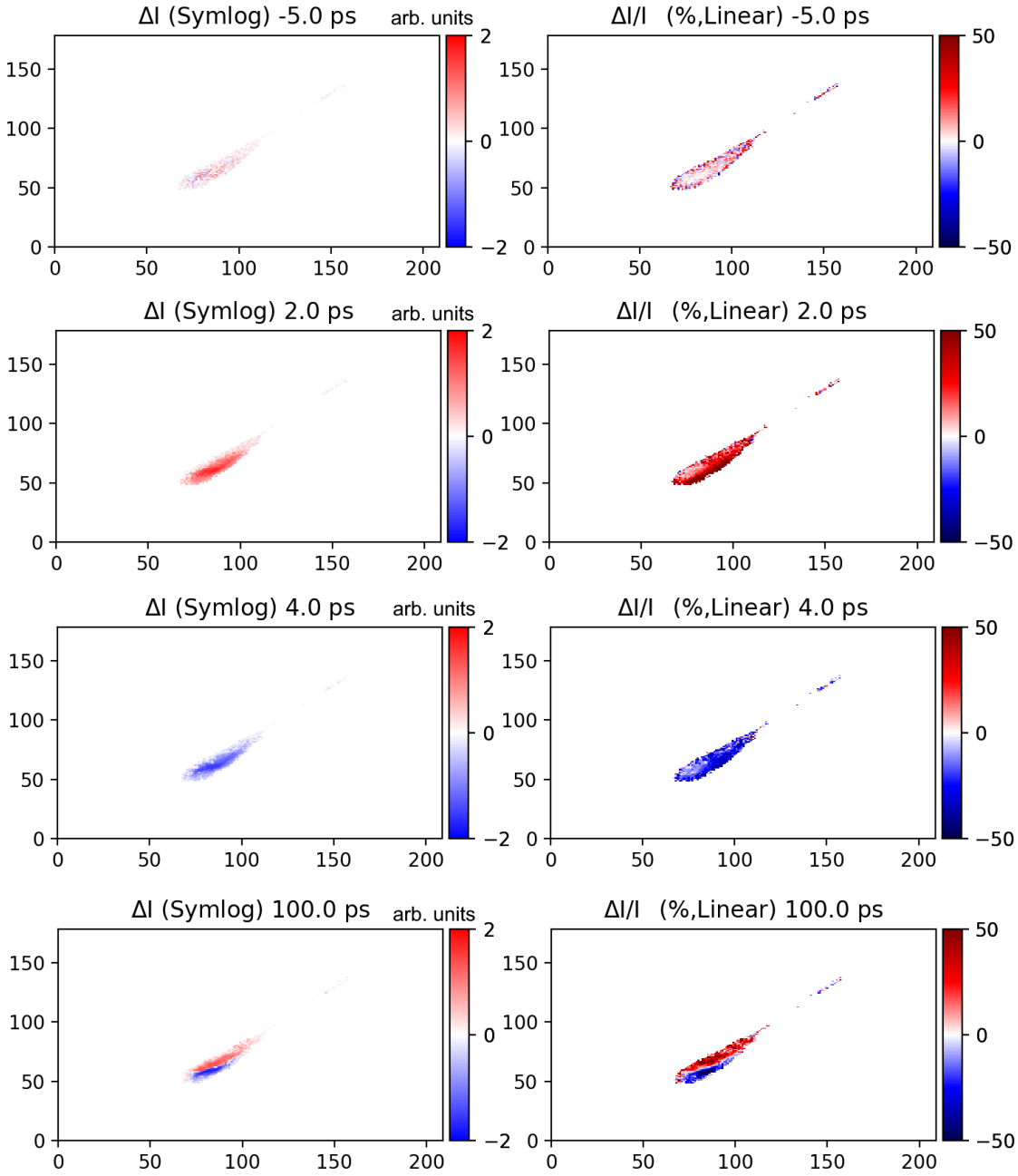

Figure C.1. Pixel-resolved (a) ΔI, with a symmetric logarithmic color scale, and (b) ΔI/I, with a linear color scale, evolution of the registered intensity at selected time delays for Bragg peak ($\bar{1}62$).

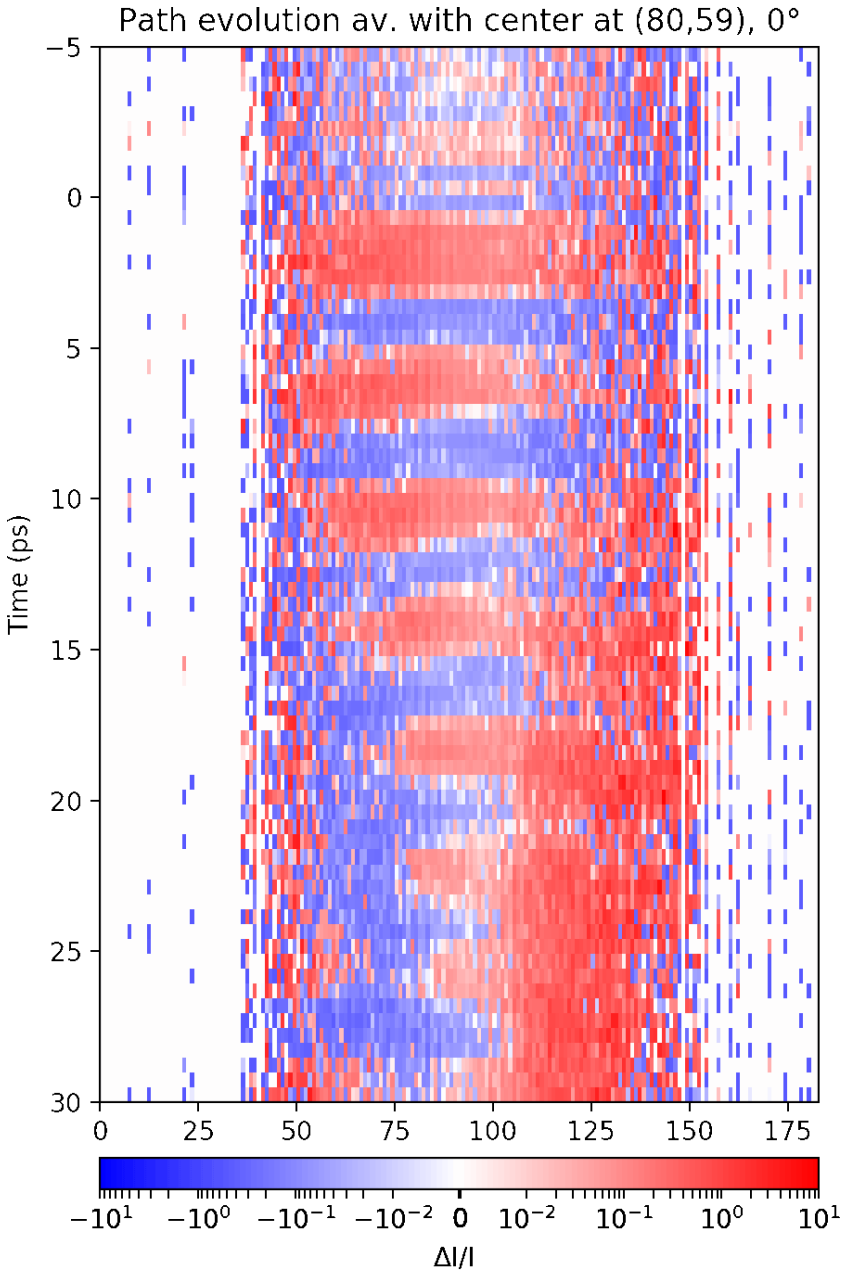

Figure C.2. Pixel-resolved ΔI/I, with a symmetric logarithmic color scale, evolution of the registered intensity for a specific saw-tooth-like cut (the few lateral pixels are used to highlight the uniformity of the effects) passing through the peak at (80,59) pixel coordinates with a 0° angle with respect to the y-axis (the same ROI was used for the panels in Fig. C.1) for Bragg peak $(\bar{1}62)$ in a smaller time-window, showing the impact of the phonon effects.

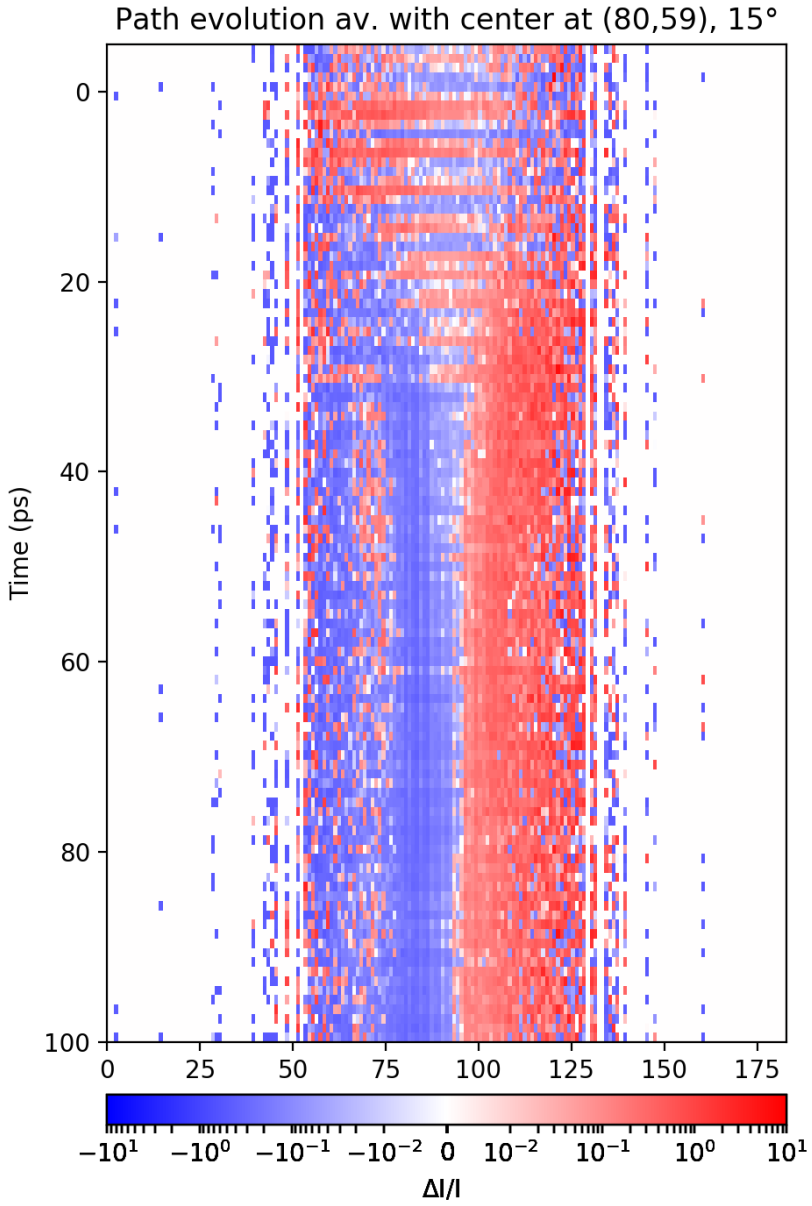

Figure C.3. Pixel-resolved ΔI/I, with a symmetric logarithmic color scale, evolution of the registered intensity for a specific saw-tooth-like cut (the few lateral pixels are used to highlight the uniformity of the effects) passing through the peak at (80,59) pixel coordinates with a 15° angle with respect to the y-axis (the same ROI was used for the panels in Fig. C.1) for Bragg peak ($\bar{1}62$) in a larger time-window.

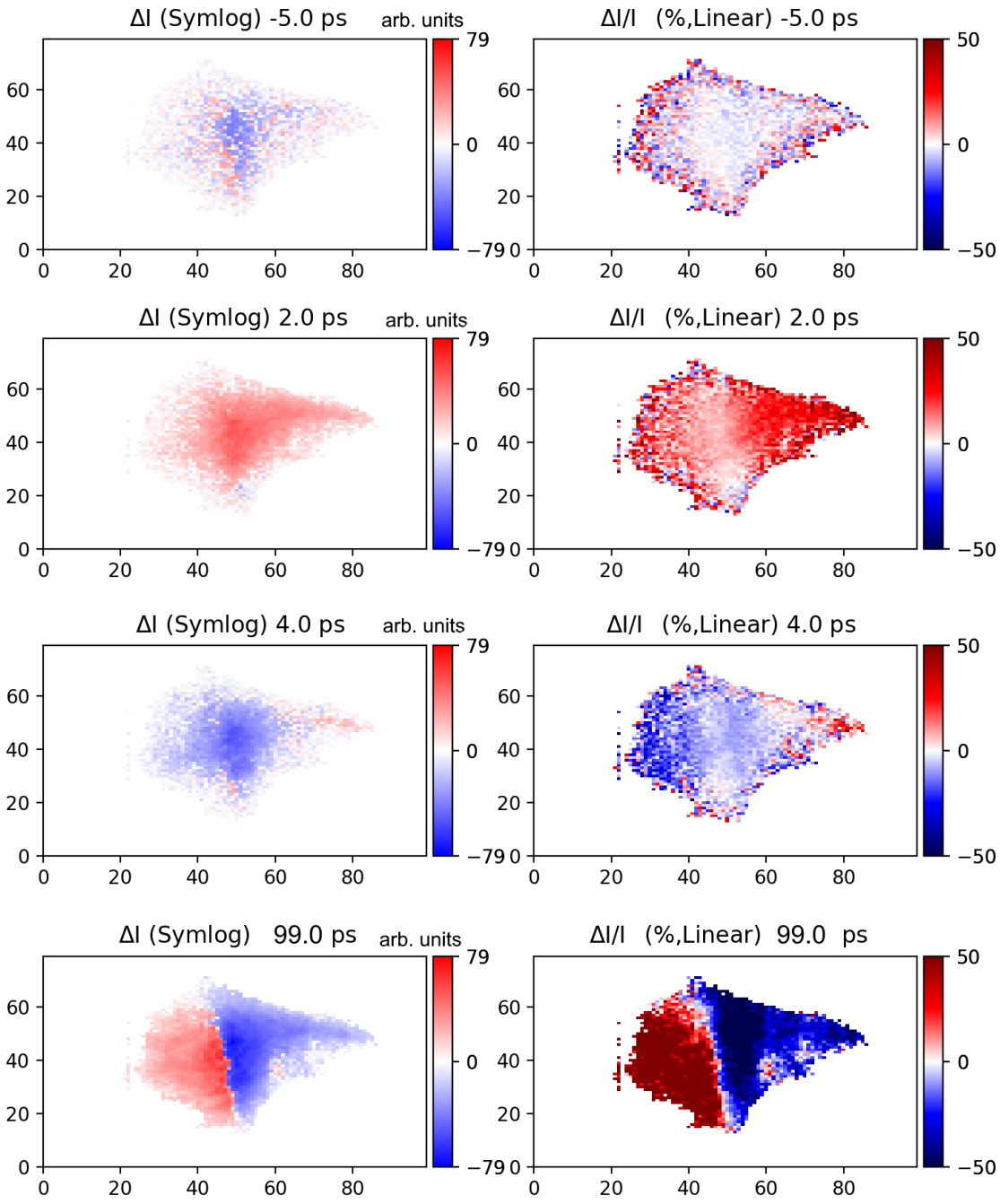

Figure C.4. Pixel-resolved (a) ΔI, with a symmetric logarithmic color scale, and (b) ΔI/I, with a linear color scale, evolution of the registered intensity at selected time delays for Bragg peak ($\bar{1}46$).

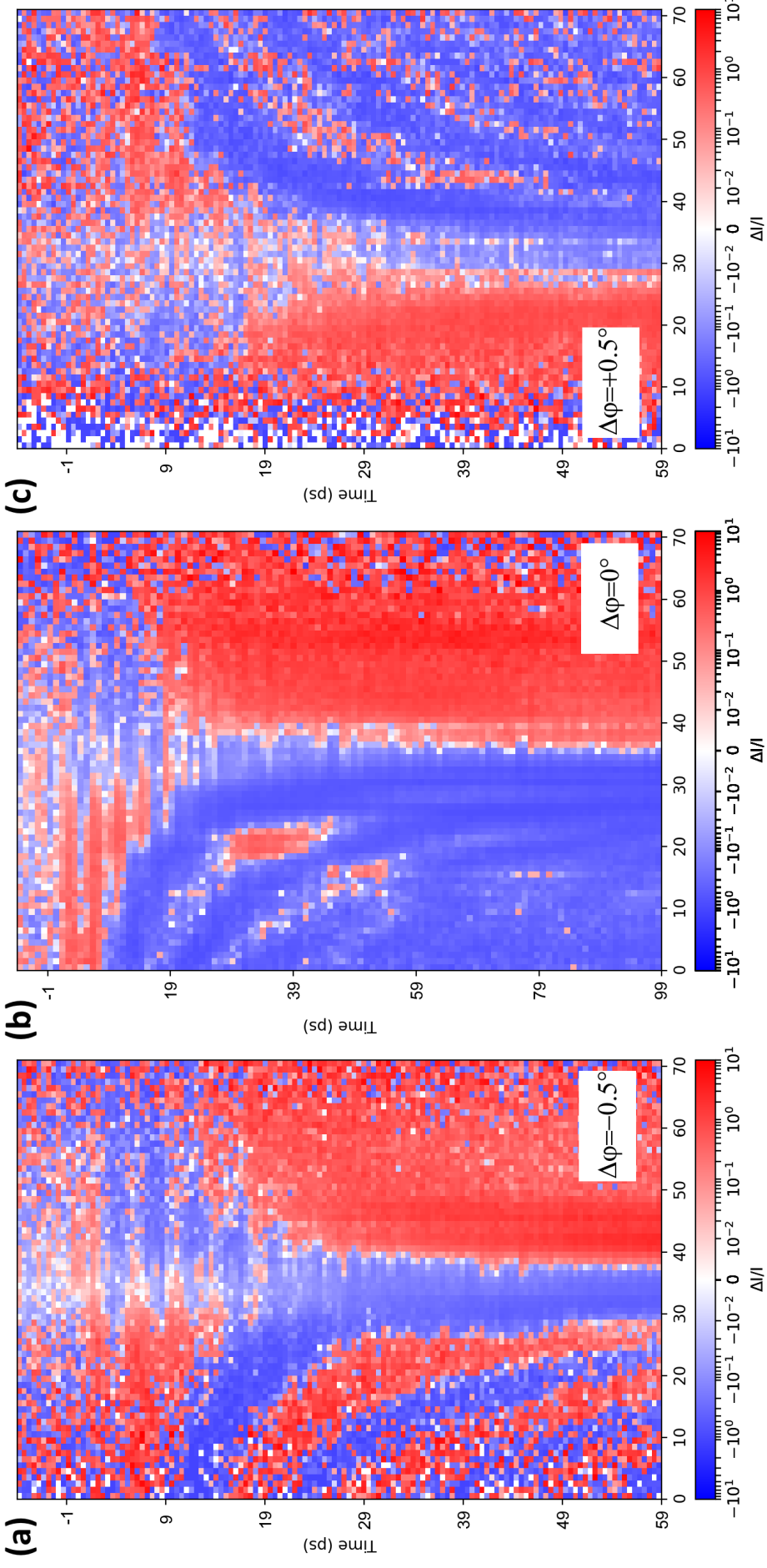

Figure C.5. Pixel-resolved ΔI/I, with a symmetric logarithmic color scale, evolution of the registered intensity for a specific cut passing through the peak maximum for (a)$\Delta\varphi$=-0.5° (b) $\Delta\varphi$=0° (c) $\Delta\varphi$=+0.5° from the optimal diffraction condition. The images are obtained as the time evolution of the data associated to a straight profile; specifically panel (b) can be visualized as a succession of profiles centered at (46,49) pixel coordinates with a 90° angle with respect to the y-axis (the same ROI was used for the panels in Fig. C.4) for Bragg peak ($\bar{1}46$); where signatures, appearing as 'blue fingers', of coherent acoustic effects are present.

APPENDIX D

Phononic impact on the charge density in WTe_2

The phonon modes in WTe_2 are also responsible for a change in the charge density. Focusing on the first two modes (0.25 and 2.5 THz), we report in Figs. D.1, D.2 the variation of the charge density difference, defined as the difference between the charge density and the one of the isolated atoms reported previously in Figs. 6.17(c),(d), 6.18(b), which we call 'shared charge', which is connected to the presence of interatomic interactions, in particular with the formation of the in-plane W-W and W-Te covalent bonds. The atomic positions shown are the equilibrium ones. This gives an indication of how the 'shared' charge moves with the phonon modes. For the shear mode (0.25 THz), we also verified that only minor differences are found when considering a uniform shift instead of the eigendisplacement (Fig. 6.5(a)) from density functional perturbation theory, where very small differences between the atomic shifts were obtained, as it was discussed in Chapter 6.

In principle, the most natural way to analyze this the charge variation connected to these different configurations would be to consider the difference between the total charge densities. However, due to the extension of the electronic clouds, the result is dominated by the shift of the 'unshared charge', *i.e.* the superposition of the atomic charge of the isolated atoms, rather than the 'shared charge'. Nevertheless, these graphs give a qualitative description to see how the bonding charge density is modified.

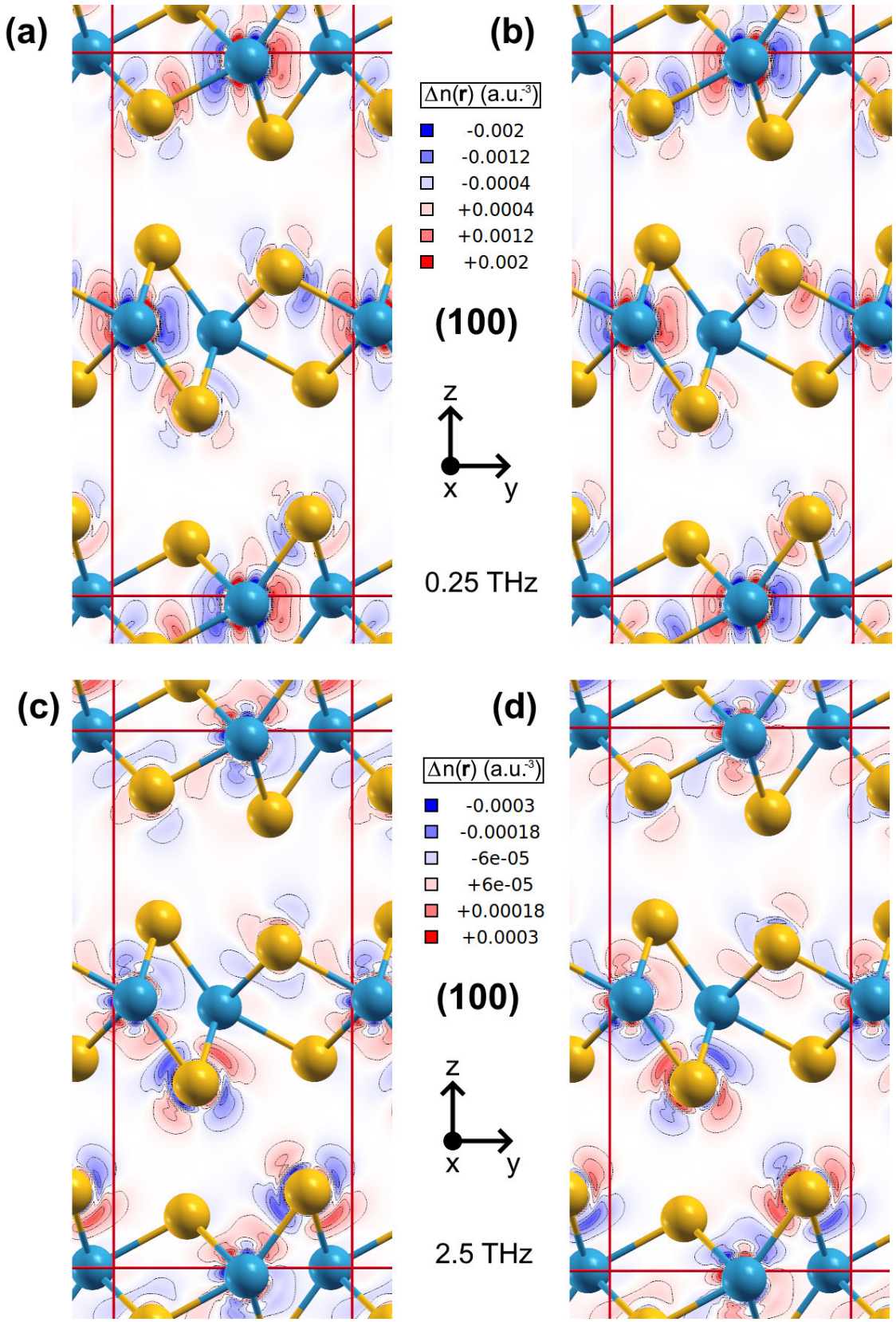

Figure D.1. Impact of the phononic displacements on the charge density difference in the (100) plane (Figs. 6.17(c),(d)). (a),(b) Effects of a 2.5 pm shift along the 0.25 THz mode in the eigendisplacements direction (see Fig. 6.5) and opposite to them respectively. (c),(d) Effects of a 300 fm W#1 z-shift along the 2.5 THz mode in the eigendisplacements direction (see Fig. 6.5) and opposite to them.

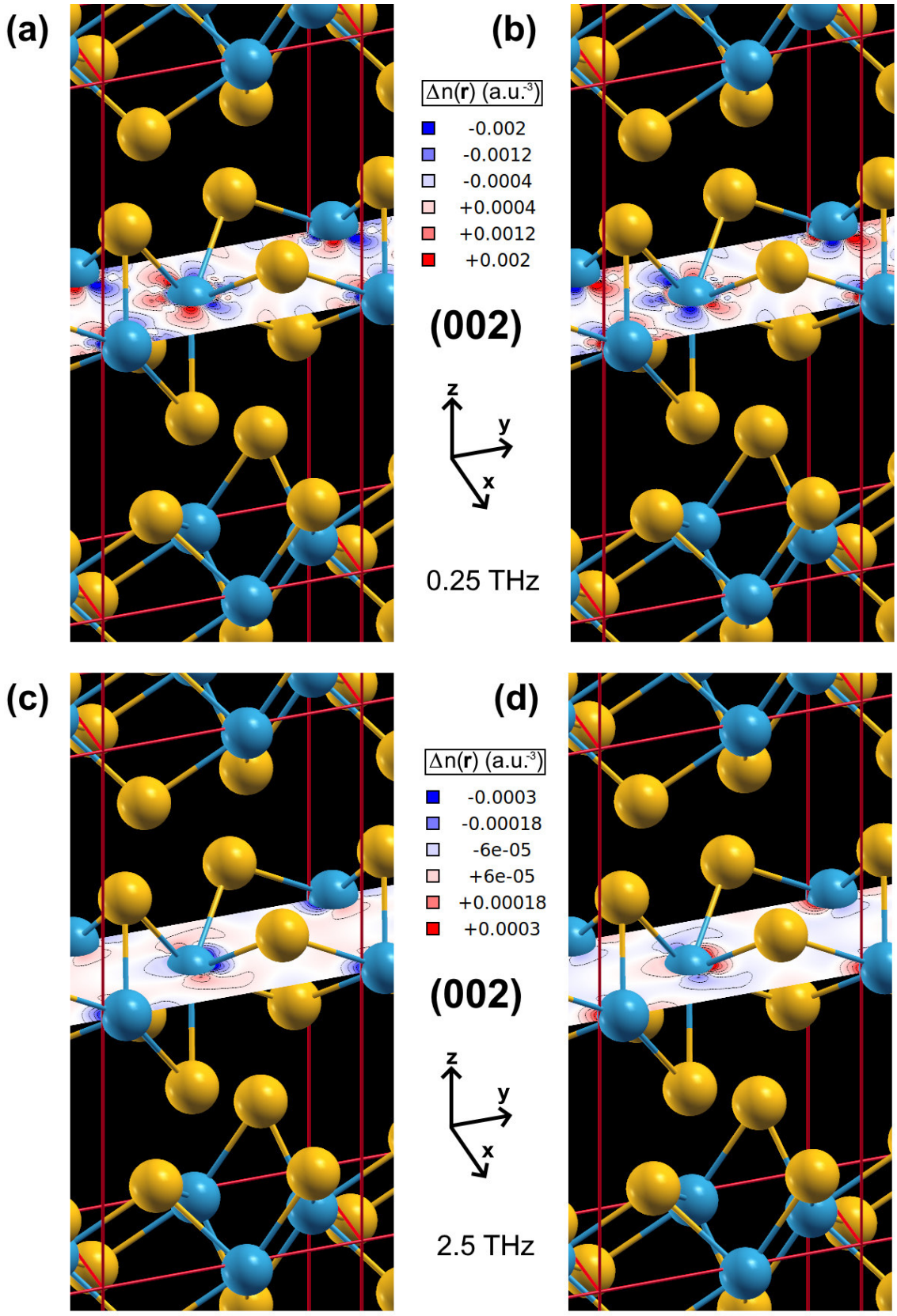

Figure D.2. Impact of the phononic displacements on the charge density difference in the (002) plane (Fig. 6.18(b)). (a),(b) Effects of a 2.5 pm shift along the 0.25 THz mode in the eigendisplacements direction (see Fig. 6.5) and opposite to them respectively. (c),(d) Effects of a 300 fm shift W#1 z-shift along the 2.5 THz mode in the eigendisplacements direction (see Fig. 6.5) and opposite to them.

APPENDIX E

2D THz spectroscopy on TaAs

In this appendix, I report the two-dimensional THz maps, both in the time and frequency domains, for TaAs, which were not included in Chapter 7.

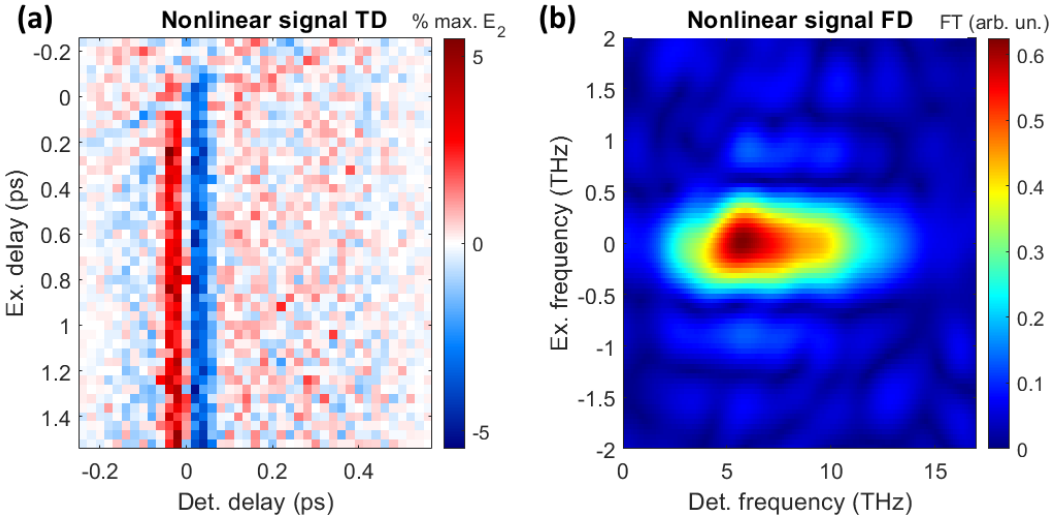

Figure E.1. Two-dimensional THz mapping of the nonlinear signal in TaAs for E_1 ∼500 kV/cm, E_2 ∼45 kV/cm and T=110 K. (a) Time domain. (b) Frequency domain.

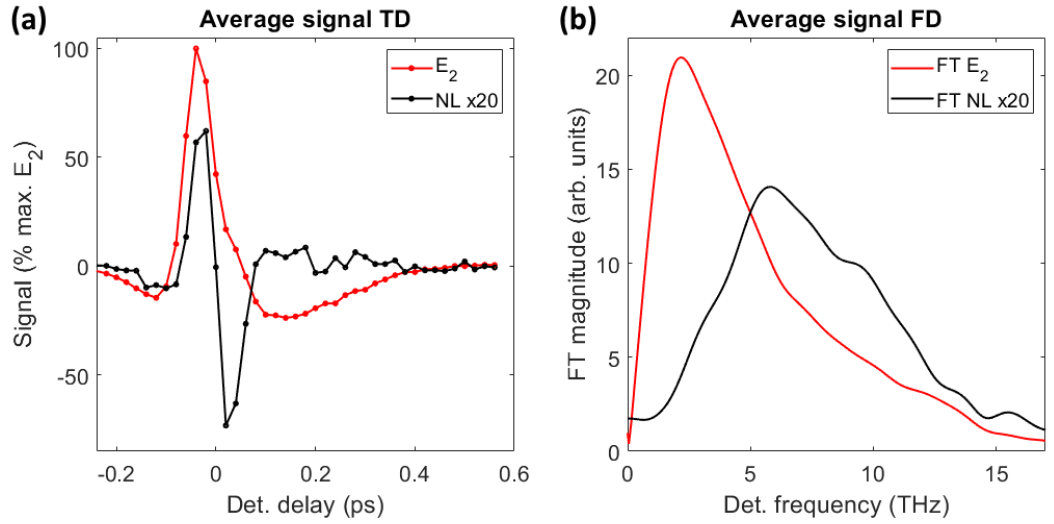

Figure E.2. Profiles extracted from the two-dimensional THz mapping in TaAs for E_1 ∼500 kV/cm, E_2 ∼45 kV/cm and T=110 K. (a) Time domain. (b) Frequency domain. For each panel E_2 and E_{nl} were extracted from the same temporal ranges (0.3-0.7 ps) and compared.

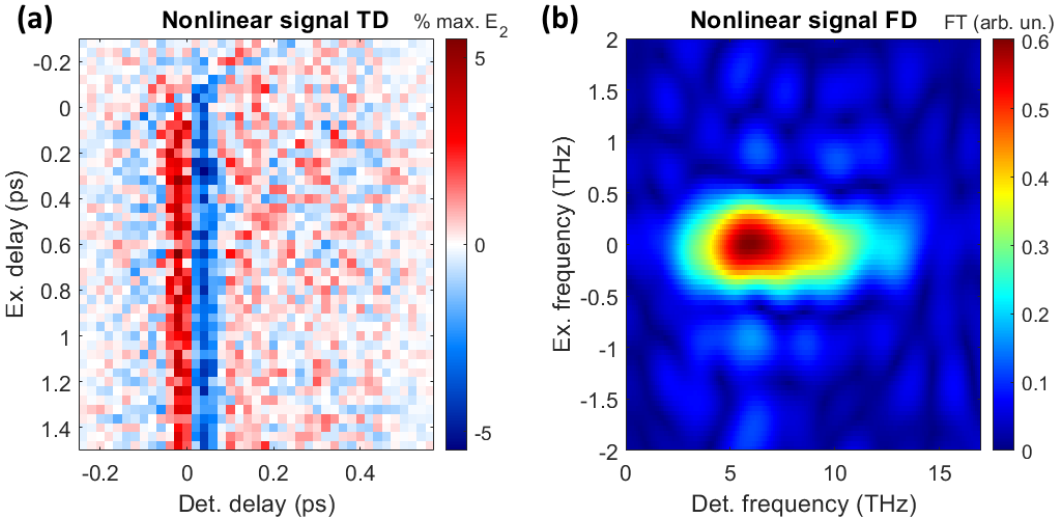

Figure E.3. Two-dimensional THz mapping of the nonlinear signal in TaAs for E_1 ∼427 kV/cm, E_2 ∼45 kV/cm and T=110 K. (a) Time domain. (b) Frequency domain.

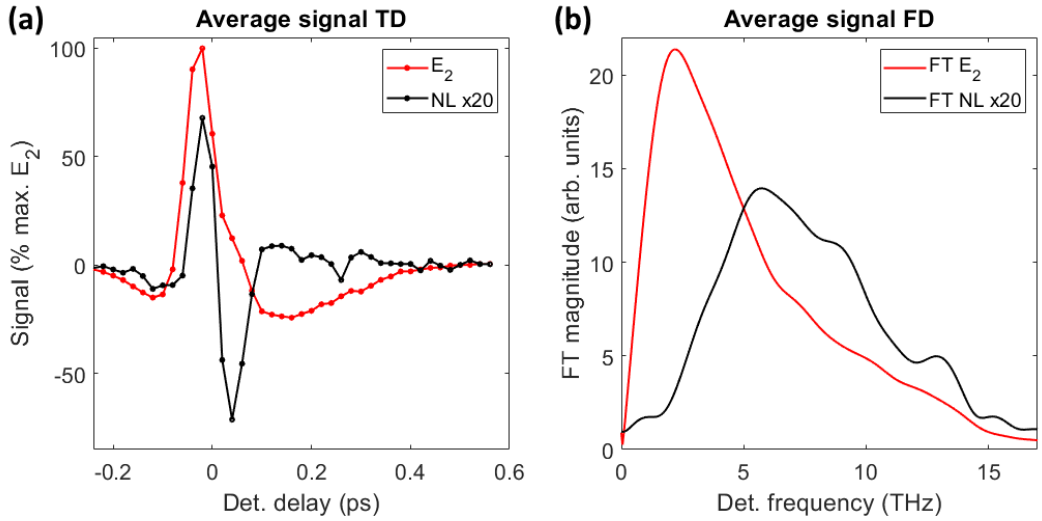

Figure E.4. Profiles extracted from the two-dimensional THz mapping in TaAs for E_1 ∼427 kV/cm, E_2 ∼45 kV/cm and T=110 K. (a) Time domain. (b) Frequency domain. For each panel E_2 and E_{nl} were extracted from the same temporal ranges (0.3-0.7 ps) and compared.

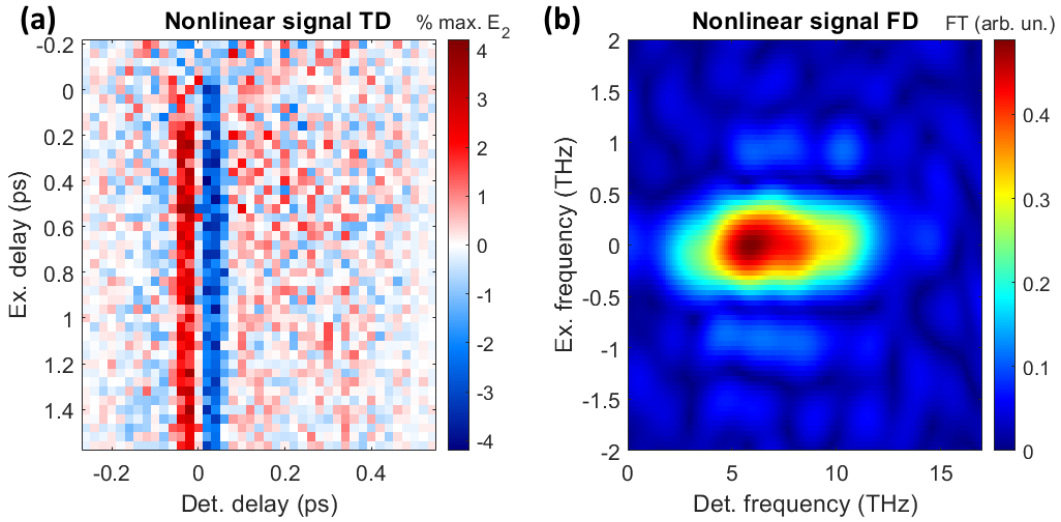

Figure E.5. Two-dimensional THz mapping of the nonlinear signal in TaAs for E_1 ∼345 kV/cm, E_2 ∼45 kV/cm and T=110 K. (a) Time domain. (b) Frequency domain.

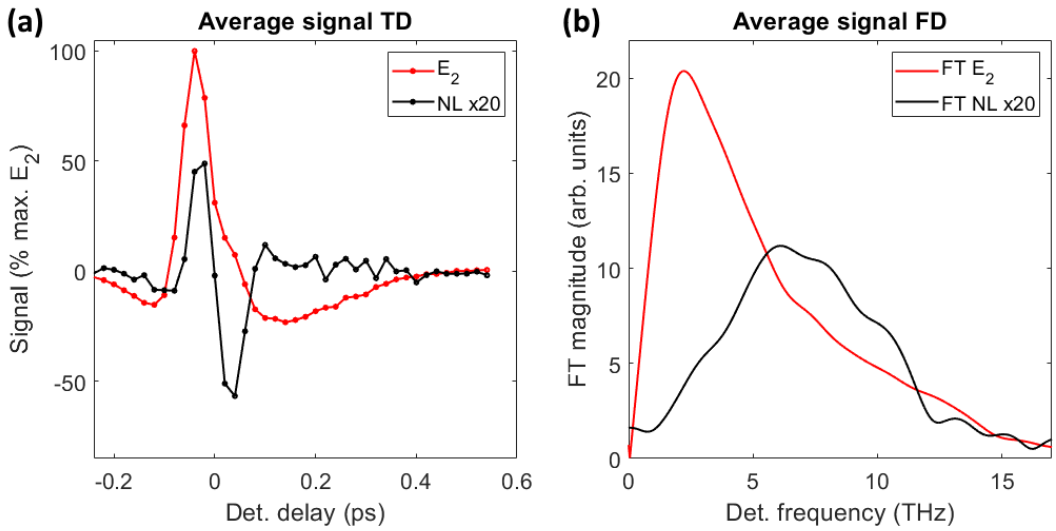

Figure E.6. Profiles extracted from the two-dimensional THz mapping in TaAs for E_1 ∼345 kV/cm, E_2 ∼45 kV/cm and T=110 K. (a) Time domain. (b) Frequency domain. For each panel E_2 and E_{nl} were extracted from the same temporal ranges (0.3-0.7 ps) and compared.

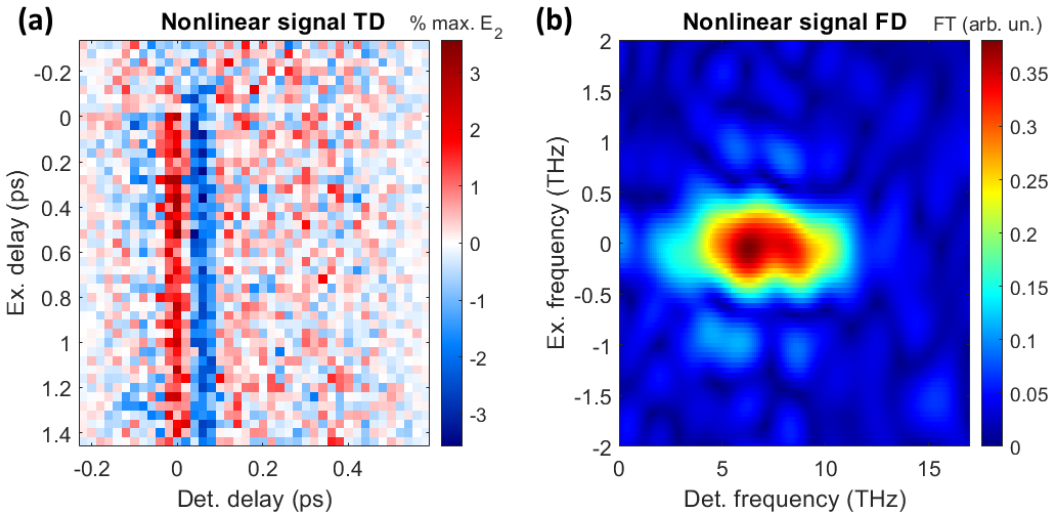

Figure E.7. Two-dimensional THz mapping of the nonlinear signal in TaAs for E_1 ∼241 kV/cm, E_2 ∼45 kV/cm and T=110 K. (a) Time domain. (b) Frequency domain.

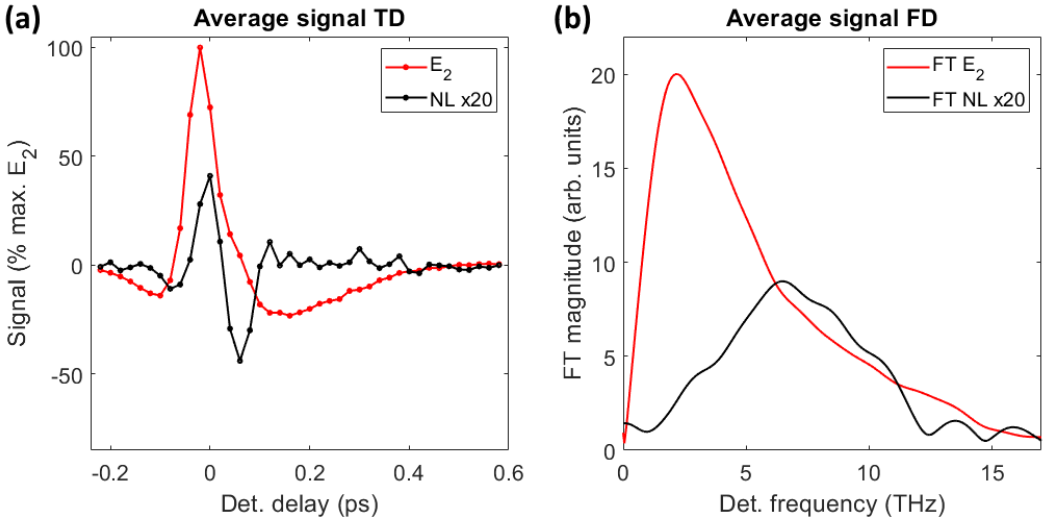

Figure E.8. Profiles extracted from the two-dimensional THz mapping in TaAs for E_1 ∼241 kV/cm, E_2 ∼45 kV/cm and T=110 K. (a) Time domain. (b) Frequency domain. For each panel E_2 and E_{nl} were extracted from the same temporal ranges (0.3-0.7 ps) and compared.

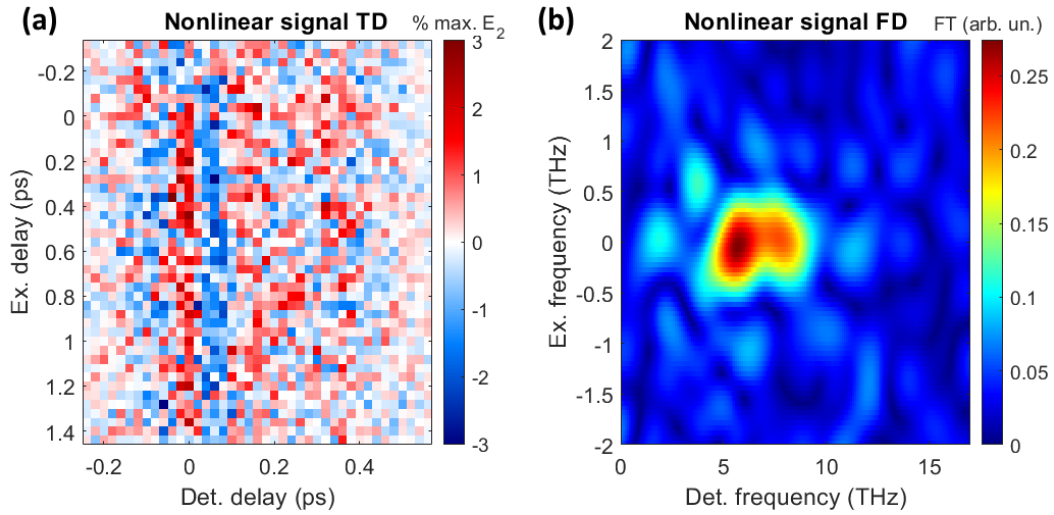

Figure E.9. Two-dimensional THz mapping of the nonlinear signal in TaAs for E_1 ∼144 kV/cm, E_2 ∼45 kV/cm and T=110 K. (a) Time domain. (b) Frequency domain.

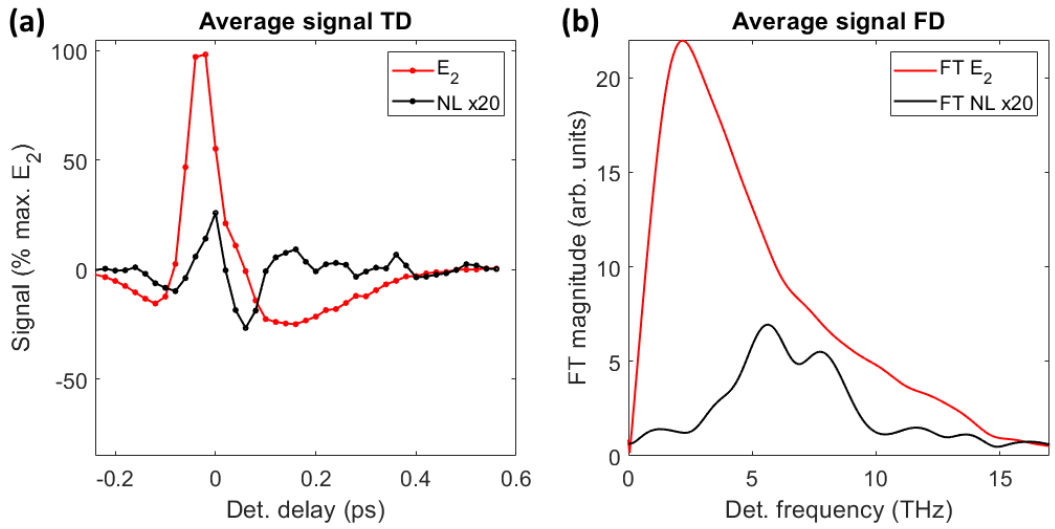

Figure E.10. Profiles extracted from the two-dimensional THz mapping in TaAs for E_1 ∼144 kV/cm, E_2 ∼45 kV/cm and T=110 K. (a) Time domain. (b) Frequency domain. For each panel E_2 and E_{nl} were extracted from the same temporal ranges (0.3-0.7 ps) and compared.

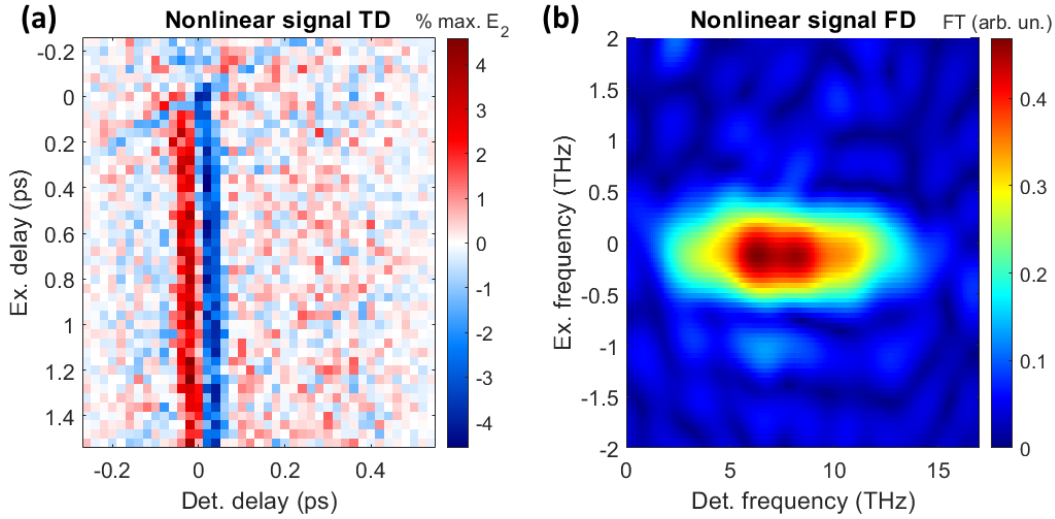

Figure E.11. Two-dimensional THz mapping of the nonlinear signal in TaAs for E_1 ∼570 kV/cm, E_2 ∼45 kV/cm and T=130 K. (a) Time domain. (b) Frequency domain.

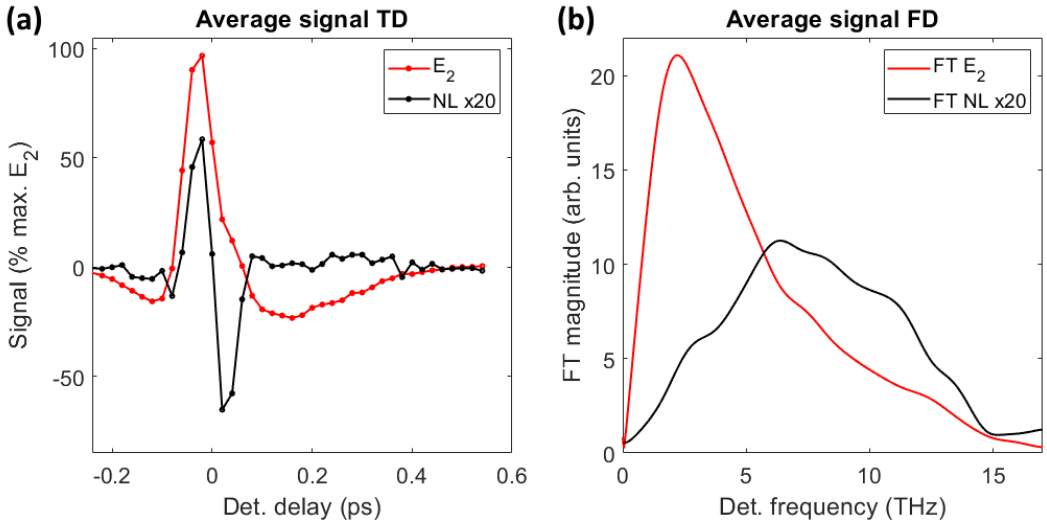

Figure E.12. Profiles extracted from the two-dimensional THz mapping in TaAs for E_1 ∼570 kV/cm, E_2 ∼45 kV/cm and T=130 K. (a) Time domain. (b) Frequency domain. For each panel E_2 and E_{nl} were extracted from the same temporal ranges (0.3-0.7 ps) and compared.

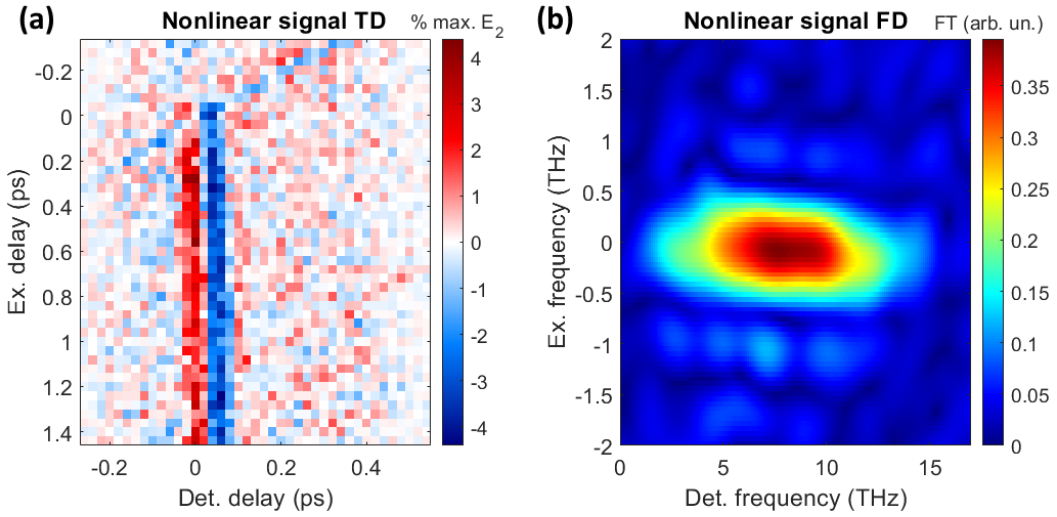

Figure E.13. Two-dimensional THz mapping of the nonlinear signal in TaAs for E_1 ∼570 kV/cm, E_2 ∼45 kV/cm and T=150 K. (a) Time domain. (b) Frequency domain.

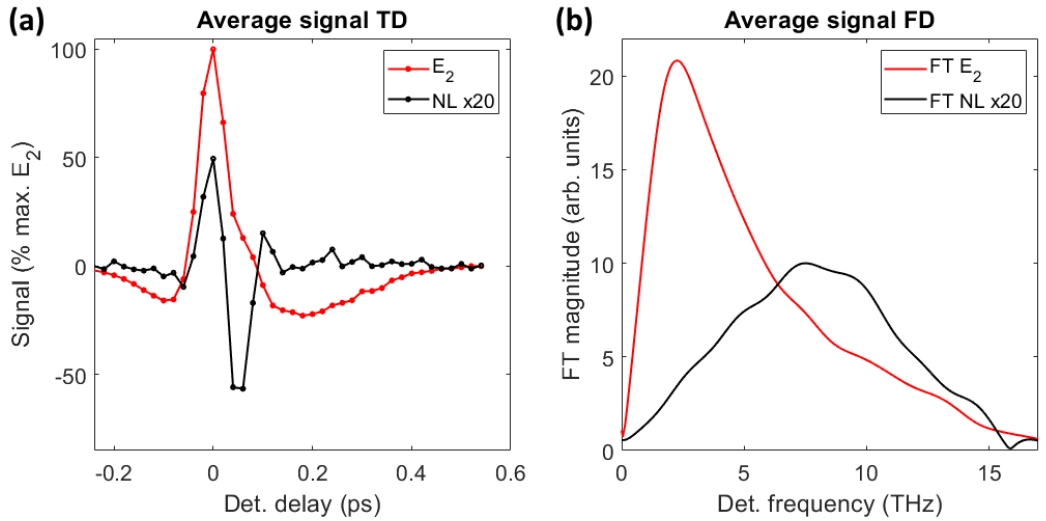

Figure E.14. Profiles extracted from the two-dimensional THz mapping in TaAs for E_1 ∼570 kV/cm, E_2 ∼45 kV/cm and T=150 K. (a) Time domain. (b) Frequency domain. For each panel E_2 and E_{nl} were extracted from the same temporal ranges (0.3-0.7 ps) and compared.

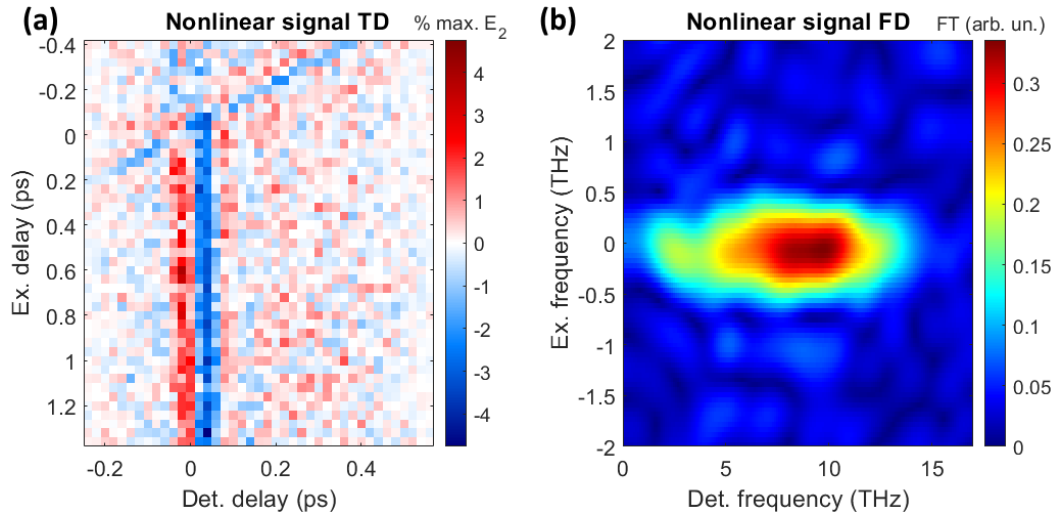

Figure E.15. Two-dimensional THz mapping of the nonlinear signal in TaAs for E_1 ∼570 kV/cm, E_2 ∼45 kV/cm and T=170 K. (a) Time domain. (b) Frequency domain.

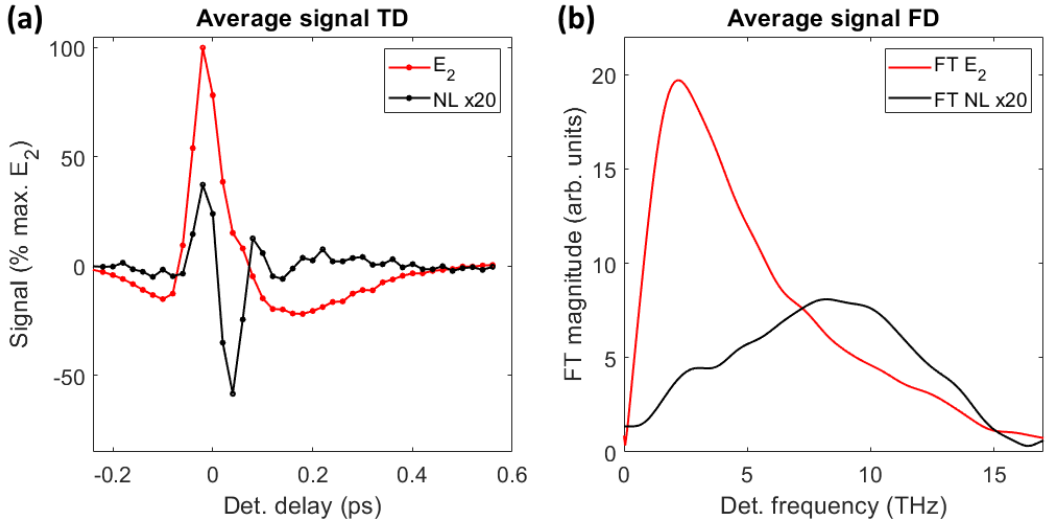

Figure E.16. Profiles extracted from the two-dimensional THz mapping in TaAs for E_1 ∼570 kV/cm, E_2 ∼45 kV/cm and T=170 K. (a) Time domain. (b) Frequency domain. For each panel E_2 and E_{nl} were extracted from the same temporal ranges (0.3-0.7 ps) and compared.

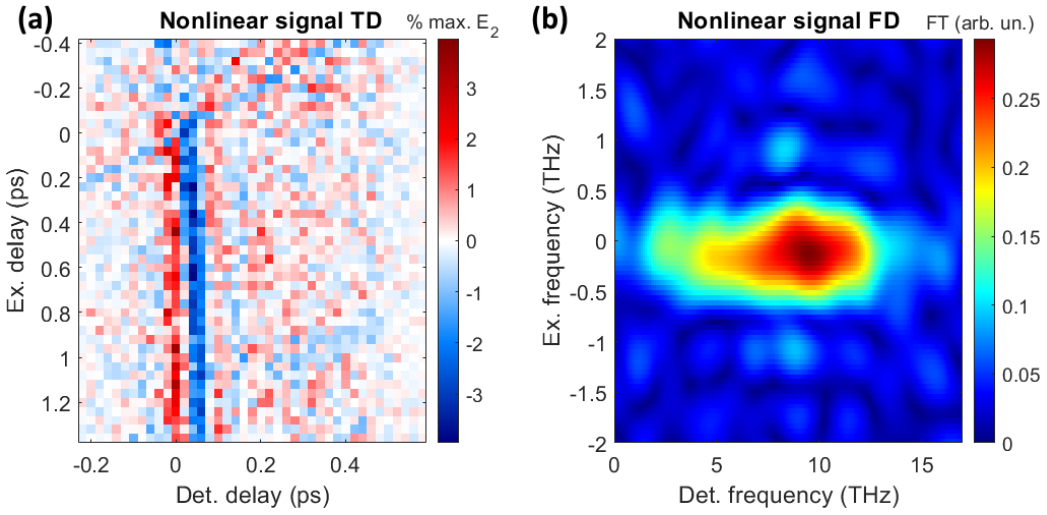

Figure E.17. Two-dimensional THz mapping of the nonlinear signal in TaAs for E_1 ∼570 kV/cm, E_2 ∼45 kV/cm and T=190 K. (a) Time domain. (b) Frequency domain.

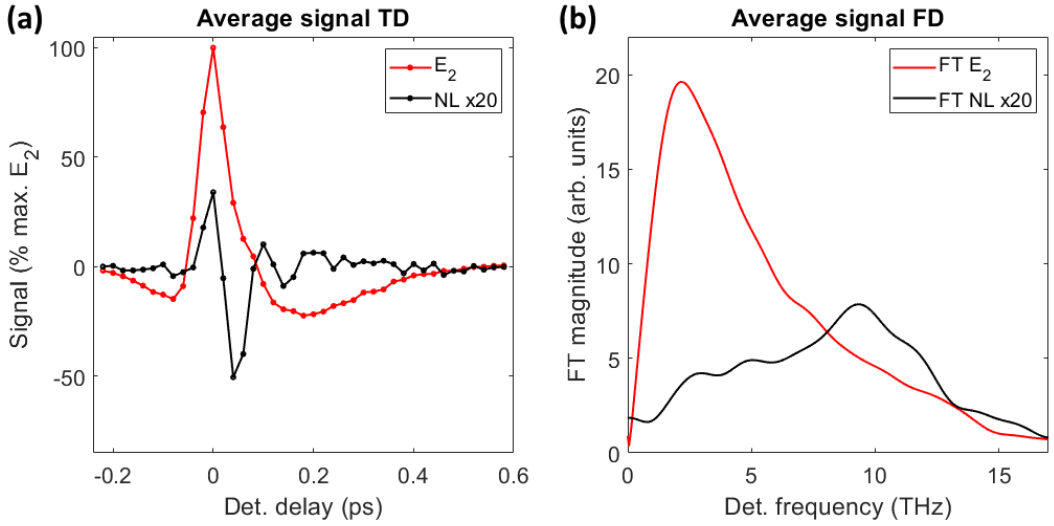

Figure E.18. Profiles extracted from the two-dimensional THz mapping in TaAs for E_1 ∼570 kV/cm, E_2 ∼45 kV/cm and T=190 K. (a) Time domain. (b) Frequency domain. For each panel E_2 and E_{nl} were extracted from the same temporal ranges (0.3-0.7 ps) and compared.

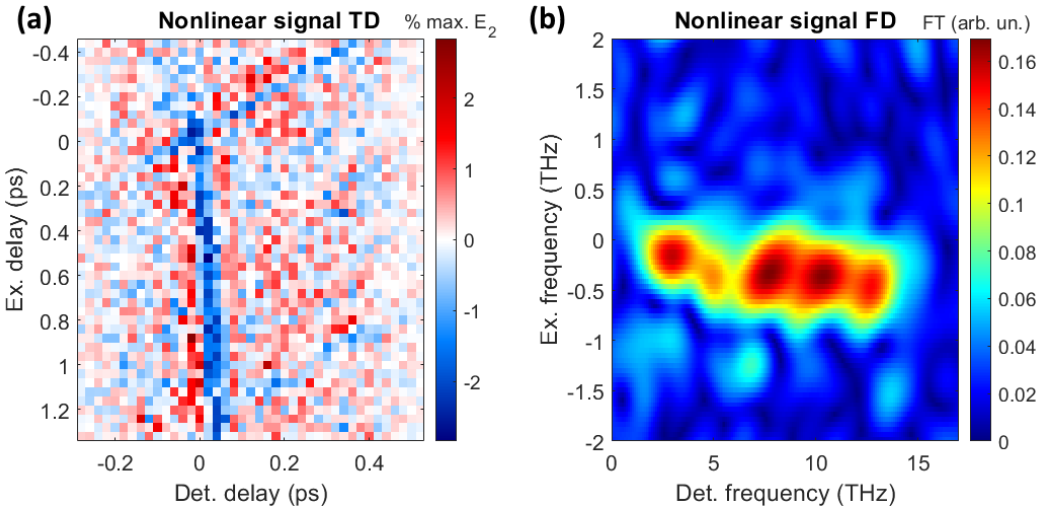

Figure E.19. Two-dimensional THz mapping of the nonlinear signal in TaAs for E_1 ∼570 kV/cm, E_2 ∼45 kV/cm and T=250 K. (a) Time domain. (b) Frequency domain.

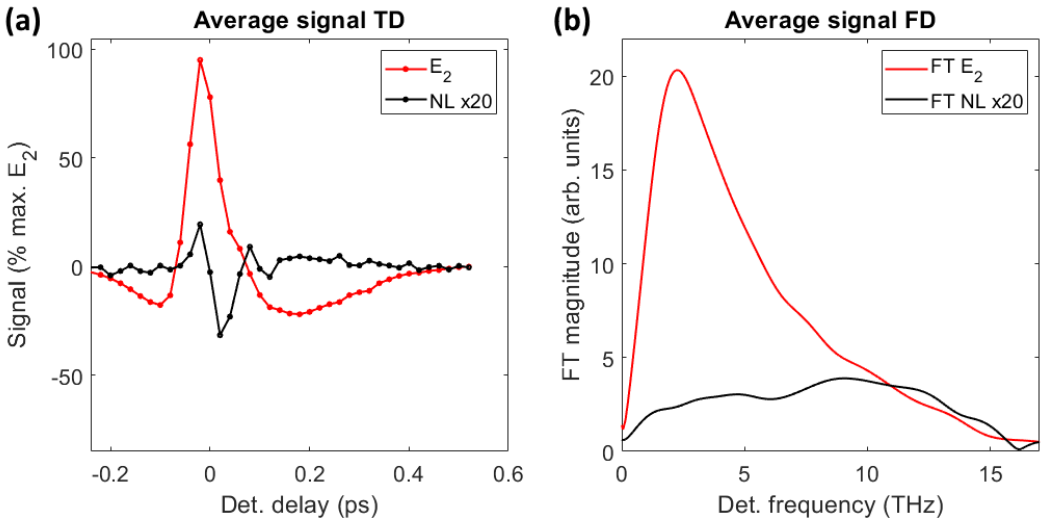

Figure E.20. Profiles extracted from the two-dimensional THz mapping in TaAs for E_1 ∼570 kV/cm, E_2 ∼45 kV/cm and T=250 K. (a) Time domain. (b) Frequency domain. For each panel E_2 and E_{nl} were extracted from the same temporal ranges (0.3-0.7 ps) and compared.

APPENDIX F

2D THz spectroscopy on WTe_2

In this appendix, I report the two-dimensional THz maps, both in the time and frequency domains, for WTe_2, which were not included in Chapter 7. The two following sections separate the data by the polarization direction for E_2, keeping E_1 perpendicular to it: E_2 || x and E_2 || y.

F.1 E_2 || x

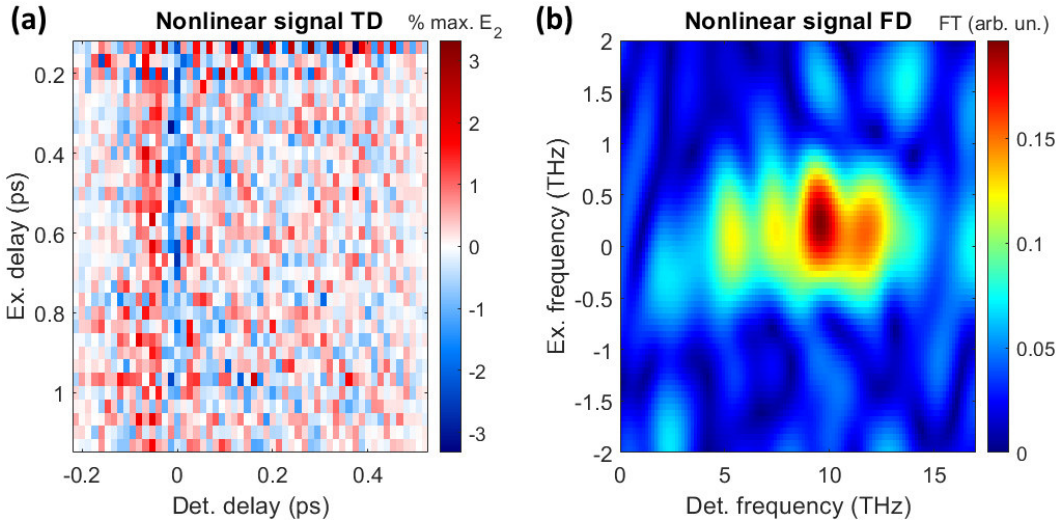

Figure F.1. Two-dimensional THz mapping of the nonlinear signal in WTe_2 with E_1 || y and E_2 || x for E_1 ∼605 kV/cm, E_2 ∼55 kV/cm and T=110 K. (a) Time domain. (b) Frequency domain.

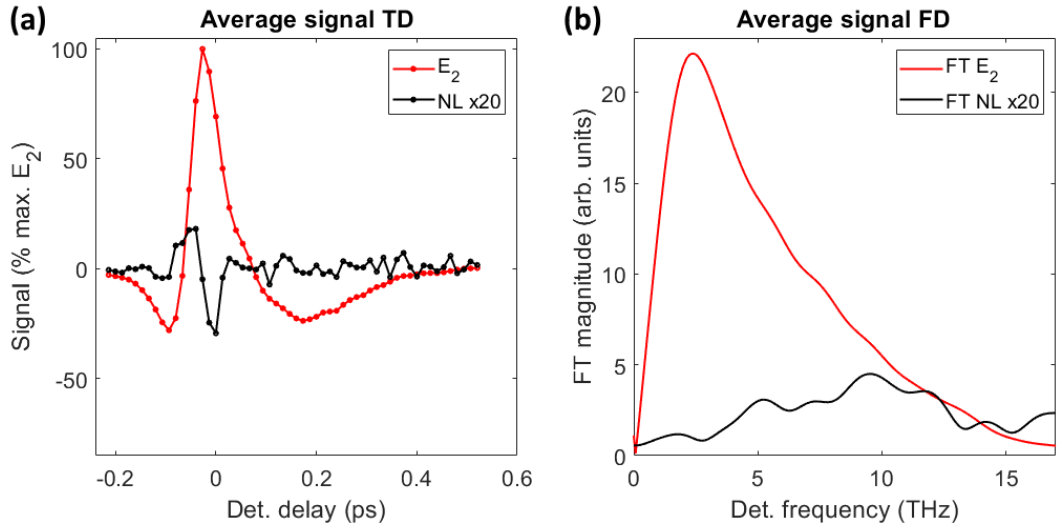

Figure F.2. Profiles extracted from the two-dimensional THz mapping in WTe_2 with E_1 || y and E_2 || x for E_1 ∼605 kV/cm, E_2 ∼55 kV/cm and T=110 K. (a) Time domain. (b) Frequency domain. For each panel E_2 and E_{nl} were extracted from the same temporal ranges (0.3-0.7 ps) and compared.

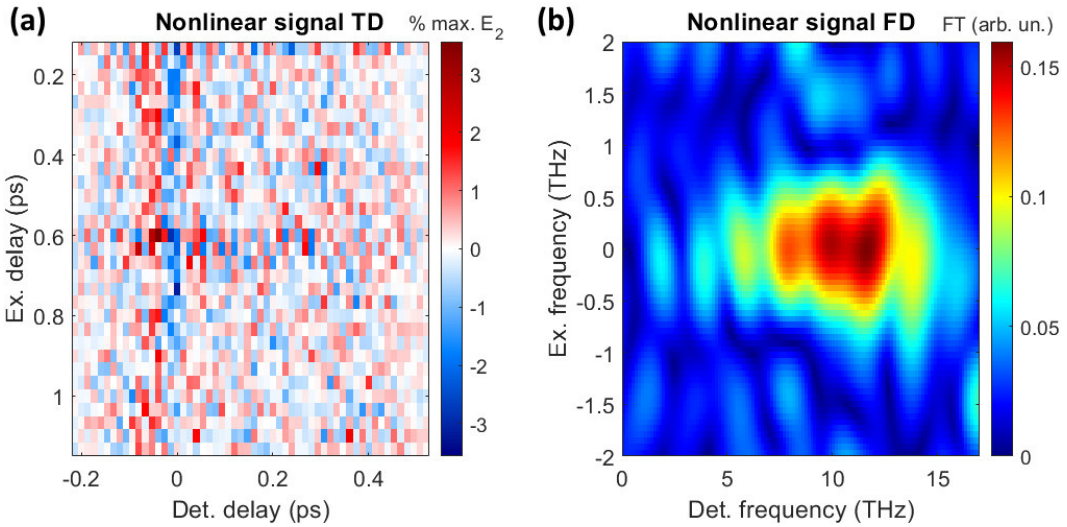

Figure F.3. Two-dimensional THz mapping of the nonlinear signal in WTe_2 with E_1 || y and E_2 || x for E_1 ∼530 kV/cm, E_2 ∼55 kV/cm and T=110 K. (a) Time domain. (b) Frequency domain.

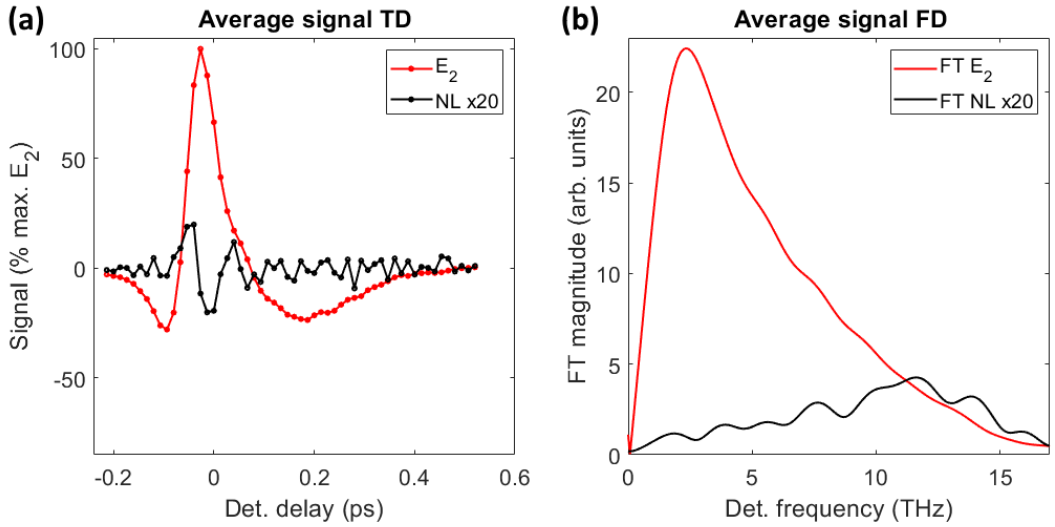

Figure F.4. Profiles extracted from the two-dimensional THz mapping in WTe_2 with E_1 || y and E_2 || x for E_1 ∼530 kV/cm, E_2 ∼55 kV/cm and T=110 K. (a) Time domain. (b) Frequency domain. For each panel E_2 and E_{nl} were extracted from the same temporal ranges (0.3-0.7 ps) and compared.

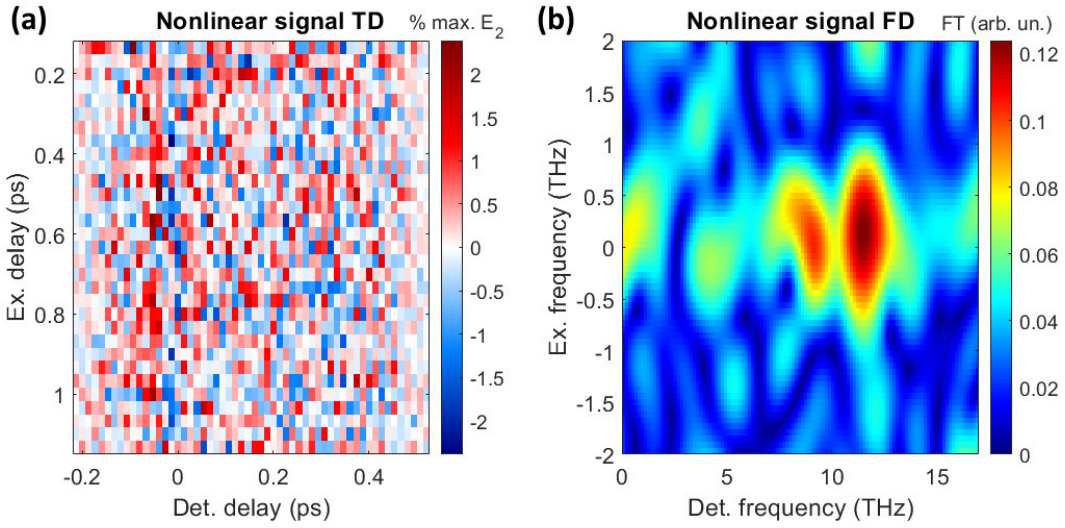

Figure F.5. Two-dimensional THz mapping of the nonlinear signal in WTe_2 with E_1 || y and E_2 || x for E_1 ∼417 kV/cm, E_2 ∼55 kV/cm and T=110 K. (a) Time domain. (b) Frequency domain.

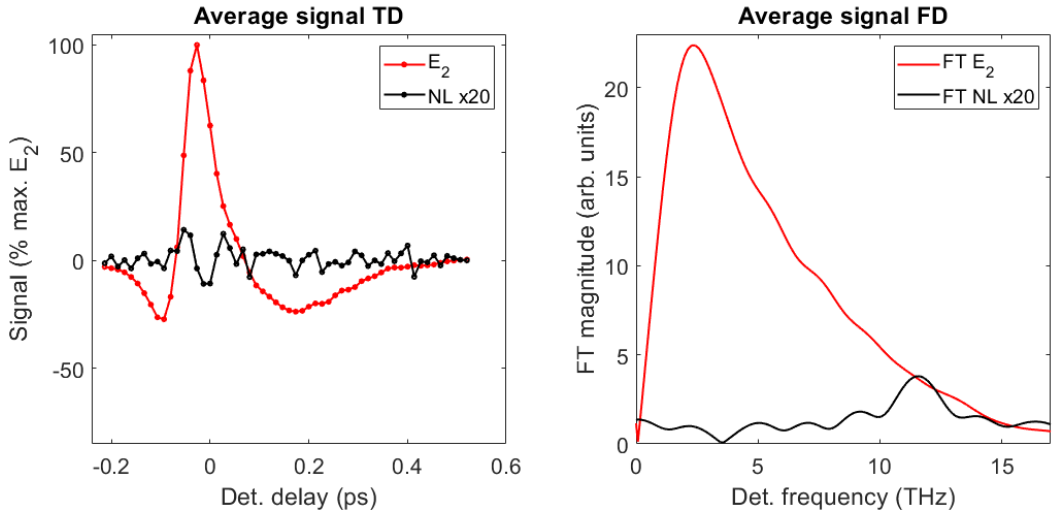

Figure F.6. Profiles extracted from the two-dimensional THz mapping in WTe_2 with E_1 || y and E_2 || x for E_1 ∼417 kV/cm, E_2 ∼ 55 kV/cm and T=110 K. (a) Time domain. (b) Frequency domain. For each panel E_2 and E_{nl} were extracted from the same temporal ranges (0.3-0.7 ps) and compared.

F.2 E_2 ||y

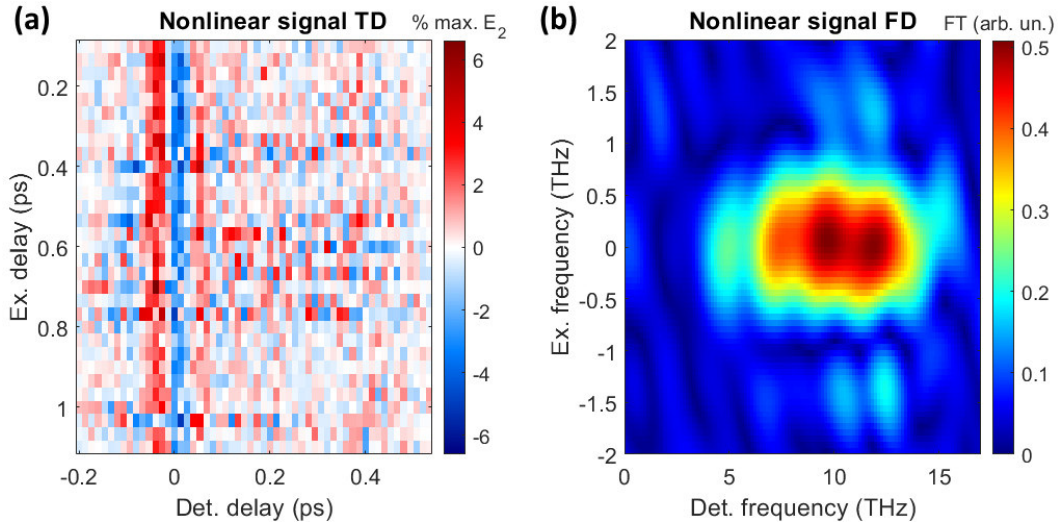

Figure F.7. Two-dimensional THz mapping of the nonlinear signal in WTe_2 with E_1 || x and E_2 || y for E_1 ~605 kV/cm, E_2 ~55 kV/cm and T=110 K. (a) Time domain. (b) Frequency domain.

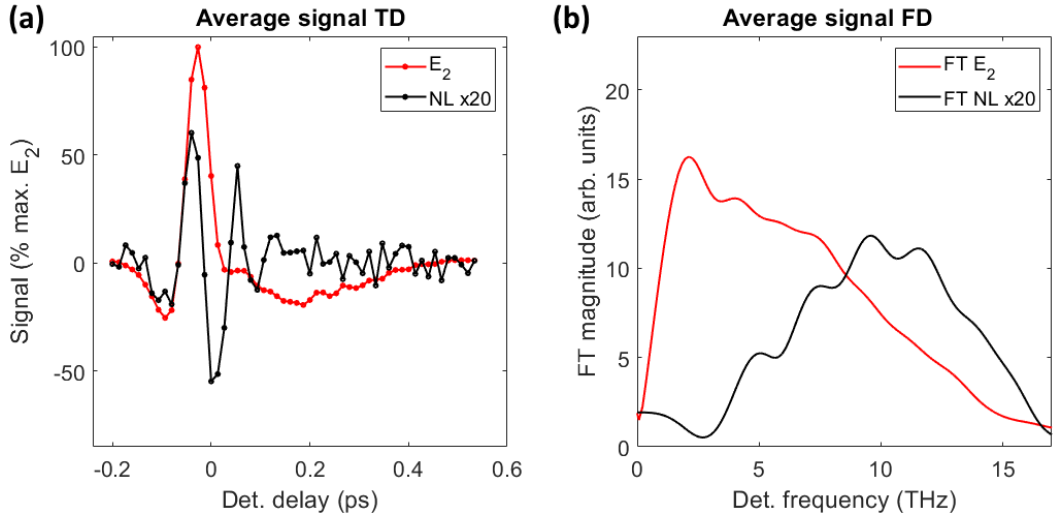

Figure F.8. Profiles extracted from the two-dimensional THz mapping in WTe_2 with E_1 || x and E_2 || y for E_1 ~605 kV/cm, E_2 ~55 kV/cm and T=110 K. (a) Time domain. (b) Frequency domain. For each panel E_2 and E_{nl} were extracted from the same temporal ranges (0.3-0.7 ps) and compared.

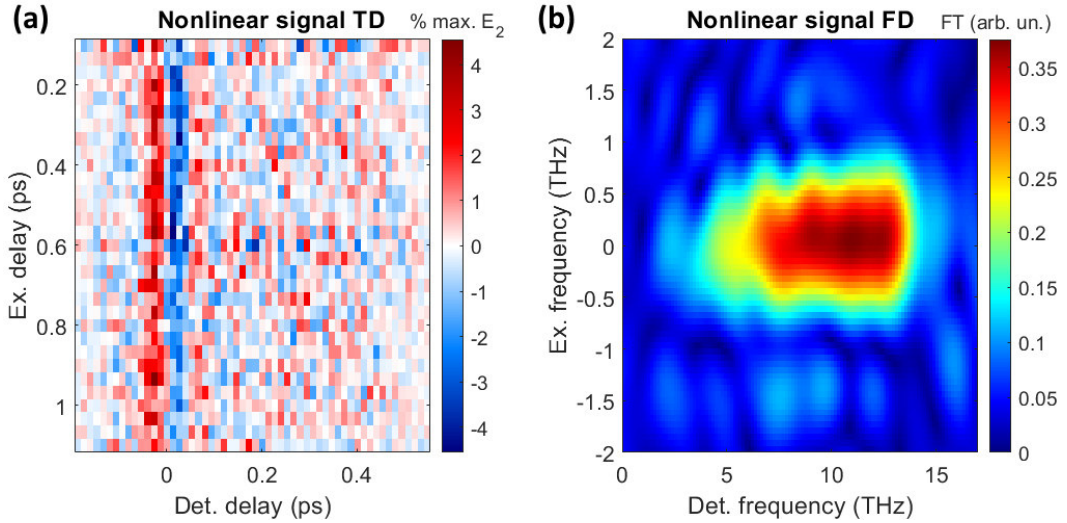

Figure F.9. Two-dimensional THz mapping of the nonlinear signal in WTe_2 with E_1 || x and E_2 || y for E_1 ∼530 kV/cm, E_2 ∼55 kV/cm and T=110 K. (a) Time domain. (b) Frequency domain.

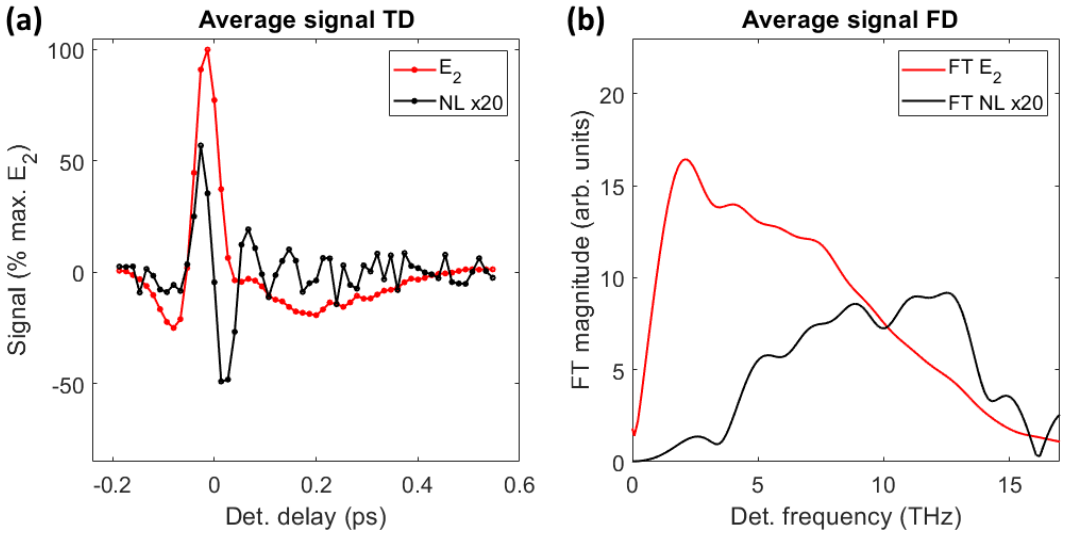

Figure F.10. Profiles extracted from the two-dimensional THz mapping in WTe_2 with E_1 || x and E_2 || y for E_1 ∼530 kV/cm, E_2 ∼55 kV/cm and T=110 K. (a) Time domain. (b) Frequency domain. For each panel E_2 and E_{nl} were extracted from the same temporal ranges (0.3-0.7 ps) and compared.

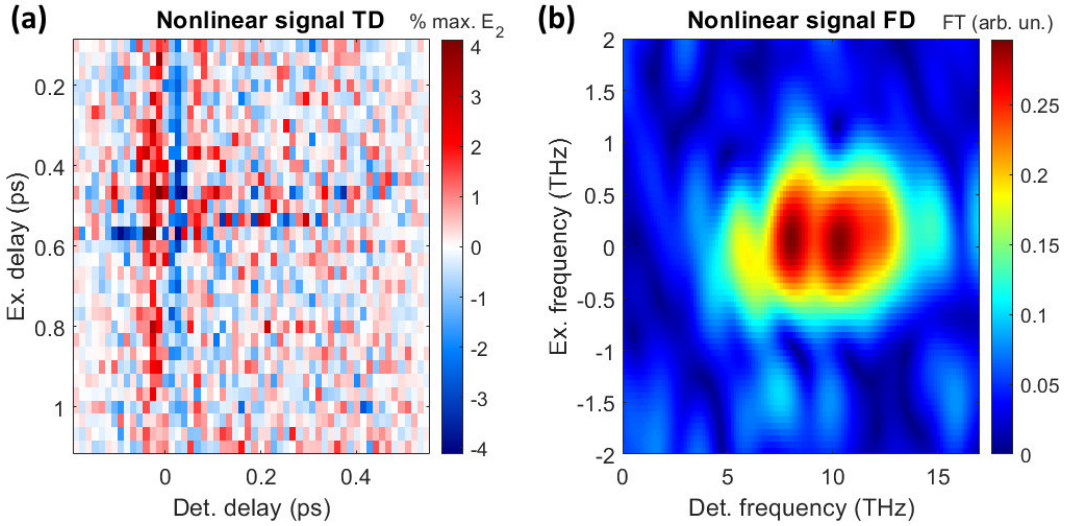

Figure F.11. Two-dimensional THz mapping of the nonlinear signal in WTe_2 with E_1 || x and E_2 || y for E_1 ∼417 kV/cm, E_2 ∼55 kV/cm and T=110 K. (a) Time domain. (b) Frequency domain.

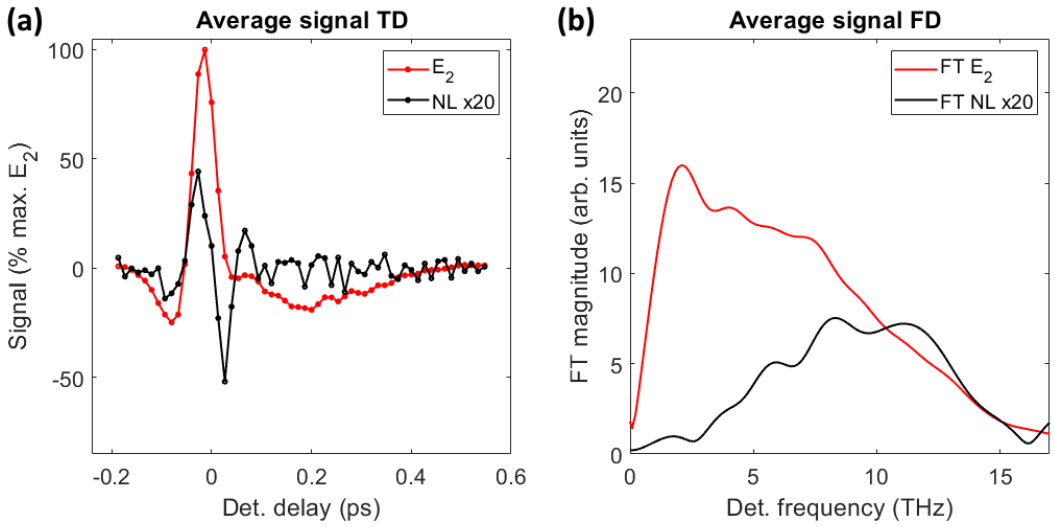

Figure F.12. Profiles extracted from the two-dimensional THz mapping in WTe_2 with E_1 || x and E_2 || y for E_1 ∼417 kV/cm, E_2 ∼55 kV/cm and T=110 K. (a) Time domain. (b) Frequency domain. For each panel E_2 and E_{nl} were extracted from the same temporal ranges (0.3-0.7 ps) and compared.

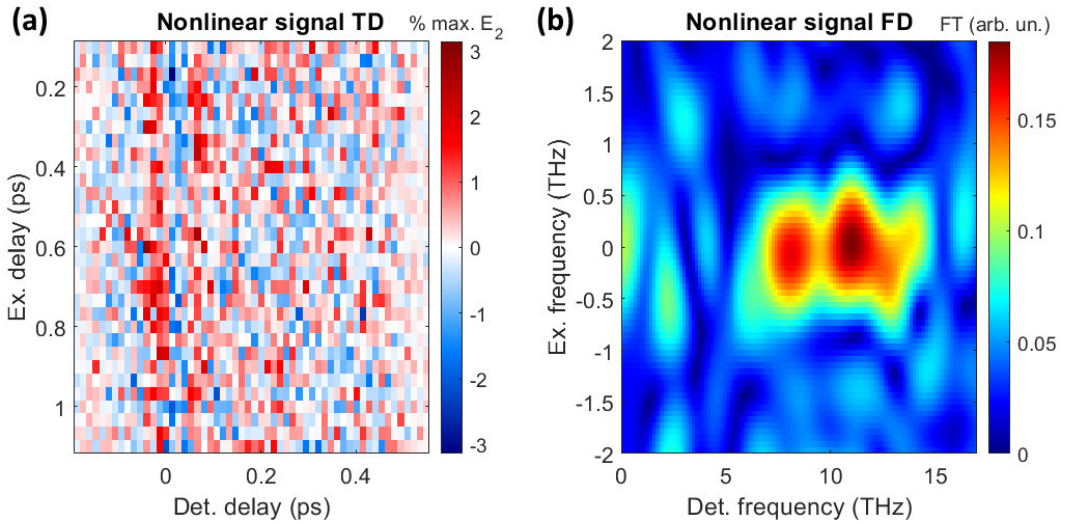

Figure F.13. Two-dimensional THz mapping of the nonlinear signal in WTe_2 with E_1 || x and E_2 || y for E_1 ∼292 kV/cm, E_2 ∼55 kV/cm and T=110 K. (a) Time domain. (b) Frequency domain.

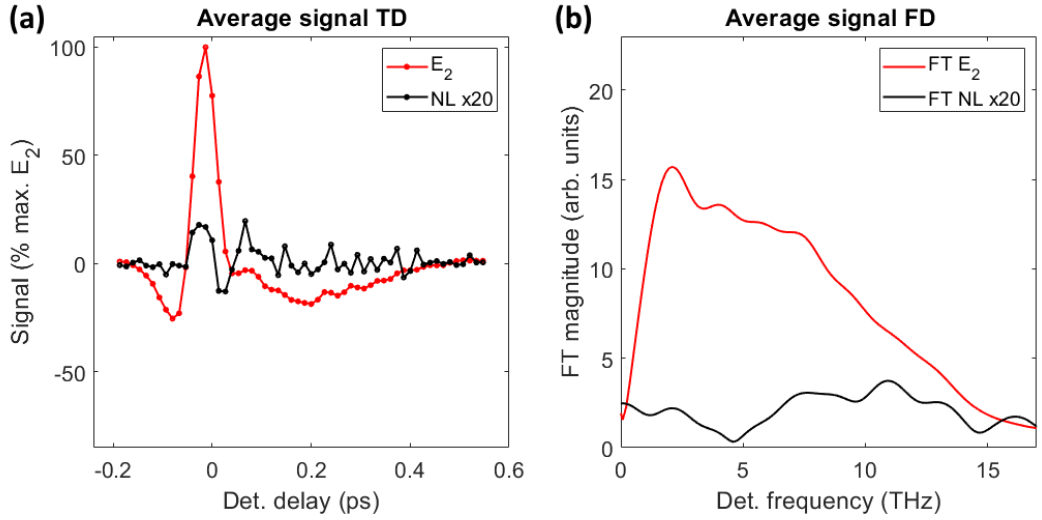

Figure F.14. Profiles extracted from the two-dimensional THz mapping in WTe_2 with E_1 || x and E_2 || y for E_1 ∼292 kV/cm, E_2 ∼55 kV/cm and T=110 K. (a) Time domain. (b) Frequency domain. For each panel E_2 and E_{nl} were extracted from the same temporal ranges (0.3-0.7 ps) and compared.

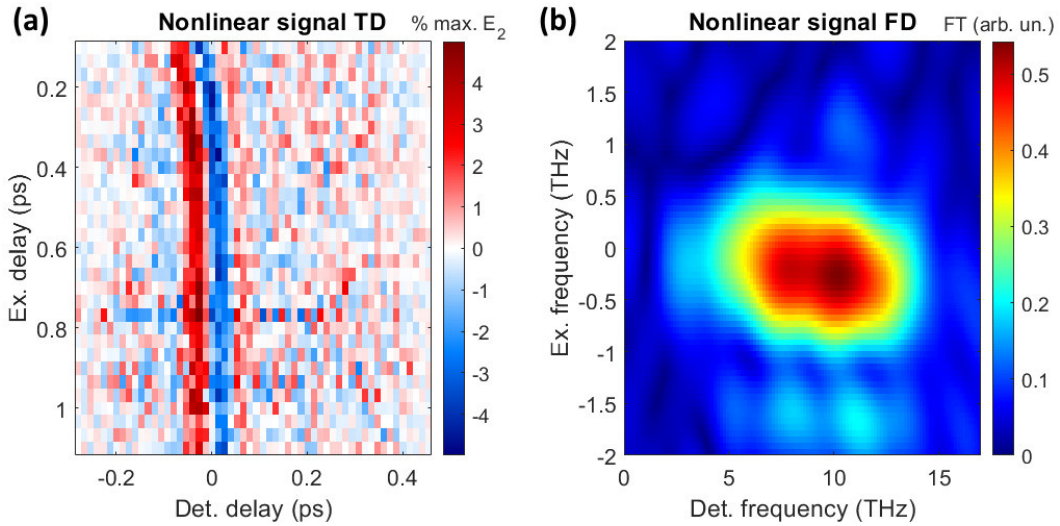

Figure F.15. Two-dimensional THz mapping of the nonlinear signal in WTe_2 with E_1 || x and E_2 || y for E_1 ∼675 kV/cm, E_2 ∼55 kV/cm and T=160 K. (a) Time domain. (b) Frequency domain.

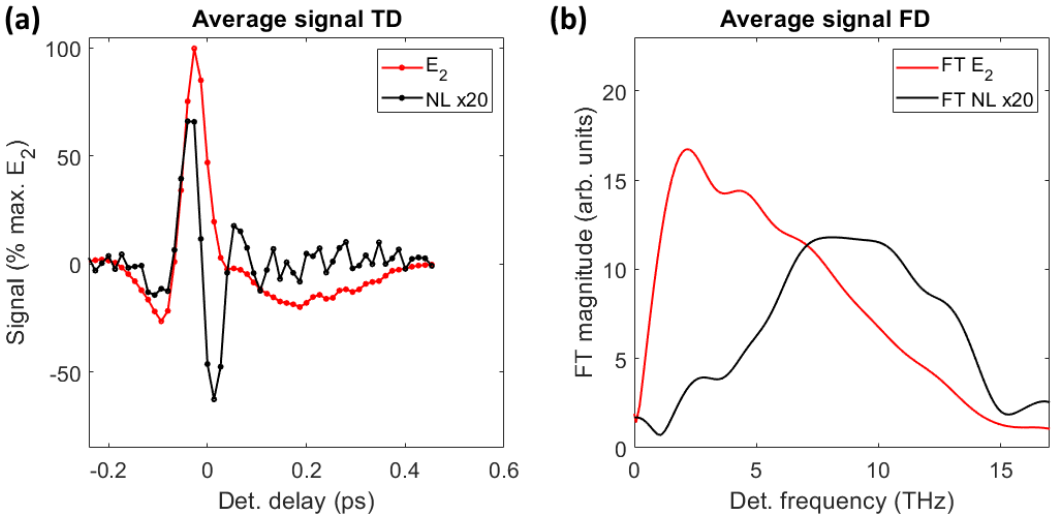

Figure F.16. Profiles extracted from the two-dimensional THz mapping in WTe_2 with E_1 || x and E_2 || y for E_1 ∼675 kV/cm, E_2 ∼55 kV/cm and T=160 K. (a) Time domain. (b) Frequency domain. For each panel E_2 and E_{nl} were extracted from the same temporal ranges (0.3-0.7 ps) and compared.

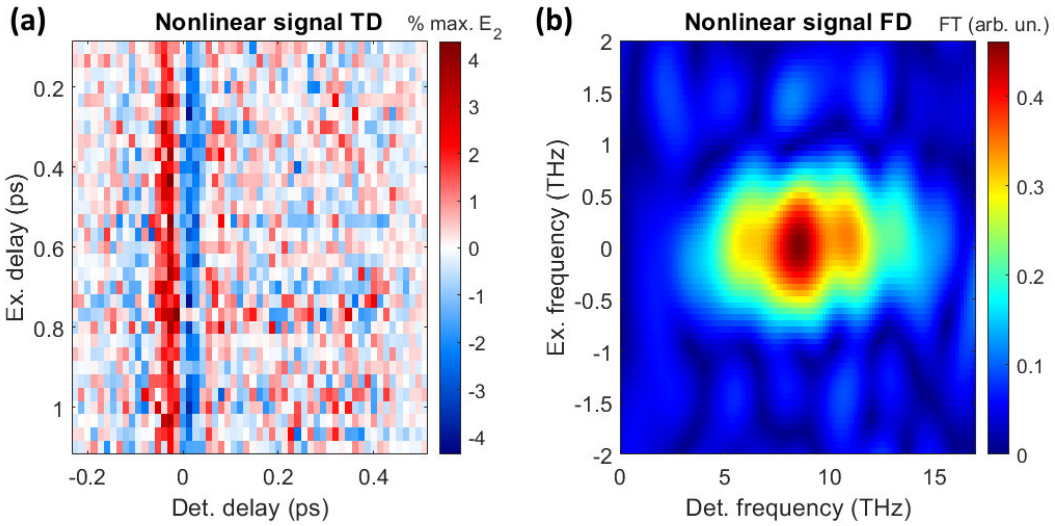

Figure F.17. Two-dimensional THz mapping of the nonlinear signal in WTe_2 with E_1 || x and E_2 || y for E_1 ∼675 kV/cm, E_2 ∼55 kV/cm and T=200 K. (a) Time domain. (b) Frequency domain.

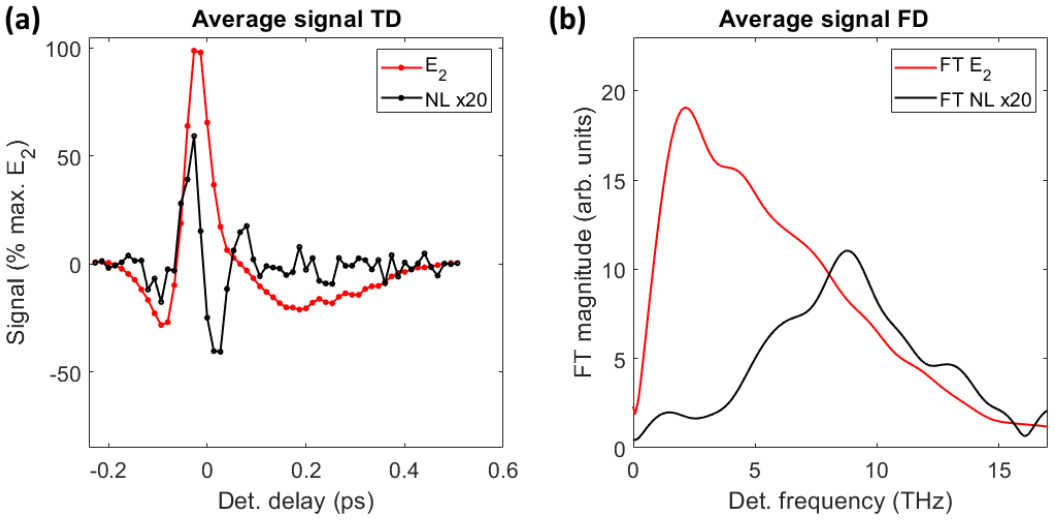

Figure F.18. Profiles extracted from the two-dimensional THz mapping in WTe_2 with E_1 || x and E_2 || y for E_1 ∼675 kV/cm, E_2 ∼55 kV/cm and T=200 K. (a) Time domain. (b) Frequency domain. For each panel E_2 and E_{nl} were extracted from the same temporal ranges (0.3-0.7 ps) and compared.

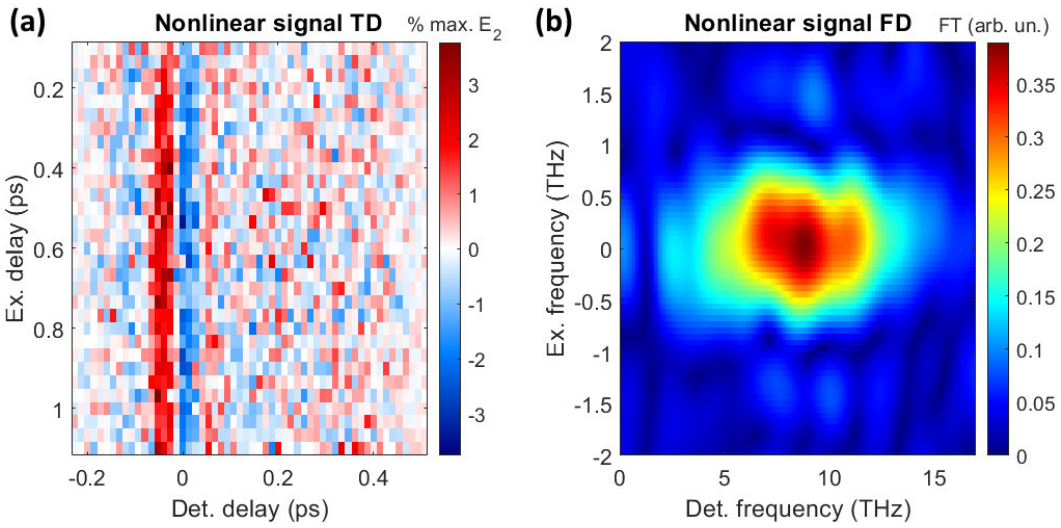

Figure F.19. Two-dimensional THz mapping of the nonlinear signal in WTe_2 with E_1 || x and E_2 || y for E_1 ∼605 kV/cm, E_2 ∼55 kV/cm and T=200 K. (a) Time domain. (b) Frequency domain.

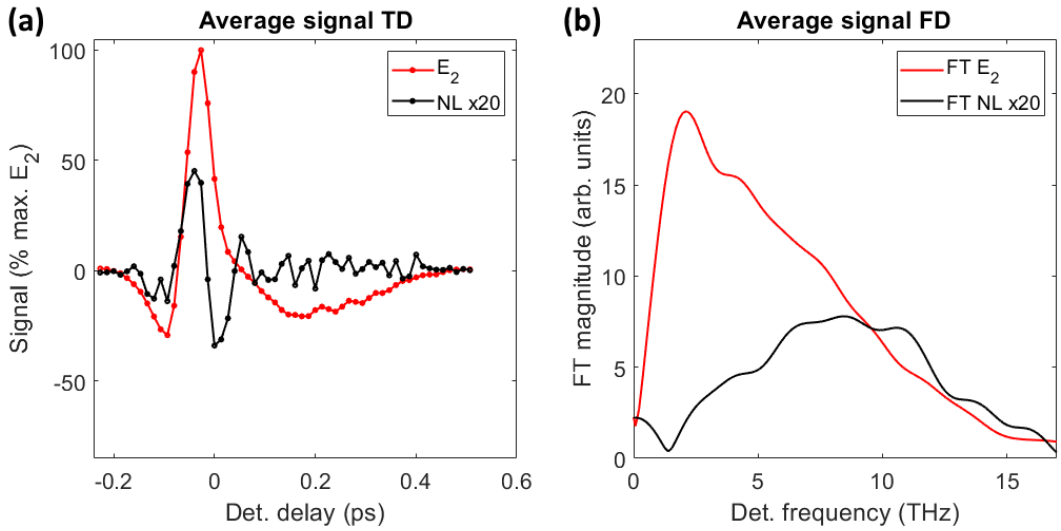

Figure F.20. Profiles extracted from the two-dimensional THz mapping in WTe_2 with E_1 || x and E_2 || y for E_1 ∼605 kV/cm, E_2 ∼55 kV/cm and T=200 K. (a) Time domain. (b) Frequency domain. For each panel E_2 and E_{nl} were extracted from the same temporal ranges (0.3-0.7 ps) and compared.

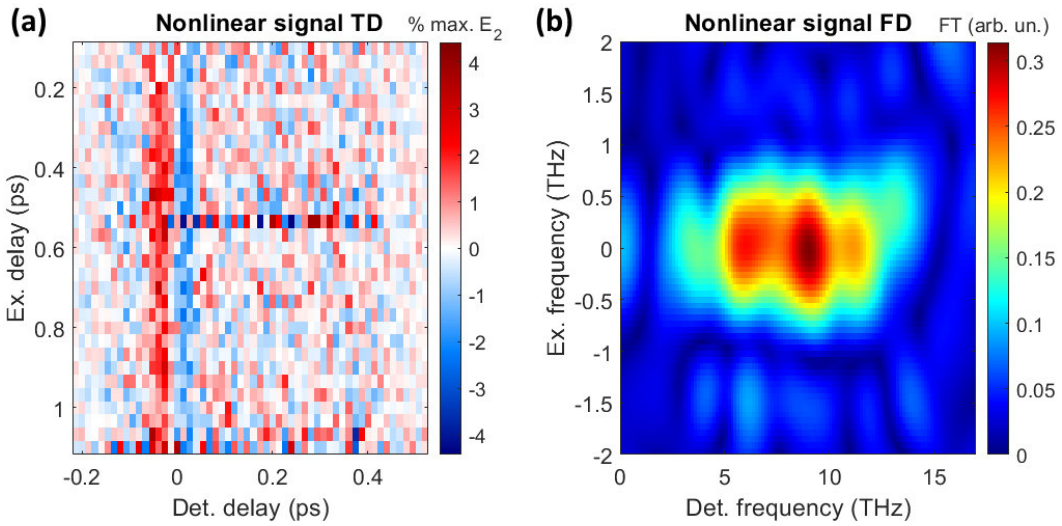

Figure F.21. Two-dimensional THz mapping of the nonlinear signal in WTe_2 with E_1 || x and E_2 || y for E_1 ∼530 kV/cm, E_2 ∼55 kV/cm and T=200 K. (a) Time domain. (b) Frequency domain.

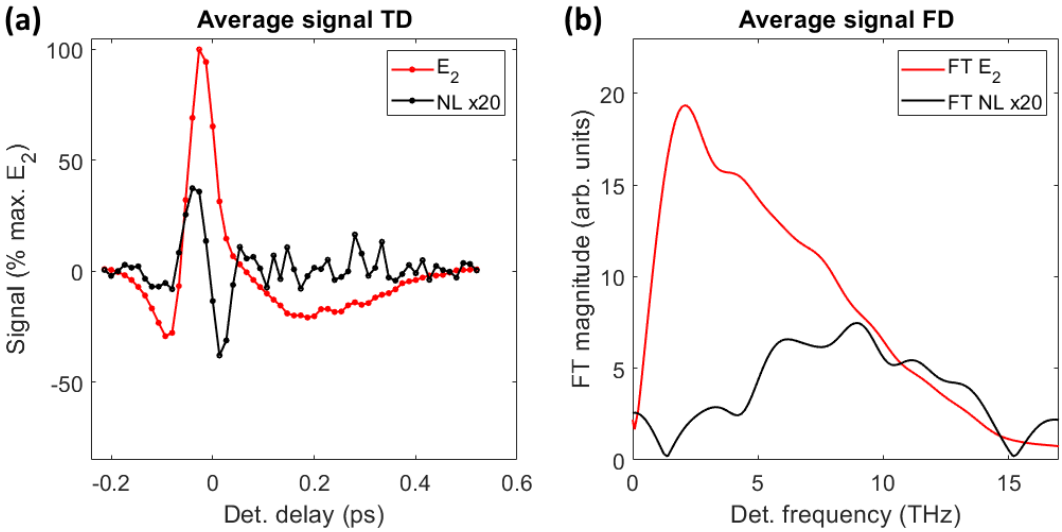

Figure F.22. Profiles extracted from the two-dimensional THz mapping in WTe_2 with E_1 || x and E_2 || y for E_1 ∼530 kV/cm, E_2 ∼55 kV/cm and T=200 K. (a) Time domain. (b) Frequency domain. For each panel E_2 and E_{nl} were extracted from the same temporal ranges (0.3-0.7 ps) and compared.

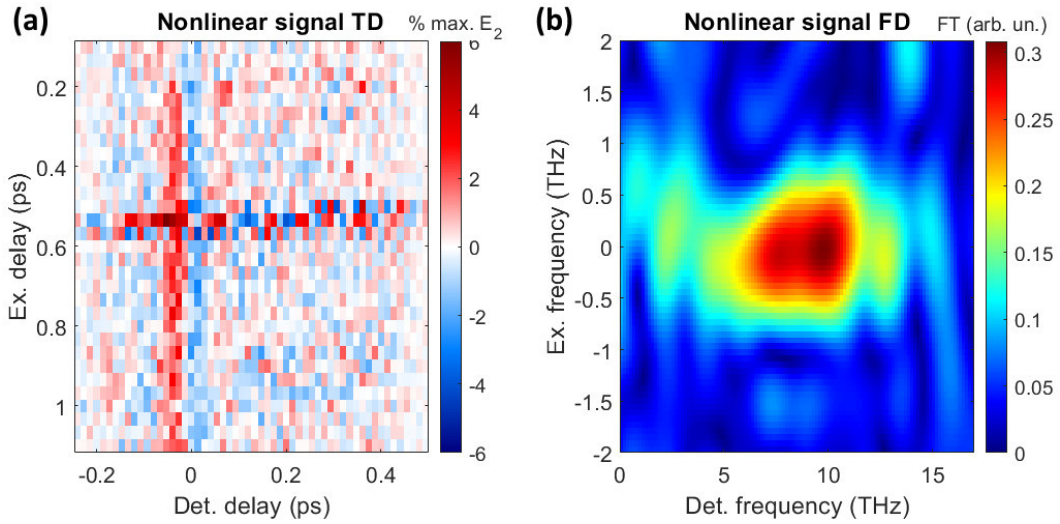

Figure F.23. Two-dimensional THz mapping of the nonlinear signal in WTe_2 with E_1 || x and E_2 || y for E_1 ∼675 kV/cm, E_2 ∼55 kV/cm and T=240 K. (a) Time domain. (b) Frequency domain.

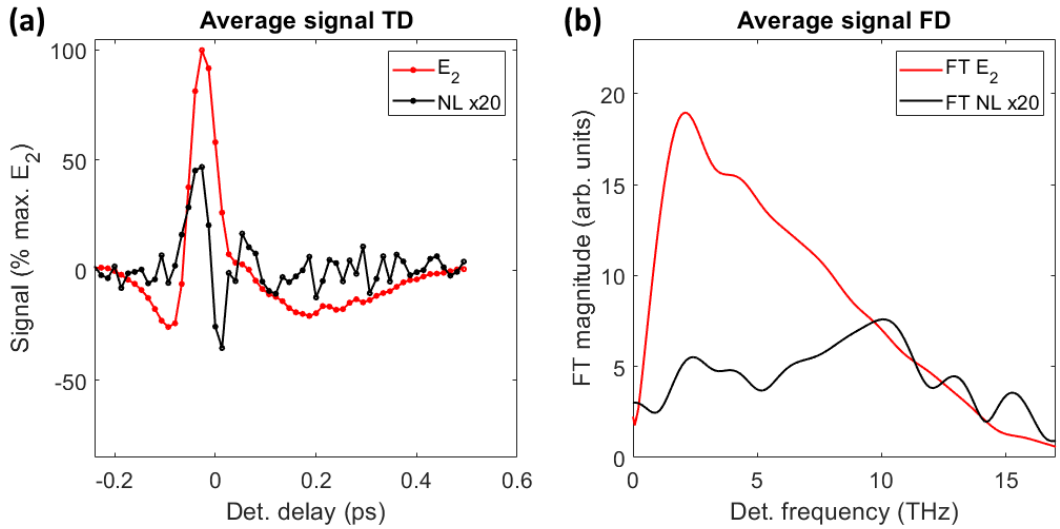

Figure F.24. Profiles extracted from the two-dimensional THz mapping in WTe_2 with E_1 || x and E_2 || y for E_1 ∼675 kV/cm, E_2 ∼55 kV/cm and T=240 K. (a) Time domain. (b) Frequency domain. For each panel E_2 and E_{nl} were extracted from the same temporal ranges (0.3-0.7 ps) and compared.

APPENDIX G

Rise time of the HgCdTe nonlinearties

Regarding the rise time, *i.e.* the time interval required for the nonlinear to reach its peak after the superposition, Fig. G.1(a) showcases its dependence on the temperature and field conditions investigated. For a systematic evaluation, the following formula was used to fit the profiles

$$f(t) = -\theta(t - t_0)|A_{nonlinear}|e^{-(t-t_0)/\tau_{rise}} + c \tag{G.1}$$

where θ is the Heaviside step function, $A_{nonlinear}$ is the absolute value of the signal plateau, t_0 represents the temporal beginning of the nonlinearity, τ_{rise} is the rise time and c is an offset constant. In Figs. G.1(b),(c) the temperature and field dependencies of $A_{nonlinear}$ and τ_{rise} are reported, depicting a similar behavior for the two quantities. Excluding low-field and high-temperature settings where the low signal may affect the accurate estimation, we observe that the rise time appears to be almost constant around 0.2-0.3 ps, without a clear-cut dependence.

This points towards the finite pulse duration of E_1 as its main source, rather that the carrier multiplication process itself.

An extended t_{ex} dependence of the nonlinear signal is reported in Fig. G.1(a), showing that the signal survives for tens of picoseconds.

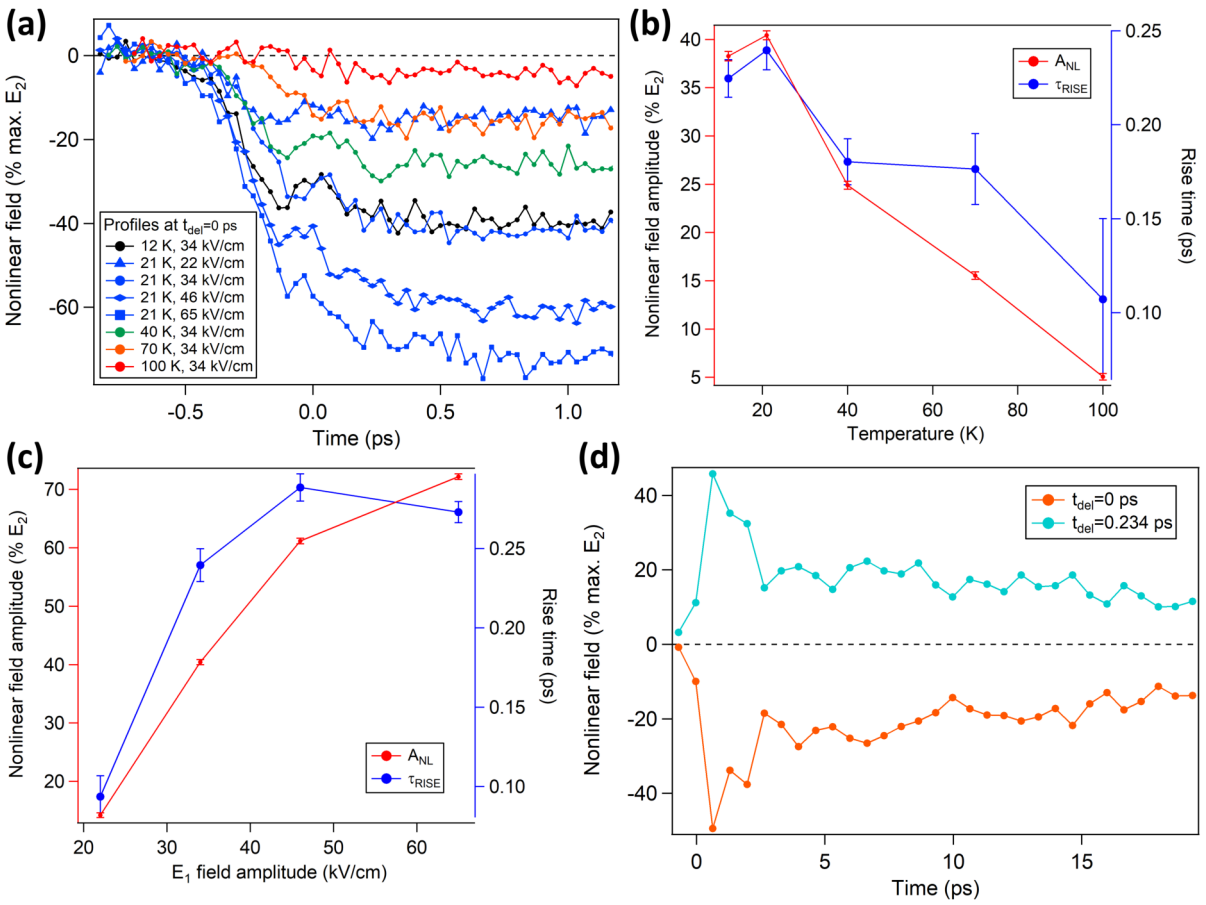

Figure G.1. (a) Evolution of the even nonlinear signal at constant t_{del}, taken along the orange dotted line in Fig. 8.5(b), for the examined conditions, varying temperature and E_1 field amplitude, keeping E_2 ∼17 kV/cm. (b) Temperature and (c) E_1 field dependence of the nonlinear signal at t_{del}. The plotted quantities $\mathrm{A_{nonlinear}}$ and τ_{rise} are the parameters obtained from fitting with Eq. G.1 the profiles in panel (a); the arrows indicate the respective left axes. (d) Longer time profiles at fixed t_{del}, taken at the same conditions as in Fig. 8.5(b) along the orange and blue dotted lines in Fig. (8.5(b)) extending the $\mathrm{t_{ex}}$ interval.

Bibliography

[1] N.W. Ashcroft and N.D. Mermin. "Solid State Physics". In: Philadelphia: Saunders College, 1976.

[2] Søren Ulstrup et al. "Extracting the temperature of hot carriers in time- and angle-resolved photoemission". In: *Review of Scientific Instruments* 85.1 (2014), p. 013907. DOI: 10.1063/1.4863322.

[3] Jinying Wang et al. "The rare two-dimensional materials with Dirac cones". In: *National Science Review* 2.1 (Jan. 2015), pp. 22–39. ISSN: 2095-5138. DOI: 10.1093/nsr/nwu080.

[4] Su-Yang Xu et al. "Discovery of a Weyl fermion semimetal and topological Fermi arcs". In: *Science* 349.6248 (2015), pp. 613–617. ISSN: 0036-8075. DOI: 10.1126/science.aaa9297.

[5] B. Q. Lv et al. "Experimental Discovery of Weyl Semimetal TaAs". In: *Phys. Rev. X* 5 (3 2015), p. 031013. DOI: 10.1103/PhysRevX.5.031013.

[6] Alexey A. Soluyanov et al. "Type-II Weyl semimetals". In: *Nature* 527 (2015), pp. 495–498. DOI: 10.1038/nature15768.

[7] M. Orlita et al. "Observation of three-dimensional massless Kane fermions in a zinc-blende crystal". In: *Nature Physics* 10.3 (2014), pp. 233–238. ISSN: 1745-2481. DOI: 10.1038/nphys2857.

[8] E. Hendry et al. "Coherent Nonlinear Optical Response of Graphene". In: *Phys. Rev. Lett.* 105 (9 2010), p. 097401. DOI: 10.1103/PhysRevLett.105.097401.

[9] S. A. Mikhailov. "Quantum theory of the third-order nonlinear electrodynamic effects of graphene". In: *Phys. Rev. B* 93 (8 2016), p. 085403. DOI: 10.1103/PhysRevB.93.085403.

[10] Kelvin J. A. Ooi and Dawn T. H. Tan. "Nonlinear graphene plasmonics". In: *Proceedings of the Royal Society A: Mathematical, Physical and Engineering Sciences* 473.2206 (2017), p. 20170433. DOI: 10.1098/rspa.2017.0433.

[11] Liang Wu et al. "Giant anisotropic nonlinear optical response in transition metal monopnictide Weyl semimetals". In: *Nature Physics* 13.4 (2017), pp. 350–355. ISSN: 1745-2481. DOI: 10.1038/nphys3969.

[12] Z. Z. Du et al. "Band Signatures for Strong Nonlinear Hall Effect in Bilayer WTe_2". In: *Phys. Rev. Lett.* 121 (26 2018), p. 266601. DOI: 10.1103/PhysRevLett.121.266601.

[13] Pan He et al. "Nonlinear magnetotransport shaped by Fermi surface topology and convexity". In: *Nature Communications* 10.1 (2019), p. 1290. ISSN: 2041-1723. DOI: 10.1038/s41467-019-09208-8.

[14] Kaifei Kang et al. "Nonlinear anomalous Hall effect in few-layer WTe_2". In: *Nature Materials* 18.4 (2019), pp. 324–328. ISSN: 1476-4660. DOI: 10.1038/s41563-019-0294-7.

[15] Qiong Ma et al. "Observation of the nonlinear Hall effect under time-reversal-symmetric conditions". In: *Nature* 565.7739 (2019), pp. 337–342. ISSN: 1476-4687. DOI: 10.1038/s41586-018-0807-6.

[16] F. Bonaccorso et al. "Graphene photonics and optoelectronics". In: *Nature Photonics* 4.9 (2010), pp. 611–622. ISSN: 1749-4893. DOI: 10.1038/nphoton.2010.186.

[17] R. D. Y. Hills, A. Kusmartseva, and F. V. Kusmartsev. "Current-voltage characteristics of Weyl semimetal semiconducting devices, Veselago lenses, and hyperbolic Dirac phase". In: *Phys. Rev. B* 95 (21 2017), p. 214103. DOI: 10.1103/PhysRevB.95.214103.

[18] Hermann Weyl. "Elektron und Gravitation. I". In: *Zeitschrift für Physik* 56.5 (1929), pp. 330–352. ISSN: 0044-3328. DOI: 10.1007/BF01339504.

[19] Michael E Peskin and Daniel V Schroeder. *An introduction to quantum field theory*. Boulder, CO: Westview, 1995.

[20] Conyers Herring. "Accidental Degeneracy in the Energy Bands of Crystals". In: *Phys. Rev.* 52 (4 1937), pp. 365–373. DOI: 10.1103/PhysRev.52.365.

[21] M. Z. Hasan and C. L. Kane. "Colloquium: Topological insulators". In: *Rev. Mod. Phys.* 82 (4 2010), pp. 3045–3067. DOI: 10.1103/RevModPhys.82.3045.

[22] N. P. Armitage, E. J. Mele, and Ashvin Vishwanath. "Weyl and Dirac semimetals in three-dimensional solids". In: *Rev. Mod. Phys.* 90 (1 2018), p. 015001. DOI: 10.1103/RevModPhys.90.015001.

[23] G.E. Volovik. *The Universe in a Helium Droplet*. International series of monographs on physics. Oxford University Press, 2009.

[24] A. H. Castro Neto et al. "The electronic properties of graphene". In: *Rev. Mod. Phys.* 81 (1 2009), pp. 109–162. DOI: 10.1103/RevModPhys.81.109.

[25] Pavan Hosur and Xiaoliang Qi. "Recent developments in transport phenomena in Weyl semimetals". In: *Comptes Rendus Physique* 14.9 (2013). Topological insulators / Isolants topologiques, pp. 857 –870. ISSN: 1631-0705. DOI: 10.1016/j.crhy.2013.10.010.

[26] Shuichi Murakami. "Phase transition between the quantum spin Hall and insulator phases in 3D: emergence of a topological gapless phase". In: *New Journal of Physics* 9.9 (2007), pp. 356–356. DOI: 10.1088/1367-2630/9/9/356.

[27] Zhijun Wang et al. "Dirac semimetal and topological phase transitions in A_3Bi (A = Na, K, Rb)". In: *Phys. Rev. B* 85 (19 2012), p. 195320. DOI: 10.1103/PhysRevB.85.195320.

[28] S. M. Young et al. "Dirac Semimetal in Three Dimensions". In: *Phys. Rev. Lett.* 108 (14 2012), p. 140405. DOI: 10.1103/PhysRevLett.108.140405.

[29] Julia A. Steinberg et al. "Bulk Dirac Points in Distorted Spinels". In: *Phys. Rev. Lett.* 112 (3 2014), p. 036403. DOI: 10.1103/PhysRevLett.112.036403.

[30] Z. K. Liu et al. "Discovery of a Three-Dimensional Topological Dirac Semimetal, Na_3Bi". In: *Science* 343.6173 (2014), pp. 864–867. ISSN: 0036-8075. DOI: 10.1126/science.1245085.

[31] Sergey Borisenko et al. "Experimental Realization of a Three-Dimensional Dirac Semimetal". In: *Phys. Rev. Lett.* 113 (2 2014), p. 027603. DOI: 10.1103/PhysRevLett.113.027603.

[32] Madhab Neupane et al. "Observation of a three-dimensional topological Dirac semimetal phase in high-mobility Cd_3As_2". In: *Nature Communications* 5.1 (2014), p. 3786. ISSN: 2041-1723. DOI: 10.1038/ncomms4786.

[33] A. Akrap et al. "Magneto-Optical Signature of Massless Kane Electrons in Cd_3As_2". In: *Phys. Rev. Lett.* 117 (13 2016), p. 136401. DOI: 10.1103/PhysRevLett.117.136401.

[34] H.B. Nielsen and M. Ninomiya. "Absence of neutrinos on a lattice: (I). Proof by homotopy theory". In: *Nuclear Physics B* 185.1 (1981), pp. 20 –40. ISSN: 0550-3213. DOI: 10.1016/0550-3213(81)90361-8.

[35] Edbert J. Sie et al. "An ultrafast symmetry switch in a Weyl semimetal". In: *Nature* 565.7737 (2019), pp. 61–66. ISSN: 1476-4687. DOI: 10.1038/s41586-018-0809-4.

[36] Meng-Xue Guan et al. *Manipulating Weyl quasiparticles by orbital-selective photoexcitation in WTe_2*. 2020. arXiv: 2004.12127 [cond-mat.mtrl-sci].

[37] Binghai Yan and Claudia Felser. "Topological Materials: Weyl Semimetals". In: *Annual Review of Condensed Matter Physics* 8.1 (2017), pp. 337–354. DOI: 10.1146/annurev-conmatphys-031016-025458.

[38] H.B. Nielsen and Masao Ninomiya. "The Adler-Bell-Jackiw anomaly and Weyl fermions in a crystal". In: *Physics Letters B* 130.6 (1983), pp. 389 –396. ISSN: 0370-2693. DOI: 10.1016/0370-2693(83)91529-0.

[39] Minping Zhang, Zongxian Yang, and Guangtao Wang. "Coexistence of Type-I and Type-II Weyl Points in the Weyl-Semimetal OsC_2". In: *The Journal of Physical Chemistry C* 122.6 (2018), pp. 3533–3538. DOI: 10.1021/acs.jpcc.8b00920.

[40] Shu-Chun Wu et al. "Hidden type-II Weyl points in the Weyl semimetal NbP". In: *Phys. Rev. B* 96 (16 2017), p. 165113. DOI: 10.1103/PhysRevB.96.165113.

[41] Z. K. Liu et al. "Evolution of the Fermi surface of Weyl semimetals in the transition metal pnictide family". In: *Nature Materials* 15.1 (2016), pp. 27–31. ISSN: 1476-4660. DOI: 10.1038/nmat4457.

[42] Su-Yang Xu et al. "Discovery of a Weyl fermion state with Fermi arcs in niobium arsenide". In: *Nature Physics* 11.9 (2015), pp. 748–754. ISSN: 1745-2481. DOI: 10.1038/nphys3437.

[43] J. Jiang et al. "Signature of type-II Weyl semimetal phase in $MoTe_2$". In: *Nature Communications* 8.1 (2017), p. 13973. ISSN: 2041-1723. DOI: 10.1038/ncomms13973.

[44] Sergey Borisenko et al. “Time-reversal symmetry breaking type-II Weyl state in $YbMnBi_2$”. In: *Nature Communications* 10.1 (2019), p. 3424. ISSN: 2041-1723. DOI: 10.1038/s41467-019-11393-5.

[45] Yun Wu et al. “Observation of Fermi arcs in the type-II Weyl semimetal candidate WTe_2”. In: *Phys. Rev. B* 94 (12 2016), p. 121113. DOI: 10.1103/PhysRevB.94.121113.

[46] Ling Lu et al. “Weyl points and line nodes in gyroid photonic crystals”. In: *Nature Photonics* 7.4 (2013), pp. 294–299. ISSN: 1749-4893. DOI: 10.1038/nphoton.2013.42.

[47] Wen-Jie Chen, Meng Xiao, and C. T. Chan. “Photonic crystals possessing multiple Weyl points and the experimental observation of robust surface states”. In: *Nature Communications* 7.1 (2016), p. 13038. ISSN: 2041-1723. DOI: 10.1038/ncomms13038.

[48] Matthias Saba et al. “Group Theoretical Route to Deterministic Weyl Points in Chiral Photonic Lattices”. In: *Phys. Rev. Lett.* 119 (22 2017), p. 227401. DOI: 10.1103/PhysRevLett.119.227401.

[49] Biao Yang et al. “Ideal Weyl points and helicoid surface states in artificial photonic crystal structures”. In: *Science* 359.6379 (2018), pp. 1013–1016. ISSN: 0036-8075. DOI: 10.1126/science.aaq1221.

[50] Masaru Onoda, Shuichi Murakami, and Naoto Nagaosa. “Hall Effect of Light”. In: *Phys. Rev. Lett.* 93 (8 2004), p. 083901. DOI: 10.1103/PhysRevLett.93.083901.

[51] Konstantin Y. Bliokh, Daria Smirnova, and Franco Nori. “Quantum spin Hall effect of light”. In: *Science* 348.6242 (2015), pp. 1448–1451. ISSN: 0036-8075. DOI: 10.1126/science.aaa9519.

[52] K. Y. Bliokh et al. “Spin–orbit interactions of light”. In: *Nature Photonics* 9.12 (2015), pp. 796–808. ISSN: 1749-4893. DOI: 10.1038/nphoton.2015.201.

[53] Xiu Gu et al. “Microwave photonics with superconducting quantum circuits”. In: *Physics Reports* 718-719 (2017). Microwave photonics with superconducting quantum circuits, pp. 1 –102. ISSN: 0370-1573. DOI: 10.1016/j.physrep.2017.10.002.

[54] Zhilin Li et al. “Weyl Semimetal TaAs: Crystal Growth, Morphology, and Thermodynamics”. In: *Crystal Growth & Design* 16.3 (2016), pp. 1172–1175. DOI: 10.1021/acs.cgd.5b01758.

[55] Liang Wu et al. “Giant anisotropic nonlinear optical response in transition metal monopnictide Weyl semimetals”. In: *Nature Physics* 13.4 (2017), pp. 350–355. ISSN: 1745-2481. DOI: 10.1038/nphys3969.

[56] B. Xu et al. “Temperature-tunable Fano resonance induced by strong coupling between Weyl fermions and phonons in TaAs”. In: *Nature Communications* 8.1 (2017), p. 14933. ISSN: 2041-1723. DOI: 10.1038/ncomms14933.

[57] Zhi Li et al. “Second harmonic generation in the Weyl semimetal TaAs from a quantum kinetic equation”. In: *Phys. Rev. B* 97 (8 2018), p. 085201. DOI: 10.1103/PhysRevB.97.085201.

[58] Y. Gao et al. “Chiral terahertz wave emission from the Weyl semimetal TaAs”. In: *Nature Communications* 11.1 (2020), p. 720. ISSN: 2041-1723. DOI: 10.1038/s41467-020-14463-1.

[59] F., Wooten. "Optical properties of solids". In: New York: Academic Press, 1972. Chap. 3. ISBN: 978-0080168463.

[60] Christina A. C. Garcia, Jennifer Coulter, and Prineha Narang. "Optoelectronic response of the type-I Weyl semimetals TaAs and NbAs from first principles". In: *Phys. Rev. Research* 2 (1 2020), p. 013073. DOI: 10.1103/PhysRevResearch.2.013073.

[61] B. E. Brown. "The crystal structures of WTe_2 and high-temperature $MoTe_2$". In: *Acta Crystallographica* 20.2 (1966), pp. 268–274. DOI: 10.1107/S0365110X66000513.

[62] Yu Tao et al. "T_d to $1T^{'}$ structural phase transition in the WTe_2 Weyl semimetal". In: *Phys. Rev. B* 102 (6 2020), p. 060103. DOI: 10.1103/PhysRevB.102.060103.

[63] Yonghui Zhou et al. "Pressure-induced Td to 1T' structural phase transition in WTe_2". In: *AIP Advances* 6.7 (2016), p. 075008. DOI: 10.1063/1.4959026. URL: 10.1063/1.4959026.

[64] Mazhar N. Ali et al. "Correlation of crystal quality and extreme magnetoresistance of WTe_2". In: *EPL (Europhysics Letters)* 110.6 (2015), p. 67002. DOI: 10.1209/0295-5075/110/67002.

[65] M N Ali et al. "Large, non-saturating magnetoresistance in WTe_2". In: *Nature* 514 (2014), p. 205. URL: 10.1038/nature13763.

[66] Sanfeng Wu et al. "Observation of the quantum spin Hall effect up to 100 kelvin in a monolayer crystal". In: *Science* 359.6371 (2018), pp. 76–79. ISSN: 0036-8075. DOI: 10.1126/science.aan6003.

[67] Pankaj Sharma et al. "A room-temperature ferroelectric semimetal". In: *Science Advances* 5.7 (2019). DOI: 10.1126/sciadv.aax5080.

[68] A. J. Frenzel et al. "Anisotropic electrodynamics of type-II Weyl semimetal candidate WTe_2". In: *Phys. Rev. B* 95 (24 2017), p. 245140. DOI: 10.1103/PhysRevB.95.245140.

[69] Y. L. Wang et al. "Origin of the turn-on temperature behavior in WTe_2". In: *Phys. Rev. B* 92 (18 2015), p. 180402. DOI: 10.1103/PhysRevB.92.180402.

[70] L. R. Thoutam et al. "Temperature-Dependent Three-Dimensional Anisotropy of the Magnetoresistance in WTe_2". In: *Phys. Rev. Lett.* 115 (4 2015), p. 046602. DOI: 10.1103/PhysRevLett.115.046602.

[71] Yang-Yang Lv et al. "Dramatically decreased magnetoresistance in non-stoichiometric WTe_2 crystals". In: *Scientific Reports* 6.1 (2016), p. 26903. ISSN: 2045-2322. DOI: 10.1038/srep26903.

[72] Jianchao Meng et al. "Large linear magnetoresistance caused by disorder in $WTe_{2-\delta}$ thin film". In: *Journal of Physics: Condensed Matter* 32.35 (2020), p. 355703. DOI: 10.1088/1361-648x/ab8d74.

[73] Steven Flynn, Mazhar Ali, and R. J. Cava. *The Effect of Dopants on the Magnetoresistance of* WTe_2. 2015. arXiv: 1506.07069 [cond-mat.mtrl-sci].

[74] Yan Song, Xiaocha Wang, and Wenbo Mi. "Spin splitting and reemergence of charge compensation in monolayer WTe_2 by 3d transition-metal adsorption". In: *Phys. Chem. Chem. Phys.* 19 (11 2017), pp. 7721–7727. DOI: 10.1039/C7CP00723J.

[75] Wei Lai Liu et al. “Effect of aging-induced disorder on the quantum transport properties of few-layer WTe_2”. In: *2D Materials* 4.1 (2016), p. 011011. DOI: 10.1088/2053-1583/4/1/011011.

[76] John M. Woods et al. “Suppression of Magnetoresistance in Thin WTe_2 Flakes by Surface Oxidation”. In: *ACS Applied Materials & Interfaces* 9.27 (2017), pp. 23175–23180. DOI: 10.1021/acsami.7b04934.

[77] Na Hyun Jo et al. “Magnetoelastoresistance in WTe_2: Exploring electronic structure and extremely large magnetoresistance under strain”. In: *Proceedings of the National Academy of Sciences* 116.51 (2019), pp. 25524–25529. ISSN: 0027-8424. DOI: 10.1073/pnas.1910695116.

[78] H. Y. Lv et al. “Perfect charge compensation in WTe_2 for the extraordinary magnetoresistance: From bulk to monolayer”. In: *EPL (Europhysics Letters)* 110.3 (2015), p. 37004. DOI: 10.1209/0295-5075/110/37004.

[79] Enze Zhang et al. “Tunable Positive to Negative Magnetoresistance in Atomically Thin WTe_2”. In: *Nano Letters* 17.2 (2017), pp. 878–885. DOI: 10.1021/acs.nanolett.6b04194.

[80] Lin Wang et al. “Tuning magnetotransport in a compensated semimetal at the atomic scale”. In: *Nature Communications* 6.1 (2015), p. 8892. ISSN: 2041-1723. DOI: 10.1038/ncomms9892.

[81] Junhong Na et al. “Tuning the magnetoresistance of ultrathin WTe_2 sheets by electrostatic gating”. In: *Nanoscale* 8 (44 2016), pp. 18703–18709. DOI: 10.1039/C6NR06327F.

[82] Xin Liu et al. “Gate tunable magneto-resistance of ultra-thin WTe_2 devices”. In: *2D Materials* 4.2 (2017), p. 021018. DOI: 10.1088/2053-1583/aa613b.

[83] Yaojia Wang et al. “Gate-tunable negative longitudinal magnetoresistance in the predicted type-II Weyl semimetal WTe2”. In: *Nature Communications* 7.1 (2016), p. 13142. ISSN: 2041-1723. DOI: 10.1038/ncomms13142.

[84] Lin Hu et al. “Significantly enhanced magnetoresistance in monolayer WTe_2 via heterojunction engineering: a first-principles study”. In: *Nanoscale* 10 (47 2018), pp. 22231–22236. DOI: 10.1039/C8NR04391D.

[85] Defen Kang et al. “Superconductivity emerging from a suppressed large magnetoresistant state in tungsten ditelluride”. In: *Nature Communications* 6.1 (2015), p. 7804. ISSN: 2041-1723. DOI: 10.1038/ncomms8804.

[86] I. Pletikosić et al. “Electronic Structure Basis for the Extraordinary Magnetoresistance in WTe_2”. In: *Phys. Rev. Lett.* 113 (21 2014), p. 216601. DOI: 10.1103/PhysRevLett.113.216601.

[87] Xing-Chen Pan et al. “Carrier balance and linear magnetoresistance in type-II Weyl semimetal WTe_2”. In: *Frontiers of Physics* 12.3 (2017), p. 127203. ISSN: 2095-0470. DOI: 10.1007/s11467-016-0629-7.

[88] Yaojia Wang et al. “Direct Evidence for Charge Compensation-Induced Large Magnetoresistance in Thin WTe_2”. In: *Nano Letters* 19.6 (2019), pp. 3969–3975. DOI: 10.1021/acs.nanolett.9b01275.

[89] A.B. Pippard. *Magnetoresistance in Metals*. Cambridge Studies in Low Temperature Physics. Cambridge University Press, 2009. ISBN: 9780521118804.

[90] Xu Du et al. "Metal-Insulator-Like Behavior in Semimetallic Bismuth and Graphite". In: *Phys. Rev. Lett.* 94 (16 2005), p. 166601. DOI: 10.1103/PhysRevLett.94.166601.

[91] Benoît Fauqué et al. "Electronic instability in bismuth far beyond the quantum limit". In: *New Journal of Physics* 11.11 (2009), p. 113012. DOI: 10.1088/1367{-}2630/11/11/113012.

[92] Y. Kopelevich et al. "Reentrant Metallic Behavior of Graphite in the Quantum Limit". In: *Phys. Rev. Lett.* 90 (15 2003), p. 156402. DOI: 10.1103/PhysRevLett.90.156402.

[93] Chandra Shekhar et al. "Extremely large magnetoresistance and ultrahigh mobility in the topological Weyl semimetal candidate NbP". In: *Nature Physics* 11.8 (2015), pp. 645–649. ISSN: 1745-2481. DOI: 10.1038/nphys3372.

[94] F. C. Chen et al. "Extremely large magnetoresistance in the type-II Weyl semimetal $MoTe_2$". In: *Phys. Rev. B* 94 (23 2016), p. 235154. DOI: 10.1103/PhysRevB.94.235154.

[95] Sangyun Lee et al. "Origin of extremely large magnetoresistance in the candidate type-II Weyl semimetal $MoTe_{2-x}$". In: *Scientific Reports* 8.1 (2018), p. 13937. ISSN: 2045-2322. DOI: 10.1038/s41598-018-32387-1.

[96] Desheng Wu et al. "Giant semiclassical magnetoresistance in high mobility $TaAs_2$ semimetal". In: *Applied Physics Letters* 108.4 (2016), p. 042105. DOI: 10.1063/1.4940924.

[97] Yilin Wang et al. "Breakdown of compensation and persistence of nonsaturating magnetoresistance in gated WTe_2 thin flakes". In: *Phys. Rev. B* 93 (12 2016), p. 121108. DOI: 10.1103/PhysRevB.93.121108.

[98] Chen-Lu Wang et al. "Evidence of Electron-Hole Imbalance in WTe_2 from High-Resolution Angle-Resolved Photoemission Spectroscopy". In: *Chinese Physics Letters* 34.9 (2017), p. 097305. DOI: 10.1088/0256-307x/34/9/097305.

[99] Valla Fatemi et al. "Magnetoresistance and quantum oscillations of an electrostatically tuned semimetal-to-metal transition in ultrathin WTe_2". In: *Phys. Rev. B* 95 (4 2017), p. 041410. DOI: 10.1103/PhysRevB.95.041410.

[100] Domenico Di Sante et al. "Three-Dimensional Electronic Structure of the Type-II Weyl Semimetal WTe_2". In: *Phys. Rev. Lett.* 119 (2 2017), p. 026403. DOI: 10.1103/PhysRevLett.119.026403.

[101] F. Y. Bruno et al. "Observation of large topologically trivial Fermi arcs in the candidate type-II Weyl semimetal WTe_2". In: *Phys. Rev. B* 94 (12 2016), p. 121112. DOI: 10.1103/PhysRevB.94.121112.

[102] Chenlu Wang et al. "Observation of Fermi arc and its connection with bulk states in the candidate type-II Weyl semimetal WTe_2". In: *Phys. Rev. B* 94 (24 2016), p. 241119. DOI: 10.1103/PhysRevB.94.241119.

[103] Peng Li et al. "Evidence for topological type-II Weyl semimetal WTe_2". In: *Nature Communications* 8.1 (2017), p. 2150. ISSN: 2041-1723. DOI: 10.1038/s41467-017-02237-1.

[104] Y. M. Dai et al. "Ultrafast carrier dynamics in the large-magnetoresistance material WTe_2". In: *Phys. Rev. B* 92 (16 2015), p. 161104. DOI: 10.1103/PhysRevB.92.161104.

[105] Bin He et al. “Coherent optical phonon oscillation and possible electronic softening in WTe_2 crystals”. In: *Scientific Reports* 6.1 (2016), p. 30487. ISSN: 2045-2322. DOI: 10.1038/srep30487.

[106] Davide Soranzio et al. “Ultrafast broadband optical spectroscopy for quantifying subpicometric coherent atomic displacements in WTe_2”. In: *Phys. Rev. Research* 1 (3 2019), p. 032033. DOI: 10.1103/PhysRevResearch.1.032033.

[107] M.-Y. Yao et al. “Observation of Weyl Nodes in Robust Type-II Weyl Semimetal WP_2”. In: *Phys. Rev. Lett.* 122 (17 2019), p. 176402. DOI: 10.1103/PhysRevLett.122.176402.

[108] Evan O. Kane. “Band structure of indium antimonide”. In: *Journal of Physics and Chemistry of Solids* 1.4 (1957), pp. 249 –261. ISSN: 0022-3697. DOI: 10.1016/0022-3697(57)90013-6.

[109] E. O. Kane. “Band structure of narrow gap semiconductors”. In: *Narrow Gap Semiconductors Physics and Applications*. Ed. by Wlodek Zawadzki. Berlin, Heidelberg: Springer Berlin Heidelberg, 1980, pp. 13–31. ISBN: 978-3-540-38382-6.

[110] Lok C. Lew Yan Voon and M. Willatzen. *The k·p method*. Berlin, Heidelberg: Springer-Verlag, 2009.

[111] Peter Yu and Manuel Cardona. *Fundamental of Semiconductors*. Berlin, Heidelberg: Springer-Verlag, 2010.

[112] M. Marchewka et al. “Massless Dirac fermions in semimetal HgCdTe”. In: *Solid State Communications* 250 (2017), pp. 104 –107. ISSN: 0038-1098. DOI: doi.org/10.1016/j.ssc.2016.11.020.

[113] F. Teppe et al. “Temperature-driven massless Kane fermions in HgCdTe crystals”. In: *Nature Communications* 7.1 (2016), p. 12576. ISSN: 2041-1723. DOI: 10.1038/ncomms12576.

[114] M. A. Kinch. In: *Fundamentals of Infrared Detectors*. SPIE Publications, 2007. Chap. 7. DOI: 10.1117/3.741688.

[115] Sang Dong Yoo and Kae Dal Kwack. “Theoretical calculation of electron mobility in HgCdTe”. In: *Journal of Applied Physics* 81.2 (1997), pp. 719–725. DOI: 10.1063/1.364212.

[116] M. Hakl et al. “Energy scale of Dirac electrons in Cd_3As_2”. In: *Phys. Rev. B* 97 (11 2018), p. 115206. DOI: 10.1103/PhysRevB.97.115206.

[117] Adriano Mosca Conte, Olivia Pulci, and Friedhelm Bechstedt. “Electronic and optical properties of topological semimetal Cd_3As_2”. In: *Scientific Reports* 7.1 (2017), p. 45500. ISSN: 2045-2322. DOI: 10.1038/srep45500.

[118] Aizhu Wang et al. “Kane Fermion in a Two-Dimensional π-Conjugated Bis(iminothiolato) nickel Monolayer”. In: *The Journal of Physical Chemistry Letters* 9.3 (2018), pp. 614–619. DOI: 10.1021/acs.jpclett.7b03021.

[119] P. Norton. “HgCdTe infrared detectors”. In: *Optoelectronics review* 3 (2002), pp. 159–174.

[120] Wen Lei, Jarek Antoszewski, and Lorenzo Faraone. “Progress, challenges, and opportunities for HgCdTe infrared materials and detectors”. In: *Applied Physics Reviews* 2.4 (2015), p. 041303. DOI: 10.1063/1.4936577.

[121] Ralf Dornhaus and Günter Nimtz. "The properties and applications of the $Hg_{1-x}Cd_xTe$ alloy system". In: *Solid-State Physics*. Berlin, Heidelberg: Springer Berlin Heidelberg, 1976, pp. 1–119. DOI: 10.1007/BFb0119322.

[122] Junhao Chu, Shichou Xu, and Dingyuan Tang. "Energy gap versus alloy composition and temperature in $Hg_{1-x}Cd_xTe$". In: *Applied Physics Letters* 43.11 (1983), pp. 1064–1066. DOI: 10.1063/1.94237.

[123] Philipp Leubner et al. "Strain Engineering of the Band Gap of HgTe Quantum Wells Using Superlattice Virtual Substrates". In: *Phys. Rev. Lett.* 117 (8 2016), p. 086403. DOI: 10.1103/PhysRevLett.117.086403.

[124] C. Brüne et al. "Quantum Hall Effect from the Topological Surface States of Strained Bulk HgTe". In: *Phys. Rev. Lett.* 106 (12 2011), p. 126803. DOI: 10.1103/PhysRevLett.106.126803.

[125] B. Andrei Bernevig, Taylor L. Hughes, and Shou-Cheng Zhang. "Quantum Spin Hall Effect and Topological Phase Transition in HgTe Quantum Wells". In: *Science* 314.5806 (2006), pp. 1757–1761. ISSN: 0036-8075. DOI: 10.1126/science.1133734.

[126] Markus König et al. "Quantum Spin Hall Insulator State in HgTe Quantum Wells". In: *Science* 318.5851 (2007), pp. 766–770. ISSN: 0036-8075. DOI: 10.1126/science.1148047.

[127] Y Betancur-Ocampo and V Gupta. "Perfect transmission of 3D massive Kane fermions in HgCdTe Veselago lenses". In: *Journal of Physics: Condensed Matter* 30.3 (2017), p. 035501. DOI: 10.1088/1361-648x/aa9ca6.

[128] G. L. Hansen and J. L. Schmit. "Calculation of intrinsic carrier concentration in $Hg_{1-x}Cd_xTe$". In: *Journal of Applied Physics* 54.3 (1983), pp. 1639–1640. DOI: 10.1063/1.332153.

[129] M. Grynberg, R. Le Toullec, and M. Balkanski. "Dielectric function in HgTe between 8 and 300°K". In: *Phys. Rev. B* 9 (2 1974), pp. 517–526. DOI: 10.1103/PhysRevB.9.517.

[130] S. P. Kozyrev, L. K. Vodopyanov, and R. Triboulet. "Structural analysis of the semiconductor-semimetal alloy $Cd_{1-x}Hg_xTe$ by infrared lattice-vibration spectroscopy". In: *Phys. Rev. B* 58 (3 1998), pp. 1374–1384. DOI: 10.1103/PhysRevB.58.1374.

[131] J. Polit et al. "Additional and canonical phonon modes in $Hg_{1-x}Cd_xTe(0.06 \leq x \leq 0.7)$". In: *Phys. Rev. B* 82 (1 2010), p. 014306. DOI: 10.1103/PhysRevB.82.014306.

[132] Katherine C. Phillips et al. "Ultrafast laser processing of materials: a review". In: *Adv. Opt. Photon.* 7.4 (2015), pp. 684–712. DOI: 10.1364/AOP.7.000684.

[133] P. Atkins and J. de Paula. *Atkins' Physical Chemistry*. OUP Oxford, 2010. ISBN: 9780199543373.

[134] Brian R. Pamplin. *Crystal growth, second edition*. Pergamon Press, 2013.

[135] Claude Rulliere. *Femtosecond Laser Pulses*. Springer-Verlag New York, 2005.

[136] C. V. Shank, R. Yen, and C. Hirlimann. "Time-Resolved Reflectivity Measurements of Femtosecond-Optical-Pulse-Induced Phase Transitions in Silicon". In: *Phys. Rev. Lett.* 50 (6 1983), pp. 454–457. DOI: 10.1103/PhysRevLett.50.454.

[137] Christian Rischel et al. "Femtosecond time-resolved X-ray diffraction from laser-heated organic films". In: *Nature* 390.6659 (1997), pp. 490–492. ISSN: 1476-4687. DOI: 10.1038/37317.

[138] F. Schmitt et al. "Transient Electronic Structure and Melting of a Charge Density Wave in $TbTe_3$". In: *Science* 321.5896 (2008), pp. 1649–1652. ISSN: 0036-8075. DOI: 10.1126/science.1160778.

[139] Simone Peli et al. "Time-resolved VUV ARPES at 10.8 eV photon energy and MHz repetition rate". In: *Journal of Electron Spectroscopy and Related Phenomena* 243 (2020), p. 146978. ISSN: 0368-2048. DOI: 10.1016/j.elspec.2020.146978.

[140] Søren Ulstrup et al. "Ultrafast electron dynamics in epitaxial graphene investigated with time- and angle-resolved photoemission spectroscopy". In: *Journal of Physics: Condensed Matter* 27.16 (2015), p. 164206. DOI: 10.1088/0953-8984/27/16/164206.

[141] Federico Cilento et al. "Dynamics of correlation-frozen antinodal quasiparticles in superconducting cuprates". In: *Science Advances* 4.2 (2018). DOI: 10.1126/sciadv.aar1998.

[142] C Manzoni and G Cerullo. "Design criteria for ultrafast optical parametric amplifiers". In: *Journal of Optics* 18.10 (2016), p. 103501. DOI: 10.1088/2040-8978/18/10/103501.

[143] D.T. Reid et al. "Advances in ultrafast optical parametric oscillators". In: *Laser Physics Letters* 8.1 (2010), pp. 8–15. DOI: 10.1002/lapl.201010085.

[144] Jinendra K. Ranka, Robert S. Windeler, and Andrew J. Stentz. "Visible continuum generation in air–silica microstructure optical fibers with anomalous dispersion at 800 nm". In: *Opt. Lett.* 25.1 (2000), pp. 25–27. DOI: 10.1364/OL.25.000025.

[145] Stuart Shizhuo Yin et al. "Supercontinuum generation in single crystal sapphire fibers". In: *Optics Communications* 281.5 (2008), pp. 1113 –1117. ISSN: 0030-4018. DOI: 10.1016/j.optcom.2007.10.099.

[146] A. Ermolov et al. "Supercontinuum generation in the vacuum ultraviolet through dispersive-wave and soliton-plasma interaction in a noble-gas-filled hollow-core photonic crystal fiber". In: *Phys. Rev. A* 92 (3 2015), p. 033821. DOI: 10.1103/PhysRevA.92.033821.

[147] R. W. Schoenlein et al. "Femtosecond studies of nonequilibrium electronic processes in metals". In: *Phys. Rev. Lett.* 58 (16 1987), pp. 1680–1683. DOI: 10.1103/PhysRevLett.58.1680.

[148] Rogier H. M. Groeneveld, Rudolf Sprik, and Ad Lagendijk. "Femtosecond spectroscopy of electron-electron and electron-phonon energy relaxation in Ag and Au". In: *Phys. Rev. B* 51 (17 1995), pp. 11433–11445. DOI: 10.1103/PhysRevB.51.11433.

[149] B. Mansart et al. "Ultrafast transient response and electron-phonon coupling in the iron-pnictide superconductor $Ba(Fe_{1-x}Co_x)_2As_2$". In: *Phys. Rev. B* 82 (2 2010), p. 024513. DOI: 10.1103/PhysRevB.82.024513.

[150] B. Mansart et al. "Temperature-dependent electron-phonon coupling in $La_{2-x}Sr_xCuO_4$ probed by femtosecond x-ray diffraction". In: *Phys. Rev. B* 88 (5 2013), p. 054507. DOI: 10.1103/PhysRevB.88.054507.

[151] M. Ligges et al. "Observation of ultrafast lattice heating using time resolved electron diffraction". In: *Applied Physics Letters* 94.10 (2009), p. 101910. DOI: 10.1063/1.3095497.

[152] T. K. Cheng et al. “Impulsive excitation of coherent phonons observed in reflection in bismuth and antimony”. In: *Applied Physics Letters* 57.10 (1990), pp. 1004–1006. DOI: 10.1063/1.104090.

[153] Kunie Ishioka et al. “Coherent optical phonons in diamond”. In: *Applied Physics Letters* 89.23 (2006), p. 231916. DOI: 10.1063/1.2402231.

[154] H. J. Zeiger et al. “Theory for displacive excitation of coherent phonons”. In: *Phys. Rev. B* 45 (2 1992), pp. 768–778. DOI: 10.1103/PhysRevB.45.768.

[155] R. Merlin. “Generating coherent THz phonons with light pulses”. In: *Solid State Communications* 102.2 (1997). Highlights in Condensed Matter Physics and Materials Science, pp. 207 –220. ISSN: 0038-1098. DOI: 10.1016/S0038-1098(96)00721-1.

[156] T. E. Stevens, J. Kuhl, and R. Merlin. “Coherent phonon generation and the two stimulated Raman tensors”. In: *Phys. Rev. B* 65 (14 2002), p. 144304. DOI: 10.1103/PhysRevB.65.144304.

[157] R. W. James. *The optical principles of the diffraction of x-rays, The crystalline state - vol. II*. London: G. Bell & Sons, 1962.

[158] C. Hammond. *The Basics of Crystallography and Diffraction*. IUCr monographs on crystallography. Oxford University Press, 2015. ISBN: 9780198738671.

[159] Donald H Bilderback, Pascal Elleaume, and Edgar Weckert. “Review of third and next generation synchrotron light sources”. In: *Journal of Physics B: Atomic, Molecular and Optical Physics* 38.9 (2005), S773–S797. DOI: 10.1088/0953-4075/38/9/022.

[160] Zhirong Huang and Kwang-Je Kim. “Review of x-ray free-electron laser theory”. In: *Phys. Rev. ST Accel. Beams* 10 (3 2007), p. 034801. DOI: 10.1103/PhysRevSTAB.10.034801.

[161] A. Mozzanica et al. “The JUNGFRAU Detector for Applications at Synchrotron Light Sources and XFELs”. In: *Synchrotron Radiation News* 31.6 (2018), pp. 16–20. DOI: 10.1080/08940886.2018.1528429.

[162] R. W. Schoenlein et al. “Generation of Femtosecond Pulses of Synchrotron Radiation”. In: *Science* 287.5461 (2000), pp. 2237–2240. ISSN: 0036-8075. DOI: 10.1126/science.287.5461.2237.

[163] P. Beaud et al. “Ultrafast Structural Phase Transition Driven by Photoinduced Melting of Charge and Orbital Order”. In: *Phys. Rev. Lett.* 103 (15 2009), p. 155702. DOI: 10.1103/PhysRevLett.103.155702.

[164] S. L. Johnson et al. “Directly Observing Squeezed Phonon States with Femtosecond X-Ray Diffraction”. In: *Phys. Rev. Lett.* 102 (17 2009), p. 175503. DOI: 10.1103/PhysRevLett.102.175503.

[165] Praveen Kumar Maroju et al. “Attosecond pulse shaping using a seeded free-electron laser”. In: *Nature* 578.7795 (2020), pp. 386–391. ISSN: 1476-4687. DOI: 10.1038/s41586-020-2005-6.

[166] J. C. H. Spence. “XFELs for structure and dynamics in biology”. In: *IUCrJ* 4.4 (2017), pp. 322–339. DOI: 10.1107/S2052252517005760.

[167] Linda Young et al. “Roadmap of ultrafast x-ray atomic and molecular physics”. In: *Journal of Physics B: Atomic, Molecular and Optical Physics* 51.3 (2018), p. 032003. DOI: 10.1088/1361-6455/aa9735.

[168] A. Singer et al. “Photoinduced Enhancement of the Charge Density Wave Amplitude”. In: *Phys. Rev. Lett.* 117 (5 2016), p. 056401. DOI: 10.1103/PhysRevLett.117.056401.

[169] F. Bencivenga and C. Masciovecchio. “FEL-based transient grating spectroscopy to investigate nanoscale dynamics”. In: *Nuclear Instruments and Methods in Physics Research Section A: Accelerators, Spectrometers, Detectors and Associated Equipment* 606.3 (2009), pp. 785 –789. ISSN: 0168-9002. DOI: 10.1016/j.nima.2009.05.147.

[170] F. Bencivenga et al. “Four-wave mixing experiments with extreme ultraviolet transient gratings”. In: *Nature* 520.7546 (2015), pp. 205–208. ISSN: 1476-4687. DOI: 10.1038/nature14341.

[171] L. Foglia et al. “First Evidence of Purely Extreme-Ultraviolet Four-Wave Mixing”. In: *Phys. Rev. Lett.* 120 (26 2018), p. 263901. DOI: 10.1103/PhysRevLett.120.263901.

[172] H A Hafez et al. “Intense terahertz radiation and their applications”. In: *Journal of Optics* 18.9 (2016), p. 093004. DOI: 10.1088/2040-8978/18/9/093004.

[173] S S Dhillon et al. “The 2017 terahertz science and technology roadmap”. In: *Journal of Physics D: Applied Physics* 50.4 (2017), p. 043001. DOI: 10.1088/1361-6463/50/4/043001.

[174] David M. Slocum et al. “Atmospheric absorption of terahertz radiation and water vapor continuum effects”. In: *Journal of Quantitative Spectroscopy and Radiative Transfer* 127 (2013), pp. 49 –63. ISSN: 0022-4073. DOI: 10.1016/j.jqsrt.2013.04.022.

[175] Klaus Reimann. “Table-top sources of ultrashort THz pulses”. In: *Reports on Progress in Physics* 70.10 (2007), pp. 1597–1632. DOI: 10.1088/0034-4885/70/10/r02.

[176] Yehoshua Socol. “High-power free-electron lasers–technology and future applications”. In: *Optics & Laser Technology* 46 (2013), pp. 111 –126. ISSN: 0030-3992. DOI: 10.1016/j.optlastec.2012.06.040.

[177] A. Perucchi et al. “The TeraFERMI terahertz source at the seeded FERMI free-electron-laser facility”. In: *Review of Scientific Instruments* 84.2 (2013), p. 022702. DOI: 10.1063/1.4790428.

[178] Kazuue Fujita et al. “Recent progress in terahertz difference-frequency quantum cascade laser sources”. In: *Nanophotonics* 7.11 (2018), pp. 1795 –1817. DOI: 10.1515/nanoph-2018-0093.

[179] Yuanyuan Huang et al. “Surface Optical Rectification from Layered MoS_2 Crystal by THz Time-Domain Surface Emission Spectroscopy”. In: *ACS Applied Materials & Interfaces* 9.5 (2017), pp. 4956–4965. DOI: 10.1021/acsami.6b13961.

[180] Nick C. J. van der Valk et al. “Influence of pump wavelength and crystal length on the phase matching of optical rectification”. In: *J. Opt. Soc. Am. B* 22.8 (2005), pp. 1714–1718. DOI: 10.1364/JOSAB.22.001714.

[181] Fabian D. J. Brunner, Arno Schneider, and Peter Günter. "Velocity-matched terahertz generation by optical rectification in an organic nonlinear optical crystal using a Ti:sapphire laser". In: *Applied Physics Letters* 94.6 (2009), p. 061119. DOI: 10.1063/1.3080214.

[182] Lucas Huber. "Nonlinear electromagnetic probes for the study of ultrafast processes in condensed matter". en. PhD thesis. Zurich: ETH Zurich, 2017. DOI: 10.3929/ethz-b-000200226.

[183] Nicholas Karpowicz et al. "Coherent heterodyne time-domain spectrometry covering the entire "terahertz gap"". In: *Applied Physics Letters* 92.1 (2008), p. 011131. DOI: 10.1063/1.2828709.

[184] Shuai Lin, Shukai Yu, and Diyar Talbayev. "Measurement of Quadratic Terahertz Optical Nonlinearities Using Second-Harmonic Lock-in Detection". In: *Phys. Rev. Applied* 10 (4 2018), p. 044007. DOI: 10.1103/PhysRevApplied.10.044007.

[185] Jianming Dai, Xu Xie, and X.-C. Zhang. "Detection of Broadband Terahertz Waves with a Laser-Induced Plasma in Gases". In: *Phys. Rev. Lett.* 97 (10 2006), p. 103903. DOI: 10.1103/PhysRevLett.97.103903.

[186] Xiaofei Lu, Nicholas Karpowicz, and X.-C. Zhang. "Broadband terahertz detection with selected gases". In: *J. Opt. Soc. Am. B* 26.9 (2009), A66–A73. DOI: 10.1364/JOSAB.26.000A66.

[187] F. Sizov. "THz radiation sensors". In: *Opto-Electronics Review* 18.1 (2010), pp. 10 –36. DOI: 10.2478/s11772-009-0029-4.

[188] R. A. Kaindl et al. "Transient terahertz spectroscopy of excitons and unbound carriers in quasi-two-dimensional electron-hole gases". In: *Phys. Rev. B* 79 (4 2009), p. 045320. DOI: 10.1103/PhysRevB.79.045320.

[189] Shuntaro Tani, Fran çois Blanchard, and Koichiro Tanaka. "Ultrafast Carrier Dynamics in Graphene under a High Electric Field". In: *Phys. Rev. Lett.* 109 (16 2012), p. 166603. DOI: 10.1103/PhysRevLett.109.166603.

[190] I. Katayama et al. "Terahertz-field-induced carrier generation in $Bi_{1-x}Sb_x$ Dirac electron systems". In: *Phys. Rev. B* 98 (21 2018), p. 214302. DOI: 10.1103/PhysRevB.98.214302.

[191] T. Dekorsy et al. "THz electromagnetic emission by coherent infrared-active phonons". In: *Phys. Rev. B* 53 (7 1996), pp. 4005–4014. DOI: 10.1103/PhysRevB.53.4005.

[192] T. Kubacka et al. "Large-Amplitude Spin Dynamics Driven by a THz Pulse in Resonance with an Electromagnon". In: *Science* 343.6177 (2014), pp. 1333–1336. ISSN: 0036-8075. DOI: 10.1126/science.1242862.

[193] Junichi Nishitani et al. "Terahertz radiation from coherent antiferromagnetic magnons excited by femtosecond laser pulses". In: *Applied Physics Letters* 96.22 (2010), p. 221906. DOI: 10.1063/1.3436635.

[194] Thomas A. A. Oliver. "Recent advances in multidimensional ultrafast spectroscopy". In: *Royal Society Open Science* 5.1 (2018), p. 171425. DOI: 10.1098/rsos.171425.

[195] W. Kuehn et al. "Phase-resolved two-dimensional spectroscopy based on collinear n-wave mixing in the ultrafast time domain". In: *The Journal of Chemical Physics* 130.16 (2009), p. 164503. DOI: 10.1063/1.3120766.

[196] P. Bowlan et al. "Ultrafast terahertz response of multilayer graphene in the nonperturbative regime". In: *Phys. Rev. B* 89 (4 2014), p. 041408. DOI: 10.1103/PhysRevB.89.041408.

[197] Courtney L. Johnson, Brittany E. Knighton, and Jeremy A. Johnson. "Distinguishing Nonlinear Terahertz Excitation Pathways with Two-Dimensional Spectroscopy". In: *Phys. Rev. Lett.* 122 (7 2019), p. 073901. DOI: 10.1103/PhysRevLett.122.073901.

[198] Jian Lu et al. "Coherent Two-Dimensional Terahertz Magnetic Resonance Spectroscopy of Collective Spin Waves". In: *Phys. Rev. Lett.* 118 (20 2017), p. 207204. DOI: 10.1103/PhysRevLett.118.207204.

[199] Jian Lu et al. "Nonlinear two-dimensional terahertz photon echo and rotational spectroscopy in the gas phase". In: *Proceedings of the National Academy of Sciences* 113.42 (2016), pp. 11800–11805. ISSN: 0027-8424. DOI: 10.1073/pnas.1609558113.

[200] S. Houver et al. "2D THz spectroscopic investigation of ballistic conduction-band electron dynamics in InSb". In: *Opt. Express* 27.8 (2019), pp. 10854–10865. DOI: 10.1364/OE.27.010854.

[201] Shaul Mukamel. *Principles of nonlinear optical spectroscopy*. 6. Oxford University Press, 1999.

[202] C. C. Homes, M. N. Ali, and R. J. Cava. "Optical properties of the perfectly compensated semimetal WTe_2". In: *Phys. Rev. B* 92 (16 2015), p. 161109. DOI: 10.1103/PhysRevB.92.161109.

[203] Herman J. C. Berendsen. *Simulating the Physical World: Hierarchical Modeling from Quantum Mechanics to Fluid Dynamics*. Cambridge University Press, 2007. DOI: 10.1017/CBO9780511815348.

[204] Friedhelm Bechstedt. *Many-Body Approach to Electronic Excitations, Concepts and Applications*. Springer-Verlag, 2015. DOI: 10.1007/978-3-662-44593-8.

[205] Kurt Lejaeghere et al. "Reproducibility in density functional theory calculations of solids". In: *Science* 351.6280 (2016). ISSN: 0036-8075. DOI: 10.1126/science.aad3000.

[206] Anubhav Jain et al. "The Materials Project: A materials genome approach to accelerating materials innovation". In: *APL Materials* 1.1 (2013), p. 011002. ISSN: 2166532X. DOI: 10.1063/1.4812323.

[207] Leopold Talirz et al. "Materials Cloud, a platform for open computational science". In: *Scientific Data* 7.1 (2020), p. 299. ISSN: 2052-4463. DOI: 10.1038/s41597-020-00637-5.

[208] D. R. Hamann, M. Schlüter, and C. Chiang. "Norm-Conserving Pseudopotentials". In: *Phys. Rev. Lett.* 43 (20 1979), pp. 1494–1497. DOI: 10.1103/PhysRevLett.43.1494.

[209] P. E. Blöchl. "Projector augmented-wave method". In: *Phys. Rev. B* 50 (24 1994), pp. 17953–17979. DOI: 10.1103/PhysRevB.50.17953.

[210] John P. Perdew et al. "Atoms, molecules, solids, and surfaces: Applications of the generalized gradient approximation for exchange and correlation". In: *Phys. Rev. B* 46 (11 1992), pp. 6671–6687. DOI: 10.1103/PhysRevB.46.6671.

[211] T. Takeda. "The scalar relativistic approximation". In: *Zeitschrift für Physik B Condensed Matter* 32.1 (1978), pp. 43–48. ISSN: 1431-584X. DOI: 10.1007/BF01322185.

[212] D. R. Hamann. "Optimized norm-conserving Vanderbilt pseudopotentials". In: *Phys. Rev. B* 88 (8 2013), p. 085117. DOI: 10.1103/PhysRevB.88.085117.

[213] Andrea Dal Corso. "Pseudopotentials periodic table: From H to Pu". In: *Computational Materials Science* 95 (2014), pp. 337 –350. ISSN: 0927-0256. DOI: 10.1016/j.commatsci.2014.07.043.

[214] James D. Pack and Hendrik J. Monkhorst. ""Special points for Brillouin-zone integrations"—a reply". In: *Phys. Rev. B* 16 (4 1977), pp. 1748–1749. DOI: 10.1103/PhysRevB.16.1748.

[215] Mitsuaki Kawamura. "FermiSurfer: Fermi-surface viewer providing multiple representation schemes". In: *Computer Physics Communications* 239 (2019), pp. 197 –203. ISSN: 0010-4655. DOI: 10.1016/j.cpc.2019.01.017.

[216] Paolo Giannozzi et al. "QUANTUM ESPRESSO: a modular and open-source software project for quantum simulations of materials". In: *Journal of Physics: Condensed Matter* 21.39 (2009), p. 395502. DOI: 10.1088/0953-8984/21/39/395502.

[217] Stefano Baroni et al. "Phonons and related crystal properties from density-functional perturbation theory". In: *Rev. Mod. Phys.* 73 (2 2001), pp. 515–562. DOI: 10.1103/RevModPhys.73.515.

[218] Nicholas Rivera, Thomas Christensen, and Prineha Narang. "Phonon Polaritonics in Two-Dimensional Materials". In: *Nano Letters* 19.4 (2019), pp. 2653–2660. DOI: 10.1021/acs.nanolett.9b00518.

[219] R.W. Boyd. *Nonlinear Optics*. Academic Press, 2008.

[220] Michele Fabrizio. *Lecture notes on many-body theory*. URL: https://cm.sissa.it/phdsection/download.php?ID=14.

[221] Richard M. Martin, Lucia Reining, and David M. Ceperley. *Interacting Electrons: Theory and Computational Approaches*. Cambridge University Press, 2016. DOI: 10.1017/CBO9781139050807.

[222] Andrea Marini et al. "Yambo: An ab initio tool for excited state calculations". In: *Computer Physics Communications* 180.8 (2009), pp. 1392 –1403. ISSN: 0010-4655. DOI: 10.1016/j.cpc.2009.02.003.

[223] Davide Sangalli et al. "Many-body perturbation theory calculations using the yambo code". In: *Journal of Physics: Condensed Matter* 31.32 (2019), p. 325902. DOI: 10.1088/1361-648x/ab15d0.

[224] P Giannozzi et al. "Advanced capabilities for materials modelling with QUANTUM ESPRESSO". In: *Journal of Physics: Condensed Matter* 29.46 (2017), p. 465901. DOI: 10.1088/1361-648X/aa8f79.

[225] Xavier Gonze et al. "The Abinitproject: Impact, environment and recent developments". In: *Computer Physics Communications* 248 (2020), p. 107042. ISSN: 0010-4655. DOI: 10.1016/j.cpc.2019.107042.

[226] Andrea Marini and Rodolfo Del Sole. "Dynamical Excitonic Effects in Metals and Semiconductors". In: *Phys. Rev. Lett.* 91 (17 2003), p. 176402. DOI: 10.1103/PhysRevLett.91.176402.

[227] Andrea Marini, Giovanni Onida, and Rodolfo Del Sole. "Plane-wave DFT-LDA calculation of the electronic structure and absorption spectrum of copper". In: *Phys. Rev. B* 64 (19 2001), p. 195125. DOI: 10.1103/PhysRevB.64.195125.

[228] Paolo Giannozzi et al. "Quantum ESPRESSO toward the exascale". In: *The Journal of Chemical Physics* 152.15 (2020), p. 154105. DOI: 10.1063/5.0005082.

[229] Matteo Rini et al. "Control of the electronic phase of a manganite by mode-selective vibrational excitation". In: *Nature* 449 (2007), p. 72. DOI: 10.1038/nature06119.

[230] Daniele Nicoletti and Andrea Cavalleri. "Nonlinear light–matter interaction at terahertz frequencies". In: *Adv. Opt. Photon.* 8.3 (2016), pp. 401–464. DOI: 10.1364/AOP.8.000401.

[231] Thomas Dekorsy, Gyu Cheon Cho, and Heinrich Kurz. "Coherent phonons in condensed media". In: *Light Scattering in Solids VIII: Fullerenes, Semiconductor Surfaces, Coherent Phonons*. Berlin, Heidelberg: Springer Berlin Heidelberg, 2000, pp. 169–209. ISBN: 978-3-540-48755-5. DOI: 10.1007/BFb0084242.

[232] Kunie Ishioka and Oleg V. Misochko. "Coherent Lattice Oscillations in Solids and Their Optical Control". In: *Progress in Ultrafast Intense Laser Science: Volume V*. Berlin, Heidelberg: Springer Berlin Heidelberg, 2010, pp. 23–46. ISBN: 978-3-642-03825-9. DOI: 10.1007/978-3-642-03825-9_2.

[233] Alex V. Kuznetsov and Christopher J. Stanton. "Theory of Coherent Phonon Oscillations in Semiconductors". In: *Hot Carriers in Semiconductors*. Boston, MA: Springer US, 1996, pp. 217–220. ISBN: 978-1-4613-0401-2. DOI: 10.1007/978-1-4613-0401-2_51.

[234] A.A. Melnikov, O.V. Misochko, and S.V. Chekalin. "Generation of coherent phonons in bismuth by ultrashort laser pulses in the visible and NIR: Displacive versus impulsive excitation mechanism". In: *Physics Letters A* 375.19 (2011), pp. 2017 – 2022. ISSN: 0375-9601. DOI: 10.1016/j.physleta.2011.03.057.

[235] Seung-Hyun Kim et al. "Coherent phonon spectroscopy of the phase transition in VO_2 single crystals and thin films". In: *Journal of Applied Physics* 117.16 (2015), p. 163107. DOI: 10.1063/1.4919756.

[236] Kunie Ishioka et al. "Coherent phonon spectroscopy characterization of electronic bands at buried semiconductor heterointerfaces". In: *Applied Physics Letters* 108.5 (2016), p. 051607. DOI: 10.1063/1.4941397.

[237] Klaus Sokolowski-Tinten et al. "Femtosecond X-ray measurement of coherent lattice vibrations near the Lindemann stability limit". In: *Nature* 422 (2003), p. 287. DOI: 10.1038/nature01490.

[238] Robert P. Chatelain et al. "Coherent and Incoherent Electron-Phonon Coupling in Graphite Observed with Radio-Frequency Compressed Ultrafast Electron Diffraction". In: *Phys. Rev. Lett.* 113 (23 2014), p. 235502. DOI: 10.1103/PhysRevLett.113.235502.

[239] Yamanouchi Kaoru, Giulietti Antonio, and Ledingham Kenneth. *Progress in Ultrafast Intense Laser Science Volume V*. Springer Berlin Heidelberg, 2010. Chap. 2. ISBN: 978-3-642-03824-2.

[240] M. F. DeCamp et al. "Dynamics and coherent control of high-amplitude optical phonons in bismuth". In: *Phys. Rev. B* 64 (9 2001), p. 092301. DOI: 10.1103/PhysRevB.64.092301.

[241] H. Katsuki et al. “All-optical control and visualization of ultrafast two-dimensional atomic motions in a single crystal of bismuth”. In: *Nature Communications* 4 (2013), p. 2801. DOI: 10.1038/ncomms3801.

[242] Arthur Mar, Stephane Jobic, and James A. Ibers. “Metal-metal vs tellurium-tellurium bonding in WTe_2 and its ternary variants $TaIrTe_4$ and $NbIrTe_4$”. In: *Journal of the American Chemical Society* 114.23 (1992), pp. 8963–8971. ISSN: 0002-7863. DOI: 10.1021/ja00049a029.

[243] B. Amin, T. P. Kaloni, and U. Schwingenschlögl. “Strain engineering of WS_2, WSe_2, and WTe_2”. In: *RSC Adv.* 4 (65 2014), pp. 34561–34565. DOI: 10.1039/C4RA06378C.

[244] Pranab Kumar Das et al. “Layer-dependent quantum cooperation of electron and hole states in the anomalous semimetal WTe_2”. In: *Nature Communications* 7 (2016), p. 10847. DOI: 10.1038/ncomms10847.

[245] Anton Kokalj. “XCrySDen—a new program for displaying crystalline structures and electron densities”. In: *Journal of Molecular Graphics and Modelling* 17.3 (1999), pp. 176 –179. ISSN: 1093-3263. DOI: 10.1016/S1093-3263(99)00028-5.

[246] Davide Soranzio. “Time-resolved optical and photoelectronic studies of semimetallic transition metal dichalcogenide WTe_2”. MA thesis. Università degli studi di Trieste, 2017.

[247] M.J. van Setten et al. “The PseudoDojo: Training and grading a 85 element optimized norm-conserving pseudopotential table”. In: *Computer Physics Communications* 226 (2018), pp. 39 –54. ISSN: 0010-4655. DOI: 10.1016/j.cpc.2018.01.012.

[248] O. V. Misochko. “Control of the Dephasing of the Coherent Phonons Excited by Femtosecond Laser Pulses in Opaque Crystals”. In: *Journal of Experimental and Theoretical Physics* 128.6 (2019), pp. 827–839. ISSN: 1090-6509. DOI: 10.1134/S1063776119060050.

[249] Muneaki Hase et al. “Ultrafast dynamics of coherent optical phonons and nonequilibrium electrons in transition metals”. In: *Phys. Rev. B* 71 (18 2005), p. 184301. DOI: 10.1103/PhysRevB.71.184301.

[250] W.-D. Kong et al. “Raman scattering investigation of large positive magnetoresistance material WTe_2”. In: *Applied Physics Letters* 106.8 (2015), p. 081906. DOI: 10.1063/1.4913680.

[251] Dominik M. Juraschek and Sebastian F. Maehrlein. “Sum-frequency ionic Raman scattering”. In: *Phys. Rev. B* 97 (17 2018), p. 174302. DOI: 10.1103/PhysRevB.97.174302.

[252] Dominik M. Juraschek, Quintin N. Meier, and Prineha Narang. “Parametric Excitation of an Optically Silent Goldstone-Like Phonon Mode”. In: *Phys. Rev. Lett.* 124 (11 2020), p. 117401. DOI: 10.1103/PhysRevLett.124.117401.

[253] Y. L. Wang et al. “Origin of the turn-on temperature behavior in WTe_2”. In: *Phys. Rev. B* 92 (18 2015), p. 180402. DOI: 10.1103/PhysRevB.92.180402.

[254] Maximilian Trescher et al. “Charge density wave instabilities of type-II Weyl semimetals in a strong magnetic field”. In: *Phys. Rev. B* 96 (20 2017), p. 201101. DOI: 10.1103/PhysRevB.96.201101.

[255] Changgu Lee et al. "Anomalous Lattice Vibrations of Single- and Few-Layer MoS_2". In: *ACS Nano* 4.5 (2010), pp. 2695–2700. DOI: 10.1021/nn1003937.

[256] Petra Hein et al. "Mode-resolved reciprocal space mapping of electron-phonon interaction in the Weyl semimetal candidate Td-WTe_2". In: *Nature Communications* 11.1 (2020), p. 2613. ISSN: 2041-1723. DOI: 10.1038/s41467-020-16076-0.

[257] Gerhard Ingold et al. "Experimental station Bernina at SwissFEL: condensed matter physics on femtosecond time scales investigated by X-ray diffraction and spectroscopic methods". In: *Journal of Synchrotron Radiation* 26.3 (2019), pp. 874–886. DOI: 10.1107/S160057751900331X.

[258] HQ graphene. http://www.hqgraphene.com/.

[259] Chia-Hui Lee et al. "Tungsten Ditelluride: a layered semimetal". In: *Scientific Reports* 5.1 (2015), p. 10013. ISSN: 2045-2322. DOI: 10.1038/srep10013.

[260] Christian M. Schlepütz et al. "Angle calculations for a (2+3)-type diffractometer: focus on area detectors". In: *Journal of Applied Crystallography* 44.1 (2011), pp. 73–83. DOI: 10.1107/S0021889810048922.

[261] Jeffrey W. Edington. *Electron Diffraction in the Electron Microscope*. Palgrave, London, 1975.

[262] P. J. Brown et al. "Intensity of diffracted intensities". In: *International Tables for Crystallography*. Vol. C. International Union of Crystallography, 2006. Chap. 6.1.

[263] B.L. Henke, E.M. Gullikson, and J.C. Davis. "X-Ray Interactions: Photoabsorption, Scattering, Transmission, and Reflection at E = 50-30,000 eV, Z = 1-92". In: *Atomic Data and Nuclear Data Tables* 54.2 (1993), pp. 181 –342. ISSN: 0092-640X. DOI: 10.1006/adnd.1993.1013.

[264] Jane E. Callanan et al. "Thermodynamic properties of tungsten ditelluride (WTe_2) I. The preparation and lowtemperature heat capacity at temperatures from 6 K to 326 K". In: *The Journal of Chemical Thermodynamics* 24.6 (1992), pp. 627 –638. ISSN: 0021-9614. DOI: 10.1016/S0021-9614(05)80034-5.

[265] David R. Lide. *CRC Handbook of Chemistry and Physics, 85th Edition*. CRC Press, 2004. ISBN: 9780849304859.

[266] Wenchao Tian et al. "A Review of the Characteristics, Synthesis, and Thermodynamics of Type-II Weyl Semimetal WTe_2". eng. In: *Materials (Basel, Switzerland)* 11.7 (2018), p. 1185. ISSN: 1996-1944. DOI: 10.3390/ma11071185.

[267] E. Lassner and W.-D. Schubert. New York: Springer US, 1999.

[268] Nicola Marzari et al. "Thermal Contraction and Disordering of the Al(110) Surface". In: *Phys. Rev. Lett.* 82 (16 1999), pp. 3296–3299. DOI: 10.1103/PhysRevLett.82.3296.

[269] Rajveer Jha et al. "Anisotropy in the electronic transport properties of Weyl semimetal WTe_2 single crystals". In: *AIP Advances* 8.10 (2018), p. 101332. DOI: 10.1063/1.5043063.

[270] Qisheng Wang et al. "Anomalous Photothermoelectric Transport Due to Anisotropic Energy Dispersion in WTe_2". In: *Nano Letters* 19.4 (2019), pp. 2647–2652. DOI: 10.1021/acs.nanolett.9b00513.

[271] Hyun-Jung Kim et al. "Origins of the structural phase transitions in $MoTe_2$ and WTe_2". In: *Phys. Rev. B* 95 (18 2017), p. 180101. DOI: 10.1103/PhysRevB.95.180101.

[272] Gang Liu et al. "Temperature effect on lattice and electronic structures of WTe_2 from first-principles study". In: *Journal of Applied Physics* 121.4 (2017), p. 045104. DOI: 10.1063/1.4974946.

[273] Yanzhong Pei et al. "Low effective mass leading to high thermoelectric performance". In: *Energy Environ. Sci.* 5 (7 2012), pp. 7963–7969. DOI: 10.1039/C2EE21536E.

[274] Ofcom. *Supporting innovation in the 100-200 GHz range*. http://www.ofcom.org.uk/consultations-and-statements/category-2/supporting-innovation-100-200-ghz/.

[275] G. S. Jenkins et al. "Three-dimensional Dirac cone carrier dynamics in Na_3Bi and Cd_3As_2". In: *Phys. Rev. B* 94 (8 2016), p. 085121. DOI: 10.1103/PhysRevB.94.085121.

[276] A. G. Markelz et al. "Interband impact ionization by terahertz illumination of InAs heterostructures". In: *Applied Physics Letters* 69.26 (1996), pp. 3975–3977. DOI: 10.1063/1.117842.

[277] F. H. Su et al. "Terahertz pulse induced intervalley scattering in photoexcited GaAs". In: *Opt. Express* 17.12 (2009), pp. 9620–9629. DOI: 10.1364/OE.17.009620.

[278] E.O. Kane. "Zener tunneling in semiconductors". In: *Journal of Physics and Chemistry of Solids* 12.2 (1960), pp. 181 –188. ISSN: 0022-3697. DOI: 10.1016/0022-3697(60)90035-4.

[279] J. R. Taylor. "An Introduction to Error Analysis: The Study of Uncertainties in Physical Measurements". In: University Science Books, 1996.

[280] Jean-Luc Déziel, Louis J. Dubé, and Charles Varin. *Delayed-rate equations model for femtosecond laser-induced breakdown in dielectrics*. 2019. arXiv: 1906.08338 [physics.comp-ph].

[281] Dmitry Turchinovich, Jørn M. Hvam, and Matthias C. Hoffmann. "Self-phase modulation of a single-cycle terahertz pulse by nonlinear free-carrier response in a semiconductor". In: *Phys. Rev. B* 85 (20 2012), p. 201304. DOI: 10.1103/PhysRevB.85.201304.

[282] B. J. Ramshaw et al. "Quantum limit transport and destruction of the Weyl nodes in TaAs". In: *Nature Communications* 9.1 (2018), p. 2217. ISSN: 2041-1723. DOI: 10.1038/s41467-018-04542-9.

[283] Edward P. J. Parrott et al. "Understanding the Dielectric Properties of Heat-Treated Carbon Nanofibers at Terahertz Frequencies: a New Perspective on the Catalytic Activity of Structured Carbonaceous Materials". In: *The Journal of Physical Chemistry C* 113.24 (2009), pp. 10554–10559. DOI: 10.1021/jp811226d.

[284] Louis Tirino et al. "Temperature dependence of the impact ionization coefficients in GaAs, cubic SiC, and zinc-blende GaN". In: *Journal of Applied Physics* 94.1 (2003), pp. 423–430. DOI: 10.1063/1.1579129.

[285] A. Neviani et al. “Positive temperature dependence of the electron impact ionization coefficient in $In_{0.53}Ga_{0.47}$/As/InPHBTs”. In: *IEEE Electron Device Letters* 18.12 (1997), pp. 619–621. DOI: 10.1109/55.644089.

[286] N. S. Waldron et al. “Positive temperature coefficient of impact ionization in strained-Si”. In: *IEEE Transactions on Electron Devices* 52.7 (2005), pp. 1627–1633. DOI: 10.1109/TED.2005.850620.

[287] Torben Winzer, Andreas Knorr, and Ermin Malic. “Carrier Multiplication in Graphene”. In: *Nano Letters* 10.12 (2010), pp. 4839–4843. DOI: 10.1021/nl1024485.

[288] Davide Grassano et al. “Validity of Weyl fermion picture for transition metals monopnictides TaAs, TaP, NbAs, and NbP from ab initio studies”. In: *Scientific Reports* 8.1 (2018), p. 3534. ISSN: 2045-2322. DOI: 10.1038/s41598-018-21465-z.

[289] G. L. Hansen, J. L. Schmit, and T. N. Casselman. “Energy gap versus alloy composition and temperature in $Hg_{1-x}Cd_xTe$”. In: *Journal of Applied Physics* 53.10 (1982), pp. 7099–7101. DOI: 10.1063/1.330018.

[290] S. Dvoretsky et al. “Growth of HgTe Quantum Wells for IR to THz Detectors”. In: *Journal of Electronic Materials* 39.7 (2010), pp. 918–923. ISSN: 1543-186X. DOI: 10.1007/s11664-010-1191-7.

[291] Paul C. M. Planken et al. “Measurement and calculation of the orientation dependence of terahertz pulse detection in ZnTe”. In: *J. Opt. Soc. Am. B* 18.3 (2001), pp. 313–317. DOI: 10.1364/JOSAB.18.000313.

[292] S. Hubmann et al. “High-frequency impact ionization and nonlinearity of photocurrent induced by intense terahertz radiation in HgTe-based quantum well structures”. In: *Phys. Rev. B* 99 (8 2019), p. 085312. DOI: 10.1103/PhysRevB.99.085312.

[293] L. A. Falkovsky and E. G. Mishchenko. “Electron-lattice kinetics of metals heated by ultrashort laser pulses”. In: *Journal of Experimental and Theoretical Physics* 88.1 (1999), pp. 84–88. ISSN: 1090-6509. DOI: 10.1134/1.558768.

[294] J.K. Chen, J.E. Beraun, and C.L. Tham. “Ultrafast thermoelasticity for short-pulse laser heating”. In: *International Journal of Engineering Science* 42.8 (2004), pp. 793 –807. ISSN: 0020-7225. DOI: 10.1016/j.ijengsci.2003.11.001.

[295] Jie Chen et al. “Hot electrons blast wave generated by femtosecond laser pulses on thin Au(111) crystal, monitored by subpicosecond X-ray diffraction”. In: *Chemical Physics Letters* 419.4 (2006), pp. 374 –378. ISSN: 0009-2614. DOI: 10.1016/j.cplett.2005.12.010.